Mathematical modelling of electrical, thermal, and chemical processes occurring within a silicon furnace

Ellen Kay Luckins

Mansfield College

University of Oxford

A thesis submitted for the degree of

Doctor of Philosophy

Trinity 2021

Acknowledgements

Firstly, I want to thank my supervisors, Jim Oliver, Colin Please, and Robert Van Gorder, for sharing with me their knowledge, insight, and enthusiasm for applied mathematics. I am very grateful for their help and encouragement with this thesis, as with everything else over the past three years.

This thesis is based on work supported by the EPSRC Centre For Doctoral Training in Industrially Focused Mathematical Modelling (EP/L015803/1) in collaboration with Elkem ASA. My industrial supervisors at Elkem ASA have been instrumental in this research. Thank you to Ben Sloman, Egil Vålandsmyr Herland, and Aasgeir Valderhaug for your guidance and interest in my work.

I am grateful to Chris Breward and Colin Please for their dedication to the InFoMM CDT, which has made my time as a DPhil student so rich, varied, and enjoyable.

Thank you to the entirety of InFoMM Cohort 4, and especially to Lingyi, Olly, and Ambrose, for support and laughter as we learn how to be researchers.

Finally, thank you to Sally and Helena, inspirational scientists, musicians, and friends, for reminding me of the importance of representation in STEM. My thesis is dedicated to you.

Abstract

Silicon is produced in submerged arc furnaces (SAFs), with the heat needed for the endothermic chemical reactions provided by an electric current. The interacting physical processes occurring in SAFs are tightly coupled, and vary over a range of timescales. As a result, SAF modelling efforts have generally neglected to include many of the chemical, thermal, and electrical effects. In this thesis, we develop a mathematical framework to understand the mechanisms by which these processes interact.

We propose a new, simplified model for electric arcs in a SAF, with heat radiation as the dominant heat loss mechanism, based on dimensional analysis of a magnetohydrodynamic model. To understand the alternating current effects, we incorporate this arc model into an equivalent-circuit model for the SAF electrical system. We investigate the effects of hot gases flowing through the porous bed of raw materials in a SAF, by studying the interaction of a counter-current flow with an endothermic, temperature-dependent chemical reaction in the asymptotic limit of large Péclet number. Having better understood these mechanisms, we then develop a tractable model for the coupled processes taking place within a SAF, combining our arc model with simplified models for the raw material bed. In order to efficiently model processes on both the fast timescale of the alternating current, and the slower timescale of heat transfer and flow of the raw materials, we perform a multiple-timescale homogenisation.

Our modelling efforts give insight into the interaction of a counter-current flow with an endothermic chemical reaction across a range of parameter values for the heat transfer coefficient between the phases. Our arc model is derived from first principles, and compares favourably with empirical models currently used in the metallurgy literature and industry. Our homogenised furnace model provides a simple framework to explore interacting furnace processes of industrial relevance; solutions provide insight into the distribution of current in the furnace, the evolution of the internal structure, and how stoking may improve furnace efficiency.

Contents

List of Figures

Chapter 1

Introduction

Submerged arc furnaces (SAFs) have many uses in the metallurgy industry. They are used in the production of minerals such as silicon, phosphorus, and magnesium, as well as iron and ferro-alloys. SAFs also find use in the production of compound chemicals, such as titanium oxide, and for recycling applications [57]. Different furnace designs and configurations are used for different applications. This includes the use of both alternating and direct current, which may be provided by a single electrode or multiple electrodes, depending upon the material produced and the scale of the process [57].

The motivation for this thesis is to better understand processes occurring within a SAF for the production of silicon, although we note that some of our models and results will also have relevance for other metallurgical processes. Our research has been undertaken in collaboration with Elkem ASA, a major global producer of silicon and ferrosilicon alloys, with activities spanning the whole production process from quartz mining through to silicon production and also including silicone manufacturing. Silicon is produced on an industrial scale by reducing quartz rock with carbon in an alternating current (AC) SAF with three electrodes [104]. As with all SAF applications, the energy required for the chemical reactions is generated by an applied electric current. The majority of the current passes through a bed of raw- and partially-reacted materials as an electric arc, a type of continuous gas discharge, which forms in a cavity beneath the electrode, and is submerged in the material bed. However, some current is also conducted directly through the material bed, in parallel with the electric arc [88].

For efficient silicon production it is important that there is an appropriate distribution of electric current, and therefore of heat dissipated, between the current paths in the furnace. Since the electrical properties in both the arc and the material bed depend on the local temperature and material composition, the heat transfer, chemical reactions, and material flow are closely linked to the current distribution.

Indeed, we expect there to be a positive feedback between the electric current density and the local temperature within both the electric arc and the alternative current paths through the material bed. This is because in both cases the electrical conductivity increases with temperature, so that at higher temperatures more current flows, generating more Ohmic heating, and so raising the temperature further still.

It is very difficult to measure the internal furnace dynamics during operation, due to the extreme temperatures. Mathematical modelling is therefore a vital tool for understanding the silicon-production process. Previous studies (outlined below in Section 1.2.2) have investigated the distribution of current, but these generally only model the electromagnetic effects, and do not account for the interaction with heat transfer, chemical reactions, and material flow. Conversely, models focussed on the chemical reactions and material flow generally neglect to include the electric current. The goal of this thesis is to develop comprehensive models incorporating electrical, thermal, and chemical processes in the silicon furnace, allowing for a more complete understanding of the mechanisms driving the distribution of current within the furnace, as well as the wider silicon production process.

In this introductory chapter, we first describe properties of the SAF used for silicon production, including properties of the electrical current distribution problem, in Section 1.1. We then provide a review of literature studying the current flow through SAFs in Section 1.2, and the related processes of heat transfer, material flow, and chemical reactions within such SAFs. We summarise our modelling approach and how our work relates to literature beyond SAF applications in Section 1.3. We describe the contents of the rest of this thesis in Section 1.4, and give a statement of originality in Section 1.5.

1.1 Submerged arc furnaces for silicon production

A diagram of the submerged arc furnace used to produce silicon by Elkem ASA is given in Figure 1.1. The raw materials used in the process are quartz rock, carbon-rich coal, and woodchips. An electric current is passed through the material in the furnace via carbon electrodes, generating the heat necessary for the endothermic, silicon-producing chemical reactions. The three electrodes, two of which are illustrated in Figure 1.1, provide a three-phase alternating current. Furnaces are usually circular, with internal diameter of around 9 m, and the three electrodes are arranged in a triangle, with centres approximately 3 m apart [1]. As described in [85] and [104], a fully operational silicon SAF consists of many regions with distinct properties.

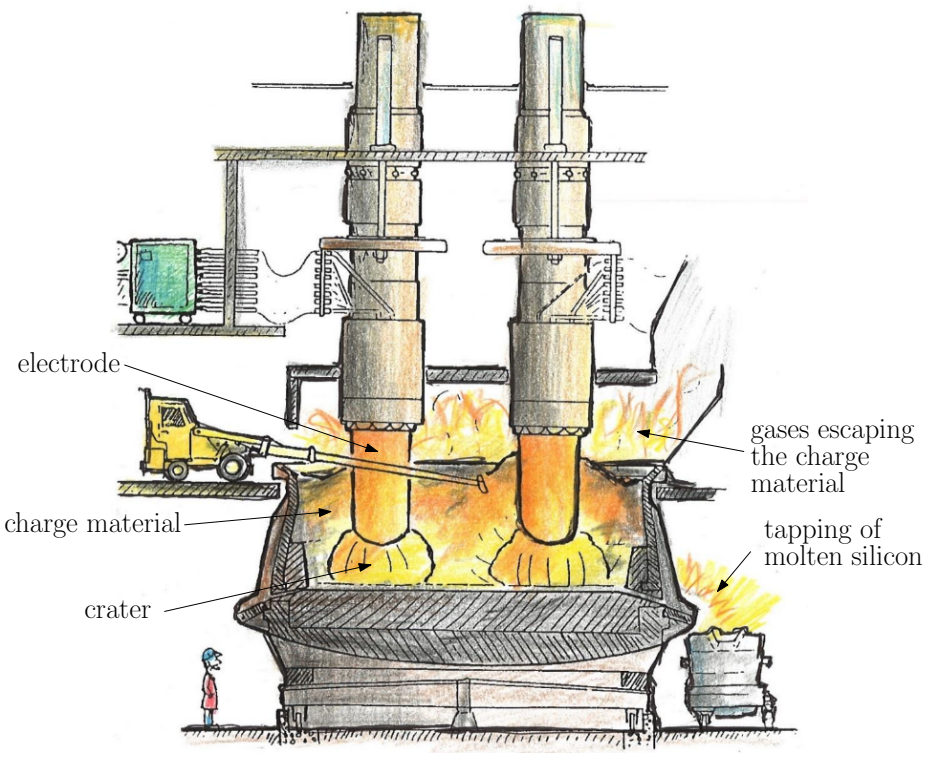

Figure 1.1: Drawing of a silicon-producing SAF, adapted from [40], showing the main regions within the furnace.

Around the base of each electrode is a cavity of hot gases, through which most of the electric current passes as an electric arc, converting the electrical energy of the system to heat. A single cavity at the base of each electrode is expected, as shown in Figure 1.1. Temperatures in these cavities, known as the craters, reach over 2300 K, and in the electric arcs themselves temperatures reach over 20,000 K, with the gas ionised to a plasma.

Each crater is surrounded by hot, partially-reacted raw materials. These raw materials, known collectively as the charge material, are added to the top of the furnace, and flow slowly down towards the craters. As the material heats up, the quartz rock softens, and begins to react with the carbon, which is partially graphitised at such high temperatures. Gases, primarily SiO and CO, are formed in these reactions, and flow back up through the porous charge material. Some of the gases condense or react with the solid materials within the charge bed, undergoing further reactions to form liquid silicon. The remaining gas escapes out of the furnace, where it oxidises again in the air, forming microsilica particles, as modelled in [36]. The full chemical system is described in Chapter 2. The liquid silicon formed in the furnace has very low viscosity, and flows easily down through the porous charge material, pooling in

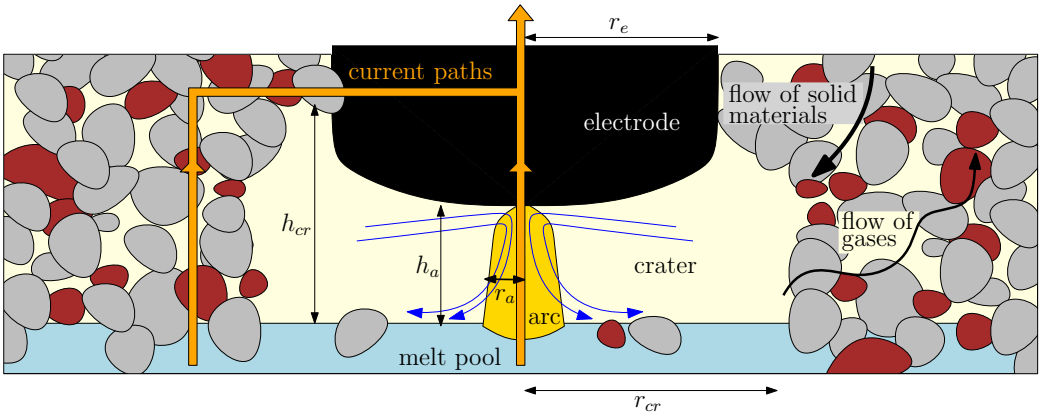

Figure 1.2: Illustration of the hottest region with the furnace, showing a single electrode, along with the resulting crater, arc, and surrounding charge material, for the part of the AC cycle when the electrode is the cathode. The flow of current is shown by orange arrows, and the blue arrows illustrate streamlines of the gas flow in and around the arc. These are reversed when the electrode is anode. Approximate lengths (or ranges) of the geometry are given in Table 1.1.

the bottom of the craters. The molten silicon is continuously tapped out from these crater pools.

The electric arcs that form in the craters beneath each electrode are a type of continuous gas discharge, where the gas is ionised into a plasma of electrons and ions which carry the electric current. The high current through each arc generates a strong magnetic field, so that a Lorentz force is exerted on the charged particles in the plasma. This generates an axial plasma flow along the electric arc from cathode to anode [104]. The flow of current through the arc generates heat by Ohmic heating, and the ionisation of the plasma — and so its electrical conductivity — increases with temperature. Heat from the arc is transferred to the surroundings by radiation and through convection of the crater gases. The highest temperature within the material bed is expected to be located in the charge material immediately surrounding each crater. The chemical reactions here are therefore the most intense, and the majority of the material consumption is expected to take place very close to the boundary between the charge and the crater. A diagram of a crater (under a single electrode) and its immediate surroundings is given in Figure 1.2, with approximate lengthscales provided in Table 1.1.

While most of the electric current passes through the arcs, some is also conducted through the charge materials, between the electrode and the furnace base, bypassing the crater. This electrical conduction primarily occurs in the hotter material surrounding the crater, where the carbon materials are more highly graphitised, and

Parameter	r_a	h_a	r_{cr}	h_{cr}	r_e
Approximate range (m)	$0.03 - 0.1$	$0.05 - 0.3$	$0.8 - 1.2$	$0.2 - 0.5$	0.6

Table 1.1: Approximate crater dimensions as shown in Figure 1.2 for an industrial silicon SAF, according to [1, 85, 104].

there is a greater abundance of electrically conductive silicon carbide (SiC). A small amount of current may also be conducted from the electrodes to the furnace walls, or between electrodes, although these current paths are expected to only carry around 1% of the total current [104]. Furnace operators attempt to control the ratio of current in each arc to that conducted in parallel through the charge by altering the height of the electrodes from the base of the furnace: the higher the electrode from the furnace base, the greater the resistance in the crater, in which case less current flows through the arc, and more through the charge. The raising and lowering of the electrodes is a continual, automated control process, with the aim of keeping a consistent proportion of current through both the arc and charge current paths, without a runaway of current in either, in order to optimise furnace efficiency. Since it is not possible to directly measure the proportion of current passing through the arc and the charge, this proportion is inferred, in practice, from the electrical measurements over the whole furnace. This electrical system and control process is described in detail in [104].

1.2 Review of SAF literature

1.2.1 Models of chemical reactions, heat transfer, and material flow in a SAF

There are various detailed models for the coupled chemical reactions, material flow, and temperature in the silicon production process, used practically by Elkem ASA, which do not include all of the electrical effects. For instance, SiMod — "a Silicon Furnace Process Model" — is a dynamic model used by Elkem ASA to simulate the furnace operation over days or weeks. Other chemical models in the academic literature include those presented in [5, 87]. Due to the heavy coupling between the chemical, flow, and heat transfer processes, both [5, 87] rely on commercial Computational Fluid Dynamics (CFD) packages to simulate the furnace structure and the production of silicon.

The heat and mass transport and chemical reaction processes of silicon production are studied mathematically in the thesis [92] and the related papers [93, 94, 95, 96]. The papers [93, 96] give a detailed analysis of the changing material compositions in the different regions of the furnace, including modelling and analysis of the formation of a crust in the charge material. The melting and flow of the charge material is studied in [95], with the charge modelled as a single fluid with temperature-dependent viscosity. In addition, models for the fine scale chemical processes are presented in [94] which are then homogenised to describe the overall bulk reaction. Many aspects of the furnace heat and mass transfer described in this work will be useful for our study of the electrical distribution in the furnace.

None of these studies modelling the chemical processes take into account the effect of the electric current: the models in [92] are for a laboratory scale pilot furnace which is heated by an induction furnace, while [87] do not model the electric current at all. In [5] the electric current in the arc is included, but with a prescribed current distribution, and it is assumed that the current has little effect on the processes elsewhere in the furnace.

1.2.2 Electrical current distribution in a SAF

Studies of the electrical conditions in SAFs may be found in the engineering and metallurgical sciences literature. These range from empirical formulae for the overall "furnace resistance" discussed in [108], through equivalent-circuit models for the electrical system including [86, 104], to full two- or three-dimensional simulations of the electromagnetic fields in the furnace in [11, 28, 101, 102].

Some of the simplest models for the electrical current within silicon-producing SAFs use analogies with electric circuits, with examples including [86, 104]. The electrical properties are modelled using lumped voltages, currents, resistances, and inductances, which are related using Kirchhoff's laws to create an equivalent-circuit (EC) model for the system. In [104], EC models are developed for the three-phase current in a silicon furnace, and are used to study the electrical control problem. In [86], a similar EC model to those of [104] is used, and a method is proposed to estimate the proportion of the total current passing through the arc compared with the charge from furnace measurements. This is done by measuring the furnace resistance at the point in the AC cycle when the arc current is zero, in order to estimate the resistance of the charge material. The study group report [19] also considers an EC model for both single-electrode, and three-electrode SAFs. Fourier analysis of the current variation over time gives insight into the effect of the arc on the three-phase

circuit model. Spatial variation, or dependence of the electrical properties of the charge material on the local temperature are not included explicitly in any of these EC models.

A continuum model for the electrical conditions in a three-phase SAF is considered in [28], in which the equation for conservation of charge is solved for the current distribution in a SAF with fixed layers of prescribed conductivity. A similar model, but with a more realistic geometry including electric arc regions, is solved in [102]. In [102] the arc, electrode, charge and crater regions are modelled as fixed regions of space with given electrical conductivities. A similar model is used to study the current and power distribution in an electric arc furnace (EAF) for smelting metals in [38]. In [11], magnetic effects are also included: Maxwell's equations are solved for the electric and magnetic fields in and between the electrodes in a cross section of the three-phase furnace, assuming that the current is vertical in the electrodes. Numerical results are used to evaluate the forces exerted by each electrode on the others. A similar electromagnetic system is solved in [100, 101]. In particular, in [101] the distribution of current when an alternating current is used is compared with a direct current (DC). Multiple arcs, or side-arcing (with the arc(s) forming between the electrode and the side wall of the crater, rather than the base) are also incorporated. Skin and proximity effects between the different electrodes and the casing of the furnace are analysed in [41]. Induction and skin effects are simulated for a ferro-manganese furnace in [33], in order to understand the effect of the alternating current on the power production in these furnaces.

In all these electromagnetic models, whether based on an electrical circuit or on Maxwell's equations, the electrical problem is entirely independent of the heat transfer, chemical reactions, and material flow, with the electrical conductivity of the furnace regions being prescribed constants, and with a prescribed domain geometry.

1.2.3 Modelling electric arcs for SAFs

As described above, the electric arcs that form in submerged arc furnaces are complicated processes involving tightly coupled electromagnetism, heat transfer, and high velocity fluid flow. The term "electric arc", however, covers a wide variety of phenomena. As described by [47, 104], the arcs in a SAF are "high pressure" (in comparison with vacuum arcs), in that they are at approximately atmospheric pressure. They are "free-burning" in the sense that they are not confined to be within a narrow region (compared with "wall-constrained" arcs, the subject of much of the arc literature and described in [47]). Finally they are "thermal", with shape and size self-determined

by a balance of heat generation and transfer to the surroundings [8, 77, 104]. As the current spreads out from the high current-density emitted at the cathode spot, it interacts with the arc's own magnetic field, generating a strong Lorentz force. This generates a plasma flow radially inwards and axially away from the cathode, so that there is an axial flow along the electric arc from cathode to anode. The fluid velocities are expected to be around $1000\,\mathrm{m\,s^{-1}}$ [104], so that the gas flow has an important effect on the temperature distribution through convection, and the movement of the charged plasma material in the magnetic field induces a secondary current. The chemical composition of the gas in which the arc forms affects the physical properties of the system, including the dependence of the electrical conductivity of the gas/plasma on the temperature. In SAFs for silicon production, the crater gas is composed mostly of carbon monoxide and silicon monoxide, in an approximately 1:1 molar ratio [85].

The complicated flow, heat transfer, and electromagnetic forces within the arc may be captured by magnetohydrodynamic (MHD) models, such as those used in [85, 103]. Here, the Navier-Stokes equations for the fluid velocity are coupled with the electromagnetic fields, modelled by Maxwell's equations, via the Lorentz force and the induced current due to the flow of charged particles. The temperature of the fluid is modelled via the conservation of energy, with heating source term due to the flow of current via Ohmic heating. The electrical conductivity of the fluid is modelled as an increasing function of the local temperature, and thus the fluid flow, electromagnetism, and heat transfer are all fully coupled. We present a MHD model for a SAF arc in Section 2.2.

In the SAF literature, MHD models for electric arcs are usually built into CFD packages and solved numerically for specific scenarios. The gas is generally modelled as compressible, and turbulence models are often used due to the high Reynolds numbers associated with the gas flows, as described in [4, 85, 107]. The heat radiation through the arc and surrounding crater gas is also discussed in [85]. The simulations from these models provide useful qualitative understanding of how we should expect arcs at high currents to behave. The model presented in [103] is for the arc in a circuit breaker, and makes use of simplifying assumptions for the heat radiation in order to retain a tractable model. MHD arc models are complicated, requiring large amounts of computing power to solve. They also have behaviour that varies over very short timescales, which generally make them impractical to include in simulations of the electrical conditions in the entire furnace, even over the fast timescale of the alternating current.

In models of the full electrical system, it is more common to use a simplified arc model. In [102], the arc is modelled as a prescribed region of the domain with constant electrical conductivity. Within EC models for the furnace electrical system, empirical arc models are often used, which describe the variation of the arc resistance over time, due to the changing voltage across the arc. Commonly-used empirical models include those due to Cassie [22] and Mayr [67, 68] which were originally developed for circuit-breaker arcs.

Lying somewhere between the empirical models and largescale MHD simulations, there is a plethora of simplified-physics arc models which attempt to capture the dominant electrical and thermal properties without solving the full, coupled, physical model [18, 26, 60, 64, 77, 80, 89, 105]. These model the arc as a cylindrical region with a purely axial electric current, and do not include any effects due to the magnetic field. The temperature within this cylindrical arc is affected by Ohmic heating, and heat losses which may include radiation, convection, and conduction.

In several of these simplified-physics models, the cross-sectional area of the (uniform, cylindrical) arc must also be either prescribed or solved for along with the radial temperature profile and the electric current. There has been much discussion about the correct way to do this in the literature. Many models use Steenbeck's minimisation principle, described in [79], which requires that the arc radius minimises both the electric field, and power dissipated by the arc. However, this is not built on any physical principle, and has been shown to give inconsistent and unphysical results [23]. Nevertheless, it remains popular in the literature, used in [8, 85, 104]. A physically consistent way to close the system is instead to couple the arc to the surrounding gas, in which the heat equation can be solved with far-field boundary conditions, which may be used to fix the position of the edge of the arc. This was done in [18], for a low-current arc in which the heat transfer was primarily by radiation in the arc, with a heat conduction transition layer at the interface with the surrounding gas.

1.3 Overview of our modelling approach, and links to wider literature

As described in Section 1.2, models of SAFs generally focus on either the chemical processes in the charge material, including a description of the heat transfer and material flow, but neglecting the electrical effects, or they only consider the electrical system, neglecting heat transfer and the chemical problem. This is partly because of the disparate timescales involved in these processes: the electrical system varies

on the alternating current timescale of around 10^{-2} s, whereas the chemical and heat transfer processes in the charge material are much slower.

The aim of this thesis is to investigate how the electrical current interacts with the other processes in the furnace, in order to determine the evolution of the internal furnace structure. We present a general model for the dynamics within a furnace including electromagnetic, chemical, material flow, and heat transfer processes, over all relevant timescales. We then explore simplifications and reductions of this general model, which still include the crucial physical processes, to gain insight into the interactions between them. In particular, we justify our model simplifications by dimensional analysis and asymptotic methods.

Coupled electrical and thermal processes of course occur in many other applications besides the study of SAFs. One area of literature which is of particular relevance is the study of thermistors. A thermistor is an electrical component with temperature dependent electrical conductivity, and is often used in fuses. Studies including [32, 58, 59] investigate the coupled electrical and thermal processes in thermistors, and derive conditions on the temperature dependence of the electrical conductivity for the blow up of temperature and runaway of the current through the device. Thermistor-like behaviours are found elsewhere in the metallurgy industry: current and temperature runaway is observed in calciners, in which granular carbon material is heated by an electric current to produce graphite [17]. Since both the electric arcs and the charge material in a SAF have electrical conductivities that increase with temperature, both may be viewed as thermistors.

The material flow and heat transfer processes in the charge material may be viewed as a counter-current flow, with hot crater gas flowing out through the cooler porous solid material, which itself flows inward towards the crater regions. In Chapter 5, we investigate how this counter-current flow interacts with the mainly endothermic chemical reactions. Mathematical analyses of endothermic systems do not appear to be common in the literature. An endothermic silicon furnace system was analysed in [93], but under the assumption that all chemical species had the same temperature locally, and so counter-current effects were not investigated. The related process of combustion in porous media, where the chemical reaction is exothermic, has been studied with applications to catalytic converters and filtration combustion [13, 20, 21, 75], smouldering cigarettes [29], and the combustion of rocket fuels [55]. In these studies, a two-temperature model including heat and mass transfer between the gas and solid phases is considered. Due to the exothermic nature of the combustion reaction, the reaction is found to take place in a hot reaction zone, which is shown

to move as a travelling wave through the domain [13, 21, 75]. Combustion waves were studied in [78] with a two-stage chemical reaction, the second of which may be endothermic. Under certain conditions on this endothermic reaction, travelling combustion waves were still found.

1.4 Summary of the rest of the thesis

In Chapter 2 we develop a general model for the coupled heat transfer, electromagnetic fields, fluid flow, and chemical reactions taking place within a SAF. This general model is fairly complicated, with processes happening over a wide range of timescales, and we do not attempt to solve this model in its entirety. Instead, we discuss the disparity of timescales, scaling choices, and the small parameters which motivate the reductions and analysis in the remainder of the thesis. In Chapter 3 we reduce the general model of Chapter 2. We use a simplified arc model with heat radiation as the dominant heat-loss mechanism, and we make a rational reduction of the radiation problem across the crater surfaces, in the limit that the radiation between these surfaces is dominant. We simplify the geometry and chemical system, focussing on the radially symmetric geometry surrounding a single electrode, and on the most important chemical reactions. We take advantage of the disparate timescales by homogenising over the fast timescale of the alternating current, obtaining an effective furnace model, applicable over the slow timescale of the motion of the charge material bed. The remainder of the thesis consists of analysis of this homogenised model.

The cell problem for the homogenised model describes the variation of the arc and electrical system over the fast AC timescale. In Chapter 4 we find solutions of this fast-timescale model, both by prescribing the electrode current, and by including an EC model for the entire three-phase furnace into this cell problem. In this context, our simplified arc model may be viewed as an alternative to empirical arc models commonly used in the literature, and we provide a comparison of these arc models. In Chapter 5 we formulate and analyse a model for an interacting counter-current flow with an endothermic, temperature-dependent chemical reaction, based on the homogenised model for the processes in the charge material derived in Chapter 3. We derive reduced models using the method of matched asymptotic expansions, in the limit of large Péclet number in the solid charge material, for different values of the convective heat transfer coefficient. Using the model reductions derived in Chapter 5, the homogenised furnace model of Chapter 3 is solved in Chapter 6. Our solutions of this model give insight into how the electrical, chemical, thermal, and material

flow processes at play within a SAF interact and influence the natural steady-state behaviours of the furnace. We also discuss how the industrial process of stoking the furnace may disrupt this natural behaviour, and lead to improved efficiency of silicon production. In Chapter 7 we summarise our results, highlight areas for future work, and discuss the implications for industrial silicon production.

1.5 Statement of originality

The modelling, analysis and numerical results in this thesis are the work of E.K. Luckins, under the supervision of J.M. Oliver, C.P. Please, and R.A. Van Gorder. A simpler version of the reduced furnace model of Chapter 3, along with parts of both Section 4.1 and Chapter 6, have been published in [65]. Section 4.2 is based on a paper recently submitted to the IMA Journal of Applied Mathematics, authored by E.K. Luckins, J.M. Oliver, C.P. Please, B.M. Sloman, A.M. Valderhaug, and R.A. Van Gorder. The electrical measurements used in Figure 4.13 were collected by Elkem ASA. At the time of submission, the asymptotic analysis of Chapter 5 has not yet been submitted for publication.

Chapter 2

Mathematical modelling of submerged arc furnaces

In this chapter we present a model for the coupled electromagnetic and thermal processes, chemical reactions, and flow of material within the furnace. A diagram of the model domain is given in Figure 2.1. Within the craters, denoted Ω_{cr} in Figure 2.1, we use a magnetohydrodynamic model to describe both the electric arc, and the cooler crater gases. In the electrodes, Ω_e, we describe the electromagnetic fields, and heat transfer, which is primarily by conduction. In the charge materials, occupying region Ω_{ch}, we use a multiphase flow model to describe the interaction and flow of the different chemical species, as well as the heat transfer between phases. We impose continuity of the electric and magnetic fields, and appropriate heat and mass flux conditions at the boundaries between regions, to fully couple the model. In particular, the boundary Γ_i at the interface between the charge material and the crater is modelled as a free boundary, with its position determined as part of the solution.

Although we do not solve it in its entirety, the model presented in this chapter will form the basis of the analysis and reduced models derived in subsequent chapters. As discussed in Chapter 1, models for silicon furnaces tend to focus on a single aspect of the process, or restrict to a certain region of the domain. Those taking into account coupled behaviours are generally constructed in CFD software, and, even then, do not attempt to capture processes on such varied timescales as the variation in the electric arc, and the motion of the crater wall Γ_i. In writing down this fairly comprehensive model, we hope to clarify how the processes interact. Our analysis in subsequent chapters, under simplifying assumptions on both the geometry and chemical systems, builds intuition for how solutions of this full model may behave, and we discuss these ideas in Chapter 7.

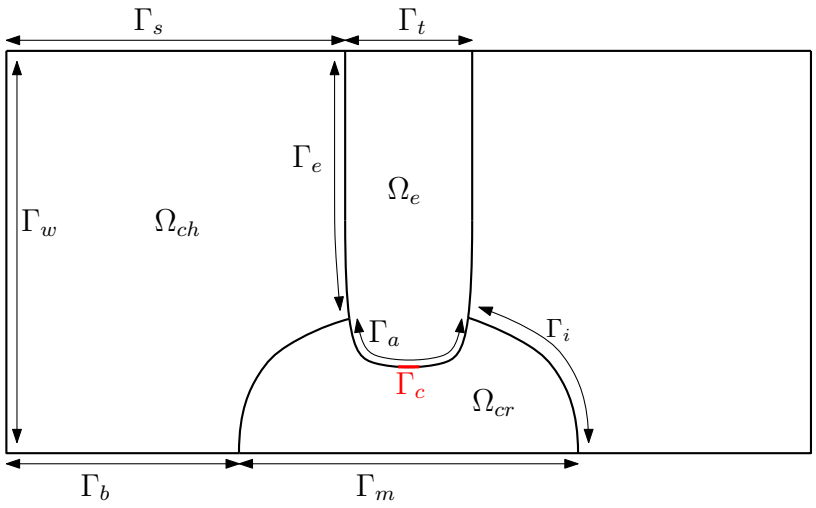

Figure 2.1: Diagram of the furnace, consisting of crater Ω_{cr}, charge material Ω_{ch}, and electrode Ω_e regions. Only one electrode and crater are shown for simplicity.

2.1 Electromagnetism

Across all regions Ω_{cr}, Ω_{ch} and Ω_e of our domain, the electric field $\boldsymbol{E}$ and magnetic field $\boldsymbol{B}$ are assumed to satisfy a simplified version of Maxwell's equations (neglecting the displacement current)

$$\nabla \times \boldsymbol{B} = \mu \boldsymbol{J}, \tag{2.1}$$

$$\nabla \cdot \boldsymbol{B} = 0, \tag{2.2}$$

$$\nabla \times \boldsymbol{E} = -\frac{\partial \boldsymbol{B}}{\partial t}, \tag{2.3}$$

$$\nabla \cdot \boldsymbol{E} = \frac{\rho_c}{\epsilon}, \tag{2.4}$$

which are Ampere's law, the solenoidal nature of $\boldsymbol{B}$, Faraday's law, and Gauss' law, respectively. Here $\boldsymbol{J}$ is the current density and ρ_c is the electrical charge density. The parameters $\mu = \mu_r \mu_0$ and $\epsilon = \epsilon_r \epsilon_0$ are the permeability and permittivity of the medium, respectively. In particular, $\mu_0 = 4\pi \times 10^{-7}\,\mathrm{m\,kg\,s^{-2}\,A^{-2}}$ and $\epsilon_0 = 1/(\mu_0 c^2) = 9 \times 10^{-12}\,\mathrm{A^2\,s^4\,kg^{-1}\,m^{-3}}$ are the magnetic permeability and permittivity of free space, respectively, where $c = 3 \times 10^8\,\mathrm{m\,s^{-1}}$ is the speed of light. The values of ϵ_r and μ_r, and the constitutive law relating the current density $\boldsymbol{J}$ to the electric and magnetic fields vary, in general, in the different regions of the domain. However, for simplicity, and following [100], we take $\mu_r = 1$ in all regions of the domain. This is justified in the crater Ω_{cr} as discussed in Section 2.2 below.

We have already simplified Ampere's law (2.1) by neglecting the displacement current term $\mu\epsilon\,\partial \boldsymbol{E}/\partial t$ [27]. This is justified since the timescales of interest, including

the rapid variation of the electric arc, are much slower than the displacement current timescale.

We also introduce the electric and magnetic potentials, ϕ and $\boldsymbol{A}$, respectively, defined by

$$\boldsymbol{B} = \nabla \times \boldsymbol{A}, \qquad \boldsymbol{E} = -\nabla\phi - \frac{\partial \boldsymbol{A}}{\partial t}, \tag{2.5}$$

so that (2.2) and (2.3) are satisfied. There is freedom in these definitions, which we fix by a Dirichlet boundary condition for ϕ and by imposing the Coulomb gauge

$$\nabla \cdot \boldsymbol{A} = 0. \tag{2.6}$$

The remaining equations (2.1) and (2.4) then simplify to

$$-\nabla^2 \boldsymbol{A} = \mu \boldsymbol{J}, \tag{2.7a}$$

$$-\nabla^2 \phi = \frac{\rho_c}{\epsilon}, \tag{2.7b}$$

in terms of the potential functions. In addition to (2.7), by taking the divergence of Ampere's law (2.1) we obtain the conservation of charge equation

$$\nabla \cdot \boldsymbol{J} = 0. \tag{2.8}$$

In Sections 2.2, 2.3 and 2.4, for each region of the domain, we will impose a constitutive law expressing $\boldsymbol{J}$ in terms of the electric and magnetic fields (and the fluid velocity, in the crater region Ω_{cr}). Using (2.5), this gives $\boldsymbol{J}$ as a function of derivatives of $\boldsymbol{A}$ and ϕ. This constitutive law, along with (2.8) and (2.7a) form an elliptic system for $\boldsymbol{A}$ and ϕ. The electric charge density ρ_c may then be computed from (2.7b), although we are not generally interested in this.

2.2 The electric arc and crater gas

In this section we present a magnetohydrodynamic model for the fluid flow, temperature, and electromagnetism in the crater region Ω_{cr}, which includes an electric arc. The electrical conductivity of the crater fluid is taken to be an increasing function of temperature, to describe the greater degree of plasma ionisation at higher temperatures. We are thus able to model both the conducting arc and the surrounding fluid with negligible conductivity using the same set of equations. We refer to the "arc" as the region of plasma which is hot enough to conduct a significant electric current. For a fixed electrode position, the shape and size of this region is determined entirely by the heat generation and transfer processes.

As described in [109], the relative permeability, μ_r, and permittivity, ϵ_r, of a plasma may be shown to be extremely close to 1, and so ϵ and μ are replaced with ϵ_0 and μ_0 in Ω_{cr}. The crater pressure is around atmospheric pressure, and so it is reasonable to assume that the gas is in local thermal equilibrium (LTE), meaning that all the gas particles (ions, electrons, and neutral particles) collide frequently enough to all have the same temperature. We also make the (physically-reasonable) assumption that the electron mass is negligible relative to that of ions and neutral particles. Under these assumptions, it is shown in [90, 97, 99], that one may combine the equations of conservation of mass, momentum and energy of the electrons, ions, and neutral particles, to derive the single-fluid MHD equations. These assumptions may be justified everywhere except at boundaries of the domain. In particular, the assumptions of LTE break down near to the cathode, where electrons are emitted, with a very different temperature to the crater fluid. Sub-models accounting for the processes in the thin layer next to the cathode are discussed in [85].

The single-fluid MHD model consists of Maxwell's equations (2.1)–(2.4) above, along with the Navier-Stokes equations, and the conservation of energy equation [90, 97], namely

$$\frac{\partial \rho}{\partial t} + \nabla \cdot (\rho \boldsymbol{v}) = 0, \tag{2.9}$$

$$\rho \left(\frac{\partial \boldsymbol{v}}{\partial t} + \boldsymbol{v} \cdot \nabla \boldsymbol{v} \right) = -\nabla p + \boldsymbol{J} \times \boldsymbol{B} + \eta \nabla^2 \boldsymbol{v} + \left(\zeta + \frac{1}{3}\eta \right) \nabla \left(\nabla \cdot \boldsymbol{v} \right), \tag{2.10}$$

$$\rho c_v \left(\frac{\partial T}{\partial t} + \boldsymbol{v} \cdot \nabla T \right) + p \nabla \cdot \boldsymbol{v} = \nabla \cdot (k \nabla T) + \frac{|\boldsymbol{J}|^2}{\sigma_a} + \mathcal{R}, \tag{2.11}$$

where ρ, p, $\boldsymbol{v}$, and T are the average density, pressure, velocity, and temperature of the fluid, respectively.

The term $\boldsymbol{J} \times \boldsymbol{B}$ in (2.10) is the Lorentz force, which drives the fluid flow. If the current in the arc is purely axial, then the magnetic field generated is purely azimuthal, and so the Lorentz force only has a radially inward component. This is sometimes referred to as the cylindrical pinch force [27]. In a SAF we expect the arc to expand from the cathode spot, so that there is also a radial component of the current density, and so an axial component to the Lorentz force. This generates a gas flow in towards the centre of the cathode spot and then axially along the arc, which is sometimes referred to as the "cathode jet" [104]. In high-current SAF arcs, the Lorentz force drives a fast fluid flow, so that the Reynolds number is large, and we may expect to see turbulent effects. In many simulations of high-current electric arcs in the metallurgy literature, a standard $k-\epsilon$ turbulence model is used, for instance, in

[4, 81]. The fluid shear and bulk viscosities are η, and ζ. As the arc plasma in a SAF is highly collisional, we may assume the viscosities are isotropic, and independent of the direction of the magnetic field [61]. We have also assumed they are independent of temperature, for simplicity. We have ignored the gravitational force, as we expect this to have negligible effect.

In (2.11), k is the thermal conductivity and c_v is the specific heat capacity. The source term $\boldsymbol{J} \cdot \boldsymbol{J}/\sigma_a$ accounts for the heat generated by Ohmic heating [61, p. 218]. The term $p\nabla \cdot \boldsymbol{v}$ is the work done by fluid expansion. The high temperatures in the arc mean that heat radiation is an important energy transfer mechanism, summarised in the term $\mathcal{R}$, and discussed in Section 2.2.2. We have neglected the work done by viscous dissipation, as this is expected to be relatively small, even for turbulent flows. We have also neglected the Thomson effect, which is the thermoelectric transport of heat due to electron drift. The Thomson effect is included in several simulations in the metallurgical literature [4], but a dimensional analysis suggests this is negligible.

We assume that the pressure, density, and temperature are related via the ideal gas law:

$$p = \rho R_s T, \tag{2.12}$$

where R_s is the specific gas constant, given by $R_s = R/M_s$ where $M_s\,[\mathrm{kg\,mol^{-1}}]$ is the molar mass of the gas and $R = 8.314\,\mathrm{J\,mol^{-1}\,K^{-1}}$ is the gas constant. This is the equation of state used in the MHD model in [103].

In addition to (2.9)–(2.11), Ohm's law, namely

$$\boldsymbol{J} = \sigma_a(T)(\boldsymbol{E} + \boldsymbol{v} \times \boldsymbol{B}), \tag{2.13}$$

may also be derived as part of the derivation of the single-fluid MHD model by combining the individual equations of conservation of momentum of the electrons and the heavier particles [90, 99]. Here $\sigma_a(T)$ is the temperature-dependent electrical conductivity of the crater gas/plasma, which we discuss in Section 2.2.1. For the partially-ionised plasma of the SAF arc we ought to include the slip velocity of the ions relative to the neutral particles in (2.13) [56], but we neglect this effect for simplicity. We have also neglected the Hall current and electron diffusion effects, as these are expected to be small due to the high collisionality of the plasma [85].

2.2.1 Electrical conductivity of the arc

The gas in the crater is a mixture of approximately equal parts CO and SiO, although small quantities of metallic impurities, including iron, calcium, aluminium,

and titanium, may also contribute to the electrical conductivity of the plasma [1, 85]. Since the gas is only conductive when ionised to a plasma, σ_a is non-negligible only at temperatures high enough for ionisation, and then continues to increase with temperature, as more atoms are dissociated into charge carriers (electrons and ions). It is stated in [14] that the arcs in steel-making furnaces — at similar currents and pressures to those in SAFs — are likely to have low ionisation fraction, with many neutral particles even at the hottest point of the arc.

From the derivation of Ohm's law [99] (for a fully ionised gas), the electrical conductivity is the ratio of the friction forces between electrons and heavier particles, to the current density, giving

$$\sigma_a = \frac{n_e e^2}{m_e \nu}, \tag{2.14}$$

where $\nu\,[\mathrm{s}^{-1}]$ is the collision frequency, $n_e\,[\mathrm{m}^{-3}]$ is the number density of electrons, $m_e\,[\mathrm{kg}]$ is the electron mass, and $e = -1.6 \times 10^{-19}\,\mathrm{C}$ is the charge on an electron. The form for σ_a for a high-pressure, monatomic gas given in [45] is

$$\sigma_a(T) \propto \frac{1}{\sqrt{p}} T^{3/4} \exp\left(\frac{eV_i}{2k_B T}\right), \tag{2.15}$$

where $k_B = 1.38 \times 10^{-23}\,\mathrm{J\,K}^{-1}$ is the Boltzmann constant, and $V_i\,[\mathrm{eV}]$ is the ionisation potential of the gas. Discussion of how one might theoretically extend (2.15) to polyatomic molecules, and to the case where there are radiative losses from the arc, is given in [45, ch. 3]. The study group report [18], studying a furnace arc, also makes use of the form (2.15), for constant pressure p.

A sensible general form for σ_a is therefore

$$\sigma_a(T) = \alpha_1 T^{\alpha_2} e^{-\alpha_3/T}, \tag{2.16}$$

for parameters $\alpha_1, \alpha_3 > 0$ and $\alpha_2 \geq 0$. In our numerical solutions in later chapters we will take $\alpha_2 = 0$ for simplicity, and use the values $\alpha_1 = 2.5 \times 10^4\,\mathrm{S\,m}^{-1}$ and $\alpha_3 = 1.4 \times 10^4\,\mathrm{K}$, chosen to give reasonable qualitative agreement of (2.16) with the data shown in [85, 107] for the crater gas of a silicon SAF.

2.2.2 Heat radiation

The temperatures in the arc are likely to be high, around 20,000 K [104] and therefore heat radiation is an important heat transfer mechanism in the arc [47]. The steady state radiative transfer equation for the radiation intensity I within the crater fluid is [72]

$$\boldsymbol{\Omega} \cdot \nabla I = \kappa(\nu)(B - I), \tag{2.17}$$

for each frequency $\nu\,[\mathrm{s}^{-1}]$ and direction vector $\mathbf{\Omega} \in S^2$, and where we have ignored scattering effects for simplicity. As derived in [72], the absorption of radiation is proportional to the intensity I, while the emission of radiation is described by Planck's function, $B(\nu, T)$, namely

$$B(\nu, T) = \frac{2h\nu^3}{c^2\left(e^{h\nu/k_B T} - 1\right)}, \tag{2.18}$$

where $h = 6.6 \times 10^{-34}\,\mathrm{J\,s}$ is Planck's constant, $c = 3 \times 10^8\,\mathrm{m\,s}^{-1}$ is the speed of light in a vacuum, and $k_B = 1.38 \times 10^{-23}\,\mathrm{J\,K}^{-1}$ is Boltzmann's constant. The constant of proportionality, $\kappa(\nu)\,[\mathrm{m}^{-1}]$, in (2.17), is the absorption coefficient of the medium, which must be the same for both the emission and absorption terms [72]. As well as the radiation frequency ν, κ also depends on temperature and pressure, in general. The absorption and emission of radiation results in a source term in the energy equation (2.11), which has the form [72]

$$\mathcal{R} = -\int_{\nu_1}^{\infty}\int_{S^2} \kappa(B - I)\mathrm{d}\mathbf{\Omega}\mathrm{d}\nu. \tag{2.19}$$

Rather than solve the full problem for radiation intensity, we wish instead to approximate (2.19). The appropriate simplification is determined by the size of the absorption coefficient κ, or on the related (dimensionless) quantity of the optical thickness τ, defined by

$$\tau(\nu) = \int_0^s \kappa(\nu)\,\mathrm{d}s, \tag{2.20}$$

which is a measure of the amount of radiation absorbed along the path s. For low values of τ, most radiation passing along path s is not absorbed, whereas for large τ, the majority of the radiation must be absorbed.

In the electric arc, we expect that $\kappa \approx 0.1\,\mathrm{m}^{-1}$ (using values for CO gas [82]) and we assume that κ is independent of ν (i.e., the grey-medium limit [72]) and of temperature, and pressure. The lengthscale of radiation paths in the crater Ω_{cr} has a maximum of around 1 m. We therefore expect an optical thickness of $\tau \approx 0.1$. For this relatively small value of τ, an optically thin simplification of (2.19) appears to be appropriate [72]. In this case, the radiation intensity $I = O(\tau)$, so that the emission term dominates in the volumetric heat loss $\mathcal{R}$. Using the form (2.18) for B, we find that (2.19) is approximated by

$$\mathcal{R} = -4\kappa\sigma_B T^4, \tag{2.21}$$

where $\sigma_B = 5.67 \times 10^{-8}\,\mathrm{W\,m}^{-2}\,\mathrm{K}^{-4}$ is the Stefan-Boltzmann constant. The relation (2.21) is correct up to $O(\tau)$, as derived in [44, 72]. (We have assumed that the

refractive index of the medium is 1.) Thus radiation is only emitted by the crater fluid at leading order, and is not absorbed. The energy emitted in this way must then be accounted for at the solid boundaries of the crater domain, as we will discuss in Section 2.5.3. This optically thin simplification is used in the arc models presented in [5, 103].

2.3 The charge material

The charge material, occupying region Ω_{ch} in Figure 2.1, consists of all the raw and partially reacted materials in the furnace, as well as all the fluids which fill the porespace. The solid charge material forms a porous, granular structure, consisting of a mixture of carbon (C) and quartz rock (SiO_2), as well as silicon carbide (SiC). As these are heated the quartz rock softens, so that it behaves like a highly viscous fluid. The gases CO and SiO produced in the reactions flow through the porespace of the granular material bed. Liquid silicon is produced by the reactions in the charge material. This silicon flows easily down through the porous structure, as it has low viscosity [5]. The solid materials are used up in the reactions, occurring mostly near the crater, and so there is an overall flow of the solid material down towards the crater under gravity, replacing the material consumed. Meanwhile, we expect a net gas flow back up through the charge material as the gases are produced in and near the crater.

We model the charge material in the framework of multiphase flow [16]. Many aspects of our model are very similar to that in [92, 93, 96]. However, we additionally model the electrical current in the charge, which provides an Ohmic heating source. We also allow the solid/liquid and gas phases to have different temperatures locally, rather than assuming the temperatures are the same as in [92, 93, 96]. The motivation for this choice is that the gas flowing out of the charge material at the surface of the furnace is generally seen to be hotter than the solid materials here [46], although it is cooler than the gases in the crater. Thus, while we expect some heat transfer between the different phases in the charge material, we do not restrict to a one-temperature model. We explore the effect of heat transfer between the phases in Chapter 5.

2.3.1 Chemical species, reactions and conservation of mass

Following [92], we model the charge material as consisting of the seven chemical species $C(s)$, $SiC(s)$, $SiO_2(s)$, $SiO_2(l)$, $Si(l)$, $CO(g)$, and $SiO(g)$ related by the chem-

ical reactions

$$(i = 1) \qquad \mathrm{SiO}(g) + 2\mathrm{C}(s) \to \mathrm{SiC}(s) + \mathrm{CO}(g), \tag{2.22}$$

$$(i = 2 \to, 3 \leftarrow) \qquad 2\mathrm{SiO}(g) \rightleftharpoons \mathrm{SiO_2}(l) + \mathrm{Si}(l), \tag{2.23}$$

$$(i = 4) \qquad \mathrm{SiO_2}(s) \to \mathrm{SiO_2}(l), \tag{2.24}$$

$$(i = 5) \qquad \mathrm{SiO}(g) + \mathrm{SiC}(s) \to 2\mathrm{Si}(l) + \mathrm{CO}(g), \tag{2.25}$$

$$(i = 6) \qquad \mathrm{SiO_2}(l) + \mathrm{C}(s) \to \mathrm{SiO}(g) + \mathrm{CO}(g), \tag{2.26}$$

$$(i = 7 \to, 8 \leftarrow) \qquad 2\mathrm{SiO_2}(l) + \mathrm{SiC}(s) \rightleftharpoons 3\mathrm{SiO}(g) + \mathrm{CO}(g), \tag{2.27}$$

where s, l, and g represent the solid, liquid, and gas phases, respectively, and we will refer to the reactions $i = 1, \ldots, 8$ including the forward- and backward-reactions separately.

At lower temperatures, away from the crater, the main reaction is expected to be (2.22), the formation of SiC from the incoming carbon material and the SiO gas flowing up from the crater [86]. Nearer the crater, however, the temperatures become high enough for the quartz rock to melt via (2.24) (at around 1996K). For temperatures greater than this, reactions (2.26) and (2.27) can occur, reacting the solid materials away to produce gases. Reasonable functional forms for the reaction rates of (2.22)–(2.26) are given in [92]. The reaction (2.27) is excluded due to a lack of kinetic data, and the fact that the kinetic parameters for the system (2.22)–(2.26) used in [92] have been calibrated to data from an operational SAF without including the effect of (2.27). We include reaction (2.27) here for completeness but, following [92], we will exclude it from our later analysis.

As in [92], we consider the charge material within the framework of multiphase flow. Each solid or liquid species X has density ρ_X, occupies a volume fraction θ_X, and has velocity $\boldsymbol{u}_X$. Species X is produced by reaction $i = 1, \ldots, 8$ corresponding to (2.22)–(2.27) with rate

$$R_i^X = \nu_i^X M_X Q_i \quad [\mathrm{kg\,m^{-3}\,s^{-1}}], \tag{2.28}$$

where Q_i $[\mathrm{mol\,m^{-3}\,s^{-1}}]$ is the rate of reaction i, M_X $[\mathrm{kg\,mol^{-1}}]$ is the molar mass of species X, and ν_i^X, dimensionless, encodes the stoichiometry, and whether the species X is consumed ($\nu_i^X < 0$) produced ($\nu_i^X > 0$) or unchanged ($\nu_i^X = 0$) by reaction i. The values of ν_i^X are given in Table 2.1. Neglecting mass diffusion, conservation of mass for each solid or liquid species is then given by

$$\frac{\partial}{\partial t}\left(\rho_X \theta_X\right) + \nabla \cdot \left(\rho_X \theta_X \boldsymbol{u}_X\right) = \sum_{i=1}^{8} R_i^X. \tag{2.29}$$

X	ν_1^X	ν_2^X	ν_3^X	ν_4^X	ν_5^X	ν_6^X	ν_7^X	ν_8^X
C(s)	-2	0	0	0	0	-1	0	0
SiC(s)	1	0	0	0	-1	0	-1	1
SiO_2(s)	0	0	0	-1	0	0	0	0
SiO_2(l)	0	1	-1	1	0	-1	-2	0
Si(l)	0	1	-1	0	2	0	0	0
CO(g)	1	0	0	0	1	1	1	-1
SiO(g)	-1	-2	2	0	-1	1	3	-3

Table 2.1: Stoichiometric constants ν_i^X for the chemical system (2.22)–(2.27).

Each of the gases occupies the gas volume fraction θ_g, but with different densities, ρ_G, and partial pressures, p_G, for species G. The velocity of gas species G is $\boldsymbol{u}_G$, and the gas is produced by chemical reactions with rate R_i^G. Thus the conservation of mass for gas species G is given by

$$\frac{\partial}{\partial t}\left(\rho_G \theta_g\right) + \nabla \cdot \left(\rho_G \theta_g \boldsymbol{u}_G\right) = \sum_{i=1}^{8} R_i^G. \tag{2.30}$$

The density and volume fraction of each solid or liquid X and gas G species are related by

$$\rho_X \theta_X = M_X C_X \qquad \text{and} \qquad \rho_G \theta_g = M_G C_G, \tag{2.31}$$

where C_X and C_G are the concentrations [$\mathrm{mol\,m^{-3}}$] of solid/liquid and gas species, respectively. Making use of Dalton's law, as described in [34], for the gas partial pressures p_G,

$$\frac{p_G}{p_g} = \frac{C_G}{C_g}, \tag{2.32}$$

where $p_g = p_{\mathrm{CO}} + p_{\mathrm{SiO}}$ and $C_g = C_{\mathrm{CO}} + C_{\mathrm{SiO}}$ are the total gas pressure and concentration, respectively, we may write our conservation of mass equations in terms of the concentrations of each species:

$$\frac{\partial C_X}{\partial t} + \nabla \cdot \left(\boldsymbol{u}_X C_X\right) = \sum_{i=1}^{8} \nu_i^X Q_i, \tag{2.33a}$$

$$\frac{\partial}{\partial t}\left(C_g \frac{p_G}{p_g}\right) + \nabla \cdot \left(\boldsymbol{u}_G C_g \frac{p_G}{p_g}\right) = \sum_{i=1}^{8} \nu_i^G Q_i. \tag{2.33b}$$

We also assume that the gases fill the porespace between the solid and liquid phases, forming a connected phase, so that the volume fractions sum to 1:

$$\theta_g + \sum_X \theta_X = 1. \tag{2.34}$$

As in [93, 96], we refer to this condition (2.34) as the "no-voids" condition: there is no gas-free "void" space in the mixture.

Finally, we assume as in [93, 96] that the concentration of the gas mixture is related to the gas pressure and temperature, T_g by the ideal gas law,

$$p_g = \frac{C_g}{\theta_g} R T_g, \tag{2.35}$$

where $R = 8.314\,\mathrm{J\,mol^{-1}\,K^{-1}}$ is the gas constant. (This is equivalent to assuming that both gases CO and SiO are individually ideal.) Furthermore, making use of Dalton's law (2.32), the ideal gas law (2.35), and the relations (2.31), the no-voids condition (2.34) may be expressed in terms of the species concentrations, as

$$\frac{R}{p_g} C_g T_g + \sum_X \frac{M_X}{\rho_X} C_X = 1. \tag{2.36}$$

2.3.2 Conservation of momentum and species velocities

We make the reasonable assumption that $\boldsymbol{u}_G = \boldsymbol{u}_g$, so that the gas velocity is the same for each species G. To determine the velocities of each species we should consider the conservation of momentum in each species. We might expect that the solid materials all move with the same velocity $\boldsymbol{u}_s$. The liquid quartz may also be approximated as having the same velocity, since it is very highly viscous, and so is not expected to flow much relative to the solid materials over the relevant timescales. The liquid silicon has low viscosity, similar to that of water at the furnace temperatures, and so we would expect it to flow easily down through the porous solid structure with velocity $\boldsymbol{u}_{\mathrm{Si}}$, different to $\boldsymbol{u}_s$, and drip into the crater pool.

We model the flow of gas through the porous structure by Darcy's law,

$$\boldsymbol{u}_g - \boldsymbol{u}_s = -\frac{\kappa_g}{\mu_g} \nabla p_g, \tag{2.37}$$

for permeability κ_g and gas viscosity μ_g. As in [92, p. 16], and the related papers [93, 96], we expect the permeability of the charge material to be very high, and the gas viscosity to be low, so that from (2.37) the gas pressure p_g is approximately uniform. Indeed, industrial measurements indicate that the pressure in the furnace crater is only around 4% above atmospheric pressure, p_{atm}, [5, 49], justifying this constant-pressure assumption, which is also used in [39]. The velocity $\boldsymbol{u}_g$ of the gas is then determined by the no-voids condition (2.36): the gas moves to retain the approximately constant pressure field.

The gas and liquid silicon flows are unlikely to significantly affect the solid flow, and so we might model the solid material as a granular fluid, using constitutive laws for the visco-plastic flow of cohesionless granular materials [31]. As the charge material becomes hot, the quartz becomes sticky, while the carbon and SiC species remain solid. Constitutive laws for the flow of cohesive granular materials are less well-studied [31], and while constitutive laws for granular flow through a viscous fluid [15] might be appropriate, it is unclear how the hot/sticky, and cold/dry regimes might be reconciled. A simpler approach would be to simply model the solid charge material as highly viscous fluid, with temperature dependent viscosity, as in [95].

We also have the added complication that the solid material is reacting away. It is unclear how the loss of material to the other phases affects the material flow. We might impose some kind of compaction law as used in the geophysical literature, for instance [42, 70, 71], of the form

$$\nabla \cdot \boldsymbol{u}_s = M. \tag{2.38}$$

Here, M is proportional to the difference between the (hydrostatic) pressure in the solid matrix, and the fluid pressure in the pores (which we might expect to be negligible in the furnace, relative to the hydrostatic pressure) [42, 70]. Furthermore, M is often related to the effective bulk viscosity, and the volume fraction of the solid phase [10]. In subsequent chapters of this thesis, for simplicity, we choose to prescribe $M = 0$ so that the solid matrix is incompressible, and does not compact as the material is reacted away. In the simple geometries used, this is sufficient to fix the velocity $\boldsymbol{u}_s$ without modelling the conservation of momentum of the solid phase.

Finally, we must consider the conservation of momentum in the low-viscosity liquid silicon phase, to derive an equation for $\boldsymbol{u}_{\mathrm{Si}}$. It is likely that the flow of liquid silicon would interact with the fast flow of gas in the opposite direction. Furthermore, it is possible that the silicon has a lubricating effect on the granular solid material, reducing the effective viscosity of the solid material in regions with high silicon volume fraction, or causing it to more easily compact. In subsequent chapters we simplify our model to neglect the liquid silicon entirely, retaining only the solid and gas phases, implicitly assuming that these effects are negligible.

2.3.3 Conservation of energy

Within the multiphase flow framework, we consider the conservation of energy in each species. We assume for simplicity that all the solid and liquid materials have the same temperature, T_s, and that the gases have the same temperature T_g. By

adding together the equations of conservation of energy of all the solid/liquid, or gas, species, respectively, we obtain an expression of the conservation of energy in each of two phases $P = g$ the gas phase, and $P = s$ the solid/liquid phase, namely

$$\begin{aligned}\frac{\partial}{\partial t}\left((\chi_s + \chi_{\mathrm{Si}})T_s\right) + \nabla\cdot\left((\chi_s \boldsymbol{u}_s + \chi_{\mathrm{Si}}\boldsymbol{u}_{\mathrm{Si}})T_s\right)& \\ = \nabla\cdot(k_s\nabla T_s) + H - S_s + \lambda(T_g - T_s) + m,& \qquad (2.39)\\ \frac{\partial}{\partial t}\left(r_g\theta_g T_g\right) + \nabla\cdot\left(r_g\theta_g\boldsymbol{u}_g T_g\right) = -S_g + \lambda(T_s - T_g) - m.& \qquad (2.40)\end{aligned}$$

Here we have used the notation

$$\chi_s = \sum_{X \text{ solid, } \mathrm{SiO_2}(l)} \rho_X\theta_X c_{p,X}, \qquad \chi_{\mathrm{Si}} = \rho_{\mathrm{Si}}\theta_{\mathrm{Si}}c_{p,\mathrm{Si}}, \qquad r_g = \sum_{G \text{ gas}} \rho_G c_{p,G}, \qquad (2.41)$$

where $c_{p,X}$ $[\mathrm{J\,kg^{-1}\,K^{-1}}]$ is the specific heat capacity of species X. We include the conduction of heat within the solid phase, with effective thermal conductivity k_s $[\mathrm{W\,m^{-1}\,K^{-1}}]$, but neglect heat conduction in the gas, as this is likely to be a negligibly small effect. In general, k_s may depend on the constitutive species' volume fractions, as well as the temperature T_s. We could additionally include the effect of heat radiation between particles with a nonlinear diffusion term $\nabla\cdot(bT_s^3\nabla T_s)$. This form for the radiative transfer through a porous material is used in [20] and [92], with b constant, and similar form is derived by a homogenisation analysis in [83]. Alternative forms are derived in [54] by considering Maxwell-type models.

The heat source H is the effective heat generated by Ohmic heating (with functional form discussed below). Since the gases are not electrically conductive, there is no Ohmic heating in the gas phase. The S_s and S_g terms are the heat lost to chemical reactions in each phase. Specifically, if reaction i consumes energy ΔH_i $[\mathrm{J\,mol^{-1}}]$ at rate Q_i, then the heat sink in phase $P = s$ or g is

$$S_P = \sum_i \alpha_i^P \Delta H_i Q_i, \qquad (2.42)$$

where α_i^P is the fraction of the total heat consumed by reaction i that is taken from phase P. We have the fraction $0 \le \alpha_i^P \le 1$ for all i and P, and for any i, $\alpha_i^g + \alpha_i^s = 1$. Data for the energy ΔH_i consumed in each reaction (2.22)–(2.26) are given in [48]. It is not immediately clear what values the α_i^P should take. To explore this, we might investigate the interacting chemical and heat transfer processes on the microscale, and upscale to find the effective values α_i^P using homogenisation techniques. We suggest this as an interesting and important area for future work. In subsequent chapters we use a simplified chemical model, and assume $\alpha_i^g = 0$ so that $\alpha_i^s = 1$, so that all the

heat for the reaction is taken from the solid reactant, rather than the surrounding gas. We therefore implicitly assume that heat can be more easily drawn out of the solid than the gas; since the thermal conductivity of the solid is likely to be greater than that of the gas, this seems a reasonable assumption.

The final two terms in each equation (2.39)–(2.40) describe the inter-phase heat transfer. Heat is not generated or consumed overall by either of these final two terms, only exchanged between the phases. The convective heat transfer is modelled to be linear in the temperature difference between the phases, with coefficient λ $[\mathrm{J\,m^{-3}\,s^{-1}\,K^{-1}}]$. As described in [16, 51], for two phase flow λ generally depends on the porosity, the porous structure, the relative velocity of the phases, and the associated Reynolds number and Prandtl number of the flow. Estimates for λ vary for different flow regimes and porous structures.

The net heat gained by phase s from phase g due to the transfer of mass (by chemical reactions) between the two phases is m. This will depend on the temperature of both phases, the chemical reaction rates, and the stoichiometry of the reactions. A discussion of these processes is given in [74], with this heat transfer depending on the interfacial temperatures (at the interface between the two phases on the microscale). For simplicity, we assume that the heat content $c_{p,P}T_P$ of phase P is carried with the material as it changes phase due to the chemical reactions, with rate equal to the rate of the reaction. This results in a simpler form for m than [74], and this form is also used in [7].

We note that we have neglected kinetic energy of each phase, as well as any kinetic energy exchange due to mass exchange, and any heat transferred between phases due to drag or friction, since we anticipate these terms are negligible. We have also neglected any work done by pressure in the gas phase, assuming that the gas is incompressible in the charge.

2.3.4 Electromagnetism in the charge material

While most of the electrical current is expected to pass through the electric arc, some passes through the charge materials. The raw materials of coal, woodchips and quartz rock have negligibly small electrical conductivity, so we expect no current conduction high up in the furnace. As the carbon materials are heated near the craters, they become partially graphitised, with increased electrical conductivity [30]. Silicon carbide, which is also electrically conductive, is formed by reaction (2.22) at sufficiently high temperatures. We therefore only expect large quantities of SiC near the hot craters. The liquid silicon is also an electrical conductor. The overall electrical

conductivity of the charge material therefore depends on both the temperature and chemical composition of the material. A number of experimental studies for the electrical conductivity of the overall charge material are summarised in [104], although studies of the functional dependence of the conductivity on temperature and material composition are very limited.

The average effect of electrical conduction and Ohmic heating in an inhomogeneous medium may be studied using spatial homogenisation methods. For instance, [83] studies problems of electrical conduction in a calciner, with the current flowing through a periodic array of conductive spheres (representing carbon material), with the void space acting as an insulator. The effective electrical conductivity tensor $\underline{\boldsymbol{\sigma}}_{\text{eff}}$ is shown to be proportional to the conductivity of the carbon material, with constant of proportionality depending on the microscale geometry. Furthermore, the effective Ohmic heating is shown to have the form

$$H = \boldsymbol{E}_0 \cdot \underline{\boldsymbol{\sigma}}_{\text{eff}} \boldsymbol{E}_0, \tag{2.43}$$

where $\boldsymbol{E}_0$ is the average electric field, which varies only over the macroscale. Several chapters of [83] are devoted to the complicated issue of contact resistance, highlighting the importance of accurate modelling of the geometry and resistance at the contact points between particles, in order to obtain an accurate homogenised model.

For the furnace charge material, we have multiple electrically conductive materials (the carbon, SiC, and liquid silicon), some of which have temperature dependent electrical conductivities, contained in a matrix of insulators (the quartz and gases). An effective electrical conductivity of the mixture might depend on volume fraction of the conductive materials relative to the insulators, and also on the local arrangement of these materials. The importance of contact resistance at the interface between two particles of conductive material was noted by [30] as well as [83]. In particular, we might expect this contact resistance to be considerably reduced if there is liquid silicon surrounding the contact points between the solid conductors.

We could attempt to extend the analysis of [83] to our multiple-conductor system, or we might use a Maxwell model for the effective electrical conductivity of the charge [52, 62]. More complicated inclusion geometries, and sophisticated models for the effective conductivity are also described in [62], and in particular the situation of coated particles is discussed in [52], which might be of particular interest if we suppose the liquid silicon is coating the charge particles.

For a particularly simple model, in the remainder of the thesis we simply assume that the electrical conductivity of the heterogeneous charge material is given by

$$\sigma_c(T_s) = \begin{cases} S_c \exp\left(-\frac{E_\sigma}{T_s - T_c}\right), & \text{for } T_s > T_c, \\ 0, & \text{otherwise,} \end{cases} \tag{2.44}$$

for constants $S_c, E_\sigma > 0$ and critical temperature T_c. This form is similar to the electrical conductivity of the carbon material that is used in [83], (although the carbon materials in the furnace charge are likely to be different to those used in the calciner). Since the contact resistance is expected to be of greatest importance we simply keep S_c constant, rather than allowing this to depend on the volume fraction of conductors as in the Maxwell or Bruggeman models. As described in [30] the conductivity of furnace-charge carbon materials increases significantly for temperatures above around $T_c = 2300\,\mathrm{K}$. From [102], the maximum charge conductivity is expected to be on the order of $400\,\mathrm{S\,m^{-1}}$, which we take as the value of S_c. In [73] the conductivity of carbon is seen to increase with heat treatment, but is bounded for large temperatures. For qualitative agreement, we use $E_\sigma = 300\,\mathrm{K}$.

Given this effective electrical conductivity σ_c, the electric current density in the charge material is related to the electric field by Ohm's law, which takes the simple form

$$\boldsymbol{J} = \sigma_c \boldsymbol{E}. \tag{2.45}$$

We note that, unlike in the crater, the flow of electrically conductive materials is very slow in the charge material, and so we neglect the small current correction $\sigma_c \boldsymbol{u} \times \boldsymbol{B}$.

The heat generated by the passing current is included via the Ohmic heating terms in (2.39), which, following [83], we assume has the form

$$H = \boldsymbol{J} \cdot \boldsymbol{E} = \sigma_c |\boldsymbol{E}|^2. \tag{2.46}$$

2.4 The electrode

The electrodes used in silicon submerged arc furnaces, shown by region Ω_e in Figure 2.1, are made of carbon, graphitised to be highly electrically conductive [88]. The electrodes act as another source of carbon for the chemical reactions in and around the crater, as they are gradually consumed by sublimation at the cathode spot, where the electric arc forms. The electrodes may also be consumed in reactions with the gas and liquid species in the charge or crater [88]. We have neglected these electrode sublimation and reaction processes in our arc model in Section 2.2, but we might

include them in boundary conditions at the surface of the electrode. The electrical current through the electrode Ω_e is governed by Ohm's law

$$\boldsymbol{J} = \sigma_e \boldsymbol{E}, \tag{2.47}$$

where the electrical conductivity σ_e is a prescribed constant.

In the electrode, heat is transferred predominantly by conduction, with thermal conductivity k_e. The electrodes can be raised and lowered as part of the control process which attempts to ensure a good distribution of current between the arc and the parallel current paths through the charge material. There is a net downwards motion of the electrode, as the electrode is slowly consumed in the crater and the material replaced from above. We suppose the electrode moves with prescribed (divergence-free) velocity $\boldsymbol{u}_e$, and prescribe the position of the electrode-crater interface Γ_a. The temperature, T_e, of the electrode satisfies the equation of conservation of energy in the electrode,

$$\frac{\partial}{\partial t}\left(\rho_e c_{p,e} T_e\right) + \boldsymbol{u}_e \cdot \nabla\left(\rho_e c_{p,e} T_e\right) = \nabla \cdot \left(k_e \nabla T_e\right) + \sigma_e |\boldsymbol{E}|^2, \tag{2.48}$$

where ρ_e and $c_{p,e}$ are the density, and specific heat capacity of the electrode material, which are assumed to be known.

We note that the electrical conductivity of the electrode σ_e is large (relative to the other regions modelled). When an alternating current is applied, we therefore expect to observe the skin effect: the majority of the electric current passes through a thin layer at the edge of the electrode, while the electric field in the core of the electrode is negligible. The depth of the conducting layer is on the order of

$$\text{skin depth} = \frac{1}{\sqrt{\pi \sigma_e f_{\text{AC}} \mu}}, \tag{2.49}$$

where f_{AC} [s^{-1}] is the frequency of the applied alternating current. Skin effects in SAF electrodes are studied in [41].

2.5 Boundary conditions

In this section we present the boundary conditions for the dependent variables in each of the regions of the domain. The boundaries Γ are shown in Figure 2.1.

2.5.1 Electromagnetism

The electromagnetic fields satisfy Maxwell's equations (2.1)–(2.4) throughout the domain $\Omega_e \cup \Omega_{cr} \cup \Omega_{ch}$. However, these equations are over-specified, and so it is easier to understand what constitutes appropriate boundary conditions for the equivalent system for the potential formulation (2.7a) and (2.8), along with Ohm's law, for ϕ and $\boldsymbol{A}$. This system is elliptic in both ϕ and $\boldsymbol{A}$, and so we require a boundary condition for each on all external boundaries.

We consider the conditions for ϕ first. At the top of the electrode Γ_t we impose the effect of the external electrical system, either by applying a voltage

$$\phi = V(t), \tag{2.50}$$

as in [106], or by applying a normal current density

$$\boldsymbol{J} \cdot \boldsymbol{n} = I(t), \tag{2.51}$$

as in [33, 69], where $\boldsymbol{n}$ is normal to the interface pointing into the domain. If multiple electrodes are modelled, we might prescribe an alternating three-phase current, as is used industrially. At the base of the domain, $\Gamma_m \cup \Gamma_b$, we prescribe the "ground" condition

$$\phi = 0. \tag{2.52}$$

At the surface of the charge material, Γ_s, and at the furnace walls Γ_w, we impose no normal current

$$\boldsymbol{J} \cdot \boldsymbol{n} = 0. \tag{2.53}$$

The boundary conditions for $\boldsymbol{A}$ are more complicated. Some numerical studies including [69, 100] impose magnetic insulation,

$$\boldsymbol{n} \times \boldsymbol{A} = \boldsymbol{0}, \tag{2.54}$$

at the edge of the furnace domain. Other studies including [11], which focusses on the electromagnetic fields in the electrodes, simply impose sufficiently fast decay of the magnetic field in the far-field of the domain,

$$\boldsymbol{B} = O\left(|\boldsymbol{x}|^{-1}\right) \quad \text{as } |\boldsymbol{x}| \to \infty. \tag{2.55}$$

As well as the above conditions on the external boundaries of the domain, we also require conditions at the internal boundaries. In general, Maxwell's equations

(2.1)–(2.4) require that at any internal boundaries, $\boldsymbol{E}$ and $\boldsymbol{B}$ satisfy

$$\left[\frac{1}{\mu}\boldsymbol{B}\times\boldsymbol{n}\right]_{-}^{+}=\boldsymbol{J}_S, \qquad [\epsilon\boldsymbol{E}\cdot\boldsymbol{n}]_{-}^{+}=\rho_S, \tag{2.56a}$$

$$[\boldsymbol{E}\times\boldsymbol{n}]_{-}^{+}=\boldsymbol{0}, \qquad [\boldsymbol{B}\cdot\boldsymbol{n}]_{-}^{+}=0, \tag{2.56b}$$

where $\boldsymbol{n}$ is normal to this boundary, $\boldsymbol{J}_S$ is a surface current, ρ_S is a surface charge density, and $[x]_{-}^{+}=x^{+}-x^{-}$, where $x^{+/-}$ is the value of x on either side of the boundary. These boundary conditions follow directly from the integral forms of Maxwell's equations (2.1)–(2.4). Since there is redundancy in Maxwell's equations, the boundary conditions (2.56) are also over-specified. It is easier to understand what constitutes appropriate boundary conditions for ϕ and $\boldsymbol{A}$. We impose continuity of ϕ, and continuity of normal current $\boldsymbol{J}\cdot\boldsymbol{n}$ across all internal boundaries Γ_a, Γ_e, and Γ_i. For the $\boldsymbol{A}$ conditions, we impose continuity of both $\boldsymbol{A}$ and $\boldsymbol{B}$.

However, we must consider the processes on the electrode–arc boundary Γ_a more closely. When the electrode is the cathode, the arc forms from a cathode spot, somewhere on the electrode surface Γ_a, shown as Γ_c in Figure 2.1. This cathode spot is a relatively small, approximately circular region on the electrode surface, which is hot enough to emit electrons by thermionic emission. The heat required for the thermionic emission is generated by the Ohmic heating at a high current density. Only a relatively small area can be maintained at the high temperatures necessary for the thermionic emission of electrons. We assume that the normal current density j_c through Γ_a is related to the electrode temperature T_e by the Richardson-Dushman law [14, 50, 104], namely

$$j_c = AT_e^2\exp\left(-\frac{W}{k_BT_e}\right), \tag{2.57}$$

where W is the work function of the electrode material, k_B is the Boltzmann constant, and A is a material-specific fitting parameter. For graphitised-carbon electrodes, $W=4.4\text{eV}$, $A\approx 6\times10^5\text{Am}^{-2}\text{K}^{-2}$ [50]. For relatively low electrode temperatures, the normal current density is negligible due to the exponential factor, and thus the current is indeed restricted to a small cathode spot. The Richardson-Dushman law only holds when the electron emission is thermionic: at much lower temperatures, electron emission would be driven by the electric field, and a different emission law, in terms of the applied electric field, would be appropriate.

The case when the electrode is the anode is less commonly studied in the SAF literature, but it is suggested in [85] that the anode may be modelled similarly to the cathode, by a relation between the surface temperature and the normal current.

2.5.2 Chemical species and material flow

The flow of materials is solved for in the crater Ω_{cr} and the charge Ω_{ch}. We require boundary conditions for the concentrations of chemical species, the gas pressure, and the phase velocities at the boundaries of the charge Γ_s, Γ_w, Γ_e, and Γ_i. We also require boundary conditions for the crater gas velocity $\boldsymbol{v}$ and pressure at the crater boundaries Γ_a, Γ_m, and Γ_i. The internal boundaries Γ_a and Γ_e have prescribed position, however the position of the interface Γ_i between the crater and charge is a free boundary, and so we must impose an extra condition to determine the position of this interface.

At the surface, Γ_s, of the charge material at the top of the furnace, we prescribe the concentrations of the raw materials (carbon and quartz),

$$C_{\mathrm{C}} = C^s_{\mathrm{C}}, \quad C_{\mathrm{SiO_2(s)}} = C^s_{\mathrm{SiO_2(s)}}, \tag{2.58}$$

and set $C_X = 0$ for all of the other solid and liquid phases $X = \mathrm{SiC}$, $\mathrm{SiO_2}(l)$, and Si. We prescribe a normal flux of the solid raw materials through Γ_s, by setting

$$\boldsymbol{u}_s \cdot \boldsymbol{n} = U. \tag{2.59}$$

This velocity U is chosen to model the addition of raw material into the furnace. On Γ_s, we also prescribe the gas pressure to be atmospheric

$$p_g = p_{\mathrm{atm}}. \tag{2.60}$$

On the furnace walls Γ_w, base Γ_b, and where the charge meets the electrode Γ_e, we prescribe no normal flux for all phases of the charge material

$$\boldsymbol{u}_s \cdot \boldsymbol{n} = \boldsymbol{u}_g \cdot \boldsymbol{n} = \boldsymbol{u}_{\mathrm{Si}} \cdot \boldsymbol{n} = 0. \tag{2.61}$$

Since all chemical species are transported purely by advection, these conditions ensure that there is no flux of any species through these boundaries. Depending on the choice of flow law for the solid and liquid-silicon phases, we may also need to impose a no slip condition at these boundaries.

At the surface Γ_i separating the crater and charge domains, solid and liquid charge material is expected to fall or drip into the crater, where it continues to react inside the melt-pool at the base of the crater, producing gas which then flows back out through the porous charge material. The dripping of material is included in the furnace model of [5], at a "dripping-rate" dependent on the local temperature. In [95] the melting and flow of the charge material is studied, with the charge modelled as a single fluid, with temperature-dependent viscosity, and the free-boundary is defined

as the isotherm where the material reaches the "dripping temperature". Rather than modelling the flow of the material, or prescribing the temperature of the surface Γ_i, we choose instead to define the boundary Γ_i to be the point where enough of the solid material has been reacted away that the structure loses integrity, and any remaining material collapses into the crater. We therefore impose that the position of the surface Γ_i is the first point (along characteristics of the flow of solid material) at which total volume fraction of solid becomes critically small,

$$\theta_{\mathrm{SiO}_2(l)} + \sum_{\text{solids } X} \theta_X = \theta_*, \tag{2.62}$$

for some prescribed constant θ_*. We also require a boundary condition for the silicon velocity $\boldsymbol{u}_{\mathrm{Si}}$ at Γ_i, the form of which depends on the type of model used for $\boldsymbol{u}_{\mathrm{Si}}$.

For a more realistic understanding of the furnace, we should model the heat transfer, current conduction, fluid flow, and chemical reactions in the melt pool at the base of the crater, as well as the silicon that is tapped from the melt pool, and then solve for the position of the interface between this pool and the crater. For the sake of simplicity, we instead assume that the boundary Γ_m has a fixed position, and that there is a prescribed flux, R_m of the two gases CO and SiO out of this boundary, into the crater Ω_{cr}, representing the net production of gas from reactions (2.22)–(2.27) in the melt pool. Thus, at Γ_m, the flux of crater fluid is given by

$$\rho \boldsymbol{v} \cdot \boldsymbol{n} = R_m, \tag{2.63}$$

where $\boldsymbol{n}$ is the normal pointing into Ω_{cr}. The electrode is impermeable, and so on Γ_a, there is no flux of fluid,

$$\boldsymbol{v} \cdot \boldsymbol{n} = 0. \tag{2.64}$$

At the interface with the charge material, Γ_i, we impose continuity of gas pressure and of gas flux, that is

$$p = p_g, \qquad \rho \boldsymbol{v} \cdot \boldsymbol{n} = \theta_g \rho_g \boldsymbol{u}_g \cdot \boldsymbol{n} \qquad \text{on } \boldsymbol{x} \in \Gamma_i. \tag{2.65}$$

At each of Γ_i, Γ_m, and Γ_a, we also impose a no slip condition for the crater fluid, by setting

$$\boldsymbol{v} \times \boldsymbol{n} = \boldsymbol{0} \qquad \text{on } \boldsymbol{x} \in \Gamma_i \cup \Gamma_m \cup \Gamma_a\,. \tag{2.66}$$

2.5.3 Temperature and heat flux

We prescribe the temperature of the solid raw materials as they are added to the furnace to be

$$T_s = T^{\text{in}} \qquad \text{on } \Gamma_s. \tag{2.67}$$

At the furnace walls we might impose a prescribed heat flux, modelling the heat loss to the surroundings. For simplicity, we instead choose to set

$$T_s = T^{\text{wall}} \qquad \text{on } \Gamma_w. \tag{2.68}$$

At the interface Γ_e between the charge Ω_{ch} and the electrode Ω_e, we require continuity of temperature and heat flux between the solid charge material and the electrode

$$T_s = T_e, \qquad k_e \nabla T_e \cdot \boldsymbol{n} = k_s \nabla T_s \cdot \boldsymbol{n} \qquad \text{on } \Gamma_e. \tag{2.69}$$

As in Section 2.2.2, we assume that the crater fluid occupying region Ω_{cr} is optically thin, and so does not absorb an appreciable amount of the radiation passing through it. All the radiation emitted by the arc is therefore incident on the surfaces on the edge of the crater, $\partial\Omega_{cr} = \Gamma_m \cup \Gamma_i \cup \Gamma_a$, which are also hot enough to radiate energy themselves, and so we also consider radiation between the crater walls.

In reality, a certain fraction of the radiation incident on these surfaces is absorbed, with the rest reflected. However, including reflection from surfaces quickly becomes complicated, as this reflected radiation must then be taken into account as it hits other surfaces, and is again partly reflected, as in [44, 72]. A discussion of this reflected radiation in the context of silicon SAF models is given in [5]. The surface in the crater which is likely to be most reflective is the base of the crater, Γ_m, where molten silicon accumulates, along with the less reflective slag and unreacted material. In [5], it is suggested that in reality 28% of incident radiation on the molten silicon is absorbed, and the rest reflected. Since the geometry of the surfaces is likely to be very uneven, it would not be sensible to try to predict the direction of reflected radiation. As a simplification, we assume that all incident radiation is absorbed at the crater wall, taking the absorption coefficient $\epsilon_{\partial\Omega_{cr}} = 1$ [5]. The heat flux condition at any point $\boldsymbol{r}$ on this boundary $\partial\Omega_{cr}$ is then given by

$$\begin{aligned}[\boldsymbol{q} \cdot \boldsymbol{n}]^+_- = \epsilon_{\partial\Omega_{cr}} \sigma_B T^4 &- \int_{\partial\Omega_{cr}} \epsilon_{\partial\Omega_{cr}} \sigma_B T^4(\boldsymbol{r}') F_S(\boldsymbol{r}, \boldsymbol{r}') \, \mathrm{d}S' \\ &- \int_{\Omega_{cr}} 4\kappa\sigma_B T^4(\boldsymbol{r}') F_V(\boldsymbol{r}, \boldsymbol{r}') \, \mathrm{d}\boldsymbol{r}'.\end{aligned} \tag{2.70}$$

The term on the left, $[\boldsymbol{q} \cdot \boldsymbol{n}]_-^+$, is the difference in the (conductive, convective) heat flux on either side of the boundary. On the right we have, respectively, the radiation emitted by the surface at $\boldsymbol{r}$, the incident radiation on $\boldsymbol{r}$ from the rest of the surface $\partial\Omega_{cr}$, and the incident volumetric radiation from the crater gas and arc.

The factors F_S and F_V in the integral terms in (2.70) are the surface and volumetric view factors, respectively. These take the geometry of the crater into account. If the region Ω_{cr} is convex, so that there is no obstacle blocking the view of any point on the surface from any other point on the surface, then these take the form [44, 72]

$$F_S(\boldsymbol{r}, \boldsymbol{r}') = \frac{\cos(\gamma)\cos(\gamma')}{\pi|\boldsymbol{r} - \boldsymbol{r}'|^2}, \qquad F_V(\boldsymbol{r}, \boldsymbol{r}') = \frac{\cos(\gamma)}{4\pi|\boldsymbol{r} - \boldsymbol{r}'|^2}. \tag{2.71}$$

Here γ is the angle between the normal vector at $\boldsymbol{r}$ and the ray from $\boldsymbol{r}'$ to $\boldsymbol{r}$, and similarly γ' is the angle between the ray $\boldsymbol{r}'$ to $\boldsymbol{r}$ and the normal vector at $\boldsymbol{r}'$.

The integral form of (2.70) makes this boundary condition difficult to implement in practice. We will simplify this condition in Chapter 3, under assumptions on the relative sizes of the terms. We also note that the boundary condition (2.70) requires knowledge of the temperature profile and heat flux through the base of the crater Γ_m, which we do not model. We might therefore prescribe the rate of conductive heat flux through this boundary to be $\boldsymbol{q} \cdot \boldsymbol{n} = H_m(T - T_m)$ for constants H_m and T_m.

The condition (2.70) may be thought of as a boundary condition for T_s at Γ_i, and T_e at Γ_a, and for the crater fluid temperature T at Γ_m. On Γ_a, we set $T = T_e$. We also require a boundary condition for the crater fluid temperature T on Γ_i to close the problem for T in Ω_{cr}. Finally, we assume that the gas flowing into the charge material is the same temperature as the crater fluid, so that

$$T = T_g \quad \text{ on } \Gamma_i. \tag{2.72}$$

2.6 Discussion

We do not yet nondimensionalise our full model, saving this analysis for the simplified models used in the subsequent chapters. However, we provide here a brief discussion of the relative sizes of various physical effects, to motivate the approaches taken in the remainder of the thesis.

2.6.1 Timescales

Firstly, there are a wide range of different timescales of the different physical and chemical processes.

The shortest timescales of interest are in the hottest part of the electric arc, where the timescale of the electromagnetic induction, fluid flow, and heat transfer is shown in Chapter 3 to be on the order of $t_{\text{arc}} = 10^{-5} - 10^{-6}$ s. The next shortest timescale is that of the applied alternating current, which has a frequency of around 50 Hz, and thus a timescale of $t_{\text{AC}} = 2 \times 10^{-2}$ s. Given the disparity of these timescales, it may seem reasonable to assume that the arc processes are quasi-steady, and so study the arc in quasi-steady state, for a slowly varying applied current or voltage. We look for such quasi-steady-state solutions in Chapter 4 but also note that the timescales associated with the fluid flow and heat transfer in the cooler main body of the arc and the crater gas are likely to be longer than t_{arc}. Furthermore, at lower imposed currents, the arc timescale increases. Thus a quasi-steady approach is unlikely to be valid for the entirety of the crater domain, or for the entirety of the AC cycle. These ideas are explored further in Chapters 3 and 4.

There are a number of timescales associated with material flow and chemical reaction rates in the charge material. In particular, the timescale of the flow of solid material through Ω_{ch} is on the order of hours, $t_{\text{charge}} = 10^3 - 10^4$ seconds. This is the same timescale over which the boundary Γ_i separating the charge and crater domains must move. In Chapter 3 we perform a multiple-timescale analysis on a simplified version of our model, homogenising over the fast variations in the arc and the flow of gas through the charge material, to derive an average model for the motion of the interface Γ_i.

At the other extreme, changes in the properties of the coal, woodchips, and quartz rock used as raw material occur over weeks or months. The SAFs for silicon production are run continuously for several years.

2.6.2 Temperatures and heat transfer

The temperature scalings in the furnace are largely determined by the current distribution, and we might expect different temperatures if the majority of the current passes through the arc, compared to if no current passes through the arc. Since we expect to be in the former case when the furnace is operating successfully, we may determine the temperature scaling in the arc for a given current by balancing the heat generation by Ohmic heating and the dominant heat loss mechanism, in (2.11). In this case the dominant heating mechanism of the charge material is the radiative or convective flux of heat from the arc, in the boundary condition (2.70) at Γ_i. We may fix the appropriate temperature scalings for T_s and T_g here, in terms of the arc temperature. We use these scaling ideas in the nondimensionalisation of Chapter 3.

Within the charge material, region Ω_{ch}, heat is transferred by conduction in the solid, and convection with the flow of each phase. In Chapter 3 we see that the Péclet number of the heat transfer in the solid phase is expected to be large, so that the advection of heat dominates over conduction in the solid phase on the lengthscale of the furnace. We therefore anticipate that the heat provided to the charge material by the arc at Γ_i does not conduct very far into the solid charge material, but is largely contained within a conduction boundary layer of width $O(\mathrm{Pe}^{-1})$ compared to the size of the furnace domain, at Γ_i. It must therefore be the heat transfer from the gas to the solid phase that is the dominant mechanism by which the solid is heated outside of this boundary layer. We explore these behaviours for a simplified version of the model in Chapter 5.

Since the electrical conductivity of the solid charge material depends strongly on T_s, we only expect current to flow in the hottest part of Ω_{ch}. Assuming, as we describe above, that the majority of the current flows through the arc, the hottest part of the charge material is the conductive boundary layer at Γ_i. The analysis in Chapters 3–6 is carried out on this basis. However, this might not be the case if the majority of the current flows through the charge material, generating heat locally by Ohmic heating. This scenario is briefly described in the further work section of Chapter 7, but it would be very interesting to investigate this case further, as this is occasionally seen in practice and is detrimental to efficient silicon production.

Chapter 3

A reduced, homogenised model for a submerged arc furnace

In this chapter we make a significant reduction of the model presented in Chapter 2, in order to derive a model which is tractable analytically. We first present a simplified model for the electric arc, motivated by a dimensional analysis of the MHD model presented in Section 2.2. We next simplify the problem for the heat radiation over the crater, and restrict to a two-phase model in the charge bed, justified by the analysis in [92]. We then choose a greatly simplified geometry of the domain, which reduces the problem in the charge material to just one spatial variable.

We nondimensionalise the simplified model in Section 3.2, and discuss the dimensionless parameters, noting in particular a disparity of timescales between the fast timescale of the alternating current, and the slower chemical, flow, and heat transfer processes in the charge material. Motivated by this, we perform a multiple-timescale homogenisation in Section 3.3, to average the effects of the alternating current, deriving a homogenised model valid over the much longer timescale of the motion of the charge. This homogenised model will be analysed in detail in Chapters 4, 5 and 6.

3.1 Model simplification

3.1.1 The electric arc

3.1.1.1 Dimensional analysis of the MHD arc model

In order to motivate a simplified model for the electric arc, we give a dimensional analysis of the MHD model, (2.1)–(2.3), (2.8), and (2.9)–(2.11), with constitutive laws (2.12), (2.13), and (2.16), presented in Chapter 2.

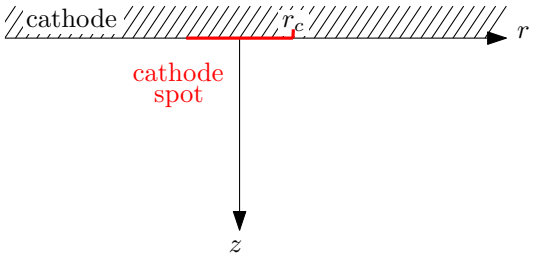

Figure 3.1: Axisymmetric, cylindrical coordinate system for the electric arc.

There are very few externally prescribed scalings for the electric arc, as its size, shape, temperature, current density, and fluid velocity are all self-determined. The hottest region in the arc, with highest current density, is expected to be at the cathode, where the current density must be very high in order to maintain the high enough temperatures in the electrode for the thermionic emission of ions. As discussed in Section 2.5.1, the current emitted by the electrode can be modelled via (2.57). At the hottest temperatures that the electrode can attain (before sublimation), of around $T_c = 4000\,\mathrm{K}$ [50], the current density $J_0 = j_c(T_c)$ that can be emitted is given by (2.57). We assume that, for all relevant furnace arcs, the cathode spot temperature is always close to T_c, and so we have a fixed current density scaling J_0, which does not depend on the total applied current I. (For sufficiently low currents I, this assumption will cease to be valid.) The cathode spot radius, r_c, however, does vary with I according to

$$r_c = \sqrt{\frac{I}{\pi J_0}}. \tag{3.1}$$

We assume that r_c is a reasonable lengthscale for the radius of the electric arc, although in reality we expect the arc to grow away from the cathode spot. The other externally prescribed lengthscale is the length of the arc, h_a, which we expect to be larger than the radius of the cathode spot, so that $\epsilon_a := r_c/h_a$ is small.

We choose to deduce the scalings for our arc variables from these parameters. We use a cylindrical coordinate system (r, θ, z) with z along the axis of the arc and r, θ in the cross-section of the arc as shown in Figure 3.1. For simplicity, we suppose the arc is axisymmetric, so that there is no θ dependence. We also assume that the magnetic field is purely azimuthal $\boldsymbol{B} = B_\theta \boldsymbol{e}_\theta$, and that all other vector dependent variables have no azimuthal component, using the notation $\boldsymbol{v} = u\boldsymbol{e}_r + v\boldsymbol{e}_z$, $\boldsymbol{J} = J_r\boldsymbol{e}_r + J_z\boldsymbol{e}_z$, and $\boldsymbol{E} = E_r\boldsymbol{e}_r + E_z\boldsymbol{e}_z$. We nondimensionalise the model in Ω_{cr} by scaling

$$z = h_a\hat{z} = \epsilon_a^{-1} r_c \hat{z}, \qquad r = r_c\hat{r}, \qquad t = t_0\hat{t}, \tag{3.2a}$$

$$\boldsymbol{J} = J_0\left(\epsilon_a \hat{J}_r \boldsymbol{e}_r + \hat{J}_z \boldsymbol{e}_z\right), \qquad \boldsymbol{B} = B_0\hat{B}_\theta \boldsymbol{e}_\theta, \qquad \sigma_a = \sigma_0\hat{\sigma}_a, \tag{3.2b}$$

$$\boldsymbol{v} = v_0 \left(\epsilon_a \hat{u} \boldsymbol{e}_r + \hat{v} \boldsymbol{e}_z\right), \qquad T = T_0 \hat{T}, \qquad \rho = \rho_0 \hat{\rho}, \tag{3.2c}$$

$$\boldsymbol{E} = E_0 \left(\hat{E}_r \boldsymbol{e}_r + \hat{E}_z \boldsymbol{e}_z\right), \qquad p = p_{\text{atm}} + p_0 \hat{p}. \tag{3.2d}$$

The radial velocity and current density are both expected to be smaller than the axial components, in order for there to be a balance in the conservation of mass equation, (2.9), and conservation of charge equation, (2.8), respectively.

Since the magnetic field is generated by the current, we fix

$$B_0 = \mu_0 r_c J_0, \tag{3.3}$$

in order to balance both the radial and axial components of Ampere's law, (2.1). The electrical field scaling is chosen to balance the current density in Ohm's law, (2.13), so that

$$E_0 = \frac{J_0}{\sigma_0}. \tag{3.4}$$

The high temperatures in the arc are due to the Ohmic heating, and so we can fix the temperature scale by balancing this heat source with the dominant heat loss mechanism. We assume that this is the heat loss to radiation, and we will see below that this leads to a consistent nondimensionalisation. We therefore fix

$$4\kappa\sigma_B T_0^4 = J_0 E_0 = \frac{J_0^2}{\sigma_0}, \tag{3.5}$$

where we have used (3.4). In the arc, there is a pressure associated with the Lorentz force, and so we scale

$$p_0 = r_c J_0 B_0 = r_c^2 \mu_0 J_0^2, \tag{3.6}$$

in order to balance the pressure gradient and Lorentz force in both the radial and axial components of (2.10). The ideal gas law then fixes the density scaling

$$\rho_0 = \frac{p_0}{R_s T_0}. \tag{3.7}$$

Since the fluid flow is generated by the Lorentz force, we balance the inertia and Lorentz force terms in (2.10), and so choose v_0 according to

$$\rho_0 \frac{v_0^2}{r_c} = J_0 B_0. \tag{3.8}$$

There are a number of possible timescales associated with this problem, but we choose the timescale of the heat generation and loss in the arc, which is

$$t_0 = \frac{\rho_0 c_v T_0}{J_0 E_0}. \tag{3.9}$$

Dropping the hat notation, the dimensionless system therefore becomes

$$J_z = \frac{1}{r}\frac{\partial}{\partial r}(rB_\theta), \tag{3.10}$$

$$J_r = -\frac{\partial B_\theta}{\partial z}, \tag{3.11}$$

$$-(\gamma-1)\frac{\partial B_\theta}{\partial t} = \epsilon_a \frac{\partial E_r}{\partial z} - \frac{\partial E_z}{\partial r}, \tag{3.12}$$

$$J_z = \sigma_a(T)(E_z + \epsilon_a \beta u B_\theta), \tag{3.13}$$

$$\epsilon_a J_r = \sigma_a(T)(E_r - \beta v B_\theta), \tag{3.14}$$

$$p + p_* = \rho T, \tag{3.15}$$

$$\beta^{-1}\frac{\partial \rho}{\partial t} + \frac{1}{r}\frac{\partial}{\partial r}(r\rho u) + \frac{\partial}{\partial z}(\rho v) = 0, \tag{3.16}$$

$$\epsilon_a \beta^{-1}\rho\frac{\partial u}{\partial t} + \epsilon_a^2 \rho\left(u\frac{\partial u}{\partial r} + v\frac{\partial u}{\partial z}\right) = -\frac{\partial p}{\partial r} - J_z B_\theta + \epsilon_a \mathrm{Re}^{-1}\left(\frac{1}{r}\frac{\partial}{\partial r}\left(r\frac{\partial u}{\partial r}\right) + \epsilon_a^2\frac{\partial^2 u}{\partial z^2}\right), \tag{3.17}$$

$$\beta^{-1}\rho\frac{\partial v}{\partial t} + \rho\left(u\frac{\partial v}{\partial r} + v\frac{\partial v}{\partial z}\right) = -\frac{\partial p}{\partial z} + J_r B_\theta + \epsilon_a^{-1}\mathrm{Re}^{-1}\left(\frac{1}{r}\frac{\partial}{\partial r}\left(r\frac{\partial v}{\partial r}\right) + \epsilon_a^2\frac{\partial^2 v}{\partial z^2}\right), \tag{3.18}$$

$$\begin{aligned}\frac{\rho}{\gamma-1}\left(\frac{\partial T}{\partial t} + \epsilon_a\beta\left(u\frac{\partial T}{\partial r} + v\frac{\partial T}{\partial z}\right)\right) = K\left(\frac{1}{r}\frac{\partial}{\partial r}\left(r\frac{\partial T}{\partial r}\right) + \epsilon_a^2\frac{\partial^2 T}{\partial z^2}\right) \\ + \frac{1}{\sigma_a(T)}\left(J_z^2 + \epsilon_a^2 J_r^2\right) - T^4 \\ - \beta\epsilon_a(p_* + p)\left(\frac{1}{r}\frac{\partial}{\partial r}(ru) + \frac{\partial v}{\partial z}\right),\end{aligned} \tag{3.19}$$

where the dimensionless parameters are

$$\beta = \mu_0\sigma_0 r_c v_0, \quad \mathrm{Re} = \frac{\rho_0 v_0 r_c}{\eta}, \quad K = \frac{kT_0}{r_c^2 J_0 E_0}, \quad p_* = \frac{p_{\mathrm{atm}}}{p_0}, \quad \gamma = \frac{c_p}{c_v}. \tag{3.20}$$

The parameter β is the magnetic Reynold's number of the fluid [27], characterising the ratio of the current due to the flow of fluid in the magnetic field to that proportional to the electric field, in Ohm's law (3.13)–(3.14). Due to our choice of scalings, this parameter also describes the ratio of the fluid flow timescale to the heat transfer timescale, and appears in the heat convection term of (3.19).

Typical parameter values for industrial SAF arcs are given in Table 3.1. Using these, we may compute the derived scales for the arc variables, which are given in Table 3.2, and the sizes of the dimensionless groups, given in Table 3.3. We notice that the magnetic Reynolds number β is less than one, but is not particularly small. However, the reduced magnetic Reynolds number, $\epsilon_a\beta$, is reasonably small, due to the small aspect ratio. This means that the vertical current J_z given by (3.13) (which is

the dominant component of the electric current), is primarily due to the electric field over the crater E_z. Even though the magnetic Reynolds number β is not small, we have significantly simplified the electromagnetic problem so that there is no induced vertical current, by assuming that the arc is long and thin.

We also note that $K \ll 1$, so that heat radiation is indeed the dominant heat loss mechanism in (3.19), justifying our choice of scaling T_0. In fact, in the limit that all of $\epsilon_a\beta$, ϵ_a, and K are small, the heat equation (3.19) simplifies considerably, to

$$\frac{\rho}{\gamma - 1}\frac{\partial T}{\partial t} = \frac{J_z^2}{\sigma_a(T)} - T^4, \tag{3.21}$$

so that the dominant heat source is the Ohmic heating due to the vertical current, and the dominant heat loss is by radiation. As well as simplified electromagnetic and thermal problems, we may also obtain a reduction of the fluid flow problem from our dimensional analysis, which is similar to the Prandtl boundary layer equations, but with the additional Lorentz force in both the radial and axial momentum equations.

The reduction of the thermal problem to (3.21) is closely linked to the analysis in the study group report [19]. In this report, the arc is modelled as a cylinder, with axial current due to a uniform axial electric field. Heat losses are due to optically thin radiation and radial heat conduction, and fluid flow is neglected. Steady-state, axisymmetric solutions are sought. As in our dimensional analysis, in [19] the heat conduction is small relative to the radiation, and so to leading order there is a balance between Ohmic heating and radiative losses. At leading order, the arc temperature is therefore piecewise constant, with a hot temperature $T = T_a$ inside the arc, and $T = 0$ outside the arc, both of which are steady states of (3.21). There is a thermal conduction transition layer at the edge of the arc, where heat conduction smooths out

Parameter	Value	Reference
J_0	$10^7\,\mathrm{A\,m^{-2}}$	(as described in Section 2.5)
r_c	$2.3 \times 10^{-2}\,\mathrm{m}$	(as described in Section 2.5)
h_a	$1\text{–}1.5\times10^{-1}\,\mathrm{m}$	[85]
k	$1\,\mathrm{W\,m^{-1}\,K^{-1}}$	[85, 107]
R_s	$2.3 \times 10^2\,\mathrm{J\,kg^{-1}\,K^{-1}}$	using a 1:1 ratio of SiO:CO
η	$10^{-4}\,\mathrm{kg\,m^{-1}\,s^{-1}}$	[107]
c_p	$10^3\,\mathrm{J\,kg^{-1}\,K^{-1}}$	[107]
σ_0	$10^4\,\mathrm{S\,m^{-1}}$	[85, 107]
κ	$10^{-1}\,\mathrm{m^{-1}}$	[82]

Table 3.1: Parameter values for the arc.

Variable Scale	Expression	Value
T_0	$(J_0^2/4\kappa\sigma_B\sigma_0)^{1/4}$	$3 \times 10^4\,\mathrm{K}$
E_0	J_0/σ_0	$10^3\,\mathrm{V\,m^{-1}}$
B_0	$\mu_0 r_c J_0$	$3 \times 10^{-1}\,\mathrm{T}$
p_0	$r_c J_0 B_0$	$10^5\ \mathrm{Pa} \approx 1\,\mathrm{atm}$
ρ_0	$p_0/R_s T_0$	$10^{-2}\,\mathrm{kg\,m^{-3}}$
v_0	$(r_c J_0 B_0/\rho_0)^{1/2}$	$2 \times 10^3\,\mathrm{ms^{-1}}$
t_0	$\mu_0 r_c^2 \sigma_0$	$7 \times 10^{-6}\,\mathrm{s}$

Table 3.2: Values of derived scalings.

Dimensionless Group	Expression	Value
β	$\mu_0\sigma_0 r_c v_0$	0.6
Re	$\rho_0 v_0 r_c/\eta$	5×10^3
K	$kT_0/r_c^2 J_0 E_0$	6×10^{-3}
p_*	p_{atm}/p_0	1
γ	c_p/c_v	1.3
ϵ_a	r_c/h_a	0.15–0.23

Table 3.3: Values of dimensionless groups.

the temperature jump, and the radius of the arc is determined from this transition layer problem. Under our nondimensionalisation above, the MHD model reduces to precisely the problem of [19], if $\epsilon_a^2\beta^2 \ll K \ll 1$.

From our dimensional analysis we expect that for a SAF arc $\epsilon_a^2\beta^2 \geq K$, and so heat convection is likely to be at least as important as heat conduction. In this case, similarly to the conductive arc of [19], we might expect a uniform hot temperature, the solution of (3.21), inside the arc, and $T = 0$ outside the arc. The radial extent of the arc would be determined by consideration of both the fluid flow and heat conduction at the boundary. Such analysis is beyond the scope of this thesis, but is discussed as future work in Chapter 7. In the simplified arc model below, we simply prescribe the radius of the electric arc to be constant.

As a final observation from the dimensional analysis, we notice that since β is around order one, the timescales of the electromagnetic induction, fluid flow, and heat transfer, are all very similar. We also note that this timescale, $t_0 \sim 10^{-6}\,\mathrm{s}$, is much shorter than the timescale of the alternating current on the order of $10^{-2}\,\mathrm{s}$. We might assume, therefore, that the arc is quasi-steady over the timescale of the alternating current. However, our scalings have all been derived assuming a high current density J_0. For smaller currents (near or at the point in the AC cycle when

the current passes through zero), the temperature will be lower. Since both the Ohmic heating and radiative heat loss terms are strongly dependent on T, we expect much slower arc variation when it is cooler, at these lower currents. The arc will not, therefore, behave quasi-steadily throughout the entirety of the AC cycle. We will explore these ideas further in Chapter 4.

3.1.1.2 Statement of a simplified arc model

We now propose a simplified arc model based on the insight gained in the previous section, returning to dimensional variables. The dimensional analysis suggests that the current is primarily axial, and due to the applied electric field rather than inductive effects. We also observed that heat radiation and Ohmic heating due to the vertical current are the most important mechanisms determining the arc temperature.

We assume for simplicity that the arc occupies a vertical, cylindrical region, with fixed, prescribed radius r_a, and a purely vertical electric current. We also assume the arc has fixed position in centre of the crater. The electrical-thermal problem for the temperature T_a, of this cylindrical arc and the vertical electric field, E_a, over the arc is given by conservation of energy including only radiative heat loss and vertical Ohmic heating, and the equation of conservation of charge, namely

$$\rho_a c_{p,a} \frac{\partial T_a}{\partial t} = \sigma_a(T_a) E_a^2 - 4\kappa\sigma_B T_a^4, \tag{3.22a}$$

$$\frac{\partial}{\partial z}\left(\sigma_a(T_a) E_a\right) = 0. \tag{3.22b}$$

Since there is no spatial dependence of T_a through (3.22a), we look for uniform solutions $T_a = T_a(t)$, a function of time only. In this case (3.22b) simply requires that $E_a = E_a(t)$ is also spatially uniform.

3.1.2 Simplification of the radiation problem in the crater

With the simplified arc model given above, all heat lost by the arc is lost as radiation. As discussed in Section 2.5.3, this radiation is incident on the surfaces of the crater, where it is absorbed, and partially re-emitted, modelled by the integral boundary condition (2.70). This integral boundary condition greatly increases the computational complexity of the problem: the heat flux condition at every point on the crater boundary $\partial\Omega_{cr}$ requires knowledge of the temperatures and heat flux at all other points of $\partial\Omega_{cr}$, and both surface integrals over $\partial\Omega_{cr}$ and volume integrals over Ω_{cr}. In this section we make a rational reduction of (2.70), showing that, in the industrially

relevant parameter regime, the surface temperature on the crater boundary $\partial\Omega_{cr}$ is uniform. This leads to a greatly simplified heat flux boundary condition (2.70).

We assume that the crater Ω_{cr} is a convex domain, so that all radiating surfaces have a line-of-view to all other points on the surface, with no obstacles blocking the radiation path. The view factors then take the form (2.71). Using the data given in Section 3.2, we may estimate the size of each of the terms in (2.70). Assuming that the volumetric radiation is dominated by the arc (rather than the much cooler surrounding crater gases), the volume integral

$$I_a := \int_{\Omega_{cr}} 4\kappa\sigma_B T^4(\boldsymbol{r}')\frac{\cos(\gamma)}{4\pi|\boldsymbol{r}-\boldsymbol{r}'|^2}\,\mathrm{d}\boldsymbol{r}' \tag{3.23}$$

has approximate order of magnitude

$$[I_a] = \frac{\kappa\sigma_B T_a^4 \pi r_a^2 h_a}{\pi \times (\text{distance from arc})^2} \approx 6\times 10^4\,\mathrm{W\,m^{-2}}, \tag{3.24}$$

where h is the length of the arc, and assuming the distance from the arc is approximately 1 m [85]. The surface emission term $\epsilon_{\partial\Omega_{cr}}\sigma_B T^4(\boldsymbol{r})$, is the same size as the incident radiation from the crater surfaces,

$$I_S := \int_{\partial\Omega_{cr}} \epsilon_{\partial\Omega_{cr}}\sigma_B T^4(\boldsymbol{r}')\frac{\cos(\gamma)\cos(\gamma')}{\pi|\boldsymbol{r}-\boldsymbol{r}'|^2}\,\mathrm{d}S', \tag{3.25}$$

the size of which may be estimated by $[I_S] = \epsilon_{\partial\Omega_{cr}}\sigma_B T_S^4 \approx 6\times 10^6\,\mathrm{W\,m^{-2}}$, using $\epsilon_{\partial\Omega_{cr}} = 1$ [5]. Nondimensionalising (2.70) we therefore write

$$\mathcal{Q}[\boldsymbol{q}\cdot\boldsymbol{n}]^+_- = T^4 - \int_{\partial\Omega_{cr}} T^4(\boldsymbol{r}')\frac{\cos(\gamma)\cos(\gamma')}{\pi|\boldsymbol{r}-\boldsymbol{r}'|^2}\,\mathrm{d}S' - \nu\int_{\Omega_{cr}} T_a^4(\boldsymbol{r}')\frac{\cos(\gamma)}{\pi|\boldsymbol{r}-\boldsymbol{r}'|^2}\,\mathrm{d}\boldsymbol{r}', \tag{3.26}$$

where $\nu := [I_a]/[I_S]$ and $\mathcal{Q}$ is the ratio of heat loss to the solid material at that point, to the radiative heat loss term.

From our order-of-magnitude estimates we see that $\nu \approx 0.01 \ll 1$ is small, so that for industrially relevant parameters the surface radiation dominates the radiation from the arc. We also expect that $\mathcal{Q} = O(\nu)$, since if $\mathcal{Q}$ were $O(1)$ then the crater surfaces could not be maintained at the required temperatures, as there would be too much heat lost from the system. In this case, expanding the surface temperature $T \sim T_0 + \nu T_1$ as $\nu \to 0$, at leading order we have

$$T_0^4(\boldsymbol{r}) = \int_{\partial\Omega_{cr}} T_0^4(\boldsymbol{r}')\frac{\cos(\gamma)\cos(\gamma')}{\pi|\boldsymbol{r}-\boldsymbol{r}'|^2}\,\mathrm{d}S'. \tag{3.27}$$

For ease of notation we define the radiation energy $y(\boldsymbol{r}) := T_0^4(\boldsymbol{r})$, and the surface view factor $F(\boldsymbol{r}, \boldsymbol{r}') := \cos(\gamma)\cos(\gamma')/(\pi|\boldsymbol{r} - \boldsymbol{r}'|^2)$, noting that, since Ω_{cr} is convex and closed, by definition F satisfies [44, 72]

$$F(\boldsymbol{r}, \boldsymbol{r}') > 0 \quad \text{for} \quad \boldsymbol{r} \neq \boldsymbol{r}' \qquad \text{and} \qquad \int_{\partial\Omega_{cr}} F(\boldsymbol{r}, \boldsymbol{r}')\,\mathrm{d}S' = 1. \tag{3.28}$$

We now prove that the only continuous, non-negative solutions $T_0^4(\boldsymbol{r})$ of (3.27), or equivalently solutions $y(\boldsymbol{r})$ of

$$y(\boldsymbol{r}) = \int_{\partial\Omega_{cr}} y(\boldsymbol{r}')F(\boldsymbol{r}, \boldsymbol{r}')\,\mathrm{d}S', \tag{3.29}$$

where F satisfies (3.28), are spatially uniform, so that $y(\boldsymbol{r}) = y_0$ for all $\boldsymbol{r} \in \partial\Omega_{cr}$. The leading-order temperature T_0, the solution of (3.27), is therefore spatially uniform on the crater boundary. Our proof of this fact has been adopted by [84]. A similar result is proved in [54] in a spherically symmetric geometry, and including heat conduction into the surface in the dominant balance, using the Cauchy-Schwarz inequality.

Our proof is by contradiction. We suppose that y is a non-constant solution of (3.29). Then, as the domain is bounded, y attains a minimum y_m, and since y is non-constant and continuous there exists a subset Γ of $\partial\Omega_{cr}$ (with non-zero measure) such that for $\boldsymbol{r} \in \Gamma$, $y(\boldsymbol{r}) > y_m$. As y is a solution of (3.29), for any $\boldsymbol{r} \in \partial\Omega_{cr} \setminus \Gamma$,

$$\begin{aligned}
y_m = y(\boldsymbol{r}) &= \int_{\partial\Omega_{cr}} y(\boldsymbol{r}')F(\boldsymbol{r}, \boldsymbol{r}')\,\mathrm{d}S' \\
&\geq \int_{\partial\Omega_{cr}\setminus\Gamma} y_m F(\boldsymbol{r}, \boldsymbol{r}')\,\mathrm{d}S' + \int_{\Gamma} y(\boldsymbol{r}')F(\boldsymbol{r}, \boldsymbol{r}')\,\mathrm{d}S' \\
&> \int_{\partial\Omega_{cr}\setminus\Gamma} y_m F(\boldsymbol{r}, \boldsymbol{r}')\,\mathrm{d}S' + \int_{\Gamma} y_m F(\boldsymbol{r}, \boldsymbol{r}')\,\mathrm{d}S' \\
&= y_m \int_{\partial\Omega_{cr}} F(\boldsymbol{r}, \boldsymbol{r}')\,\mathrm{d}S' \\
&= y_m \qquad \text{using (3.28)},
\end{aligned} \tag{3.30}$$

which gives the contradiction. Hence the only solutions of (3.29) are spatially uniform. Physically, since the heat radiation between surfaces is the dominant process, the temperature of these surfaces all equilibrate to the same, uniform temperature.

To fix the value of this uniform surface temperature T_0, we must find a solvability condition by continuing to next order in ν, where we see that

$$[\boldsymbol{q}\cdot\boldsymbol{n}]_-^+ = 4T_0^3T_1 - \int_{\partial\Omega_{cr}} 4T_0^3T_1(\boldsymbol{r}')\frac{\cos(\gamma)\cos(\gamma')}{\pi|\boldsymbol{r} - \boldsymbol{r}'|^2}\,\mathrm{d}S' - \int_{\Omega_{cr}} T_a^4(\boldsymbol{r}')\frac{\cos(\gamma)}{\pi|\boldsymbol{r} - \boldsymbol{r}'|^2}\,\mathrm{d}\boldsymbol{r}'. \tag{3.31}$$

Integrating (3.31) over the whole surface $\partial\Omega_{cr}$, and exchanging the order of integration, the first two terms on the right-hand side cancel, leaving

$$\int_{\partial\Omega_{cr}} [\boldsymbol{q}\cdot\boldsymbol{n}]_-^+ \,\mathrm{d}S = -\int_{\partial\Omega_{cr}}\int_{\Omega_{cr}} T_a^4(\boldsymbol{r}')\frac{\cos(\gamma)}{\pi|\boldsymbol{r}-\boldsymbol{r}'|^2}\,\mathrm{d}\boldsymbol{r}'\mathrm{d}S, \tag{3.32}$$

which may be interpreted as a global conservation of energy. The left-hand side depends on the surface temperature T_0, and hence this is a solvability condition, fixing T_0. Furthermore, since we assume T_a is uniform in a prescribed arc region, (3.32) reduces to simply

$$\int_{\partial\Omega_{cr}} [\boldsymbol{q}\cdot\boldsymbol{n}]_-^+ \,\mathrm{d}S = -T_a^4, \tag{3.33}$$

by the definition of the volumetric view factor. The left-hand side of (3.33) may also take a simple form, since T_0 is uniform on $\partial\Omega_{cr}$. We note that even without the assumption that $\nu \ll 1$ we may integrate (2.70) over $\partial\Omega_{cr}$ and regain (3.32), since the two surface terms cancel by definition of the view factor. However, we require $\nu \ll 1$ in order to justify taking the temperature T_0 of the surface to be spatially uniform.

The boundary condition (3.33) allows us to include the radiation effects of an optically thin arc contained in the crater in a relatively straightforward manner when coupling the arc model with the heat transfer and electrical system in the surrounding charge material.

3.1.3 Reduced chemical system

In Section 2.3.1, we presented a seven-species chemical system for the production of silicon in the bed of charge material Ω_{ch}. This system has been analysed in detail by Sloman et al. in [93]. In particular, it is shown that in the hottest part of the furnace, the dominant behaviour is the melting of quartz via reaction (2.24), which then further reacts with carbon via (2.26). As well as being the dominant change of chemical species, the endothermic reaction (2.26) is also shown to be the most significant energy sink in this region of charge material. In cooler regions of the furnace, the dominant reactions are shown to be the condensation of the SiO gas via (2.23), and its reaction with carbon to form SiC via (2.22). Both these reactions occur higher in the furnace, and are exothermic, releasing energy into the system.

For a simplest possible model, we neglect the condensation reaction (2.23) and the production of SiC (2.22) and focus on the dominant, endothermic behaviour due to the melting of quartz and its reaction with carbon occurring in the hottest part of the

furnace. This simplification, motivated by the findings of [93], reduces the chemical process to just the two reactions (2.24) and (2.26), which we write again for clarity:

$$\mathrm{SiO_2}(s) \rightarrow \mathrm{SiO_2}(l), \tag{3.34a}$$

$$\mathrm{SiO_2}(l) + \mathrm{C}(s) \rightarrow \mathrm{SiO}(g) + \mathrm{CO}(g). \tag{3.34b}$$

Furthermore, the rate of melting of the quartz (3.34a) is expected to be much slower than that of reaction (3.34b) [93], so that reaction (3.34b) is limited by (3.34a). Thus we may reduce the system to only the four chemical species, $\mathrm{SiO_2}(s)$, $\mathrm{C}(s)$, $\mathrm{SiO}(g)$, and $\mathrm{C}(g)$, related by the reaction

$$\mathrm{SiO_2}(s) + \mathrm{C}(s) \rightarrow \mathrm{SiO}(g) + \mathrm{CO}(g), \tag{3.35}$$

with reaction rate that of (3.34a). Since the solid materials are consumed in a 1:1 molar ratio by (3.35), and the gases likewise are produced in a 1:1 ratio, we make the further simplification of modelling only two phases: solid and gas. In order for this assumption to make sense we require that the raw materials fed into the furnace are also in a 1:1 molar ratio of carbon and quartz molecules.

Thus we reduce the full chemical system described in Section 2.3.1 to simply two phases, solid and gas, with the solid converted into gas,

$$\text{solid} \rightarrow \text{gas}, \tag{3.36}$$

at the rate of reaction (3.34a). In [93], this rate of reaction (3.34a) is assumed to be zero below a certain critical temperature, and linearly increasing with temperature above this point. In contrast, here we choose to use an Arrhenius chemical reaction rate for reaction (3.34a) of the form

$$Q = \bar{k}_Q C_{\mathrm{SiO_2}} e^{-a/T_s} = k_Q C_s e^{-a/T_s}, \tag{3.37}$$

where k_Q [s^{-1}] is the rate constant, a [K] encodes the activation energy of the reaction, and we have used the fact that the combined concentration of solid $C_s = C_{\mathrm{C}} + C_{\mathrm{SiO_2}}$ may be expressed as $C_s = 2C_{\mathrm{SiO_2}}$, since $C_{\mathrm{C}} = C_{\mathrm{SiO_2}}$ (thus we write the rate constant $k_Q = \bar{k}_Q/2$). Arrhenius reaction rates are commonly used for many types of reaction, and are fitted to give good agreement with experimental data. Unlike a piecewise linear model, the Arrhenius form (3.37) has the benefit of a smooth transition between an exponentially small reaction rate at low temperatures, and, while increasing with temperature, remains bounded, and so may be sensibly used over a wide temperature-range. A shortage of experimental data means that the parameters k_Q and a are not well known. We take the values $k_Q = 5 \times 10^{-2}\,\mathrm{s}^{-1}$ and $a = 10^4\,\mathrm{K}$ to give reasonable qualitative agreement with the model used in [92].

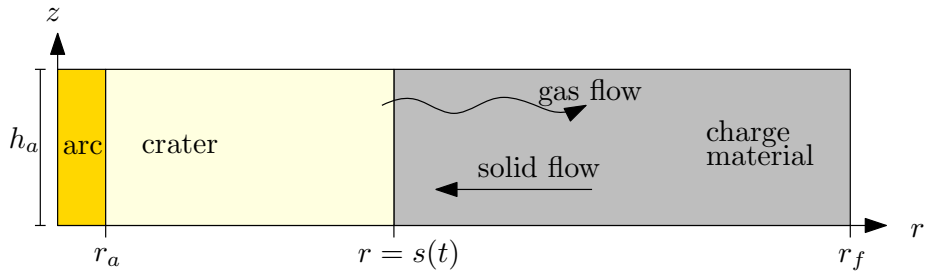

Figure 3.2: Idealised, axisymmetric geometry of nested cylinders for the arc, crater, and charge regions of the domain.

3.1.4 Cylindrical 1D geometry

We now restrict to a very simple, idealised domain geometry of axisymmetric nested cylinders, as illustrated in Figure 3.2, focussing on the behaviour under and around a single electrode, and using a cylindrical polar coordinate system (r, z). The geometry consists of the cylindrical electric arc, radius r_a and centred at $r = 0$, surrounded by a region of crater gas in the annulus $[r_a, s(t))$. The charge material Ω_{ch} forms another annulus around the crater, in $r \in [s(t), r_f]$, where the fixed position r_f is a "furnace radius", representing the surface of the furnace Γ_s, while $r = s(t)$ is the free boundary Γ_i. We assume that the height h_a of the domain is prescribed. The charge is heated by the radiation from the arc and a vertical current passing through the charge. In particular, we do not solve for the temperature profile or current density within the electrode. We assume that both the solid and gas velocities are purely radial, so that

$$\boldsymbol{u}_g = u_g \boldsymbol{e}_r \qquad \text{and} \qquad \boldsymbol{u}_s = -u_s \boldsymbol{e}_r, \tag{3.38}$$

for non-negative u_g and u_s. The species concentrations, velocities, and temperatures in the charge material are assumed to be independent of z, and are therefore functions of r and t only. With the simplified arc model (3.22), the arc variables T_a and E_a are uniform in space.

This 1D simplification is expected to describe well the case when charge material is pushed in under the electrode. If the crater extends to outside the electrode, as illustrated in Figure 1.2, the surface area of the interface Γ_i is increased, and a spherical geometry might be a more appropriate simplification. The result from Section 3.1.2 that the temperature at the interface Γ_i is spatially uniform justifies the assumption that the temperatures T_s and T_g in the charge material are independent of z, and therefore that all the dependent variables in the charge material are independent of z. By assuming 1D velocity fields we have lost any behaviours driven by the 3D material flow but, as discussed in Section 2.3.2, modelling the flow of the solid material would

not be straightforward. Our assumption that the solid material is being pushed in underneath the electrode, rather than flowing down the side of the crater, results in a fully 1D model. As we will see in Chapter 5, we often expect the majority of the heating and chemical consumption to occur in a thin boundary layer at Γ_i. The flow fields and geometry further away from the crater are therefore less important, providing some justification for the flow-field simplification and 1D geometry, as well as the choice to only study the region surrounding a single electrode, rather than the three electrodes commonly used in silicon SAFs.

As discussed in Section 2.3.2, the no-voids condition (2.36) fixes u_g in the high-permeability limit of Darcy's law. We make the assumption that the matrix of solid charge material is incompressible, and does not compact as material is reacted away, so that $M = 0$ in (2.38). Assuming the purely radial form (3.38) this fixes

$$u_s = \frac{U r_f}{r}, \tag{3.39}$$

with the flux $U r_f$ [$\mathrm{m^2\,s^{-1}}$] fixed by the imposed material flux at $r = r_f$.

The electrical conductivity σ_c of the charge material, given by (2.44), is a function of T_s, and therefore also varies radially. We assume that in our idealised geometry, the upper and lower surfaces are equipotentials, so that the current through the charge material is purely vertical,

$$\boldsymbol{J} = \sigma_c(T_s) E_{ch} \boldsymbol{e}_z, \tag{3.40}$$

with vertical electric field $\boldsymbol{E} = E_{ch}(z,t)\boldsymbol{e}_z$ over the charge material. By the conservation of charge equation,

$$\nabla \cdot \boldsymbol{J} = 0, \tag{3.41}$$

this vertical electric field E_{ch} must be independent of z, and thus $E_{ch} = E_{ch}(t)$ is a function of t only.

With this simplified geometry and the reduced chemical system presented in Section 3.1.3, we may add together the equations of conservation of mass (2.33) for the solids C and SiO_2, and the gases CO and SiO, respectively, to give the equations of conservation of mass in $r \in (s(t), r_f)$,

$$\frac{\partial C_s}{\partial t} - \frac{U r_f}{r}\frac{\partial C_s}{\partial r} = -Q(C_s, T_s), \tag{3.42}$$

$$\frac{\partial C_g}{\partial t} + \frac{1}{r}\frac{\partial}{\partial r}(r u_g C_g) = Q(C_s, T_s), \tag{3.43}$$

in the solid, and the gas phases. Here we have used our assumption that the gases are in a 1:1 ratio, so that the partial pressures $p_{\mathrm{CO}} = p_{\mathrm{SiO}} = p_g/2$. The equations of

conservation of energy (2.39)–(2.40) in the solid and gas phases of the charge material are similarly

$$c_{p,s}M_s\left(\frac{\partial}{\partial t}\left(C_sT_s\right)-\frac{Ur_f}{r}\frac{\partial}{\partial r}(C_sT_s)\right)=\frac{k_s}{r}\frac{\partial}{\partial r}\left(r\frac{\partial T_s}{\partial r}\right)+\sigma_cE_{ch}^2-\Delta HQ + \lambda(T_g-T_s)-c_{p,s}M_sT_sQ, \tag{3.44}$$

$$c_{p,g}M_g\left(\frac{\partial}{\partial t}\left(C_gT_g\right)+\frac{1}{r}\frac{\partial}{\partial r}(ru_gC_gT_g)\right)=\lambda(T_s-T_g)+c_{p,s}M_sT_sQ, \tag{3.45}$$

assuming that the specific heat capacities and thermal conductivity of the solid material are constants. In (3.44)–(3.45) we have used the notation

$$c_{p,s}M_s=c_{p,\mathrm{C}}M_{\mathrm{C}}+c_{p,\mathrm{SiO_2}}M_{\mathrm{SiO_2}},\qquad c_{p,g}M_g=c_{p,\mathrm{CO}}M_{\mathrm{CO}}+c_{p,\mathrm{SiO}}M_{\mathrm{SiO}}. \tag{3.46}$$

We have also assumed that all the heat ΔH for reaction (3.36) is taken from the solid material, since the solid is the reactant of (3.36). We note that we may absorb the heat transfer to the gas due to mass transfer term, $c_{p,s}M_sT_sQ$ into the advection term of the left of (3.44), by using the conservation of mass equation (3.42). The equation for conservation of energy in the solid, (3.44), then becomes

$$c_{p,s}M_sC_s\left(\frac{\partial T_s}{\partial t}-\frac{Ur_f}{r}\frac{\partial T_s}{\partial r}\right)=\frac{k_s}{r}\frac{\partial}{\partial r}\left(r\frac{\partial T_s}{\partial r}\right)+\sigma_cE_{ch}^2-\Delta HQ+\lambda(T_g-T_s). \tag{3.47}$$

Furthermore, with just the two species of solid and gas, the no-voids condition (2.36) becomes

$$\frac{M_s}{\rho_s}C_s+\frac{R}{p_{\mathrm{atm}}}C_gT_g=1, \tag{3.48}$$

where we have used that fact that $p_g=p_{\mathrm{atm}}$ is approximately uniform, and where we write

$$\frac{M_s}{\rho_s}=\frac{M_{\mathrm{C}}}{\rho_{\mathrm{C}}}+\frac{M_{\mathrm{SiO_2}}}{\rho_{\mathrm{SiO_2}}}. \tag{3.49}$$

These five equations (3.42), (3.43), (3.45), (3.47), and (3.48) form a closed system for C_s, C_g, T_s, T_g, and u_g. In this geometry and chemical system, the boundary conditions at the edge of the furnace Γ_s as described in Section 2.5, become

$$T_s=T^{\mathrm{in}},\quad C_s=C_s^{\mathrm{in}}\qquad \text{at } r=r_f. \tag{3.50}$$

The position of the free boundary $r=s(t)$ is determined by (2.62), which we can express in terms of the solid concentration as

$$C_s=C_*\qquad \text{at } r=s(t), \tag{3.51}$$

for some prescribed constant C_* corresponding to θ_* in (2.62).

We interpret the heat flux condition (3.33) as a statement of conservation of energy in the solid materials at the edge of the crater, and we therefore view this as a boundary condition for T_s. Since we do not solve for the heat transfer within the crater pool or electrode, we approximate the heat lost through a point on these boundaries by a Newton-cooling term $H_m(T - T^\infty)$, where T^∞ is a constant, small temperature (in Chapter 3 we will set $T^\infty = 0$). As discussed in Section 2.5, we expect some gas to be produced in reactions in the melt-pool at the base of the crater, Γ_m, via (2.63). These reactions are endothermic so that this contributes a heat loss to (3.33). We suppose these melt-pool reactions produce SiO and CO gases with constant rate R_m [$\mathrm{kg\,m^{-2}\,s^{-1}}$], in a 1:1 ratio. We estimate R_m by assuming that the gas is produced by reaction (3.36) in a thin volume depth $d_p \sim 10^{-4} - 10^{-3}\,\mathrm{m}$ in the pool, so that $R_m = [Q]M_g d_p$, where $[Q]$ is the approximate size of the reaction rate (3.37). The heat loss due to this reaction is $R_m(c_{p,s}T_s + \Delta H/M_s)$ per unit surface area of Γ_m. This assumption that the reaction rate in the pool is constant is a simplification, and means that we do not have to keep track of the mass of reactants lost from the charge material (gained by the melt pool) when it collapses at $r = s$. If C_* is small, we expect that this simplification will not make significant changes to the results of the model. However if large amounts of material are falling into the crater pool and reacting here, so that a significant proportion of the material consumption occurs in the melt pool, then we should include a more accurate model for this reaction rate R_m. Extending the model in this way is an important area for future work.

We neglect any conductive heat transfer between the solid crater boundaries and the crater gas, as this is expected to be relatively small. Using the fact that the surface temperature on all the crater boundaries is the same as that on $r = s(t)$, we may compute the integral on the left of (3.33), leaving the boundary condition

$$\pi s^2 H_m(T_s - T^\infty) + \pi s^2 R_m \left(c_{p,s}T_s + \frac{\Delta H}{M_s} \right) = 2\pi s h_a \left(c_{p,s} M_s \frac{U r_f}{s} C_s T_s + k_s \frac{\partial T_s}{\partial r} \right) + (\pi r_a^2 h_a) 4\kappa\sigma_B T_a^4 \quad \text{at } r = s(t). \tag{3.52}$$

This is precisely the conservation of energy over the entire surface of the crater: the total heat radiation from the arc must equal the total heat conducted into the crater surfaces, and lost to the chemical reactions in the pool. The heat in the solid material which collapses into the crater, effectively flowing through the boundary $r = s$, is lost from the charge bed, but is gained by the material in the melt pool. Thus we include the advection term (the first term on the right of (3.52)) in this boundary condition. Due to our choice of cylindrical geometry, the heat losses through to the electrode

and melt pool are quadratic in s, while the heat losses through $r = s(t)$ are linear, or constant, in s.

We also require boundary conditions at $r = s(t)$ for C_g and T_g. In Section 2.5 we imposed continuity of gas flux and temperature with the crater gases at the interface Γ_i. However, we now have a much simpler model (3.22a) for the temperature of the arc, and so we do not explicitly solve for either the flow or heat transfer within the crater gas in $r \in (r_a, s(t))$. Instead, we assume that the density of crater gas is constant. Expressing the rate of change of the total gas in the crater in terms of the rate, R_m per unit area, at which gas is produced in the pool Γ_m, and the rate of gas flow through the charge surface Γ_i, we find that in our cylindrical geometry,

$$2\pi h_a \rho_g s\dot{s} = \pi s^2 R_m - 2\pi s h_a \rho_g \theta_g (u_g - \dot{s}). \tag{3.53}$$

Making use of (2.31), we see that (3.53) implies the boundary condition for C_g given by

$$C_g \left(u_g + \frac{1-\theta_g}{\theta_g}\dot{s} \right) = \frac{sR_m}{2h_a M_g} \qquad \text{at } r = s(t). \tag{3.54}$$

Using the approximate form of R_m and writing $1 - \theta_g = \theta_s = M_s C_* / \rho_s$ at $r = s$, we find that

$$C_g \left(u_g + \frac{M_s C_*}{\rho_s - M_s C_*}\dot{s} \right) = \frac{s[Q]d_p}{2h_a} \qquad \text{at } r = s(t). \tag{3.55}$$

For the boundary condition for T_g at $r = s(t)$, it might be intuitive to simply assume that $T_g = T_s$ at $r = s(t)$. It is preferable, however, to instead impose conservation of energy in the crater gas, in order to track and understand all the transfers of energy in the system. We do not solve explicitly for the temperature of the crater gas, but instead consider the overall conservation of energy in the crater gas, similarly to the conservation of mass argument above. In our simplified arc model (3.22a), the arc loses heat only by optically-thin radiation, which is incident onto the crater surface, and so the electric arc does not directly heat the crater gas. (For a more accurate crater model, we could assume that some proportion of the heat dissipated by the arc is passed to the crater gas, with the remainder incident on the solid crater wall, although it is not clear how this proportion should be determined.) The only heat source for the crater gas is therefore the energy gained when it is produced in the chemical reactions in the melt-pool. Arguing as for the mass flux above, the rate of change of energy inside the crater must equal the flux of energy gained by the gas as it is produced in the melt-pool at Γ_m minus the flux of heat as the gas flows out

of the crater into the porous charge material at $r = s(t)$. This gives the boundary condition

$$c_{p,g}T_g\left(2\pi h_a \rho_g s\dot{s}\right) = c_{p,s}T_s(\pi s^2 R_m) - c_{p,g}T_g\left(2\pi s h_a \rho_g \theta_g(u_g - \dot{s})\right) \qquad \text{at } r = s(t). \tag{3.56}$$

Using (3.53), this condition reduces to a boundary condition on T_g, namely

$$T_g = \frac{c_{p,s}}{c_{p,g}}T_s \qquad \text{at } r = s(t). \tag{3.57}$$

With this choice of boundary condition (3.57) for T_g, the only loss of energy from the entire crater system is that to the electrode and melt-pool via the Newton-cooling term in (3.52): all other heat transfers between the arc, crater gas, and solid charge material are accounted for.

3.1.5 Electrical constraints

Finally, we consider the electrical constraints in our idealised system. Since we are modelling only the region around the base of a single electrode, we assume that the voltages across the two current paths (the arc and the charge) are equal, and hence that

$$E := E_a = E_{ch}. \tag{3.58}$$

The electrode current $I(t)$ must equal the sum of the currents through the arc and the charge, according to

$$I = \int_{\text{arc}} \sigma_a(T_a)E\,\mathrm{d}V + \int_{\text{charge}} \sigma_c(T_s)E\,\mathrm{d}V = E\left(\pi r_a^2\,\sigma_a(T_a) + 2\pi\int_{r=s(t)}^{r_f} \sigma_c(T_s)r\,\mathrm{d}r\right). \tag{3.59}$$

The constraint (3.59) gives an equation relating $E(t)$ to the total current $I(t)$. To complete the electrical model, we might couple our reduced model above into an equivalent-circuit model for the furnace, such as those used in [104], and so solve for the total current $I(t)$. Alternatively, we might choose to prescribe the total current $I(t)$. Both approaches are investigated in Chapter 4 below. In either case, the current through the arc is influenced by the amount of current flowing through the charge according to (3.59), and the two regions are fully coupled.

3.2 Nondimensionalisation

Under all these simplifications, our model reduces to the arc heat equation (3.22a) for $T_a(t)$, and the system (3.42)–(3.43), (3.45), (3.47), and (3.48) for the concentrations C_s and C_g, temperatures T_s and T_g, and gas velocity u_g in the charge region $r \in (s(t), r_f)$. These equations are closed with the boundary conditions (3.50) at $r = r_f$ and (3.51), (3.55), (3.57), and (3.52) at $r = s(t)$. Finally, the arc and charge regions are coupled by the total current constraint (3.59).

In this section we nondimenionalise this model. We rescale our variables via

$$\begin{aligned} &t = [t]\hat{t} && s = [r]\hat{s}(\hat{t}), && r = [r]\hat{r}, && u_g = [u_g]\hat{u_g}, && E = [E]\hat{E}, \\ &T_a = [T_a]\hat{T}_a, && T_s = [T_s]\hat{T}_s, && T_g = [T_g]\hat{T}_g, && C_g = [C_g]\hat{C}_g, && C_s = [C_s]\hat{C}_s, \\ &Q = [Q]\hat{Q}, && I = [I]\hat{I}, && \sigma_c = [\sigma_c]\hat{\sigma}_c, && \sigma_a = [\sigma_a]\hat{\sigma}_a. \end{aligned} \tag{3.60}$$

The temperature scalings $[T_s]$ and $[T_a]$ will be fixed by a balance of the dominant heat sources and losses in each of the arc and charge. We fix $[T_g] = [T_s]$, however, since these temperatures are expected to be similar.

The solid concentration scaling is chosen for the boundary condition at $r = r_f$,

$$[C_s] = C_s^{\text{in}}, \tag{3.61}$$

while the gas concentration is taken to be

$$[C_g] = \frac{p_{\text{atm}}}{R[T_g]} = \frac{p_{\text{atm}}}{R[T_s]} \tag{3.62}$$

for a balance in the no-voids condition (3.48).

We define the dimensionless parameter δ to be the inverse Péclet number in the solid material,

$$\delta = \text{Pe}^{-1} = \frac{k_s}{c_{p,s} M_s [C_s] U r_f}, \tag{3.63}$$

which is the ratio of the size of the heat conduction term to the heat advection in (3.47). For physically relevant parameters (as we will see below), we expect $\delta \ll 1$ to be small. Since heat advection therefore dominates conduction in the solid material, we expect that the radiative heat from the arc at $r = s(t)$ only penetrates a short, $O(\delta[r])$, distance into the solid charge material. The hottest region of charge material is therefore expected to be this $O(\delta[r])$ conduction boundary layer at $r = s(t)$, and since the chemical reaction rate is temperature dependent, we expect the majority of the solid material consumption to occur within this boundary layer. In order for steady-state solutions of the system to exist, we expect that the rate of incoming solid

material balances the rate at which material can be consumed in this hot thin layer of charge material. This imposes a balance between advection and consumption of material in (3.42), which fixes the lengthscale $[s]$ of the crater radius

$$[s] = \sqrt{\frac{[C_s]Ur_f}{\delta[Q]}}. \tag{3.64}$$

This is the natural lengthscale for the crater in our problem, and so we take $[r] = [s]$. We note that for physically relevant parameters, the lengthscale of the furnace domain, $r_f \approx 4\,\mathrm{m}$ [1, 88] is likely to be on a similar order to $[s]$.

We now fix the temperature scalings. The arc temperature scaling is fixed in terms of the electric field scaling, by balancing the radiative loss with the Ohmic heating in the arc temperature equation (2.11). This gives

$$[T_a] = \left(\frac{[\sigma_a]}{4\kappa\sigma_B}\right)^{1/4} [E]^{1/2}, \tag{3.65}$$

where $[E]$ is not yet determined. In order to fix the electric field scaling, $[E]$, and temperature scaling, $[T_s]$, we need to know whether the majority of the current passes through the arc or the charge. A measure of the ratio of charge to arc current is given by the parameter

$$\alpha := \frac{2\delta[s]^2[\sigma_c]}{r_a^2[\sigma_a]}. \tag{3.66}$$

If $\alpha < 1$, then we expect more current to flow through the arc than through the charge material. We will see in the following section that for industrially relevant parameters, $\alpha \approx 0.24$, and so indeed we expect the majority of the current to pass through the electric arc. In this case, we choose the electric field scaling

$$[E] = \frac{[I]}{\pi r_a^2[\sigma_a]}, \tag{3.67}$$

to balance the applied current in (3.59). We also see that the parameter α describes the ratio of heating of the solid charge by volumetric Ohmic heating to the surface radiation, and so for $\alpha < 1$ the radiative heating from the arc dominates the Ohmic heating within the charge. We choose

$$[T_s] = \frac{2r_a^2\kappa\sigma_B[T_a]^4\delta}{k_s} \tag{3.68}$$

as an approximate balance of the radiative flux boundary condition (3.52). As well as balancing the solid conservation of mass equation (3.42), we fix $[u_g]$ by a balance

in the gas conservation of mass equation (3.43), again over the thin $O(\delta)$ layer at $r = s(t)$ in which Q is expected to be largest, which gives

$$[u_g] = \frac{[Q]\delta[s]}{[C_g]}. \tag{3.69}$$

There are many timescales in our problem, but for now we choose the longest timescale to nondimensionalise over — that over which s evolves — by balancing the time-derivative and advection terms in (3.42). This gives

$$[t_s] = \frac{[s]^2}{U r_f}. \tag{3.70}$$

Using these scalings, and dropping the hat notation, the dimensionless model for C_s, C_g, u_g, T_s, T_g, s, E, and T_a is given by

$$\delta\left(\frac{\partial C_s}{\partial t} - \frac{1}{r}\frac{\partial C_s}{\partial r}\right) = -Q, \tag{3.71a}$$

$$\xi\frac{\partial C_g}{\partial t} + \frac{\delta}{r}\frac{\partial}{\partial r}\left(r u_g C_g\right) = Q, \tag{3.71b}$$

$$C_g T_g + \theta^{\text{in}} C_s = 1, \tag{3.71c}$$

$$\delta C_s\left(\frac{\partial T_s}{\partial t} - \frac{1}{r}\frac{\partial T_s}{\partial r}\right) = \frac{\delta^2}{r}\frac{\partial}{\partial r}\left(r\frac{\partial T_s}{\partial r}\right) + \alpha\sigma_c E^2 - \gamma\mathcal{Q} + \delta\mu(T_g - T_s), \tag{3.71d}$$

$$K\left(\xi\frac{\partial}{\partial t}\left(C_g T_g\right) + \frac{\delta}{r}\frac{\partial}{\partial r}\left(r u_g C_g T_g\right)\right) = T_s Q - \delta\mu(T_g - T_s), \tag{3.71e}$$

in $r \in (s(t), r_f)$ subject to the boundary conditions

$$C_s = 1, \quad T_s = T_s^{\text{in}} \qquad \text{at } r = r_f, \tag{3.71f}$$

and

$$\left.\begin{aligned} &s^2 H(T_s - T^\infty) + s^2 R_p(T_s + \gamma) = (1 + s\dot{s})\, C_s T_s + \delta s\frac{\partial T_s}{\partial r} + T_a^4, \\ &C_s = C_*, \qquad T_g = K^{-1} T_s, \qquad \left(u_g + \xi\frac{\theta^{\text{in}} C_*}{1 - \theta^{\text{in}} C_*}\dot{s}\right) C_g = R_p s \end{aligned}\right\} \quad \text{at } r = s(t), \tag{3.71g}$$

along with the arc energy equation and electrical constraint (from (3.22a) and (3.59))

$$\epsilon\chi\frac{\partial T_a}{\partial t} = \sigma_a(T_a)E^2 - T_a^4, \tag{3.71h}$$

$$I = E\left(\sigma_a(T_a) + \alpha\delta^{-1}\int_{r=s(t)}^{r_f} \sigma_c r\,\mathrm{d}r\right). \tag{3.71i}$$

Parameter/Scaling	Value/Range	Reference
U	$5 \times 10^{-5}\,\mathrm{m\,s^{-1}}$	[1]
r_f	$4\,\mathrm{m}$	[1]
$M_g = M_s$	$3.6 \times 10^{-2}\,\mathrm{kg\,mol^{-1}}$	Average molar mass of C and SiO_2 in a 1:1 ratio
ρ_s	$2.1 \times 10^{3}\,\mathrm{kg\,m^{-3}}$	[1]
C_s^{in}	$3.8 \times 10^{4}\,\mathrm{mol\,m^{-3}}$	$\theta^{\mathrm{in}}\rho_s/M_s$ taking the input volume fraction $\theta^{\mathrm{in}} = 0.65$ for a random packed structure [3]
p_g	$1\,\mathrm{atm}$	[5]
k_s	$10\,\mathrm{W\,m^{-1}\,K^{-1}}$	[5]
$[\sigma_c]$	$4 \times 10^{2}\,\mathrm{S\,m^{-1}}$	Section 2.3.4
$[Q]$	$10^{2}\,\mathrm{mol\,m^{-3}\,s^{-1}}$	[92]
$c_{p,s}$	$1.47 \times 10^{3}\,\mathrm{J\,kg^{-1}\,K^{-1}}$	[1]
$c_{p,g}$	$9.72 \times 10^{2}\,\mathrm{J\,kg^{-1}\,K^{-1}}$	[1]
ΔH	$7.9 \times 10^{5}\,\mathrm{J\,mol^{-1}}$	[48]
R_m	$\sim 10^{-2}\,\mathrm{kg\,m^{-2}\,s^{-1}}$	Section 2.3
H_m	$\sim 10\,\mathrm{W\,m^{-2}\,K^{-1}}$	Estimated from thermal conductivity data of the electrode and melt-pool [5]
ρ_a	$2 \times 10^{-2}\,\mathrm{kg\,m^{-3}}$	[107]
$c_{p,a}$	$10^{3}\,\mathrm{J\,kg^{-1}\,K^{-1}}$	[107]
κ	$10^{-1}\,\mathrm{m^{-1}}$	[82]
$[\sigma_a]$	$2.5 \times 10^{4}\,\mathrm{S\ m^{-1}}$	[85, 107]
h	$0.1\,\mathrm{m}$	[85]
r_a	$\sim 0.1\,\mathrm{m}$	[85]
$[I]$	$8 \times 10^{4}\,\mathrm{A}$	[1]
t_{AC}	$2 \times 10^{-2}\,\mathrm{s}$	$50\,\mathrm{Hz}$ frequency

Table 3.4: Dimensional parameter values.

We have used the dimensionless parameters

$$\begin{aligned} K &= \frac{c_{p,g}}{c_{p,s}}, \quad \gamma = \frac{\Delta H}{c_{p,s} M_s [T_s]}, \quad \mu = \frac{\lambda \delta [s]^2}{k_s}, \quad H = \frac{H_m [s]^2}{2 h_a c_{p,s} M_s U r_f [C_s]}, \\ R_p &= \frac{d_p}{2 h_a \delta}, \quad \xi = \delta \frac{[C_g]}{[C_s]}, \qquad \epsilon = \frac{t_{\mathrm{AC}}}{[t_s]}, \qquad \chi = \frac{\rho_a c_{p,a} [T_a]}{[\sigma_a][E]^2 t_{\mathrm{AC}}}, \end{aligned} \tag{3.72}$$

along with δ given in (3.63), and α in (3.66), as well as the appropriately rescaled r_f, T_s^{in}, and C_*.

In Table 3.4 we present industrially relevant parameter values, typical for an operational furnace. We use these data to compute the variable scalings and dimensionless parameters, which are given in Tables 3.5 and 3.6. For the industrial parameter val-

Scaling	Value/Range
$[s]$	$1.7\,\mathrm{m}$
$[t_s]$	$1.5 \times 10^4\,\mathrm{s}$
$[C_s]$	$3.8 \times 10^4\,\mathrm{mol\,m^{-3}}$
$[C_g]$	$3.7\,\mathrm{mol\,m^{-3}}$
$[T_s]$	$3.2 \times 10^3\,\mathrm{K}$
$[T_g]$	$3.2 \times 10^3\,\mathrm{K}$
$[T_a]$	$1.0 \times 10^4\,\mathrm{K}$
$[u_g]$	$1.2\,\mathrm{m\,s^{-1}}$
$[E]$	$1.0 \times 10^2\,\mathrm{V\,m^{-1}}$

Table 3.5: Derived scalings using the data in Table 3.4.

ues, we note that $\delta \ll 1$, justifying our assumption that the hot layer of charge material at the edge of the crater is thin. The scaling for the crater size $[s] \approx 1.7\,\mathrm{m}$ is on the order of metres for the applied current chosen, which is reasonable for industrial furnaces [85, 104]. We have determined the scaling for $[s]$ by balancing the heat radiated by the arc with the conductive heat lost into the charge material. There are clearly several other heat loss mechanisms in (3.71g), and so in practice we will expect to see solutions with dimensionless $s < 1$. Using these values of δ and $[s]$, we see that the thin, hot layer of charge material at the edge of the crater is on the order of centimetres thick. We notice that $\alpha < 1$, justifying our choice of temperature scaling $[T_s]$, but this is not particularly small. While there is likely to be more current through the arc than through the charge, therefore, we expect that the charge current is non-negligible. Like α, the parameters γ, K, H, and R_p are of order unity.

As mentioned previously, there are a variety of timescales in this model. The timescale $[t_s]$, used for the nondimensionalisation is the timescale of the motion of the free boundary $r = s(t)$, which we see occurs over a timescale of hours. Since all of ϵ, χ, ξ are less than 1, $[t_s]$ is the longest timescale in the model. The gas timescale $\xi[t_s]$ is very fast, meaning that we might expect the gas flow to be quasi-static. We have written the timescale of the arc temperature evolution as the product of the ratio ϵ of the AC timescale to $[t_s]$, and the ratio χ of the timescale of the arc temperature evolution to the AC timescale. Clearly $\epsilon \ll 1$, as the current oscillates much more quickly than the crater–charge boundary moves. Since $\chi < 1$, we might expect the arc to behave quasi-steadily over the AC timescale. However, as discussed in Section 3.1.1, it is helpful to consider $\chi = O(1)$, as we do not expect the behaviour to be truly quasi-steady. We take advantage of these disparate timescales in Section 3.3 below.

The only dimensionless parameter we have not computed is μ. This is because the

Dimensionless Parameter	Typical Value
α	0.24
δ	2.5×10^{-2}
ξ	2.4×10^{-6}
ϵ	1.3×10^{-6}
χ	4.0×10^{-2}
γ	4.6
K	0.66
H	0.4
R_p	0.2

Table 3.6: Dimensionless parameters using the data in Table 3.4.

dimensional heat transfer coefficient λ is difficult to estimate, and it is not clear what value μ should take. After the multiple-timescales analysis in Section 3.3 below, our averaged model contains only order one parameters, except for $\delta \ll 1$, and μ, whose size we do not know. In Chapter 5 we look for asymptotic solutions of the homogenised model for different distinguished limits corresponding to different sizes of μ.

3.3 Multiple timescale homogenisation

As discussed above, there are many different timescales in our model. We chose to nondimensionalise over the longest timescale, $[t_s]$, over which the crater radius $s(t)$ varies. The parameters $\delta \sim 10^{-3}$, and $\xi, \epsilon \sim 10^{-6}$ are the ratios of the charge solid concentration timescale, gas concentration timescale, and AC timescale to $[t_s]$, respectively. Finally, $\chi \sim 10^{-2}$ is the ratio of the arc temperature timescale to the AC timescale. In this section we exploit these disparate timescales, and the expected quasi-periodicity of the system over the period of the alternating current, to homogenise the model over the timescale of the alternating current, taking ϵ as the small parameter.

We therefore introduce the fast timescale $\tau = \epsilon^{-1}t$, and assume all dependent variables are functions of both t and τ, independently, and that all variables are periodic, period 1, in τ. For the purposes of the multiple scales analysis, we assume that both δ and χ are $O(1)$ in ϵ, since, while small, they are many orders of magnitude greater than ϵ. By contrast, ξ is of a similar order to ϵ. If instead we had $\xi \ll \epsilon$ then we might immediately consider the gas to be quasi-steady, before beginning the multiple scales analysis, or if $\xi \gg \epsilon$, we might suppose it to be $O(1)$ for the purposes

of the homogenisation. The most interesting and physically relevant case is when $\xi = O(\epsilon)$, and this is the case we will consider. We let $\xi = \zeta\epsilon$, for $\zeta = O(1)$.

Since the electric current is assumed to vary periodically over the AC period, we suppose that the total current takes the form

$$I(t,\tau) = \hat{I}(t) I_{AC}(\tau), \tag{3.73}$$

where $I_{AC}(\tau)$ is periodic, with period one. Different choices of I_{AC} are investigated in Chapter 4 below.

To incorporate both timescales t and τ into the model we change variables, replacing all time derivatives in (3.71) with

$$\frac{\partial}{\partial t} \to \frac{\partial}{\partial t} + \epsilon^{-1}\frac{\partial}{\partial \tau}. \tag{3.74}$$

We also expand all dependent variables F in powers of ϵ, setting

$$F \sim F^0(t,\tau,r) + \epsilon F^1(t,\tau,r) + \cdots \tag{3.75}$$

as $\epsilon \to 0$. Using the change of time variables (3.74), and the expansions (3.75) we find that at leading order in ϵ, (3.71) gives

$$\frac{\partial C_s^0}{\partial \tau} = \frac{\partial T_s^0}{\partial \tau} = \frac{\partial s^0}{\partial \tau} = 0, \tag{3.76}$$

from (3.71a), (3.71d), and (3.71g) respectively. Thus the solid concentration and temperature, and the position of the free boundary $r = s$, do not vary at leading order over the timescale of the alternating current. The leading-order problem for the gas variables, however, is

$$\zeta\frac{\partial C_g^0}{\partial \tau} + \frac{\delta}{r}\frac{\partial}{\partial r}(r u_g^0 C_g^0) = Q^0, \tag{3.77a}$$

$$C_g^0 T_g^0 + \theta^{\text{in}} C_s^0 = 1, \tag{3.77b}$$

$$K\left(\zeta\frac{\partial}{\partial \tau}(C_g^0 T_g^0) + \frac{\delta}{r}\frac{\partial}{\partial r}(r u_g^0 C_g^0 T_g^0)\right) = T_s^0 Q^0 - \delta\mu(T_g^0 - T_s^0), \tag{3.77c}$$

for $r \in (s_0, r_f)$, from (3.71b), (3.71c), and (3.71e), respectively. Here we have used the shorthand $Q^0 := Q(C_s^0, T_s^0)$. Using the fact that s^0 is independent of τ we see that the boundary conditions for the gas variables (3.71g) become

$$u_g^0 C_g^0 = R_p s^0, \quad T_g^0 = K^{-1} T_s^0 \qquad \text{at } r = s^0(t), \tag{3.77d}$$

at leading order. Thus the gas dynamics play out on the fast AC timescale. Since all of s^0, C_s^0, and T_s^0 are independent of τ, it is intuitive that the leading-order gas

variables u_g^0, C_g^0, and T_g^0, given by (3.77) are actually independent of τ as well. We can indeed prove that the leading-order gas variables are independent of τ by showing that there exists a τ-independent solution of (3.77), and that the solution of (3.77) is unique. The uniqueness proof is similar to the general proof of uniqueness for quasi-linear hyperbolic systems presented in [25], adapted to use r as the time-like variable rather than τ, and to allow for the periodicity of the solution in τ, rather than τ initial conditions. Given this fact, we may drop the τ derivatives in (3.77), leaving a quasi-steady system for the leading-order gas dynamics.

At leading order, the arc temperature equation (3.71h) and the total current constraint (3.71i) become

$$\chi \frac{\partial T_a^0}{\partial \tau} = \sigma_a(T_a^0)(E^0)^2 - (T_a^0)^4, \tag{3.78a}$$

$$\hat{I} I_{AC}(\tau) = E^0 \left(\sigma_a(T_a^0) + \alpha\delta^{-1} \int_{r=s^0}^{r_f} \sigma_c^0 r \, \mathrm{d}r \right). \tag{3.78b}$$

These equations do vary over the τ timescale, and so E^0 and T_a^0 are genuine functions of both τ and t. The system (3.78) may be solved numerically for $E^0(t,\tau)$ and $T_a^0(t,\tau)$, as functions of τ, for each value of the imposed current amplitude $\hat{I} = \hat{I}(t)$ and charge conductivity

$$\sigma_{\mathrm{ch}}(t) = \alpha\delta^{-1} \int_{r=s^0}^{r_f} \sigma_c^0 r \, \mathrm{d}r, \tag{3.79}$$

which is independent of τ, since s^0 and T_s^0 are both independent of τ. The arc model (3.78) is explored in more detail in the Chapter 4. For now, however, we assume that we may solve (3.78) for E^0 and T_a^0, and continue with the homogenisation analysis.

While the system (3.77), with the knowledge that C_g^0 is independent of τ, consists of equations for u_g^0, C_g^0, and T_g^0, the leading-order equations for the solid variables only showed that these were independent of τ. To find equations for the solid variables we must look at the next-order problem in ϵ. The next-order solid equations are

$$\delta \left(\frac{\partial C_s^0}{\partial t} + \frac{\partial C_s^1}{\partial \tau} - \frac{1}{r}\frac{\partial C_s^0}{\partial r} \right) = -Q^0, \tag{3.80a}$$

$$\delta C_s^0 \left(\frac{\partial T_s^0}{\partial t} + \frac{\partial T_s^1}{\partial \tau} - \frac{1}{r}\frac{\partial T_s^0}{\partial r} \right) = \frac{\delta^2}{r}\frac{\partial}{\partial r}\left(r \frac{\partial T_s^0}{\partial r} \right) + \alpha\sigma_c^0 (E^0)^2 - \gamma Q^0 + \delta\mu(T_g^0 - T_s^0), \tag{3.80b}$$

for $r \in (s_0, r_f)$. The boundary conditions are

$$C_s^0 = 1, \quad T_s^0 = T_s^{\mathrm{in}} \qquad \text{at } r = r_f, \tag{3.80c}$$

and

$$C_s^0 = C_*, \tag{3.80d}$$

$$(s^0)^2 H(T_s^0 - T^\infty) + (s^0)^2 R_p(T_s^0 + \gamma) = \left(1 + s^0\left(\frac{\partial s^0}{\partial t} + \frac{\partial s^1}{\partial \tau}\right)\right) C_s^0 T_s^0 + \delta s^0 \frac{\partial T_s^0}{\partial r} + (T_a^0)^4, \tag{3.80e}$$

at $r = s^0(t)$. Using the periodicity of all variables in τ, we may average each of the equations (3.80) over the period $(\tau, \tau+1)$ of τ. Since all of C_s^0, T_s^0, T_g^0, and s^0 are independent of τ, we obtain

$$\delta\left(\frac{\partial C_s^0}{\partial t} - \frac{1}{r}\frac{\partial C_s^0}{\partial r}\right) = -Q^0, \tag{3.81a}$$

$$\delta C_s^0\left(\frac{\partial T_s^0}{\partial t} - \frac{1}{r}\frac{\partial T_s^0}{\partial r}\right) = \frac{\delta^2}{r}\frac{\partial}{\partial r}\left(r\frac{\partial T_s^0}{\partial r}\right) + \alpha\sigma_c^0\langle(E^0)^2\rangle - \gamma Q^0 + \delta\mu(T_g^0 - T_s^0), \tag{3.81b}$$

and at $r = s^0(t)$

$$(s^0)^2 H(T_s^0 - T^\infty) + (s^0)^2 R_p(T_s^0 + \gamma) = \left(1 + s^0\frac{\partial s^0}{\partial t}\right) C_s^0 T_s^0 + \delta s^0 \frac{\partial T_s^0}{\partial r} + \langle(T_a^0)^4\rangle, \tag{3.81c}$$

while (3.80c) and (3.80d) remain unchanged. Here, we use the notation

$$\langle\,\cdot\,\rangle := \int_{\tau=0}^{1} \cdot \quad \mathrm{d}\tau \tag{3.82}$$

to denote the average over a τ-period. This completes the homogenisation analysis.

3.3.1 Statement of the homogenised model

In summary, we have shown that the only leading-order variables which depend on the fast timescale τ are E and T_a (dropping the superscript 0 notation), which solve

$$\chi\frac{\partial T_a}{\partial \tau} = \sigma_a(T_a)E^2 - T_a^4, \tag{3.83a}$$

$$\hat{I} I_{AC}(\tau) = E\left(\sigma_a(T_a) + \sigma_{\mathrm{ch}}\right), \tag{3.83b}$$

for a given $\hat{I}$. This fast scale problem depends on the averaged system for the remaining (τ-independent) variables via the overall charge conductivity

$$\sigma_{\mathrm{ch}}(t) = \alpha\delta^{-1}\int_{r=s}^{r_f} \sigma_c r\,\mathrm{d}r. \tag{3.84a}$$

Conversely, the averaged equations in the charge material depend on $\langle E^2 \rangle$ and $\langle T_a^4 \rangle$. Since the gas dynamics are now known to be quasi-steady at leading order, we may re-write the equations in terms of the concentration flux, $f = u_g C_g$, of the gas. This simplifies the system as we need not impose the no-voids condition (3.71c) (although we may use this constraint after the fact to find C_g, and then $u_g = f/C_g$, if desired). We also therefore simplify the notation by setting $C := C_s$ for the solid concentration, dropping the subscript since this is now the only concentration remaining in the model. The resulting system is given by

$$\delta \left(\frac{\partial C}{\partial t} - \frac{1}{r} \frac{\partial C}{\partial r} \right) = -Q, \tag{3.84b}$$

$$\frac{\delta}{r} \frac{\partial}{\partial r}(rf) = Q, \tag{3.84c}$$

$$\delta C \left(\frac{\partial T_s}{\partial t} - \frac{1}{r} \frac{\partial T_s}{\partial r} \right) = \frac{\delta^2}{r} \frac{\partial}{\partial r} \left(r \frac{\partial T_s}{\partial r} \right) + \alpha \sigma_c \langle E^2 \rangle - \gamma Q + \delta \mu (T_g - T_s), \tag{3.84d}$$

$$\frac{K\delta}{r} \frac{\partial}{\partial r}(rfT_g) = T_s Q - \delta \mu (T_g - T_s), \tag{3.84e}$$

for $r \in (s(t), r_f)$, with

$$s^2 H (T_s - T^\infty) + s^2 R_p (T_s + \gamma) = (1 + s\dot{s})\, C T_s + \delta s \frac{\partial T_s}{\partial r} + \langle T_a^4 \rangle, \tag{3.84f}$$

$$C = C_*, \quad f = R_p s, \quad T_g = K^{-1} T_s, \tag{3.84g}$$

at $r = s(t)$, and

$$C = 1, \qquad T_s = T^{\text{in}}, \tag{3.84h}$$

at $r = r_f$. Since we have two-way coupling between the slowly-varying charge problem, and the fast-varying arc problem, we must in general iterate between the two problems in order to find a solution numerically. Alternatively, we may solve the fast-timescale arc problem (3.83) for a range of (constant) values of σ_{ch} and of the prescribed $\hat{I}$. We may then generate a table of the numerical values of $\langle E^2 \rangle$ and $\langle T_a^4 \rangle$ as functions of σ_{ch} (and $\hat{I}$), which can be used to solve the slow-timescale problem (3.84). In this way, the fast-timescale arc problem (3.83) may be viewed as the "cell problem" for the homogenised problem.

The homogenised model (3.83)–(3.84) derived in this chapter forms the basis of Chapters 4, 5, and 6 below. In Chapter 4 we study the fast-timescale cell problem (3.83) for various forms of the prescribed electrode current $I_{AC}(\tau)$. In Chapter 5 we study a simplified version of the slow-timescale model (3.84), neglecting the electrical coupling, to understand the interaction between the thermal and chemical processes

in the charge material. In Chapter 6 we then return to the full homogenised problem (3.83)–(3.84), combining the solutions of the cell problem (3.83) from Chapter 4 with the asymptotic reductions of the charge model (3.84) from Chapter 5. In this way, we are able to investigate the steady states and slow-timescale dynamics of the silicon furnace.

Chapter 4

Alternating current effects

In this chapter we study the cell problem of the homogenised furnace model derived in Chapter 3. The cell problem consists of the arc and electrical system, varying over the fast timescale of the alternating current. In Section 4.1 we assume for simplicity that the current in the electrode is known, and study solutions of (3.83) for both DC and AC applied currents. In Section 4.2, rather than assuming a prescribed electrode current, we incorporate an equivalent-circuit model for the entire furnace system into the cell problem for the homogenised model, and thereby solve for the electrode current as part of the solution of the cell problem. As discussed in Chapter 1, different types of SAF incorporate different electrical set-ups, some with DC applied currents, and with different numbers of electrodes, depending on the application. In most industrial silicon furnaces an alternating three-phase current is used. It is nevertheless instructive to study the simpler cases of prescribed DC and AC applied currents, before taking the full three-phase electrical system into account, since the AC behaviour is closely related to the DC solutions.

4.1 The fast-timescale arc model

In this section we study the system (3.83) for the τ-variation of E and T_a. In Section 4.1.1 we set the prescribed electrode current I_{AC} to be constant, corresponding to the case of DC applied current, while in Section 4.1.2 we use a prescribed sinusoidal electrode current I_{AC} as a model for an alternating current.

4.1.1 Direct (DC) applied current

In this section we impose a constant electrode current $I_{AC} = 1$ so that the total applied current $I(t, \tau) = \hat{I}(t)$, is a function of t only, and so does not vary over the

fast timescale τ. In this way we model the scenario of a direct (DC) applied current.

To understand the fast-timescale arc dynamics, it is helpful to combine (3.83) into a single equation for T_a by eliminating E, giving

$$\chi \frac{\partial T_a}{\partial \tau} = I^2 \frac{\sigma_a(T_a)}{(\sigma_a(T_a) + \sigma_{\text{ch}})^2} - T_a^4. \tag{4.1}$$

The heat loss by radiation is a simple quartic function of T_a, whereas the heat generated by Ohmic heating,

$$H_a := I^2 \frac{\sigma_a(T_a)}{(\sigma_a(T_a) + \sigma_{\text{ch}})^2}, \tag{4.2}$$

is not monotone in T_a, and depends on the values of I and σ_{ch}. In this section we assume both I and σ_{ch} are prescribed constants, since these vary over the much slower t timescale.

As discussed in Section 2.2.1, the arc conductivity is expected to take the form

$$\sigma_a(T_a) = \alpha_1 T_a^{\alpha_2} \exp\left(-\frac{\alpha_3}{T_a}\right). \tag{4.3}$$

for constants α_i, $i = 1, 2, 3$, with $\alpha_1, \alpha_3 > 0$, and $\alpha_2 \geq 0$. With this form of σ_a, we see that $H_a \propto \sigma_a$ is exponentially small as $T_a \to 0$ for non-zero σ_{ch}. If conversely $\sigma_{\text{ch}} = 0$, so that no current can pass through the charge, then $H_a \propto \sigma_a^{-1}$, which blows up as $T_a \to 0$. We assume that $\sigma_{\text{ch}} > 0$ hereafter, as this is the case of industrial interest. We note that H_a is bounded as $T_a \to \infty$. Furthermore, σ_a is monotone increasing in T_a, so that $\sigma_a'(T_a) > 0$. We therefore see that

$$\frac{\mathrm{d}H_a}{\mathrm{d}T_a} = \frac{I^2}{(\sigma_a(T_a) + \sigma_{\text{ch}})^3} (\sigma_{\text{ch}} - \sigma_a) \sigma_a'(T_a) \tag{4.4}$$

has the same sign as $\sigma_{\text{ch}} - \sigma_a$. Thus H_a increases with T_a up to a maximum at the point $T_a^*(\sigma_{\text{ch}})$, defined to be the point where $\sigma_{\text{ch}} = \sigma_a(T_a^*)$, while for $T_a > T_a^*$, H_a is decreasing. A sketch of $H_a(T_a)$, along with the radiation loss T_a^4, is given in Figure 4.1.

We notice that, for given values of I and σ_{ch}, the equation (4.1) may have 1, 2, or 3 steady-state solutions, corresponding to the intersections of the curves $H_a(T_a)$ and T_a^4. There is always (for $\sigma_{\text{ch}} > 0$) a steady state at $T_a = 0$, corresponding to the case of a cold arc, conducting no electricity. For sufficiently large I, and sufficiently small σ_{ch}, the curves T_a^4 and H_a may meet tangentially (so that there is a second steady state), or intersect twice more (giving a total of three steady states, which we denote $T_{a,0} = 0 < T_{a,1} \leq T_{a,2}$), as shown in Figure 4.1.

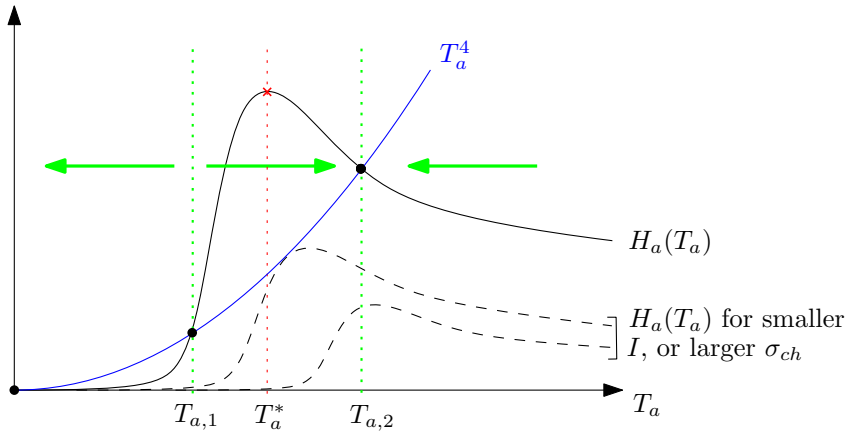

Figure 4.1: Schematic of the radiative loss term T_a^4 (blue), and Ohmic heating $H_a(T_a)$ (black, solid) as functions of T_a, assuming a DC applied current. The steady-state solutions are marked at the intersection of the curves, with dynamics indicated by the green arrows. The dashed black curves are $H_a(T_a)$ for smaller values of I, or larger σ_{ch}, for which there are only 2, or only 1 steady-state solution.

We note from (4.1) that, in the case of three steady states, we have

$$\frac{\partial T_a}{\partial \tau} < 0, \qquad \text{if } T_a \in (0, T_{a,1}) \cup (T_{a,2}, \infty), \tag{4.5}$$

$$\frac{\partial T_a}{\partial \tau} > 0, \qquad \text{if } T_a \in (T_{a,1}, T_{a,2}), \tag{4.6}$$

as shown by the green arrows in Figure 4.1. The $T_{a,0} = 0$ steady state is therefore locally stable, since the radiative heat loss is greater than the Ohmic heating for small T_a. The largest steady-state solution $T_{a,2}$ is also stable, while the intermediate state $T_{a,1}$ is unstable. The timescale over which T_a approaches a steady state is χ, which is very fast (even compared with the AC timescale). Thus for the purposes of the overall furnace behaviour we expect that $T_a(t) = T_{a,2}(I(t), \sigma_{\text{ch}}(t))$ is quasi-steady, so long as I and σ_{ch} remain at values which permit the existence of the steady state. We note that our model has no capacity for arc ignition: if at some time t the values of $I(t)$ and $\sigma_{\text{ch}}(t)$ are such that only the $T_a = 0$ steady-state solution exists, then $T_a = 0$ for all later times.

We plot the non-zero, stable, steady-state solution $T_{a,2}$, and the corresponding electric field E, as functions of σ_{ch} for various values of I in Figure 4.2, taking $\alpha_1 = 1, \alpha_2 = 0$, and $\alpha_3 = 1.4$ (as discussed in Section 2.2.1). For easy comparison with the sinusoidal applied current studied in Section 4.1.2, we use the "root mean squared" values

$$I = \sqrt{\int_{\tau=0}^{1} \left(\hat{I}_{AC} \sin(2\pi\tau)\right)^2 \, \mathrm{d}\tau} = \frac{\hat{I}_{AC}}{\sqrt{2}}, \tag{4.7}$$

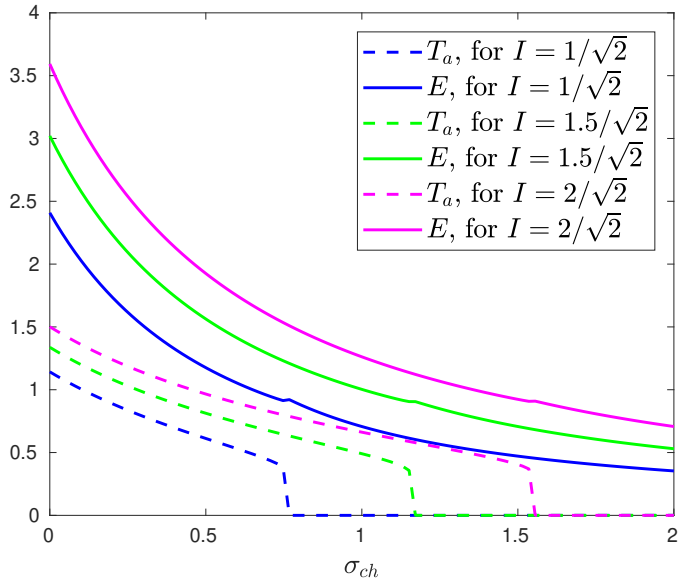

Figure 4.2: The largest steady-state (DC) solution $T_{a,2}$ of (3.83), and the corresponding value of E, as functions of σ_{ch}.

where $\hat{I}_{AC}$ are the values of the current magnitude used for the numerical solutions in Section 4.1.2. We note that, as expected from our discussion above, for each I there is maximum value of σ_{ch}, above which there is no steady-state solution except for $T_a = 0$, and this maximum σ_{ch} increases with I.

For the slow-timescale homogenised problem (3.84), we require the τ-averaged values $\langle E^2 \rangle$ and $\langle T_a^4 \rangle$. In this DC case, of course, E^2 and T_a^4 are independent of τ and so are equal to their averages.

4.1.2 Alternating (AC) sinusoidal applied current

We now suppose that

$$I_{AC}(\tau) = \sin(2\pi\tau) \tag{4.8}$$

is sinusoidal in τ, which is a simple model for an alternating electrode current.

As in the DC case, we solve the fast-timescale arc problem (3.83), for prescribed, constant values of the total charge conductivity σ_{ch} and current amplitude $\hat{I}$. The numerical solutions of the differential-algebraic system (3.83) are calculated using the MATLAB in-built solver ode15s, which is a multistep solver, using numerical differentiation formulas (NDFs) of order 1-5 [91]. The simulations are initialised at a non-trivial initial state, and run until the solution is periodic.

Such periodic solutions are shown in Figures 4.3 and 4.4, in which we explore varying the parameters σ_{ch} and χ, respectively. The prescribed current is sinusoidal, but, as seen in Figures 4.3a and 4.4a, the solution $E(\tau)$ is not sinusoidal. This is because for low currents the arc is relatively cold and the majority of the current flows through the charge material, but as the current increases a greater proportion of current flows through the arc, as seen in Figures 4.3b and 4.4b. Here we define

$$I_a(\tau) := E(\tau)\sigma_a(T_a(\tau)) \qquad \text{and} \qquad I_c(\tau) := E(\tau)\sigma_{\text{ch}} \tag{4.9}$$

to be the electric currents through the arc and charge, respectively.

As discussed in Section 3.1.1, we might naively have assumed that the arc system (3.83) would be quasi-steady even in the AC case because $\chi \sim 10^{-2}$ is quite small. We see from these numerical solutions that this is not the case. In particular, we note that, while the only DC solution of (3.83) when the current $I = 0$ is $T_a = 0$, in the AC case we have non-zero T_a as the current I passes through zero. This is because when $I = 0$ (and so $E = 0$), there is no arc heating, but the decay of T_a is due to the radiation, scaling like T_a^4, and so is extremely slow.

The arc temperature T_a in Figures 4.3a and 4.4a oscillates over the AC cycle, with period half of the AC period. We observe that there is a time-delay, with the arc temperature minimum occurring after the current passes through zero. In Figure 4.3a we see that for larger values of σ_{ch}, less current passes through the arc, so that the temperature T_a is lower. The time-delay of the arc temperature is more pronounced for larger σ_{ch}, and an asymmetry is visible: there is a faster increase in temperature as the arc ignites, and a slower decay as the current passes through zero.

Arc signature plots (showing electric field $E(\tau)$ against arc current $I_a(\tau)$) corresponding to the solutions in Figure 4.3a are shown in Figure 4.3c. Industrially, these arc signatures are used to visualise the electrical conditions in the furnace. Our arc signatures are qualitatively similar to those seen in industrial furnaces [85, 88, 104], in the asymmetry of the increasing- and decreasing-current parts of the cycle, which cause the figure-of-eight shape. We see larger current and voltage maxima for smaller σ_{ch}, and a more sharply-pointed shape. In Figure 4.3d, T_a is plotted against the magnitude of the electric field $|E|$ for various σ_{ch}. In Figure 4.3d we also plot, in black, the steady-state solution of the arc temperature equation, $T_{a,2}$ as discussed in the direct current (DC) case above. We observe that the τ-varying curves pass through the steady-state curve at the maximum electric field. For smaller σ_{ch}, when a greater proportion of the current passes through the arc, the τ-varying curve more

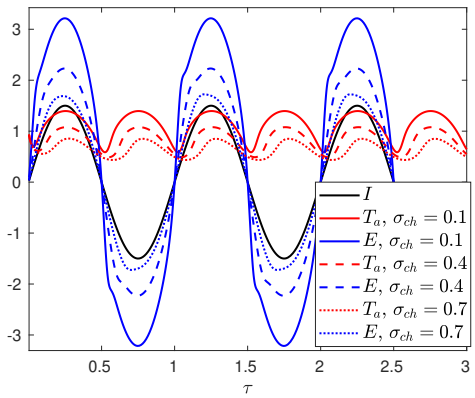

(a) Solutions T_a and E.

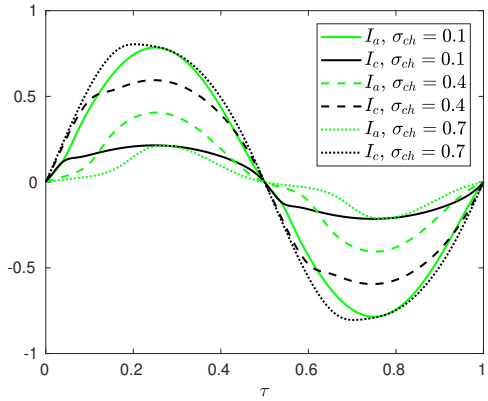

(b) Arc and charge currents.

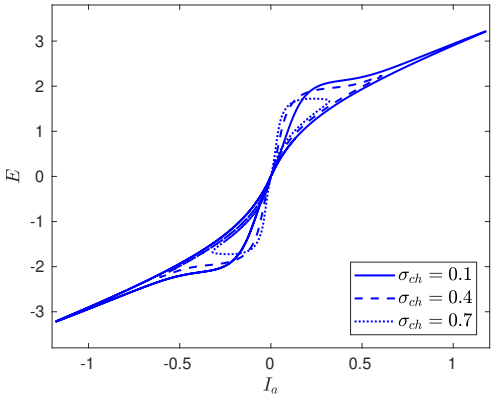

(c) Arc signature plots.

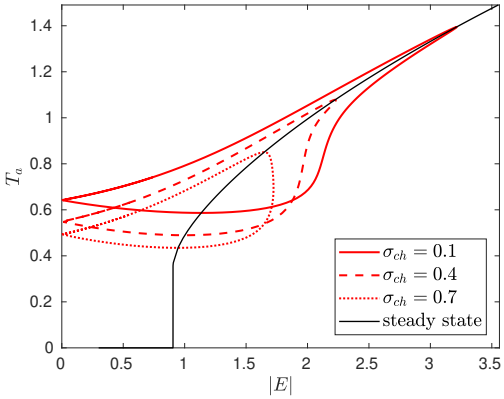

(d) T_a as a function of $|E|$ as τ varies.

Figure 4.3: Solutions of (3.83), varying σ_{ch}, with $\sigma_a(T_a) = \exp(-1.4/T_a)$, $\hat{I} = 1.5$, and $\chi = 0.04$ throughout.

closely follows the steady-state curve. It is this behaviour which may also be seen in the variety of arc signature shapes in Figure 4.3c.

In Figure 4.4 we investigate varying the value of χ. We see in Figures 4.4a and 4.4b that the overall amplitudes of T_a, E, I_c and I_a do not vary much with χ, but that for larger χ the arc adapts much more slowly, smoothing out the jumps caused as the arc essentially turns on and off. This smoothing effect is most clearly visible in the arc signatures, and the variation of T_a against $|E|$ in Figures 4.4c and d.

From the τ-varying solutions computed for this sinusoidal I_{AC}, we may compute the averaged quantities $\langle E^2 \rangle$ and $\langle T_a^4 \rangle$ needed for the homogenised problem (3.84) in the charge material, by averaging the periodic solutions over the AC period. As in the DC case above, we compute these averaged quantities $\langle E^2 \rangle^{1/2}$ and $\langle T_a^4 \rangle^{1/4}$ for a given applied current amplitude $\hat{I}$, and for a range of values of σ_{ch}, as shown in Figure 4.5a, with very similar results to the DC case, shown in Figure 4.2. In the DC

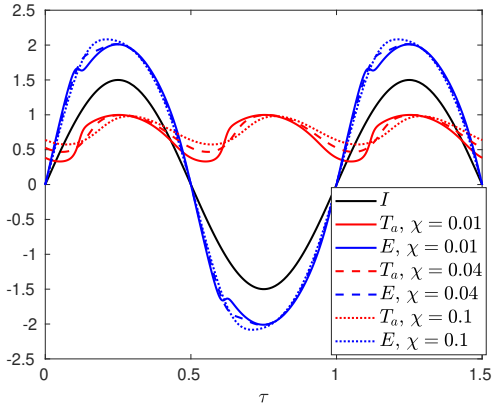

(a) Solutions T_a and E.

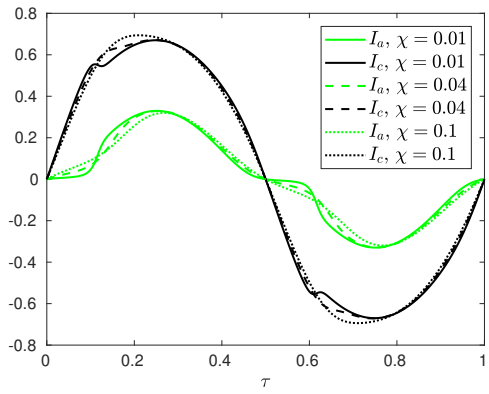

(b) Arc and charge currents.

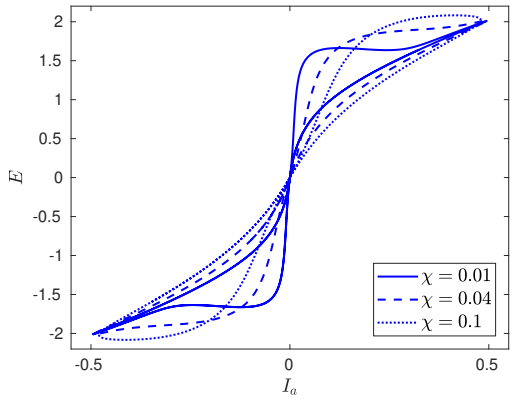

(c) Arc signature plots.

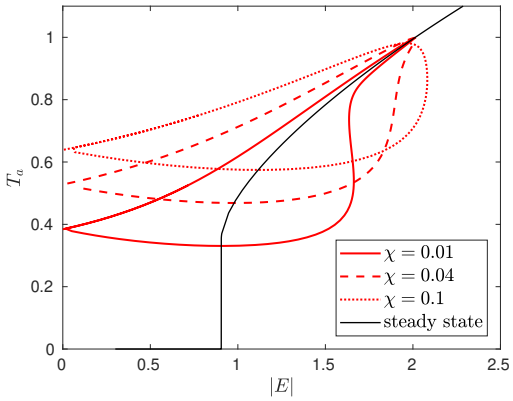

(d) T_a as a function of $|E|$ as τ varies.

Figure 4.4: Solutions of (3.83) varying χ, with $\sigma_a(T_a) = \exp(-1.4/T_a)$, $\hat{I} = 1.5$, and $\sigma_{\text{ch}} = 0.5$ throughout.

case, we saw that below a critical electrical field, $\langle E^2 \rangle_{\text{crit}}^{1/2}$, there is no non-trivial DC solution of the arc temperature equation (for $\hat{I} = 1.5$ as in Figures 4.3d and 4.4d, this critical value is $\langle E^2 \rangle_{\text{crit}}^{1/2} \approx 0.91$). Below this same $\langle E^2 \rangle_{\text{crit}}^{1/2}$, we see in Figure 4.5a that $\langle T_a^4 \rangle = 0$, and that there is therefore no arc in the AC case either. In Figure 4.5b we show the fraction of the average of the magnitude of the currents passing through the arc and charge material respectively, namely

$$\tilde{I}_a := \frac{\pi \langle |\sigma_a(T_a) E| \rangle}{2\hat{I}} \quad \text{and} \quad \tilde{I}_c := \frac{\pi \sigma_{\text{ch}} \langle |E| \rangle}{2\hat{I}}, \tag{4.10}$$

where we have divided by the average of the magnitude of the total current, $\langle |I| \rangle = 2\hat{I}/\pi$, to impose $\tilde{I}_a + \tilde{I}_c = 1$. We observe that $\tilde{I}_a$ decreases with σ_{ch}, as more current flows instead through the charge material. We also note that, as in the DC case above, for each $\hat{I}$ there is a critical value of σ_{ch} above which $\langle E^2 \rangle^{1/2} < \langle E^2 \rangle_{\text{crit}}^{1/2}$ and

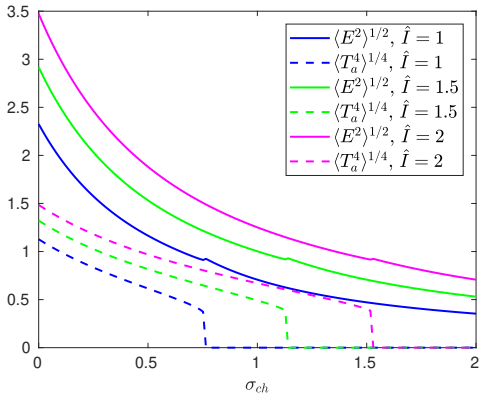

(a) Variation of $\langle E^2\rangle^{1/2}$ and $\langle T_a^4\rangle^{1/4}$ with σ_{ch}.

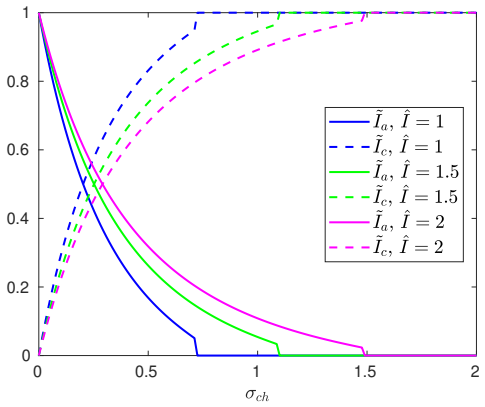

(b) Average current fractions $\tilde{I}_a$ and $\tilde{I}_c$.

Figure 4.5: Variation of the time-averaged quantities with σ_{ch} and $\hat{I}$, with $\sigma_a(T_a) = \exp(-1.4/T_a)$, $\hat{I} = 1.5$, and $\chi = 0.04$.

the average arc temperature $\langle T_a^4\rangle$ becomes zero, so that in Figure 4.5b we have $\tilde{I}_a = 0$, and $\tilde{I}_c = 1$, and all current passes through the charge. The averaged quantities do not depend strongly on the value of χ.

We note that, while our solutions generally appear to give good qualitative agreement with industrial observations, we do not observe the phase shift expected in practice between the current and electric field. This phase shift is caused by inductance effects due to the three-phase current, explored in the following section.

4.2 Three-phase equivalent-circuit model

So far, we have focussed on the electrical behaviour around the base of a single electrode, assuming that the current I through the electrode is known. However, we may instead couple our model into the wider electrical system of the submerged arc furnace, and solve for the electrode current I in terms of the voltages applied across the furnace. To do this, we incorporate the three-phase equivalent-circuit (EC) model for silicon furnaces presented in [104], into our cell problem.

In [104], the arc resistance is related to the voltage across the arc using a Cassie arc model [22]. This is one of several empirical models for arc resistance commonly used in the SAF literature. Others include the Mayr model [67, 68], and hybrid models, discussed in [37, 76, 110]. These models have all been developed for the electric arcs in circuit breakers, to understand short-circuiting phenomena. Nevertheless, they are widely used for the arcs in SAFs and open-air electric arc furnaces (EAFs) [6, 9, 12, 14, 35, 63]. Other semi-empirical arc models such as the "channel arc models"

(CAMs) have been developed that are designed to take into account additional heating and heat loss mechanisms [85]. Although simpler than MHD models, the CAMs are much more detailed than the Cassie and Mayr models.

The Cassie and Mayr models are based on the assumption that the heat loss from the arc is convective or conductive [76]. As discussed in Section 3.1.1 we expect that the dominant heat loss from the furnace arcs is actually heat radiation. This motivated our choice of simplified arc model (3.83a). We have not found arc models of the form (3.83a), based on purely radiative heat loss, used in the literature of SAFs.

In this section we include our fast-timescale arc model (3.83a) into the electrical circuit system of [104]. The analysis may be viewed in two ways: firstly as including a more accurate electrical system into our homogenised model of Chapter 3, and secondly as including a new arc model — our model (3.83a) based on radiative heat loss — into the equivalent-circuit system, with the goal of comparing our radiation model with the empirical Cassie and Mayr models currently used in the literature.

In Section 4.2.1 we introduce the (dimensional) EC model of [104], and show how our radiation arc model (3.83a) may be combined into this model. We also introduce the Cassie and Mayr models, and compare these with the radiation model. In Section 4.2.2 we nondimensionalise the EC model, and numerical solutions are found in Section 4.2.3. In order to compare the different arc models, we use a different nondimensionalisation than that in Chapter 3 and Section 4.1 above. Results can nevertheless be qualitatively compared with those of Section 4.1, and the averaged quantities could be used in the homogenised problem (3.84) after appropriate rescaling.

4.2.1 Equivalent-circuit model

The equivalent-circuit (EC) model used by [104] is illustrated in Figure 4.6. The electrical power is supplied to the system via three transformers, to create the three prescribed sinusoidal voltages v_{T1}, v_{T2}, and v_{T3}, each 120° out of phase with the others, as shown at the top of the diagram in Figure 4.6. The current passes through each of the three electrodes, and through the arc and charge in parallel at the base of the electrode, shown in more detail in Figure 4.7. The three current paths meet in the base of the furnace, which consists of conductive carbon and silicon-rich materials. In both Figures 4.6 and 4.7, the subscripts T, e, b, c, ec, a, and m refer respectively to the transformers, electrode, base of the furnace, charge material, part of the electrode in the crater, electric arc, and molten silicon in the pool at the base of each crater. We will also refer to the hearth of each phase as the region of parallel currents (through

the electric arc and charge material) at the base of each electrode, with subscript h. We denote "phase j" for $j = 1, 2, 3$ as the overall current path from the junction with the transformer circuit (at the top of Figure 4.6) to the point where the three current paths meet at the base of the furnace.

Following [104], we assume for simplicity that the inductive effects due to the magnetic fields from both the electrode's own current (the "self-inductance") and the other currents in the furnace may be combined into the single parameter, L_j, for each phase. Similarly, we assume that the each transformer has self-inductance L_{Tj}. All the inductances are assumed to be prescribed constants.

The voltage, v_{Tj}, supplied to each of the transformers $j = 1, 2, 3$, is assumed to be

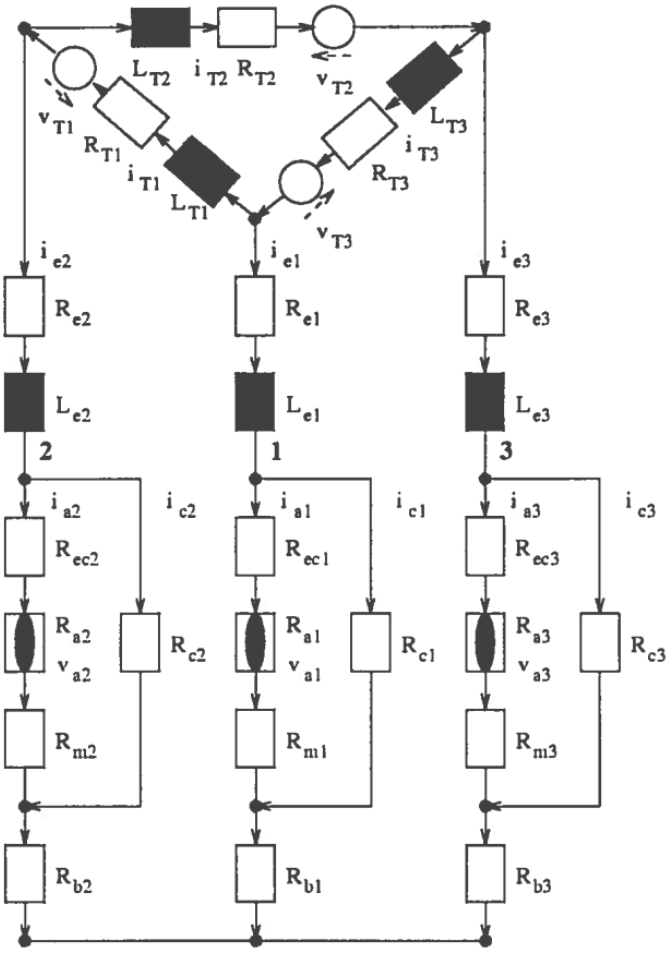

Figure 4.6: Diagram of the equivalent circuit for the three-phase electrical system in the furnace, taken from [104]. Resistive, and inductive circuit elements are shown as white, and black rectangles, respectively. The white circles denote applied voltages, and the arcs (non-linear resistors) are shown by a black ellipse within a white rectangle.

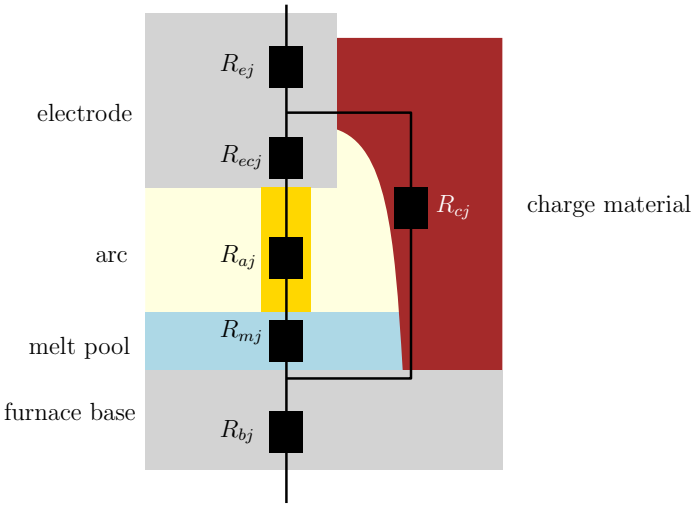

Figure 4.7: Circuit diagram for phase j, showing the resistance of elements of the electrode, and furnace hearth.

a prescribed function of time t. As in [104], we take this to be a standard three-phase system, with

$$v_{Tj}(t) = V_T \sin\left(2\pi\left(f_{\mathrm{AC}}t - \frac{j-1}{3}\right)\right), \tag{4.11}$$

where V_T is a prescribed, constant amplitude, and f_{AC} is the frequency of the alternating current. The resistance, R_T, of each of the three transformers are assumed to be equal.

To coincide with [104], we now change notation from the earlier part of this chapter, and denote the current through phase j, equal to the current in electrode j, by i_{ej}. The voltage across phase j is given by

$$v_j = R_j i_{ej} + L_j \frac{\mathrm{d}i_{ej}}{\mathrm{d}t}, \tag{4.12}$$

where R_j is the total resistance of phase j, given by

$$R_j = R_{ej} + R_{bj} + \frac{1}{\frac{1}{R_{cj}} + \frac{1}{R_{ecj}+R_{aj}+R_{mj}}}. \tag{4.13}$$

Using Kirchhoff's laws for the voltages and currents in the circuit, we may relate the phase voltages v_j to the voltages across the transformer circuit, and also relate the currents i_{ej} through each phase to the transformer currents i_{Tj}. Combining and manipulating these equations to eliminate all i_{Tj} and v_j, we may derive the following

differential equations for the phase currents

$$\frac{\mathrm{d}i_{e1}}{\mathrm{d}t} = \frac{1}{l_*}\Big((l_2+l_3)v_{T1} + l_2 v_{T2} + (l_3 r_2 - l_2 r_3)i_{e2} - \left[(l_2+l_3)r_1 + l_2 r_3\right] i_{e1}\Big), \tag{4.14}$$

$$\frac{\mathrm{d}i_{e2}}{\mathrm{d}t} = \frac{1}{l_*}\Big(-l_3 v_{T1} + l_1 v_{T2} + (l_3 r_1 - l_1 r_3)i_{e1} - \left[(l_1+l_3)r_2 + l_1 r_3\right] i_{e2}\Big), \tag{4.15}$$

in terms of the prescribed transformer voltages. The current in the third electrode is simply given by $i_{e3} = -i_{e1} - i_{e2}$. For ease of notation, we have here defined

$$l_j = L_j + \frac{L_T}{3}, \qquad l_* = l_1 l_2 + l_2 l_3 + l_1 l_3, \qquad r_j = R_j + \frac{R_T}{3}. \tag{4.16}$$

The two equations (4.14)–(4.15), along with the form (4.13) of the total resistance R_j of phase j, provide a system for the electric currents in each phase. Following [104], we assume that all the components have constant, prescribed resistances, except for the electric arc. To close the electrical circuit system, we require an equation for each of the arc resistances R_{aj}, which we discuss in the following subsection.

4.2.1.1 Models for the arc resistance

We now transform our (dimensional) arc temperature model (3.22a), assuming radiation is the only heat-loss mechanism, into an equation for the arc resistance R_a, in order to include it in the EC model. We also present the empirical Cassie and Mayr models for R_a, commonly-used in the SAF literature, and compare these to our radiation model.

Radiation arc model To make use of our arc model (3.22a), we assume that each of the three arcs have temperature T_{aj} satisfying (3.22a). To combine (3.22a) with the electric circuit system, and for easy comparison with the Cassie and Mayr models, we transform (3.22a) to be an equation for the electrical resistance of the arc R_{aj}, using the change of variables

$$R_{aj} = \frac{h_a}{\pi r_a^2 \sigma_a(T_{aj})} = \frac{h_a}{\alpha_1 \pi r_a^2} \exp\left(\frac{\alpha_3}{T_{aj}}\right), \tag{4.17}$$

where r_a is the arc radius and h_a the arc height, and we have used the form (4.3) for $\sigma_a(T_a)$, with $\alpha_2 = 0$. We also use the voltage v_{aj} across arc j, and so make the change of variables $v_{aj} = h_a E$. The equation (3.22a) then becomes

$$\frac{\mathrm{d}R_{aj}}{\mathrm{d}t} = \frac{1}{\beta_r} \frac{R_{aj}}{(\log(bR_{aj}))^2} \left(1 - \frac{v_{aj}^2 \log(bR_{aj})^4}{P_r R_{aj}}\right), \tag{4.18}$$

where the parameters are

$$b = \frac{\alpha_1 \pi r_a^2}{h_a}\,\Omega^{-1}, \qquad \beta_r = \frac{\rho_a c_{p,a}}{4\kappa\sigma_B \alpha_3^3}\,\mathrm{s}, \qquad P_r = 4\kappa\sigma_B \alpha_3^4 \pi r_a^2 h_a\,\mathrm{W\,m^{-3}}. \tag{4.19}$$

From the electric circuit, the arc voltage v_{aj} is given in terms of R_{aj}, R_c, and i_{ej}, by

$$v_{aj} = R_{aj} i_{aj} = R_{aj} \frac{R_{cj}}{R_{ecj} + R_{aj} + R_{mj} + R_{cj}} i_{ej}. \tag{4.20}$$

This equation (4.20) is effectively the same as the current constraint (3.59), although now we view i_{ej} as an unknown, and include additional resistances elements R_m and R_{ec}. The equation (4.18) for each phase $j = 1, 2, 3$ along with (4.20) closes the EC system. The averaged quantities needed for the homogenised model are

$$\langle T_{aj}^4 \rangle = \langle \alpha_3^4 / \log(b R_{aj})^4 \rangle \quad \text{and} \quad \langle (v_{hj})^2 \rangle, \tag{4.21}$$

where v_{hj}, the voltage across the entire hearth region of phase j, is given by

$$v_{hj} = \frac{R_{ec} + R_m + R_{aj}}{R_{aj}} v_{aj}. \tag{4.22}$$

This is different from $\langle E^2 \rangle$ used in Section 4.1 only because there we neglected the pool and electrode resistances, and so effectively assumed that $R_m = R_{ec} = 0$.

Empirical models for the arc resistance Although it is not how they were originally formulated, both the Cassie and Mayr arc models may be understood in terms of the total conservation of energy in the arc, namely [37]

$$\frac{\mathrm{d}Q_j}{\mathrm{d}t} = P_j - P_j^{\mathrm{loss}} = \frac{v_{aj}^2}{R_{aj}} - P_j^{\mathrm{loss}}, \tag{4.23}$$

where Q_j is the heat content in arc j, heat is lost through the P_j^{loss} term, and the power generated in the arc is given by the Ohmic heating term

$$P_j = \frac{v_{aj}^2}{R_{aj}}. \tag{4.24}$$

The different arc models in the literature take different forms for Q_j and P_j^{loss}. For instance, for our radiation-based model (4.18), we used the forms

$$P_j^{\mathrm{loss}} = 4\kappa\sigma_B \pi r_a^2 h_a T_{aj}^4 \qquad \text{and} \qquad Q_j = \pi r_a^2 h_a \rho_a c_{p,a} T_{aj}. \tag{4.25}$$

We obtain the Cassie model if we take [37, 76, 104]

$$P_j^{\mathrm{loss}} = \frac{U^2}{R_{aj}} \qquad \text{and} \qquad Q_j = \frac{\beta_c}{U^2 R_{aj}}, \tag{4.26}$$

Model	radiation	Cassie	Mayr
Source	$\frac{R_a}{\beta_r \log(bR_a)^2}$	$\frac{R_a}{\beta_c}$	$\frac{R_a}{\beta_m}$
Sink	$\frac{i_e^2 R_c^2}{\beta_r P_r} \frac{R_a^2 \log(bR_a)^2}{(R_a+R_c+R_m+R_{ec})^2}$	$\frac{i_e^2 R_c^2}{\beta_c U^2} \frac{R_a^3}{(R_a+R_c+R_m+R_{ec})^2}$	$\frac{i_e^2 R_c^2}{\beta_m P_m} \frac{R_a^2}{(R_a+R_c+R_m+R_{ec})^2}$

Table 4.1: The source and sink terms in each of the arc models (4.18), (4.27), and (4.29), as functions of the arc resistance R_a.

for constants β_c and U^2. This model is expected to give a good fit when heat loss from the arc is "mainly convective" [37, 76], and is generally held to be a reasonable model for high-current arcs [14, 76, 104]. With these functional forms, the conservation of energy equation (4.23) may be written as

$$\frac{\mathrm{d}R_{aj}}{\mathrm{d}t} = \frac{R_{aj}}{\beta_c}\left(1 - \left(\frac{v_{aj}}{U}\right)^2\right). \tag{4.27}$$

The Mayr model, by contrast, may be obtained with the parameterisation

$$P_j^{\text{loss}} = P_m \qquad \text{and} \qquad Q_j = -\frac{\beta_m}{P_m}\log(R_{aj}). \tag{4.28}$$

Here, the constant heat loss P_m is intended to be a good model for conductive heat loss [37, 76]. The heat content Q_j is logarithmic in R_{aj}, which follows from an assumption that Q_j is proportional to T and that the arc conductivity $\sigma = R_{aj}^{-1}$ is proportional to $\exp(T/\text{constant})$. Using (4.28) in the conservation of energy equation, (4.23), gives

$$\frac{\mathrm{d}R_{aj}}{\mathrm{d}t} = \frac{R_{aj}}{\beta_m}\left(1 - \frac{v_{aj}^2}{P_m R_{aj}}\right). \tag{4.29}$$

This Mayr model, (4.29), is generally used for low-current arcs [37, 76], and so is less-often used than the Cassie model in SAF applications.

Comparison of arc models Along with any of the Cassie (4.27), Mayr (4.29), or radiation (4.18) models, the system of ODEs (4.14)–(4.15) comprise a closed, fully-coupled system for the five unknowns i_{e1}, i_{e2}, R_{a1}, R_{a2}, and R_{a3}.

Since arc resistance decreases with increasing arc temperatures, the heat loss term in (4.23) becomes a source term in each of the equations (4.18), (4.27), and (4.29) for R_{aj}, while the Ohmic heating becomes a sink term. Since v_{aj}, given by (4.20), depends on both R_{aj} and i_{ej}, this Ohmic heating term is nonlinear for all three of the arc models. The dependences of these terms on R_{aj} are summarised in Table 4.1.

We may compare the three models by examining the steady-state solution(s) of each model, in a similar way to the DC analysis of Section 4.1.1. (For our radiation

model, the steady-state solutions are of course closely related to the DC solutions in Section 4.1.1.) For each of the three arc models, the source term (due to heat loss) and sink term (due to Ohmic heating), summarised in Table 4.1, are illustrated in Figures 4.8a-c, as functions of the arc resistance, R_a. The values of R_c, R_m, R_{ec}, and the model parameters are considered constants, and we also suppose there is a constant electrode current i_e. Steady-state solutions are the intersection(s) of the source and sink curves, and the stability is shown by the arrows in Figures 4.8a-c.

We note that — as for both the DC and prescribed-current AC models in Section 4.1 above — for all the arc models, there is no steady-state solution if i_e is smaller than some critical value i_e^{crit} (which is different for each of the three arc models, and may depend on the other parameters R_c, R_m, and R_{ec}). For $i_e < i_e^{\text{crit}}$, we expect $R_{aj} \to \infty$ for the dynamic solutions. The Cassie model has a single non-trivial steady-state solution for $i_e \geq i_e^{\text{crit}}$, whereas both the Mayr and radiation models may have one non-trivial steady state (when the source and sink curves meet tangentially, at $i_e = i_e^{\text{crit}}$) or two non-trivial steady states for $i_e > i_e^{\text{crit}}$. All three of the models have exactly one stable steady-state solution, labelled R_a^* in Figures 4.8a-c (although we note that for both the Mayr and radiation models, at the critical current i_e^{crit}, the single steady state is only an attracting point for $R_a < R_a^*$, not for $R_a > R_a^*$, as the two steady states coalesce into one at this point).

It is helpful to consider the arc current-voltage relationship (or "IV characteristic") of these steady-state solutions. At a (non-zero) steady-state solution of the radiation arc model we see from the equation (4.18), and the relationship $i_{aj} = v_{aj}/R_{aj}$ that we must have

$$v_{aj} = \pm\sqrt{\frac{P_r R_{aj}}{\log(bR_{aj})^4}}, \qquad i_{aj} = \frac{v_{aj}}{R_{aj}} = \pm\frac{\sqrt{P_r}}{\sqrt{R_{aj}}\log(bR_{aj})^2}. \tag{4.30}$$

For the Cassie model, we see from the equation (4.27) that steady states require $v_{aj} = \pm U$ to be constant, whereas for the Mayr model (4.29) we must have $v_{aj} = \pm\sqrt{P_m R_{aj}}$, and so $i_{aj} = v_{aj}/R_{aj} = \pm P_m/v_{aj}$. These steady-state IV characteristics are plotted for each of the three models in Figure 4.8d. We note that since the arc resistance equations depend on v_{aj}^2, both the positive and negative solutions correspond to the same steady state in terms of R_a: the arc resistance does not depend on the direction of the current flow through the arc. All the non-trivial steady-state solutions (stable and unstable) lie on the IV characteristic for that arc model. We may think of the IV characteristic as being parameterised by the electrode current i_e. The three arc models have very different IV characteristics, with the arc voltage v_a decreasing for the

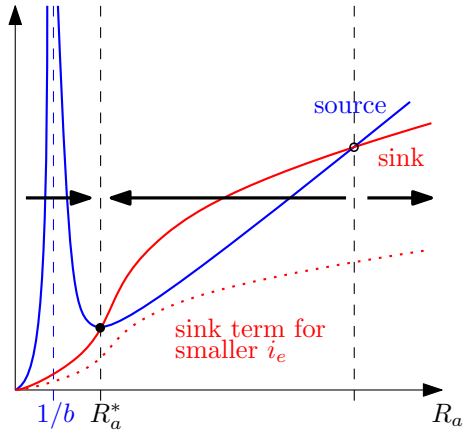

(a) Terms in the radiation arc model (4.18).

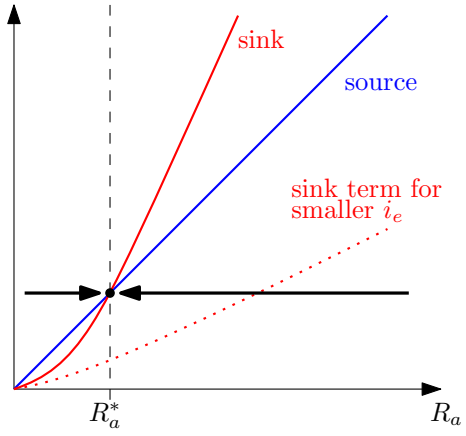

(b) Terms in the Cassie arc model (4.27).

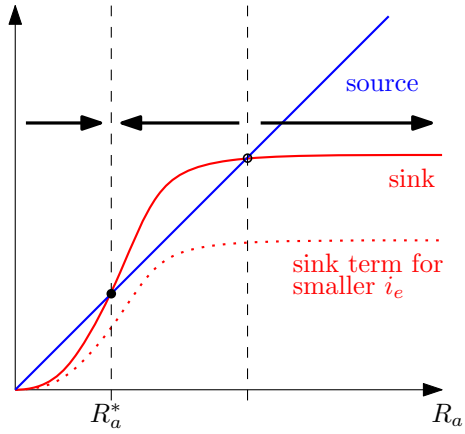

(c) Terms in the Mayr arc model (4.29).

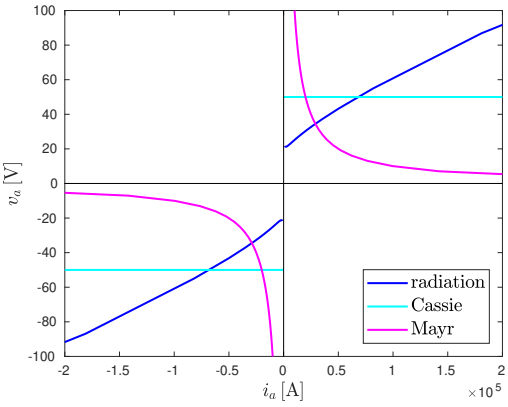

(d) IV characteristics for each arc model.

Figure 4.8: Comparison of the arc models. In (a)–(c), for the radiation, Cassie, and Mayr models, we give an illustration of the source and sink terms in the arc resistance equation, as in Table 4.1 and the steady-state solution(s). Black arrows indicate the direction of evolution of dynamic solutions. In (d) we show typical steady-state current-voltage relationships (IV characteristics) for each arc model.

Mayr model, constant for the Cassie model, and increasing for the radiation model, with increasing i_a.

At high currents, and for sufficiently fast arc variation (corresponding to sufficiently small β_r, β_c, or β_m) we expect the AC simulations to follow the steady-state IV characteristics closely, and indeed we observe this behaviour in the numerical simulations in Section 4.2.3 below. These differences in the steady-state behaviour are important, as they give insight into the high-current behaviour of the dynamic AC solutions. IV characteristics are found by [85] for AC simulations of both a magnetohydrodynamic (MHD) arc model, and also for a semi-empirical channel arc model (CAM) designed for SAF arcs, which is simpler than the full MHD model, but still

considerably more complicated than the Cassie, Mayr or radiation models. Both these more sophisticated models in [85] show IV characteristics that are rising at high currents, not falling or constant as for the Cassie or Mayr models. This provides some validation for the radiation arc model, which is the only one of the three with a rising steady-state IV characteristic.

4.2.1.2 Initial conditions

The EC model is a first order ODE system for variables i_{ej} and R_{aj} and so requires an initial condition for each of the i_{ej} and R_{aj}. In the numerical solutions of Section 4.2.3 we prescribe the initial conditions

$$i_{e1} = i_{e2} = 0 \quad \text{and} \quad R_{a1} = R_{a2} = R_{a3} = R_0 \quad \text{at } t = 0, \tag{4.31}$$

and solve forward in time until the solution is periodic. As in Section 4.2.1.1, there is exactly one non-trivial steady-state solution for each of the arc models (for sufficiently high i_e), to which the dynamic solution will evolve during the AC period. We therefore expect that periodic solutions will not depend on the choice of initial conditions, and we indeed find this to be the case in the numerical simulations of Section 4.2.3.

4.2.1.3 Industrial measurements

In an industrial setting, it is not possible to observe all variables in our model directly: only the total current, i_{ej}, through each phase, and total voltage, v_j, across each phase j can be measured. The electrode currents i_{ej} are computed as the solution of the model, and the phase voltages v_j may be found from (4.12) using the forms of $\frac{\mathrm{d}i_{ej}}{\mathrm{d}t}$ from (4.14)–(4.15). For instance, v_1 may be expressed as

$$v_1 = R_1 i_{e1} + \frac{L_1}{l_*}\left((l_2 + l_3)v_{T1} + l_2 v_{T2} + (l_3 r_2 - l_2 r_3)i_{e2} - \left[(l_2 + l_3)r_1 + l_2 r_3\right] i_{e1}\right). \tag{4.32}$$

4.2.2 Nondimensionalisation

We now nondimensionalise the equivalent-circuit model and each of the three arc models presented in Section 4.2.1, using industrially relevant parameter values. The nondimensionalisation is different to that in Section 4.1, in order to most easily understand the EC system. We discuss the dimensionless parameters at the end of this section, before solving the dimensionless model numerically in Section 4.2.3.

We nondimensionalise the system (4.13), (4.14)–(4.15), (4.20), and the arc resistance equation (either (4.18), (4.27), or (4.29)) using the rescalings

$$\begin{aligned} R_{cj} &= \frac{V_T}{[i]}\hat{R}_{cj}, \quad R_{aj} = \frac{V_T}{[i]}\hat{R}_{aj}, \quad R_j = \frac{V_T}{[i]}\hat{R}_j, \quad r_j = \frac{V_T}{[i]}\hat{r}_j, \\ v_{aj} &= V_T\hat{v}_{aj}, \qquad i_{ej} = [i]\hat{i}_j, \qquad\quad t = \frac{1}{f_{\mathrm{AC}}}\hat{t}, \end{aligned} \tag{4.33}$$

where the hat notation denotes dimensionless variables. We have chosen the timescale of the alternating current, prescribed the current scaling to be $[i]$, and chosen the scalings of the resistances so that the voltage drop due to resistance balances the forcing due to the transformer voltages in (4.14)–(4.15). Using these rescalings, the dimensionless system (dropping the hat notation) is

$$\begin{aligned} \zeta_I \frac{\mathrm{d}i_1}{\mathrm{d}t} &= (1+\lambda_2)\sin(2\pi t) + \lambda_2 \sin\left(2\pi\left(t-\frac{1}{3}\right)\right) \\ &\qquad + (r_2 - \lambda_2 r_3) i_2 - \left((1+\lambda_2)r_1 + \lambda_2 r_3\right) i_1, \end{aligned} \tag{4.34a}$$

$$\begin{aligned} \zeta_I \frac{\mathrm{d}i_2}{\mathrm{d}t} &= -\sin(2\pi t) + \lambda_1 \sin\left(2\pi\left(t-\frac{1}{3}\right)\right) \\ &\qquad + (r_1 - \lambda_1 r_3) i_1 - \left((1+\lambda_1)r_2 + \lambda_1 r_3\right) i_2, \end{aligned} \tag{4.34b}$$

where $i_3 = -i_1 - i_2$, and

$$r_j = r_{ej} + \frac{1}{\frac{1}{R_{cj}} + \frac{1}{r_{crj}+R_{aj}}}, \quad v_{aj} = \frac{R_{aj}R_{cj}i_j}{R_{aj}+R_{cj}+r_{crj}}, \quad \text{for } j = 1,2,3, \tag{4.35}$$

along with one of the following arc models:

$$\text{Radiation:} \qquad \zeta_r \frac{\mathrm{d}R_{aj}}{\mathrm{d}t} = \frac{R_{aj}}{\log(BR_{aj})^2}\left(1 - \frac{v_{aj}^2 \log(BR_{aj})^4}{p_r R_{aj}}\right), \tag{4.36a}$$

$$\text{Cassie:} \qquad \zeta_c \frac{\mathrm{d}R_{aj}}{\mathrm{d}t} = R_{aj}\left(1 - \frac{v_{aj}^2}{p_c}\right), \tag{4.36b}$$

$$\text{Mayr:} \qquad \zeta_m \frac{\mathrm{d}R_{aj}}{\mathrm{d}t} = R_{aj}\left(1 - \frac{v_{aj}^2}{p_m R_{aj}}\right). \tag{4.36c}$$

Here we have introduced the dimensionless parameters for the electrical system,

$$\begin{aligned} \zeta_I &= \frac{l_* f_{\mathrm{AC}}[i]}{l_3 V_T}, \qquad \lambda_1 = \frac{l_1}{l_3}, \qquad \lambda_2 = \frac{l_2}{l_3}, \\ r_{ej} &= \frac{[i]}{V_T}\left(R_{ej} + R_{bj} + \frac{R_T}{3}\right), \qquad r_{crj} = \frac{[i]}{V_T}\left(R_{ecj} + R_{mj}\right), \quad \text{for } j = 1,2,3, \end{aligned} \tag{4.37}$$

and, depending on the arc model used, the dimensionless parameters, for $j = 1, 2, 3$,

$$\text{Radiation:} \qquad \zeta_{rj} = \beta_{rj} f_{\mathrm{AC}}, \qquad p_{rj} = \frac{P_{rj}}{V_T[i]}, \qquad B_j = \frac{b_j V_T}{[i]}, \tag{4.38}$$

$$\text{Cassie:} \qquad \zeta_{cj} = \beta_{cj} f_{\mathrm{AC}}, \qquad p_{cj} = \frac{U_{cj}^2}{V_T^2}, \tag{4.39}$$

$$\text{Mayr:} \qquad \zeta_{mj} = \beta_{mj} f_{\mathrm{AC}}, \qquad p_{mj} = \frac{P_{mj}}{V_T[i]}. \tag{4.40}$$

For comparison with industrial measurements, we also nondimensionalise (4.32), using the additional scaling $v_1 = V_T \hat{v}_1$. Dropping the hat notation, this gives

$$\begin{aligned} v_1 = {} & (r_1 - \rho_T) i_1 \\ & + \frac{\lambda_1 - \lambda_T}{\lambda_1 + \lambda_2 + \lambda_1 \lambda_2} \Bigg((\lambda_2 + 1) \sin(2\pi t) + \lambda_2 \sin\left(2\pi \left(t - \frac{1}{3}\right)\right) \\ & \qquad + (r_2 - \lambda_2 r_3) i_2 - ((\lambda_2 + 1) r_1 + \lambda_2 r_3) i_1 \Bigg), \end{aligned} \tag{4.41}$$

and we have similar expressions for v_2 and v_3. Here we have introduced the additional dimensionless parameters

$$\rho_T = \frac{R_T[i]}{3V_T} \qquad \text{and} \qquad \lambda_T = \frac{L_T}{3l_3}. \tag{4.42}$$

We use the arc conductivity parameter α_3 (defined in (4.3)) as the scaling for the arc temperature T_{aj}, and V_T as the scaling for v_{hj}. Dropping the hat notation, the dimensionless averaged quantities (4.21) then become

$$\langle 1/\log(BR_{aj})^4 \rangle \quad \text{and} \quad \langle (v_j^h)^2 \rangle, \tag{4.43}$$

where

$$\langle \cdot \rangle := \int_{t=0}^{1} \cdot \, \mathrm{d}t \tag{4.44}$$

is the dimensionless time-average.

Physically relevant data values are given in Table 4.2, including the sizes of the radiation parameters given by (4.19) using data from Table 3.4. Since the parameters for the Cassie and Mayr models are empirical, and must be chosen to fit data, we do not include these in Table 4.2. Using the data of Table 4.2, the corresponding values for the dimensionless parameters are listed in Table 4.3.

As expected, we note that both r_{cr} and r_e are relatively small, so that the resistance of the charge material or of the arc dominates the total resistance through each phase.

Parameter/Scaling	Value
f_{AC}	$50\,\mathrm{s}^{-1}$
V_T	$260\sqrt{2}\,\mathrm{V}$
$[i]$	$1.65 \times 10^5\,\mathrm{A}$
R_e	$1 \times 10^{-4}\,\Omega$
R_b	$3 \times 10^{-4}\,\Omega$
R_m	$1 \times 10^{-4}\,\Omega$
R_{ec}	$2 \times 10^{-5}\,\Omega$
R_T	$1.0 \times 10^{-7}\,\Omega$
L	$2.0 \times 10^{-6}\,\Omega\,\mathrm{s}$
L_T	$6.3 \times 10^{-7}\,\Omega\,\mathrm{s}$
P_r	$1.1 \times 10^7\,\mathrm{W\,m}^{-3}$
β_r	$1.5 \times 10^{-4}\,\mathrm{s}$
b	$5.2 \times 10^3\,\Omega^{-1}$

Table 4.2: Industrially relevant data values [1] used for the nondimensionalisation. The arc parameters β_r, P_r, and b are computed using data in Table 3.4.

Dimensionless Parameter	Value
ζ_I	1.3×10^{-1}
r_e	1.8×10^{-1}
r_{cr}	5.4×10^{-2}
ζ_r	7.6×10^{-3}
p_r	1.8×10^{-1}
B	1.2×10
ρ_T	1.4×10^{-5}
λ_T	1.1×10^{-1}
λ_1, λ_2	≈ 1

Table 4.3: Dimensionless parameters, computed using the data in Table 4.2.

The value ρ_T is negligibly small, and so we may neglect the effect of the transformer resistances when computing the phase voltages v_j in (4.41). The inductance of the transformers is small, but not negligible in comparison with the electrode inductances, since $\lambda_T \approx 0.11$. The asymmetry of the system is encoded in the parameters λ_1, λ_2 (which are both 1 if the electrode inductances are equal), the different values of r_{ej}, r_{crj}, and the arc parameters B_j, ζ_{rj}, and p_{rj} (or equivalent arc parameters for the Cassie or Mayr models). Since both the inductance parameter, ζ_I, and especially the arc resistance time-constant, ζ_r, are small, we anticipate stiffness in the ODE system, as in Section 4.1.2.

Compared with the cell problem studied in Section 4.1, there are many more dimensionless parameters in this model. The parameter ζ_r plays the same role of arc

time-constant as χ in Section 4.1.2, and the charge resistance R_c is inversely related to the charge conductance σ_{ch} in Section 4.1.2. We have two further parameters in the radiation arc model, B and p_r, compared with in Section 4.1.2, because of the different choice of nondimensionalisation. The equivalent parameter in Section 4.1.2 is the electrode current magnitude $\hat{I}$, which we have here scaled out by assuming we know the value $[i]$.

4.2.3 Numerical solutions

In this section we solve numerically the system (4.34) with each of the arc models (4.36), using ode15s in MATLAB, as in Section 4.1.2. As discussed in Section 4.2.1.2, we initialise at the (appropriately nondimensionalised) initial conditions (4.31), and solve forward in time until the solutions are periodic (usually within one or two periods). We observe that the periodic solution is independent of the choice of initial value R_0, so long as this is sufficiently large that periodic solutions may be found.

We have made several simplifying assumptions in the model presented above, but there are still a large number of dimensionless parameters in the model. For simplicity, in the remainder of this section we restrict to a symmetric model, assuming that all the parameters (including the arc parameters) for each of the three phases are equal. Specifically, we set $\lambda_1 = \lambda_2 = 1$, and use the notation R_c, r_e, r_{cr}, ζ_r, p_r, B, ζ_c, p_c, ζ_m, and p_m for each of R_{cj}, r_{ej}, r_{crj}, ζ_{rj}, p_{rj}, B_j, ζ_{cj}, p_{cj}, ζ_{mj}, and p_{mj}, for $j = 1, 2, 3$, respectively. We only present solutions for phase 1; the solutions for the other phases are the same up to phase shift.

4.2.3.1 The radiation arc model

Periodic numerical solutions of the system (4.34) using the radiation arc model (4.36a) are shown in Figure 4.9, where we vary the arc-model parameters p_r and ζ_r, while holding B, and the parameters of the external electric circuit, constant. In Figures 4.9a, c, and e we show the currents through the electrode i_1, arc $i_{a1} = v_{a1}/R_{a1}$, and the charge material $i_{c1} = v_{h1}/R_c$ for various p_r and ζ_r, and in Figures 4.9b, d, and f we show the associated arc signature plots of arc current i_{a1} against arc voltage v_{a1}.

We observe very similar behaviour to in the prescribed-current AC case in Section 4.1.2, with the arc signature evolving towards the steady-state IV characteristic (discussed in Section 4.2.1.1), shown by the pink curves in Figure 4.9. Varying ζ_r, like varying χ in Section 4.1.2, affects the rate at which the arc adapts to the changing voltage across it, so that for small ζ_r (solid lines in Figure 4.9) the arc adapts very

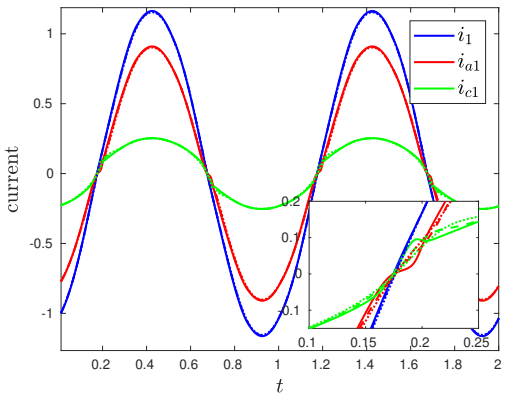

(a) Distribution of currents, $p_r = 0.18$

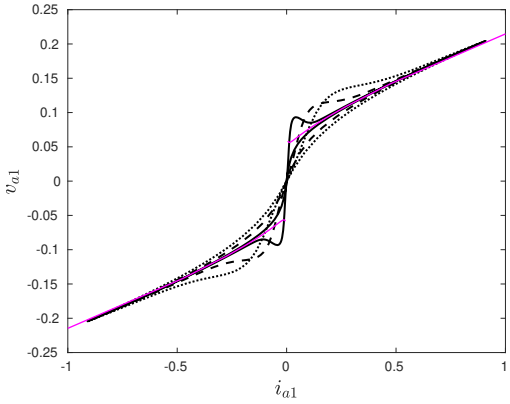

(b) Arc signature, $p_r = 0.18$.

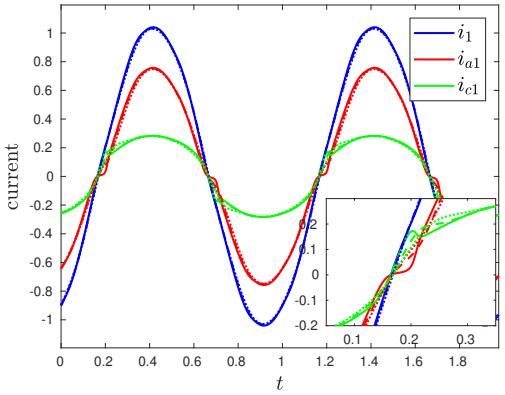

(c) Distribution of currents, $p_r = 0.6$

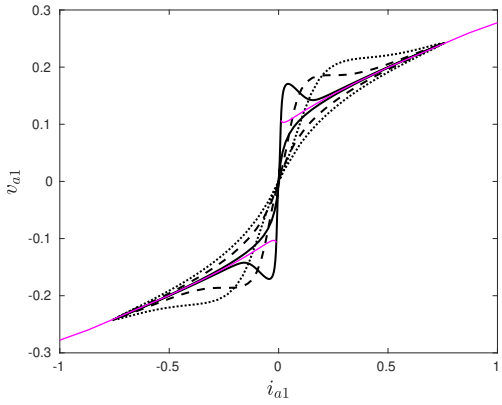

(d) Arc signature, $p_r = 0.6$.

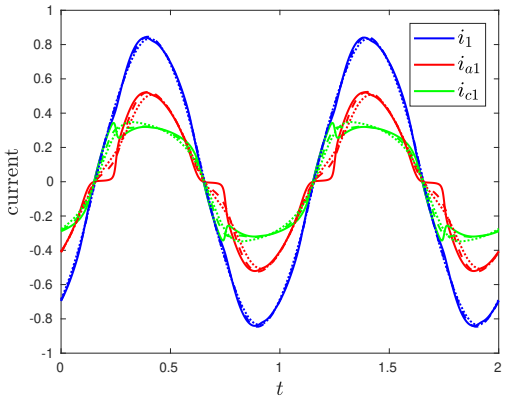

(e) Distribution of currents, $p_r = 2$

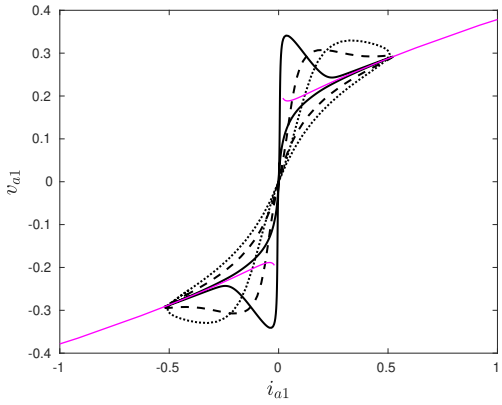

(f) Arc signature, $p_r = 2$.

Figure 4.9: Numerical solutions using the radiation arc model (4.36a), varying p_r and ζ_r. In (a), (c), and (e), the currents are shown through the electrode (i_1, blue), arc (i_{a1}, red), and charge (i_{c1}, green) of phase 1. The insets in (a) and (c) show detail near current zero. In (b), (d), and (f), the arc signature (arc voltage against arc current) is shown. The thin pink curves show the "steady state" or DC solution of the radiation arc model (4.36a). In all plots (a)–(f), solid lines correspond to $\zeta_r = 1 \times 10^{-3}$, dashed lines to $\zeta_r = 7.6 \times 10^{-3}$, and dotted lines to $\zeta_r = 2 \times 10^{-2}$. We take $B = 12$ and $R_c = 1$, and choose the circuit parameters $\zeta_I = 0.13$, $r_{cr} = 0.054$, $r_e = 0.18$ throughout.

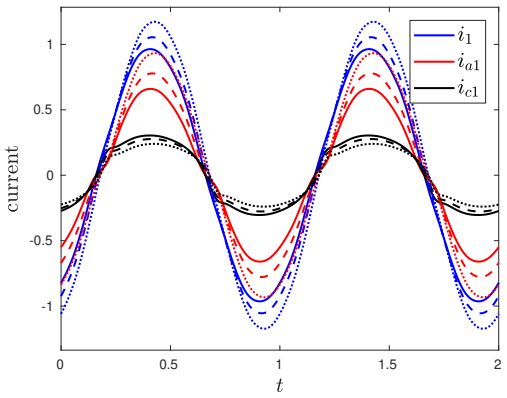

(a) Distribution of currents for various B.

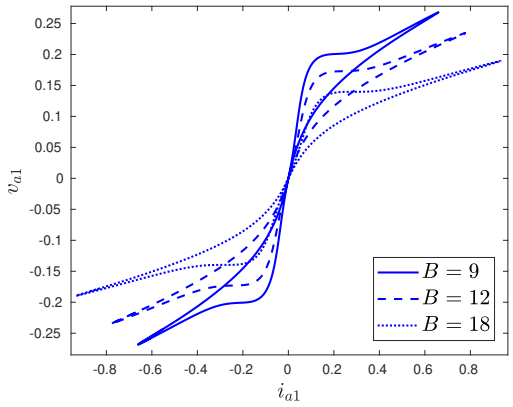

(b) Arc signature for various B.

Figure 4.10: Numerical solutions using the radiation arc model (4.36a), varying parameter B. In (a) the currents are shown through the electrode (i_1, blue), arc (i_{a1}, red), and charge (i_{c1}, black) of phase 1, with solid lines ($B = 9$), dashed lines ($B = 12$), and dotted lines ($B = 18$) as in (b). In (b) the arc signature is shown for each value of B in (a). In both plots we take $p_r = 1$, $\zeta_r = 7.6 \times 10^{-3}$, $R_c = 1$, and the circuit parameters as in Table 4.3.

quickly, whereas for larger ζ_r (dotted lines) there is a much slower evolution. Varying ζ_r does not appear to significantly affect the overall current distribution between the arc and the charge, nor the total current i_1 through that phase.

For small p_r, the arc resistance drops very quickly after the total current passes through zero, so that there is only a small time interval after the total current is zero for which the arc current is low. As p_r is increased, so that the Ohmic heat source is smaller, we see that the current is charge-dominated for a longer time after the total current passes through zero, as it takes longer to heat up the arc. Because the arc is cooler for larger p_r, it varies more slowly with the applied voltage, and so we see a bigger effect of varying ζ_r. For larger p_r we also observe that a smaller proportion of current passes through the arc, and more through the charge. However, from Figures 4.9b, d, and f we see that the maximum arc voltage decreases with increasing p_r, and the maximum arc current increases, so that the overall gradient of the arc signature is steeper. We also see from Figure 4.9a, c, and e that the amplitude of the total current i_1 decreases as p_r increases.

In Figure 4.10 we investigate the effect of varying the parameter B, for fixed p_r and β_r. We note that for larger B there is a higher amplitude of the total current i_1, as well as a larger arc current i_{a1}. The amplitude of the charge current i_{c1} decreases as B increases. From the definition (4.19) of the arc parameters, we see that B is

proportional to the conductivity magnitude α_1 of the gas forming the arc. It therefore is natural that larger values of B, corresponding to more conductive gases, result in larger currents through the arc. We note that for sufficiently small B (below around 8 for the parameters used in Figure 4.10), or for sufficiently large p_r (larger than the values chosen in Figure 4.9), the periodic solution of our model has no current through the arc, so that $i_{a1} = 0$ for all time t, and $i_{c1} = i_1$. Since B is proportional to α_1, a poorly conductive gas will correspond to small B, and so no arc forms. We also note that p_r is linearly proportional to h_a, the height or length of the electric arc, and B is inversely proportional to h_a. For a fixed gas composition, increasing h_a therefore has the effect of both decreasing B and increasing p_r. We therefore expect no solution to exist for sufficiently big arc lengths h_a, as is indeed seen in practice.

4.2.3.2 Cassie and Mayr arc models

Using the same electric circuit parameters as in the previous section, we now investigate solutions of (4.34) using the Cassie (4.36b) and Mayr (4.36c) arc models instead of the radiation arc model.

Solutions of (4.34) using the Cassie model (4.36b), and varying the Cassie parameters, are shown in Figure 4.11. We observe qualitatively similar behaviour of solutions using the Cassie model and those using the radiation model in Figure 4.9. In the same way as when increasing p_r in the radiation model, we see that increasing p_c in the Cassie model has the effect of decreasing both the total current i_1 and the proportion of current through the arc. Increasing ζ_c also has the effect of increasing the delay time of the arc, and therefore smooths out the arc signature plots. The main qualitative difference between solutions using the Cassie model in Figure 4.11 and the radiation model in Figure 4.9 is the slope of the arc signature at high current/voltage, which now follows the constant v_a steady-state IV characteristic, shown in pink, as discussed in Section 4.2.1.1.

Solutions of (4.34) using the Mayr model (4.36c) are shown in Figure 4.12. We find limited qualitative variation in the solutions with the parameters ζ_m and p_m, for the values of these parameters for which periodic solutions appear to exist. In particular, the arc signatures do not seem to follow the steady-state (DC) curves closely. This is likely to be because we require relatively large values of ζ_m in order to observe periodic solutions numerically.

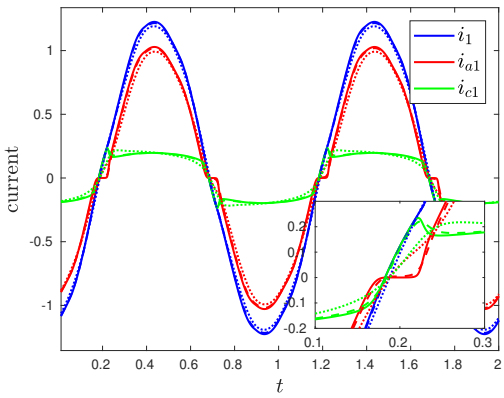

(a) Distribution of currents, $p_c = 0.02$

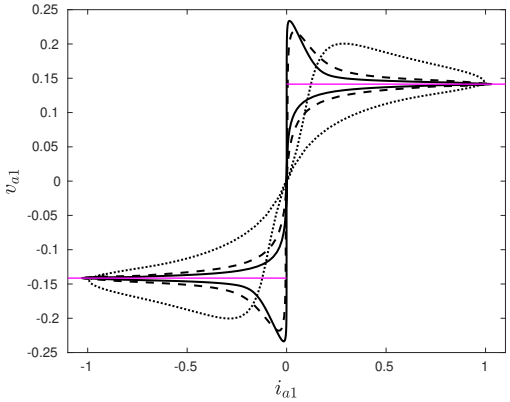

(b) Arc signature, $p_c = 0.02$

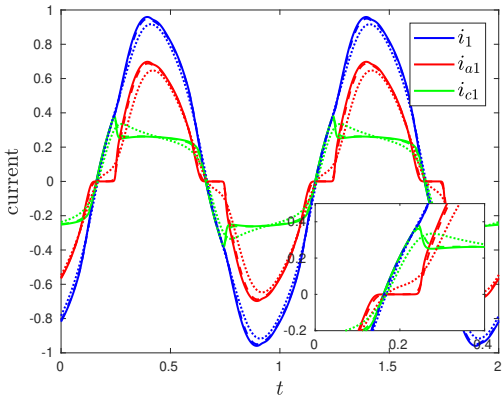

(c) Distribution of currents, $p_c = 0.05$

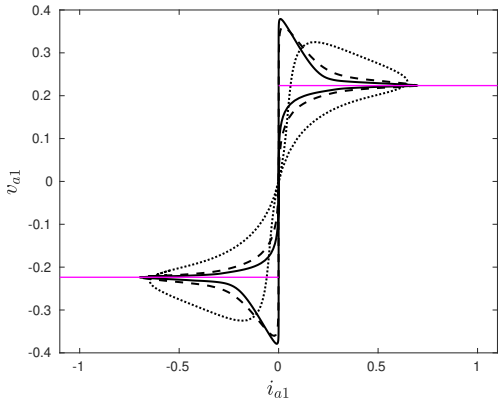

(d) Arc signature, $p_c = 0.05$

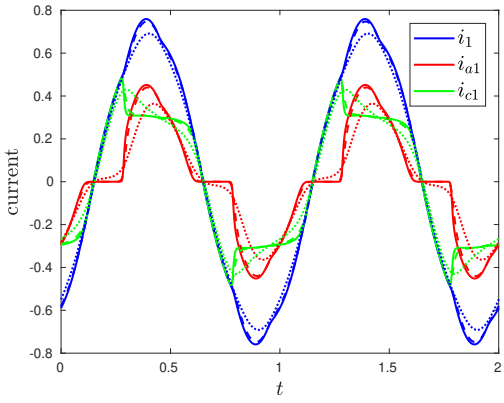

(e) Distribution of currents, $p_c = 0.08$

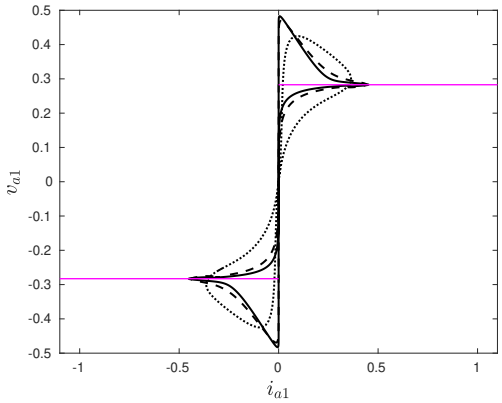

(f) Arc signature, $p_c = 0.08$

Figure 4.11: Numerical solutions using the Cassie arc model (4.36b), varying p_c and ζ_c. In (a), (c), and (e), the currents are shown through the electrode (i_1, blue), arc (i_{a1}, red), and charge (i_{c1}, green) of phase 1. The insets in (a) and (c) show detail near to where the current is equal to zero. In (b), (d), and (f) the arc signature (arc voltage against arc current) is shown, along with the steady-state (DC) solution $v_{a1} = \pm\sqrt{p_c}$ in pink. In all plots (a)–(f), solid lines correspond to $\zeta_c = 5 \times 10^{-3}$, dashed lines to $\zeta_c = 1 \times 10^{-2}$, and dotted lines to $\zeta_c = 5 \times 10^{-2}$. We take $R_c = 1$, and the circuit parameters $\zeta_I = 0.13$, $r_{cr} = 0.054$, $r_e = 0.18$ throughout.

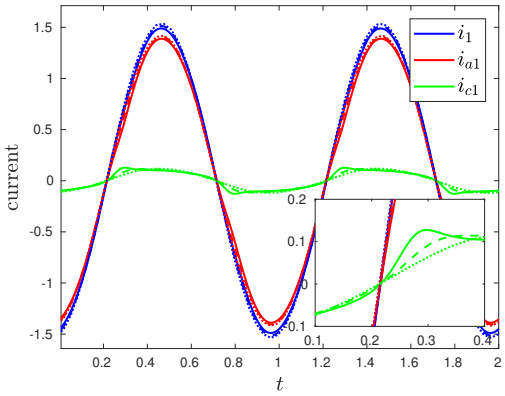

(a) Distribution of currents, $p_m = 0.03$

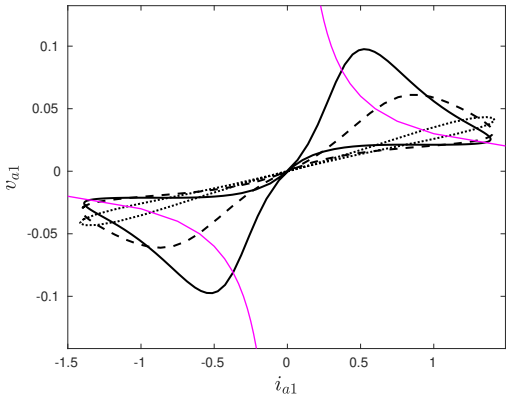

(b) Distribution of currents, $p_m = 0.03$

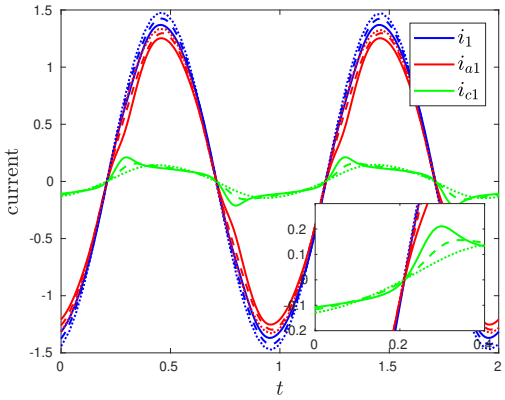

(c) Distribution of currents, $p_m = 0.05$

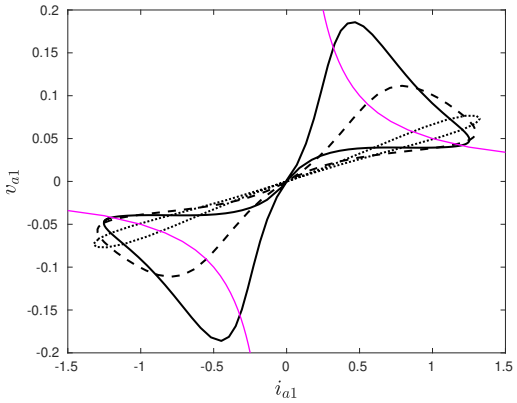

(d) Distribution of currents, $p_m = 0.05$

Figure 4.12: Numerical solutions using the Mayr arc model (4.36c), varying p_m and ζ_m. In (a) and (c), the currents are shown through the electrode (i_1, blue), arc (i_{a1}, red), and charge (i_{c1}, green) of phase 1. The insets in (a) and (c) show detail near to where the current is zero. In (b) and (d), the arc signature (arc voltage against arc current) is shown, along with the steady-state (DC) solution $v_{a1} = p_m/i_{a1}$ in pink. In all plots (a)–(d), solid lines correspond to $\zeta_m = 0.05$, dashed lines to $\zeta_m = 0.1$, and dotted lines to $\zeta_m = 0.5$. For all plots, we take $R_c = 1$, and choose the circuit parameters $\zeta_I = 0.13$, $r_{cr} = 0.054$, $r_e = 0.18$.

4.2.3.3 Comparison with furnace data

Having explored the dependence of our solutions on the arc model parameters, we now compare the solution of our EC model with measurements from an operational silicon furnace, with data provided by Elkem ASA. We use our radiation arc model, and parameter values based on the physical values in Table 4.3.

We note that there are two additional dimensionless parameters, ρ_T and λ_T, which appear in the form of the phase voltages v_j (4.41), which were not needed in the

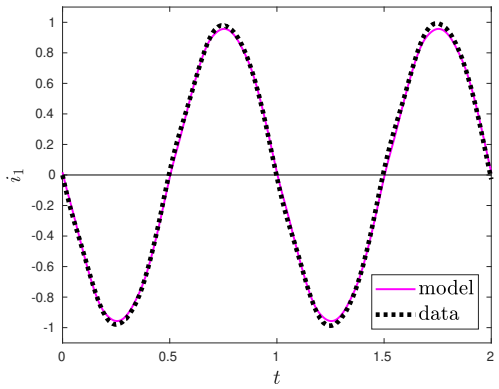

(a) Measured and computed current i_1.

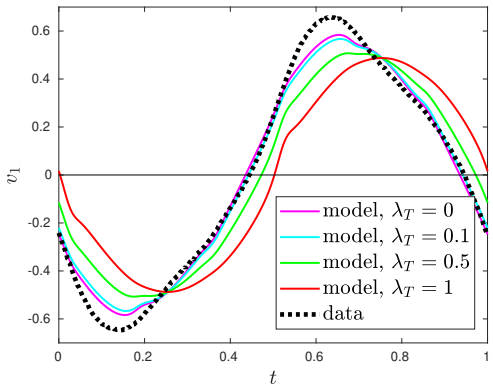

(b) Measured and computed voltage v_1 for various λ_T.

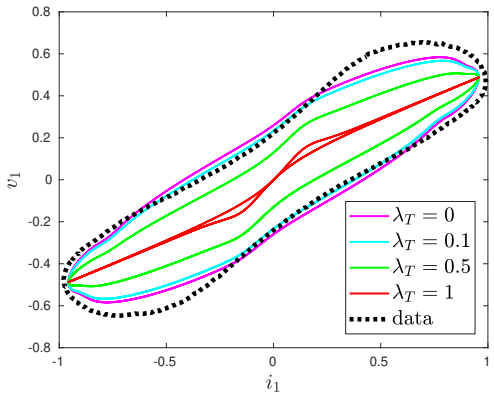

(c) Lissajous plots: current, i_1, against voltage, v_1, for various λ_T.

Figure 4.13: Comparison of furnace measurements (data collected by Elkem ASA [1]) with numerical simulations using the radiation arc model, with arc parameters $p_r = 0.2$, $\zeta_r = 8 \times 10^{-3}$, $B = 10$, circuit parameters $\zeta_I = 0.13$, $r_e = 0.22$, and $r_{cr} = 0.054$, and where we have chosen $R_c = 2.5$ for reasonable agreement with the data.

solution of the ODE system (4.34) with the arc model. The parameters ρ_T and λ_T describe, respectively, the proportion of the phase resistance, and proportion of the phase inductance that is due to the transformer circuit. As in Section 4.2.2,we expect $\rho_T \approx 10^{-5}$ to be small, and so take the limit $\rho_T = 0$ for our simulations in this section.

The effect of the transformer inductance, while smaller than the electrode inductance, is not negligible. In Figure 4.13 we plot the same solution of the (4.34) and (4.36a), but for multiple values of λ_T, and compare these solutions with the furnace data. Specifically, in order to compare with the furnace data we show the Lissajous plot of total current i_1 against the voltage v_1 across phase 1 in Figure 4.13c, not the

arc signature plots of i_{a1} against v_{a1} used in Figures 4.9–4.12. In the (unphysical) case of $\lambda_T = 1$ (where all of the inductive effect is in the transformer and none is in the electrode), we see from (4.41) that the voltage is purely resistive, $v_j = i_j R_j$. The voltage v_1 is therefore in phase with the electrode current i_1, as seen in Figure 4.13b. For smaller λ_T, there is non-zero induction within the electrode, introducing a phase shift in v_1 relative to i_1. This phase shift is most easily seen as the width of the Lissajous plot, shown in Figure 4.13b. The overall gradient of the Lissajous plot is loosely interpretable as the overall resistance.

The parameters of the arc model (4.36a) used in the solutions shown in Figure 4.13 are those listed in Table 4.3, based on physical values in Table 4.2. There is reasonable qualitative agreement in the overall shape of the solutions, especially for $\lambda_T = 0.1$. The predominant difference between the simulation and data is the shape of the voltage curve near its peak, where our model solution is significantly below the model data. This indicates that our arc model has a faster reduction in the arc resistance at high voltage than is the case in reality. From our arc-parameter investigation in Section 4.2.3.1, we might expect to get a better fit with the data in Figure 4.13 for much larger values of both p_r and ζ_r, so that the arc evolves more slowly at high voltages, although the circuit parameters would then need to be altered to compensate. In reality, it is likely that we are missing some physical effects in our radiation arc model, which would slow down the arc evolution, and increase the rate of heat loss from the arc at high voltages. One possibility is the heat loss to convection: as in Section 3.1.1 the fluid flow in and around the arc is generated by the Lorentz force, which increases in magnitude with the current flowing through the arc. Another consideration may be the inductive effects of the arc itself, which may change through the AC cycle, and are not captured by the constant inductance L_j of the phase. It is important to highlight that the full model has many parameters, and so reasonable agreement with the same data may be seen for parameter sets in different regimes of the parameter-space.

4.2.3.4 Time-averaged quantities for the homogenised model

Finally, we compute the averaged quantities (4.43), which we might use (rescaled appropriately) in the homogenised model (3.84). Using the same model parameters as in Section 4.2.3.3 above, we compute these averaged quantities (4.43) for a range of charge resistances R_c. For ease of qualitative comparison with the solutions found

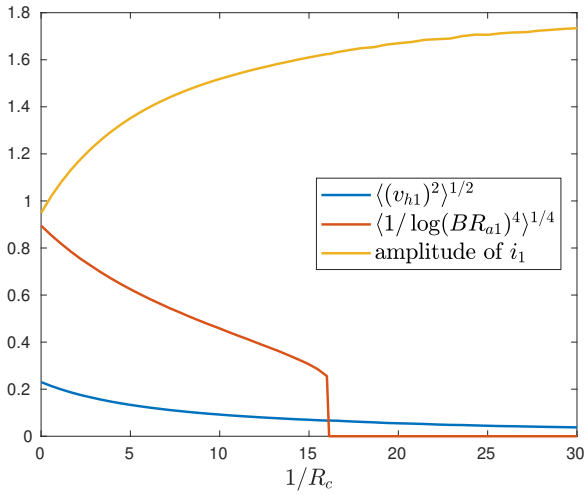

Figure 4.14: Plot of the time-averaged arc temperature $\langle 1/\log(BR_{a1})^4 \rangle^{1/4}$, time-averaged hearth voltage $\langle v_{h1}^2 \rangle^{1/2}$, and the amplitude of i_1, as functions of the charge conductance $1/R_c$.

in Section 4.1, in Figure 4.14 we plot the values

$$\langle 1/\log(BR_{a1})^4 \rangle^{1/4} \qquad \text{and} \qquad \langle v_{h1}^2 \rangle^{1/2}, \tag{4.45}$$

as functions of the charge conductance $1/R_c$. As for the DC and prescribed-current AC cases, we see that as the charge conductance increases, the rms voltage across the hearth decreases, and the average arc radiation also decreases, as less current passes through the arc, and more passes through the charge. For sufficiently large charge conductance, the only periodic solution of our model has $i_a = 0$, so that all the current passes through the charge, and there is no heat radiated by the arc.

With the full EC model, we solve for the electrode current i_1 as part of the solution of our model, and we see in Figure 4.14 that the amplitude of the electrode current increases with the charge conductance. This is the main qualitative difference between the averaged quantities computed from the EC model, and those from the prescribed-current AC model in Section 4.1.2.

4.3 Discussion

In Sections 4.1 and 4.2 we studied the cell problem of the homogenisation analysis, which describes how the electrical system, and in particular the electric arc, vary over the timescale of the alternating current. In Section 4.1 we studied both the DC and AC electrical system in and below a single electrode, assuming that the electrode

current I was known. In Section 4.2 we incorporated an equivalent-circuit model for the electrical system in the entire three-phase furnace, and so solved for the electrode currents as part of the solution of the cell problem. Several more detailed equivalent-circuit models (including more sophisticated inductance models, specified cathode and anode voltage drops, and including electric current directly between electrodes [104]) have been studied in the SAF literature; these might also be incorporated into our homogenised model in much the same way.

In both Sections 4.1 and 4.2 we found that the arc(s) evolved over a faster timescale than that of the alternating current, at least for high currents. The steady-state or DC solutions of the arc models therefore gave a good indication of the behaviour of the AC system for the high-current parts of the AC cycle. The AC system is not truly quasi-steady, however, since the arc evolves much more slowly when it is cooler, as the current passes through zero.

The EC framework of Section 4.2 allows comparison of our simplified arc model based on heat loss by radiation, presented in Section 3.1.1, with commonly-used empirical models for the arc resistance in the SAF literature. Our radiation arc model has several advantages over the Cassie and Mayr models. It is derived from first principles rather than semi-empirical, hence the model parameters have physical meaning and may be estimated from properties of the arc gases. The radiation model is also designed for SAF arcs (rather than for circuit-breaker arcs), taking into account the heat radiation which is known to be important for such high-current arcs. The radiation model is simple, with only one more parameter than either the Cassie or Mayr models. It also has a rising steady-state IV profile at the low arc resistances expected in a real furnace, which is also predicted by more sophisticated SAF arc models in the literature [85]. In comparison, the Cassie model has a constant-voltage profile, while the Mayr model has a falling profile. Our radiation model, of course, also allows the EC system to be combined with the slow-timescale homogenised model: it is not clear how the heat lost from the Cassie and Mayr arc models would be transferred to the surrounding charge material.

Chapter 5

Asymptotic analysis of a model problem: counter-current flow and endothermic chemical reaction

In this chapter, we employ the method of matched asymptotic expansions to analyse a model of coupled counter-current heat transfer, and an endothermic chemical reaction, similar to the homogenised model (3.84), derived in Chapter 3. We study a slightly simpler system than (3.84) in this chapter, in a Cartesian 1D geometry, and using an idealisation of the thermal coupling with the electric arc. The aim of this simplification is to draw out the interaction between the counter-current flow, and the endothermic chemical reaction, without unnecessary complications due to the electrical system, or radiation over the crater.

As discussed in Section 1.3, asymptotic analysis of two-temperature, multiphase models with endothermic reaction systems does not appear to be widely studied in the literature. Endothermic, multiphase systems do, however, arise in several metallurgical systems in addition to silicon furnaces, including the production of rutile titanium dioxide [2], the pyrolysis of aluminium [66], and the production of cement [98]. We anticipate that the asymptotic results found in this chapter would be relevant to these systems, as well as to our intended furnace application.

In this chapter, we study the limit of large Péclet number in the solid material, or of small δ, which we observed to be the industrially-relevant limit in the dimensional analysis of Chapter 3. As discussed in Chapter 3, the size of the dimensionless convective heat transfer coefficient, μ, is difficult to determine accurately. We therefore identify various distinguished limits for different sizes of μ (relative to the small parameter δ), ranging from negligible μ to the limit $\mu \to \infty$, which give a range of different asymptotic solution structures. From these asymptotic structures, we are

able to identify the distinguished limits that appear most relevant to a silicon furnace. In addition, by studying distinguished limits for large μ, we can understand how our model approaches a single-temperature model, which has been used for simplicity in other furnace models including [93, 96]. The analysis of this chapter may be extended to the radial domain of the furnace problem (3.84). In Chapter 6 we summarise the resulting reduced models for (3.84), and find solutions of these numerically.

In Section 5.1 we present the simplified model studied in this chapter. In Section 5.2 we give an overview of the asymptotic analysis, which is given in detail in Sections 5.3–5.8. Numerical solutions of the reduced models are computed in Section 5.9, and our composite asymptotic solutions are compared with numerical solutions of the full model in Section 5.10.

5.1 Statement of the simplified model

As a simplified version of (3.84), in this chapter we consider a Cartesian, 1D domain $x \in [s(t), 1]$, illustrated in Figure 5.1. We study the simplified model for the unknowns $C(x,t)$, $f(x,t)$, $T_s(x,t)$, $T_g(x,t)$, and the position $s(t)$ of the free boundary, given by

$$\delta\left(\frac{\partial C}{\partial t} - \frac{\partial C}{\partial x}\right) = -Q, \tag{5.1a}$$

$$\delta\frac{\partial f}{\partial x} = Q, \tag{5.1b}$$

$$C\left(\frac{\partial T_s}{\partial t} - \frac{\partial T_s}{\partial x}\right) = \delta\frac{\partial^2 T_s}{\partial x^2} + \mu(T_g - T_s) - \frac{\gamma}{\delta}Q, \tag{5.1c}$$

$$K\frac{\partial}{\partial x}(fT_g) = \frac{1}{\delta}T_s Q - \mu(T_g - T_s), \tag{5.1d}$$

on the domain $x \in (s(t), 1)$, where the dimensionless chemical reaction rate is

$$Q(C, T_s) = C\exp\left(A\left(1 - \frac{1}{T_s}\right)\right), \tag{5.1e}$$

and with boundary conditions

$$C = C_*, \quad f = f_*, \quad T_s = T_g = \frac{\rho}{s} \qquad \text{at } x = s(t), \tag{5.1f}$$

$$C = 1, \quad T_s = T^{\text{in}} \qquad \text{at } x = 1. \tag{5.1g}$$

As well as changing geometry, we have dropped the Ohmic heating term $\sigma_c\langle E^2\rangle$ from the solid heat equation (5.1c). We have also simplified the boundary conditions at the free boundary $x = s(t)$, to reduce the complexity of the problem. In particular we use the Dirichlet condition $T_s = \rho/s$, for some parameter ρ, as a crude model for

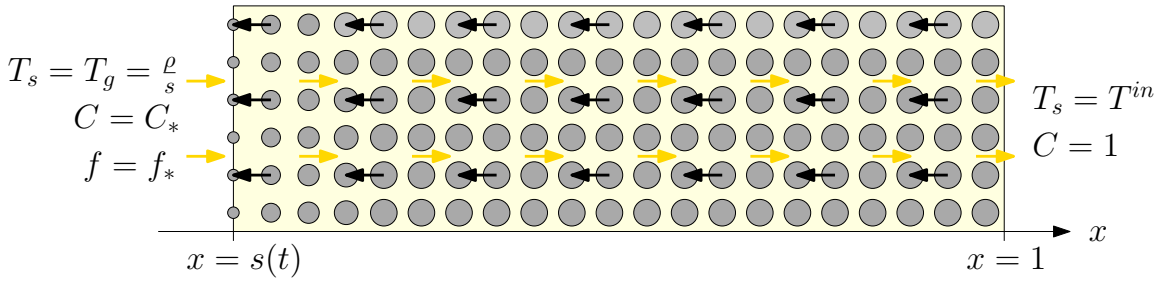

Figure 5.1: Schematic of the simplified, dimensionless model domain $x \in [s, 1]$, with granular solid (grey) moving right-to-left as shown by the black arrows, surrounded by gas (pale yellow) flowing left-to-right as shown by the yellow arrows. The solid particles become smaller nearer to the free boundary $x = s(t)$, as solid mass is reacted away. The boundary conditions are shown at $x = s(t)$ and $x = 1$.

a radiative heat source incident on $x = s(t)$. However, all the analysis in this chapter can also be done with the boundary conditions (3.84f)–(3.84h), without any change to the solution structures.

In addition to (5.1), we require initial conditions for C, f, T_g, T_s and s. The system (5.1) is a 5th order differential system of equations, with an additional degree of freedom in the position s of the free boundary. The model is correctly specified since we impose six boundary conditions.

Throughout this chapter, the dimensionless parameters K, γ, A, ρ, C_*, and f_* in the model (5.1) are assumed to be order 1. The inverse Péclet number, $\delta \approx 10^{-3} - 10^{-2} \ll 1$, is the smallest parameter in the system. We also assume that the input temperature of the solid, T^{in}, is small. Specifically, we require

$$\delta T^{\text{in}} \gg \exp\left(A\left(1 - \frac{1}{T^{\text{in}}}\right)\right), \tag{5.2}$$

so that the rate of reaction at this temperature is much less than the rate at which material moves through the whole domain by advection. Thus if there were no heating, we would expect the solid material not to appreciably react away over the time it spends moving through the domain. (When analysing the correction terms in specific cases, namely cases A, Ea, and Fa, we further assume that $\delta \ll T^{\text{in}}$.) The final dimensionless parameter is μ; we will consider various sizes of μ relative to δ.

5.2 Overview of asymptotic analysis

In Sections 5.3–5.8, we will consider a range of different distinguished limits corresponding to different values of μ, in terms of functions of δ. We refer to these

distinguished limits as cases A–F, studied in Sections 5.3–5.8, respectively, in order of increasing μ, with case A being the small-μ limit, $\mu \to 0$, (which we show is valid for $\mu \ll 1/\log(1/\delta)$), and case F the large-μ limit, $\mu \gg \delta^{-1}$. A schematic of the solution structures in each of the cases A–F is shown in Figure 5.2. Detailed schematics are given for each case in Sections 5.3–5.8.

The asymptotic results that we present in this chapter are mostly determined by the various dominant balances of the equation of conservation of energy in the solid, (5.1c). We label the terms in this equation as follows

$$\underbrace{C\left(\frac{\partial T_s}{\partial t} - \frac{\partial T_s}{\partial x}\right)}_{1} = \underbrace{\delta\frac{\partial^2 T_s}{\partial x^2}}_{2} + \underbrace{\mu(T_g}_{3} - \underbrace{T_s)}_{4} - \underbrace{\frac{\gamma}{\delta}C\exp\left(A\left(1-\frac{1}{T_s}\right)\right)}_{5}, \tag{5.3}$$

for explicit reference in our analysis. Terms 1 and 2 describe the advection and conduction, respectively, of heat within the solid material. Terms 3 and 4 describe the heat transferred to the solid by the gas, and are labelled separately since T_s and T_g may have different sizes in different regions of the domain. Term 5 is the heat absorbed by the endothermic chemical reaction.

Since $\delta \ll 1$, heat conduction in the solid material (term 2 in (5.3)), has negligible effect through most of the domain. However, for all sizes of μ, we will find a boundary layer of width $O(\delta)$ at $x = s(t)$, in which heat conduction (term 2) is important. It is only in this thin layer that the heating of the solid material from the radiation incident onto the boundary as in (5.1f) is felt. This boundary layer is the region of largest T_s in the domain: in all other regions we will find $T_s \ll 1$. Since the chemical reaction rate is temperature-dependent, the most intense material consumption also therefore occurs in this $O(\delta)$ boundary layer at $x = s(t)$. In all cases A–F, the reduced model in this boundary layer determines the position $s(t)$ of the free boundary. For some moderate values of μ the behaviour in the outer regions is coupled to the boundary-layer problem at leading order, and so also affects the position s.

Outside of this boundary layer there can be several types of behaviour depending on the size of μ. For small μ (case A), very little happens outside the boundary layer, with the solid temperature simply equal to its input value $T_s = T^{\text{in}}$ at leading order. For moderate μ (cases B–D), there is a balance between the transfer of heat from the gas to the solid (term 3 in (5.3)), and the energy consumed by the chemical reaction (term 5). In these cases, this balance determines the natural solid temperature scaling

$$\eta := \frac{A}{\log\left(\frac{1}{\delta\mu}\right)}, \tag{5.4}$$

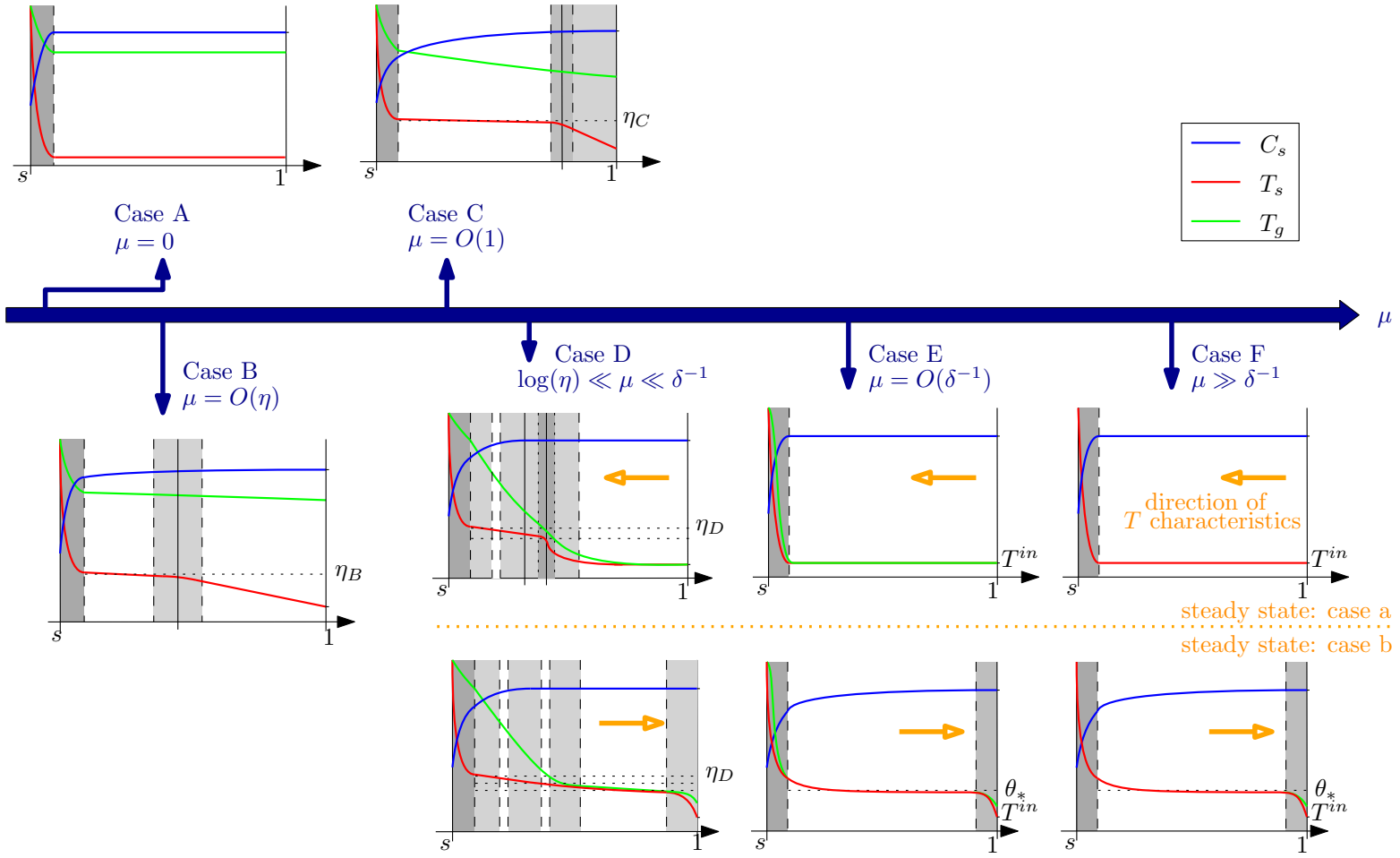

Figure 5.2: Schematics of the different asymptotic solution structures (in steady state for cases D–F) for increasing μ. In each case, the solutions, T_s red, T_g green, and C blue are illustrated in the domain $x \in [s(t), 1]$, with boundary layers and transition layers shown by the grey regions.

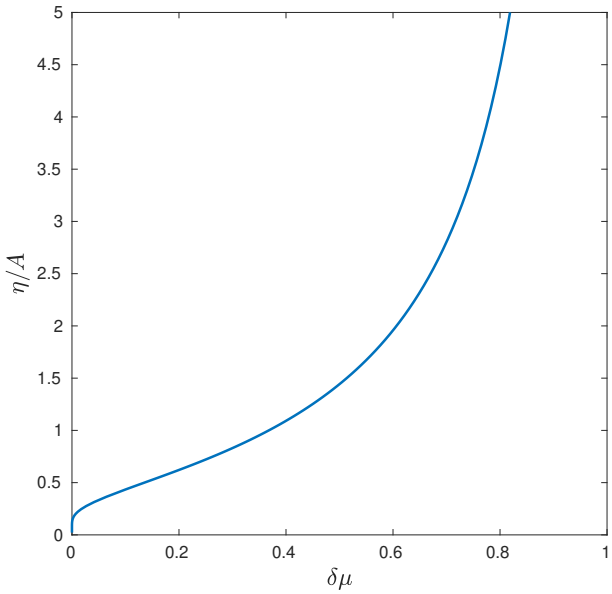

Figure 5.3: The variation of η/A with $\delta\mu$. The curve approaches the origin as $\delta\mu \to 0$, and becomes unbounded as $\delta\mu \to 1$.

and we find that $T_s \approx \eta$ is uniform throughout such regions of the domain. Since η depends on μ, for the different sizes of μ in cases B–D the value of η is different. The ratio η/A is plotted as a function of $\delta\mu$ in Figure 5.3. We note that η is monotone increasing in $\delta\mu$, with $\eta \to 0$ as $\delta\mu \to 0$ very slowly, and that η blows up as $\delta\mu \to 1$. In all cases B–D we have $\delta\mu \ll 1$, so that $\eta \ll 1$ is small, although due to the logarithmic form of η, we have $\delta \ll \eta$.

For large μ (cases D–F), we find that the heat transfer between phases, terms 3 and 4, dominate at leading order over an $O(1)$ lengthscale, so that we obtain a single-temperature model in the outer region of the domain. By combining the equations of conservation of energy for the gas and solid phases, we derive a single equation for the common, leading-order temperature $T_s = T_g = T$ in the $O(1)$-lengthscale regions of the domain. We observe interesting counter-current behaviour in these cases D–F: since the gas and solid material flow in opposite directions, the net direction of advection for the common temperature T may be in either direction, and the dominant behaviour is different in either case. In particular, if the net heat flow is left-to-right (with the gas flow) then the natural temperature scaling of the steady-state case is determined by a balance of advection, term 1, and heat consumed by the chemical reaction, term 5, giving the temperature scaling θ_*, the solution of

$$\delta\theta_*^2 = \exp\left(-\frac{A}{\theta_*}\right). \tag{5.5}$$

Conversely, if the net heat flow is right-to-left with the solid, the temperature remains approximately uniform at the solid input temperature T^{in}. These are referred to as the subcases b and a respectively.

The asymptotic structures that we derive in cases B and C, characterised by the balance of heat transfer between the phases and material consumption over an $O(1)$ lengthscale, are quite different to the single-temperature behaviour of cases E and F. The analysis in case D includes aspects of both these types of behaviour, and so demonstrates how the system varies from case C to E as μ is increased.

In each of the cases considered in Sections 5.3–5.8 below, we find explicit steady-state solutions at leading order, in every region of the domain except the boundary layer at $x = s(t)$. We construct composite, leading-order solutions in each case (restricting to steady state in cases D–F for simplicity).

5.3 Case A: $\mu = 0$, no heat transfer

Firstly, we suppose that there is no heat transfer between the gas and solid phases over the lengthscale of the entire domain, so that $\mu = 0$. We will see that this case is valid for $\mu \ll 1/\log(1/\delta)$: in case B below we explore the case $\mu = O(1/\log(1/\delta))$. The diagram in Figure 5.4 is a schematic of the asymptotic structure in this case, and the changes of variable that we will make in each region of the domain are summarised in Table 5.1. As in Figure 5.4, throughout this chapter we number the regions of the domain with roman numerals I, II etc., from left-to-right within the domain.

Since $\mu = 0$, the gas problem decouples from the solid problem, and we may study the reduced problem for the solid variables only. This is, for $x \in (s(t), 1)$, (5.1a) and (5.1c) (with $\mu = 0$) and the boundary conditions for C and T_s as in (5.1g)–(5.1f).

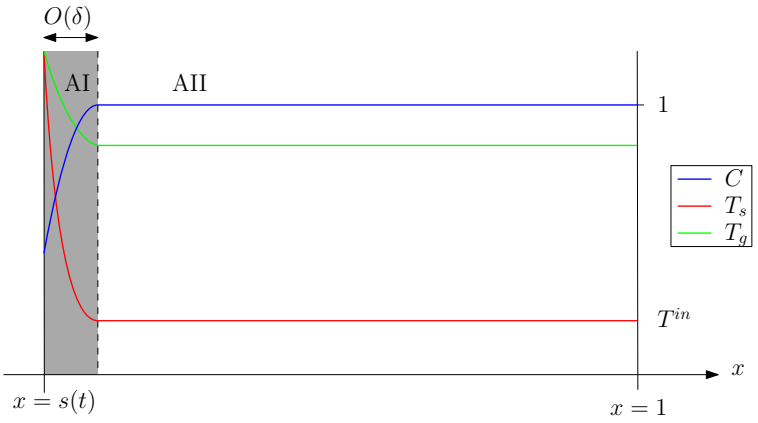

Figure 5.4: Schematic of the solution structure in case A: $\mu = 0$.

Region	Spatial Variable	Size of Q	Dominant terms in (5.3)	Dependent Variables
AI	$x = s(t) + \delta X$	$Q = O(1)$	1, 2, 5	C, f, T_s, T_g
AII	x	$Q \ll \delta T^{\text{in}}$	1	$C = \hat{C}$, $f = \hat{f}$, $T_s = T^{\text{in}}\hat{T}_s$, $T_g = \hat{T}_g$

Table 5.1: Summary of the asymptotic regions of the domain, and the changes of variable in these regions, for case A: $\mu = 0$.

We may then integrate (5.1b) and (5.1d), using the boundary conditions for f and T_g at $x = s(t)$ given by (5.1f). This gives the gas variables f and T_g in terms of the solution s, C, and T_s of the solid problem:

$$f = f_* + \delta^{-1} \int_{x=s}^{1} C \exp\left(A\left(1 - \frac{1}{T_s}\right)\right) \, \mathrm{d}x, \tag{5.6a}$$

$$T_g = \frac{f_* T_s|_{x=s} + (\delta K)^{-1} \int_{x=s}^{1} T_s C \exp\left(A\left(1 - \frac{1}{T_s}\right)\right) \, \mathrm{d}x}{f_* + \delta^{-1} \int_{x=s}^{1} C \exp\left(A\left(1 - \frac{1}{T_s}\right)\right) \, \mathrm{d}x}. \tag{5.6b}$$

We will see in the following analysis that the integral terms in (5.6) are $O(\delta)$, and so f and T_g are regular as $\delta \to 0$.

5.3.1 Region AII

We begin by considering the behaviour over an $O(1)$ lengthscale, which we denote region AII in Figure 5.4. We recall that $T^{\text{in}} \ll 1$ is small, in the specific sense (5.2). At the boundary $x = 1$ we have $T_s = T^{\text{in}}$, and we therefore look for a solution expansion of the form

$$T_s = T^{\text{in}}\left(\hat{T}_s^0 + o\left(T^{\text{in}}\right)\right), \qquad C = \hat{C}^0 + o\left(T^{\text{in}}\right), \tag{5.7}$$

and also expand the gas variables in region AII by

$$T_g = \hat{T}_g^0 + o\left(T^{\text{in}}\right), \qquad f = \hat{f}^0 + o\left(T^{\text{in}}\right). \tag{5.8}$$

(Here we use hat notation to differentiate from the variables used in region AI below.) Since by (5.2) we have that $Q(T^{\text{in}}) \ll \delta T^{\text{in}}$, at leading order in (5.1a) and (5.1c) we obtain

$$\frac{\partial \hat{C}^0}{\partial t} - \frac{\partial \hat{C}^0}{\partial x} = 0, \qquad \hat{C}^0\left(\frac{\partial \hat{T}_s^0}{\partial t} - \frac{\partial \hat{T}_s^0}{\partial x}\right) = 0. \tag{5.9}$$

Solving, using the boundary conditions at $x = 1$, we must have, for all x:

$$\hat{T}_s^0 = 1, \qquad \hat{C}^0 = 1. \tag{5.10}$$

Since $\hat{T}_s$ and $\hat{C}$ are constant to leading order, the gas variables in this region, given by (5.6), are also uniform. The error in these leading-order solutions is $O\left(\delta^{-1}Q\left(T^{\text{in}}\right)\right) = o\left(T^{\text{in}}\right)$, since $Q \ll \delta T^{\text{in}}$.

5.3.2 Region AI

We note that we cannot impose the boundary conditions at the free boundary $x = s(t)$ on the constant solution found in the previous section. We therefore look for a boundary layer at $x = s(t)$, denoted region AI, where $T_s = O(1) \gg T^{\text{in}}$. Since $\delta \ll 1$, we change variables, setting $x = s(t) + \delta X$. Since $T^{\text{in}} \gg \delta$, we look for an expansion in powers of T^{in} in region AI, setting

$$T_s = T_s^0(X,t) + T^{\text{in}}T_s^1(X,t) + O\left(\left(T^{\text{in}}\right)^2\right), \tag{5.11a}$$

$$C = C^0(X,t) + T^{\text{in}}C^1(X,t) + O\left(\left(T^{\text{in}}\right)^2\right), \tag{5.11b}$$

$$s = s_0(t) + T^{\text{in}}s_1(t) + O\left(\left(T^{\text{in}}\right)^2\right). \tag{5.11c}$$

We also expand the gas variables in powers of T^{in}, taking

$$T_g = T_g^0(X,t) + O(T^{\text{in}}), \qquad f = f^0(X,t) + O\left(T^{\text{in}}\right). \tag{5.12}$$

Substituting the expansions (5.11) into (5.1a) and (5.1c), at leading order we obtain

$$-\left(\dot{s}_0 + 1\right)\frac{\partial C^0}{\partial X} = -C^0 \exp\left(A\left(1 - \frac{1}{T_s^0}\right)\right), \tag{5.13a}$$

$$-\left(\dot{s}_0 + 1\right)C^0\frac{\partial T_s^0}{\partial X} = \frac{\partial^2 T_s^0}{\partial X^2} - \gamma C^0 \exp\left(A\left(1 - \frac{1}{T_s^0}\right)\right), \tag{5.13b}$$

where the dot notation denotes a time derivative, $\dot{s}_0 = \mathrm{d}s_0/\mathrm{d}t$. From (5.1f), we have the boundary conditions

$$C^0 = C_*, \qquad T_s^0 = \frac{\rho}{s_0}, \qquad \text{at } X = 0. \tag{5.13c}$$

As $X \to \infty$ we match with the outer region AII, and so require

$$C^0 \to 1, \qquad T_s^0 \to 0 \qquad \text{as } X \to \infty. \tag{5.13d}$$

This reduced system (5.13) in region AI determines T_s^0, C^0, and also the position $s_0(t)$ of the free boundary of the domain. The far-field temperature must approach

zero in (5.13d) so that the chemical reaction rate Q approaches zero in this limit. This is necessary for the problem to be correctly specified, as we show in Appendix A. This system (5.13) may be solved numerically, to find the leading-order solution in region AI, which is done in Section 5.9 below. In fact, we obtain similar boundary layer problems to (5.13) in many of the non-zero μ cases explored below.

Given the solution of this solid problem (5.13), from (5.6) with the change of variables $x = s(t) + \delta X$, we see that the leading-order gas variables in region AI are

$$f^0(X,t) = f_* + (1+\dot{s}_0)(C^0 - C_*), \tag{5.14a}$$

$$T_g^0(X,t) = \frac{\frac{f_*\rho}{s_0} + K^{-1}\int_{\bar{X}=0}^{X} T_s^0 C^0 \exp\left(A\left(1-\frac{1}{T_s^0}\right)\right)\,\mathrm{d}\bar{X}}{f_* + (1+\dot{s}_0)(C^0 - C_*)}. \tag{5.14b}$$

In region AII both $\hat{T}_g^0$ and $\hat{f}^0$ are uniform. By matching with region AI at $x = s_0$, we find

$$\hat{f}^0(t) = F_s(t) := f_* + (1+\dot{s}_0)(1 - C_*), \tag{5.15a}$$

$$\hat{T}_g^0(t) = G_s(t) := \frac{\frac{f_*\rho}{s_0} + K^{-1}\int_{\bar{X}=0}^{\infty} T_s^0 C^0 \exp\left(A\left(1-\frac{1}{T_s^0}\right)\right)\,\mathrm{d}\bar{X}}{f_* + (1+\dot{s}_0)(1 - C_*)}. \tag{5.15b}$$

5.3.3 Switchback error

Since $T_s = T^{\mathrm{in}} \ll 1$ in region AII, we must have an $O(T^{\mathrm{in}})$ correction to the leading-order solution in the boundary layer AI. This type of correction in the boundary layer due to the outer solution is termed a "switchback" correction in [43]. The problem for the correction terms C^1 and T_s^1 in region AI is the $O(T^{\mathrm{in}})$ correction to the equations (5.1a) and (5.1c) using the expansions (5.11), namely

$$-(\dot{s_0}+1)\frac{\partial C^1}{\partial X} - \dot{s}_1\frac{\partial C^0}{\partial X} = -\exp\left(A\left(1-\frac{1}{T_s^0}\right)\right)\left(C^1 + AC^0\frac{T_s^1}{(T_s^0)^2}\right), \tag{5.16a}$$

$$\begin{aligned}-(\dot{s}_0+1)\left(C^1\frac{\partial T_s^0}{\partial X} + C^0\frac{\partial T_s^1}{\partial X}\right) - \dot{s}_1 C^0\frac{\partial T_s^0}{\partial X} \\ = \frac{\partial^2 T_s^1}{\partial X^2} - \gamma\exp\left(A\left(1-\frac{1}{T_s^0}\right)\right)\left(C^1 + AC^0\frac{T_s^1}{(T_s^0)^2}\right),\end{aligned} \tag{5.16b}$$

where $\dot{s}_1 = \mathrm{d}s_1/\mathrm{d}t$, and with the boundary conditions at $X = 0$

$$C^1 = 0, \qquad T_s^1 = -\frac{\rho s_1}{s_0^2}. \tag{5.16c}$$

As $X \to \infty$ we must match with the $O(T^{\mathrm{in}})$ solutions in region AII: the $O(T^{\mathrm{in}})$ temperature is $\hat{T}_s^0 = 1$ while there is no $O(T^{\mathrm{in}})$ correction to the concentration in

region AII, hence the matching is

$$T_s^1 \to 1, \qquad C^1 \to 0, \qquad \text{as } X \to \infty. \tag{5.16d}$$

Like the leading-order problem (5.13), this system (5.16) must be solved numerically. Although we do not solve (5.16) in this thesis, this problem is correctly specified, as proved in Appendix A.

5.3.4 Composite solution

We construct composite leading-order solutions for case A as follows. Since C, f, and T_g are $O(1)$ in all regions of the domain, and uniform to leading order in region AII, the leading-order composite solutions in case A (which we denote by superscript A) are simply

$$C^{\mathrm{A}} = C^0\left(\frac{x - s_0(t)}{\delta}, t\right), \qquad f^{\mathrm{A}} = f^0\left(\frac{x - s_0(t)}{\delta}, t\right), \qquad T_g^{\mathrm{A}} = T_g^0\left(\frac{x - s_0(t)}{\delta}, t\right). \tag{5.17}$$

However, T_s is $O(1)$ in region AI, but $O(T^{\mathrm{in}})$ in region AII. We therefore have some freedom in how to choose the leading-order composite expansion [43]. For greatest accuracy, we should solve the switchback problem (5.16) in region AI to find the $O(T^{\mathrm{in}})$ correction, and then form a two-term composite expansion accurate to $O(T^{\mathrm{in}})$ in the entire domain. However, for simplicity we choose to set the $O(T^{\mathrm{in}})$ correction in region AI to be uniform, and equal to T^{in}. Thus we form the composite expansion

$$T_s^{\mathrm{A}} = T_s^0\left(\frac{x - s_0(t)}{\delta}\right) + T^{\mathrm{in}}, \tag{5.18}$$

which has $O(T^{\mathrm{in}})$ error in region AI, and $O\left(\delta^{-1}Q(T^{\mathrm{in}})\right)$ error in region AII.

In case A, we have seen that all the material consumption (chemical reaction) occurs within the boundary layer AI at $x = s(t)$, and that all variables have constant, uniform profiles in the outer region AII. We also notice that the behaviour is quasi-steady throughout the domain, with the time-derivatives of s in region AI the only time-derivatives in the reduced problem.

5.4 Case B: $\mu = O(\eta)$, small heat transfer

We now let $\mu > 0$, and study the distinguished limit $\mu = O(\eta)$. In this section, we write $\mu = M\eta_B \ll 1$, where $M = O(1)$ and $\eta_B = \eta_B(\delta, A)$ is the solution of

$$\eta_B = \frac{A}{\log\left(\frac{1}{\delta\eta_B}\right)}. \tag{5.19}$$

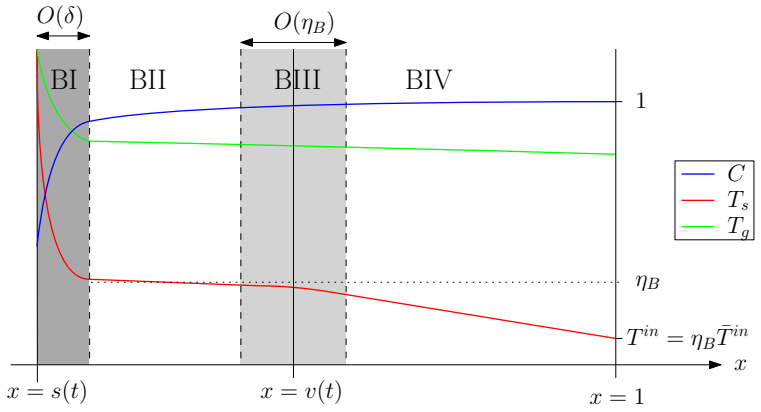

Figure 5.5: Schematic of the solution structure in case B: $\mu = O(\eta_B)$.

We note that for sufficiently small δ there are two positive solutions of (5.19), namely

$$\eta_{B,1} = \frac{1}{\delta}\exp(W_{-1}(-A\delta)), \quad \eta_{B,2} = \frac{1}{\delta}\exp(W_0(-A\delta)), \tag{5.20}$$

where W_0 and W_{-1} are (real) branches of the Lambert W function, and $\eta_{B,1} \leq \eta_{B,2}$. Graphically, these solutions are the intersections of the curve η/A in Figure 5.3 with the straight line of gradient $1/(\delta A)$ through the origin. We are interested in the small, non-zero root $\eta_{B,1}$, and write $\eta_B = \eta_{B,1}$ hereafter. For real negative z, as $z \to 0$ we have [24]

$$W_{-1}(z) = \log(-z) - \log(-\log(-z)) + O\left(\frac{\log(-\log(-z))}{\log(-z)}\right), \tag{5.21}$$

and we therefore see that

$$\eta_B = \eta_{B,1} = \frac{A}{-\log(A\delta)}\left(1 + O\left(\frac{\log(-\log(A\delta))}{-\log(A\delta)}\right)\right) \to 0 \qquad \text{as } \delta \to 0. \tag{5.22}$$

This case B with $\mu = O(\eta)$ is therefore equivalently expressed as the case $\mu = O(1/\log(1/\delta))$. In this section, we will expand our dependent variables in powers of η_B (rather than in powers of T^{in} as in case A), but to leading order this is equivalent to expanding in powers of $1/-\log(\delta)$. We choose to retain the η_B notation as it makes for easy comparison with subsequent cases. A schematic of the asymptotic structure in case B is shown in Figure 5.5, and the changes of variable are given Table 5.2.

5.4.1 Region BI

As in Case A, we look for an $O(\delta)$ boundary layer at $x = s(t)$, denoted region BI in Figure 5.5. We look for an expansion solution in powers of η_B in region BI, namely

$$T_s = T_s^0(X,t) + \eta_B T_s^1(X,t) + O(\eta_B^2), \quad C = C^0(X,t) + \eta_B C^1(X,t) + O(\eta_B^2), \tag{5.23a}$$

$$T_g = T_g^0(X,t) + \eta_B T_g^1(X,t) + O(\eta_B^2), \quad f = f^0(X,t) + \eta_B f^1(X,t) + O(\eta_B^2), \tag{5.23b}$$

Region	Spatial Variable	Size of Q	Dominant terms in (5.3)	Dependent Variables
BI	$x = s(t) + \delta X$	$Q = O(1)$	1, 2, 5	C, f, T_s, T_g
BII	x	$Q = O(\delta\eta_B)$	3, 5	$C = \hat{C}$ $f = \hat{f}$, $T_s = \eta_B(1 + \eta_B\hat{T}_s)$, $T_g = \hat{T}_g$
BIII	$x = v(t) + \eta_B y$	$Q = O(\delta\eta_B)$	1, 3, 5	$C = \tilde{C}$, $f = \tilde{f}$, $T_s = \eta_B(1 + \eta_B\tilde{T}_s)$, $T_g = \tilde{T}_g$
BIV	x	$Q \ll \delta\eta_B$	1, 3	$C = \bar{C}$, $f = \bar{f}$, $T_s = \eta_B\bar{T}_s$, $T_g = \bar{T}_g$

Table 5.2: Summary of the asymptotic regions of the domain, and the changes of variable in these regions, for case B: $\mu = O(\eta_B)$.

$$s = s_0(t) + \eta_B s_1(t) + O(\eta_B^2). \tag{5.23c}$$

Substituting into (5.1), the equations (5.1b) and (5.1d) for the gas variables decouple on this lengthscale, and so we obtain exactly the same system at leading order for just the solid variables T_s^0, C^0, and s_0 as in case A, namely (5.13). We will find below that $C = 1 + O(\eta_B)$ everywhere outside of region BI, and so the matching conditions as $X \to \infty$ are also identical to case A, given by (5.13d).

5.4.2 Region BII

Since $\mu > 0$, unlike case A, the equations for the gas variables do not decouple in (5.1) in the entire domain. Instead, outside the boundary layer BI, we must have heat transfer between the solid and gas phases, and expect the solid temperature scaling $T_s \approx \eta_B$. We therefore make the rescaling

$$T_s = \eta_B(1 + \eta_B\hat{T}_s), \tag{5.24}$$

in the $O(1)$-lengthscale outer region, denoted region BII, and for clarity of notation we also write $C = \hat{C}$, $f = \hat{f}$, and $T_g = \hat{T}_g$. The chemical reaction rate here is therefore

$$\hat{Q}(\hat{C}, \hat{T}_s) = \hat{C}\exp\left(A\left(1 - \frac{1}{T_s}\right)\right) = \hat{C}e^A\delta\eta_B\left(e^{A\hat{T}_s} + O(\eta_B)\right), \tag{5.25}$$

and thus the heat consumed by the chemical reaction at this temperature η_B is the same order ($\delta\eta_B$) as the heat transferred from the gas to the solid. The equations (5.1) in region BII therefore become

$$\frac{\partial\hat{C}}{\partial t} - \frac{\partial\hat{C}}{\partial x} = -\eta_B\hat{C}\exp\left(A\left(1 + \hat{T}_s\right)\right) + O(\eta_B^2), \tag{5.26a}$$

$$\frac{\partial\hat{f}}{\partial x} = \eta_B C\exp\left(A\left(1 + \hat{T}_s\right)\right) + O(\eta_B^2), \tag{5.26b}$$

$$\eta_B^2 \hat{C}\left(\frac{\partial \hat{T}_s}{\partial t} - \frac{\partial \hat{T}_s}{\partial x}\right) = \delta\eta_B^2 \frac{\partial^2 \hat{T}_s}{\partial x^2} + M\eta_B(\hat{T}_g - \eta_B(1+\eta_B\hat{T}_s)) - \gamma\eta_B\hat{C}\exp\left(A\left(1+\hat{T}_s\right)\right) + O(\eta_B^2), \tag{5.26c}$$

$$K\frac{\partial}{\partial x}(\hat{f}\hat{T}_g) = \eta_B^2(1+\eta_B\hat{T}_s)\hat{C}\exp\left(A\left(1+\hat{T}_s\right)\right) - M\eta_B(\hat{T}_g - \eta_B(1+\eta_B\hat{T}_s)) + O(\eta_B^3). \tag{5.26d}$$

We expand all dependent variables in powers of $\eta_B \ll 1$, setting

$$\begin{aligned} \hat{T}_s &= \hat{T}_s^0(x,t) + O(\eta_B), \quad \hat{C} = \hat{C}^0(x,t) + O(\eta_B), \\ \hat{T}_g &= \hat{T}_g^0(x,t) + O(\eta_B), \quad \hat{f} = \hat{f}^0(x,t) + O(\eta_B), \end{aligned} \tag{5.27}$$

At leading order we see from (5.26b) and (5.26d) that $\hat{f}^0$ and $\hat{T}_g^0$ are uniform in x. Matching at $x = s(t)$ with region BI, using the same notation as in (5.15), we find

$$\hat{f}^0 = F_s, \qquad \hat{T}_g^0 = G_s. \tag{5.28}$$

From (5.26a), $\hat{C}^0$ is conserved along characteristics travelling right-to-left through region BII. As we will see below, C is uniform to leading order over all regions to the right of this, and so by using the boundary condition at $x = 1$, and matching, we will find that $\hat{C}^0 = 1$ is constant throughout region BII. The solid heat equation (5.26c), at leading order (order η_B), reduces to

$$M\hat{T}_g^0 = \gamma\hat{C}^0\exp\left(A(1+\hat{T}_s^0)\right), \tag{5.29}$$

so that $\hat{T}_s^0$ is also uniform, and given by

$$\hat{T}_s^0 = \frac{1}{A}\log\left(\frac{MG_s}{\gamma}\right) - 1. \tag{5.30}$$

This completes the leading-order analysis in region BII. Physically, in this region all the heat transferred from the gas to the solid is used for the chemical reaction, so that the solid temperature remains uniform.

5.4.3 Region BIV

For this size of $\mu = O(\eta_B)$, there is also a second possible dominant balance on an $O(1)$ lengthscale, namely the balance of advection (term 1 in (5.3)) with the heat transfer from the gas (term 3 in (5.3)), when the chemical reaction rate is small $Q \ll \delta\eta_B$. We see that this balance occurs at the right-hand side of the domain (denoted region

BIV) since, near the boundary $x = 1$, $T_s \approx T^{\text{in}}$, and we note that $\eta_B > T^{\text{in}}$, by the assumption (5.2). In region BIV, we change variables

$$T_s = \eta_B \bar{T}_s, \tag{5.31}$$

for $\bar{T}_s < 1$, and we write the boundary value $T^{\text{in}} = \eta_B \bar{T}^{\text{in}}$, where by (5.2) $\bar{T}^{\text{in}} < 1$. For clarity of notation we also write $C = \bar{C}$, $f = \bar{f}$, and $T_g = \bar{T}_g$ in this region BIV. Then the chemical reaction rate in BIV is

$$Q = \bar{C} \exp\left(A\left(1 - \frac{1}{\eta_B \bar{T}_s}\right)\right) = \bar{C} e^A (\delta\eta_B)^{1/\bar{T}_s} \ll \delta\eta_B. \tag{5.32}$$

With this change of variables, the equations (5.1) in region BIV become

$$\frac{\partial \bar{C}}{\partial t} - \frac{\partial \bar{C}}{\partial x} = -\bar{C} e^A \delta^{(1-\bar{T}_s)/\bar{T}_s} \eta_B^{1/\bar{T}_s}, \tag{5.33a}$$

$$\frac{\partial \bar{f}}{\partial x} = \bar{C} e^A \delta^{(1-\bar{T}_s)/\bar{T}_s} \eta_B^{1/\bar{T}_s}, \tag{5.33b}$$

$$\bar{C}\left(\frac{\partial \bar{T}_s}{\partial t} - \frac{\partial \bar{T}_s}{\partial x}\right) = \delta \frac{\partial^2 \bar{T}_s}{\partial x^2} + M(\bar{T}_g - \eta_B \bar{T}_s) - \gamma \bar{C} e^A \delta^{(1-\bar{T}_s)/\bar{T}_s} \eta_B^{(1-\bar{T}_s)/\bar{T}_s}, \tag{5.33c}$$

$$K \frac{\partial}{\partial x}(\bar{f}\bar{T}_g) = \eta_B \bar{T}_s \bar{C} e^A \delta^{(1-\bar{T}_s)/\bar{T}_s} \eta_B^{1/\bar{T}_s} - M\eta_B(\bar{T}_g - \eta_B \bar{T}_s). \tag{5.33d}$$

Again we expand in powers of η_B, namely

$$\begin{aligned} \bar{T}_s &= \bar{T}_s^0(x,t) + O(\eta_B), \quad \bar{C} = \bar{C}^0(x,t) + O(\eta_B), \\ \bar{T}_g &= \bar{T}_g^0(x,t) + O(\eta_B), \quad \bar{f} = \bar{f}^0(x,t) + O(\eta_B). \end{aligned} \tag{5.34}$$

At leading order in (5.33a), (5.33b) and (5.33d), we see that $\bar{C}^0, \bar{f}^0$, and $\bar{T}_g^0$ are all uniform through region BIV. From (5.33c) we find that $\bar{T}_s^0$ satisfies

$$\bar{C}^0\left(\frac{\partial \bar{T}_s^0}{\partial t} - \frac{\partial \bar{T}_s^0}{\partial x}\right) = M\bar{T}_g^0. \tag{5.35}$$

By the method of characteristics, applying the boundary conditions at $x = 1$, we find

$$\bar{T}_s^0 = \bar{T}^{\text{in}} + \int_{\xi=0}^{1-x} \frac{M\bar{T}_g^0(t + x - 1 + \xi)}{\bar{C}^0(t + x - 1 + \xi)}\, \mathrm{d}\xi. \tag{5.36}$$

The integrand in (5.36) is positive, and so for any fixed t, $\bar{T}_s^0$ increases monotonically as x decreases from 1 into the domain. Thus in region BIV no chemical reaction occurs since the solid material is below the critical temperature η_B, and the transfer of heat from the gas to the solid has the effect of heating up the solid material.

5.4.4 Region BIII

The solution in region BIV is only valid so long as $\bar{T}_s^0 < 1$. As $\bar{T}_s^0$ approaches 1, there must be a transition region, denoted region BIII, over which the chemical reaction rate (term 5 in (5.3)) enters the dominant balance. To analyse this region we use the change of variables

$$T_s = \eta_B(1 + \eta_B \tilde{T}_s). \tag{5.37}$$

The other variables are denoted $C = \tilde{C}$, $f = \tilde{f}$, and $T_g = \tilde{T}_g$ in region BIII for clarity. Since we require all of the heat loss to the chemical reaction (term 5 in (5.3)), heat transfer from gas to solid (term 3), and advection of heat within the solid (term 1) to balance, we require an $O(\eta_B)$ lengthscale, and so make the change of variables $x = v(t) + \eta_B y$, where $y = O(1)$, and $v(t)$, to be determined, is the position of the transition layer BIII. The equations (5.1) in this region therefore become

$$\eta_B \frac{\partial \tilde{C}}{\partial t} - (\dot{v} + 1)\frac{\partial \tilde{C}}{\partial y} = -\eta_B^2 \tilde{C} \exp\left(A\left(1 + \tilde{T}_s\right)\right) + O(\eta_B^3), \tag{5.38a}$$

$$\frac{\partial \tilde{f}}{\partial y} = \eta_B^2 \tilde{C} \exp\left(A\left(1 + \tilde{T}_s\right)\right) + O(\eta_B^3), \tag{5.38b}$$

$$\begin{aligned}\tilde{C}\left(\eta_B \frac{\partial \tilde{T}_s}{\partial t} - (\dot{v} + 1)\frac{\partial \tilde{T}_s}{\partial y}\right) &= \frac{\delta}{\eta_B}\frac{\partial^2 \tilde{T}_s}{\partial y^2} + M\left(\tilde{T}_g - \eta_B(1 + \eta_B \tilde{T}_s)\right) \\ &\quad - \gamma \tilde{C} \exp\left(A\left(1 + \tilde{T}_s\right)\right) + O(\eta_B),\end{aligned} \tag{5.38c}$$

$$\begin{aligned}K\frac{\partial}{\partial y}(\tilde{f}\tilde{T}_g) &= \eta_B^3(1 + \eta_B \tilde{T}_s)\tilde{C} \exp\left(A\left(1 + \tilde{T}_s\right)\right) \\ &\quad - M\eta_B^2\left(\tilde{T}_g - \eta_B(1 + \eta_B \tilde{T})\right) + O(\eta_B^4),\end{aligned} \tag{5.38d}$$

where we use the notation $\dot{v} = \mathrm{d}v/\mathrm{d}t$. We expand all dependent variables in powers of η_B, setting

$$\begin{aligned}\tilde{T}_s &= \tilde{T}_s^0(y,t) + O(\eta_B), \quad \tilde{C} = \tilde{C}^0(y,t) + O(\eta_B), \\ \tilde{T}_g &= \tilde{T}_g^0(y,t) + O(\eta_B), \quad \tilde{f} = \tilde{f}^0(y,t) + O(\eta_B),\end{aligned} \tag{5.39}$$

and, as in regions BII and BIV, we see from (5.38a), (5.38b) and (5.38d) that $\tilde{C}^0$, $\tilde{f}^0$, and $\tilde{T}_g^0$ are all uniform through region BIII. Matching to both left (region BII) and right (region BIV), we see that throughout regions BII–BIV

$$\tilde{C}^0 = \hat{C}^0 = \bar{C}^0 = 1, \qquad \tilde{f}^0 = \hat{f}^0 = \bar{f}^0 = F_s(t), \qquad \tilde{T}_g^0 = \hat{T}_g^0 = \bar{T}_g^0 = G_s(t). \tag{5.40}$$

At leading order in region BIII, (5.38c) therefore reduces to the ODE

$$-(\dot{v} + 1)\frac{\partial \tilde{T}_s^0}{\partial y} = MG_s - \gamma \exp\left(A\left(1 + \tilde{T}_s^0\right)\right), \tag{5.41}$$

which has solution

$$\tilde{T}_s^0 = -1 - \frac{1}{A}\log\left(\frac{\gamma}{MG_s}\left(1 + B\exp\left(\frac{AMG_s}{\dot{v}+1}y\right)\right)\right). \tag{5.42}$$

The position, $v(t)$, of the transition layer, and the constant of integration, $B(t)$, must be determined by matching with the neighbouring regions. We first note that

$$\tilde{T}_s^0 \to \frac{1}{A}\log\left(\frac{MG_s}{\gamma}\right) - 1 = \hat{T}_s^0 \qquad \text{as } y \to -\infty, \tag{5.43}$$

and so the solution matches with region BII automatically, for any v and any B. Since $T_s = \eta_B(1 + \eta_B\tilde{T}_s^0)$, the leading-order matching as $y \to \infty$ with the solution (5.36) in region BIV requires

$$1 = \bar{T}_s^0\Big|_{x=v} = \bar{T}^{\text{in}} + M\int_{\xi=0}^{1-v} G_s(t+v-1+\xi)\,\mathrm{d}\xi, \tag{5.44}$$

which fixes the position $v(t)$. Since the integrand $G_s > 0$ is positive, the integral is decreasing with v, and there is therefore a unique solution, $v(t) < 1$, of (5.44), for every t. The value of B in (5.42) may be fixed by matching at higher order. We do not explicitly give this analysis, but it is similar to that in case C, detailed in Appendix B.

We notice that the position, $v(t)$, of the transition layer lies within the domain so long as $v(t) > s_0(t)$. From the equation (5.44) for $v(t)$, we see that if any of M, G_s, or $1 - s_0$ are too small, then $v(t) < s_0(t)$. In this case there is no region BII or BIII: region BIV fills the entire domain $[s_0(t), 1]$, except for the boundary layer at $x = s_0$. We see that our solution approaches the solution for case A in Section 5.3 as M becomes small, since in this case $v(t) < s_0(t)$, and so everywhere in $[s_0(t), 1]$ we must have

$$C \sim 1, \qquad f \sim F_s, \qquad T_g \sim G_s, \qquad T_s = \eta_B\bar{T}_s^0 = \eta_B(\bar{T}^{\text{in}} + O(M)) \sim T^{\text{in}}. \tag{5.45}$$

5.4.5 Composite solution

Since C, f, and T_g are uniform at leading order outside region BI, the leading-order composite solutions are simply

$$C^{\text{B}} = C^0\left(\frac{x - s_0(t)}{\delta}\right), \qquad f^{\text{B}} = f^0\left(\frac{x - s_0(t)}{\delta}\right), \qquad T_g^{\text{B}} = T_g^0\left(\frac{x - s_0(t)}{\delta}\right). \tag{5.46}$$

As in case A, we note that $T_s = O(1)$ in region BI, but is $O(\eta_B)$ in all other regions. We construct a leading-order composite solution by assuming that the $O(\eta_B)$ correction

in region BI is simply uniform, and equal to η_B, so that the composite T_s solution is accurate with $O(\eta_B)$ error in region BI, and with $O(\eta_B^2)$ error in regions BII–BIV. The solution is defined piecewise on either side of the transition layer BIII, centred at the point $x = v(t)$, where the solution is continuous by construction. We therefore use the composite solution

$$T_s^{\mathrm{B}} = \begin{cases} T_s^0\left(\frac{x-s_0(t)}{\delta}\right) + \eta_B, & \text{if } x < v(t), \\ \eta_B \bar{T}_s^0(x,t), & \text{if } x \geq v(t), \end{cases} \tag{5.47}$$

where $\bar{T}_s^0$ is given by (5.36).

Thus in case B, while $\mu = O(\eta_B)$ is non-zero and so there is some heat transfer between phases, only an $O(\eta_B)$ amount of chemical reaction occurs outside region BI, and this only if $v(t) > s_0(t)$. The primary role of the heat transferred from the gas to the solid is to heat up the solid material. While this does not affect the leading-order problem in region BI, which is the same as that in AI in case A, it reduces its accuracy: there is now an $O(\eta_B)$ "switchback" correction term in region BI, greater than the $O(T^{\mathrm{in}})$ correction in case A.

5.5 Case C: $\mu = O(1)$, moderate heat transfer

In this section we suppose $\mu = O(1)$, so that heat transfer from the gas to the solid is significant over the domain $[s(t), 1]$. As in case B, over an $O(1)$ domain we have a balance between the heat transferred gas to solid (term 3) and the heat consumed by the chemical reaction (term 5) in (5.3). Since now $\mu = O(1)$, both these terms must be $O(1)$, and the temperature scaling η, given by (5.4), is

$$\eta_C = \frac{A}{\log\left(\frac{1}{\delta}\right)}. \tag{5.48}$$

We note that $\delta \ll \eta_B < \eta_C \ll 1$. With $T_s \sim \eta_C$, the chemical reaction rate has $O(1)$ effect in the equations of mass conservation (5.1a)–(5.1b). Thus, unlike in cases A and B, we expect $O(1)$ material consumption in both the boundary layer, region CI, at $x = s(t)$, and also in an $O(1)$ region of the domain. In fact, as we will show in Section 5.6 below, the analysis for case C holds so long as $\mu \ll O(\log(\log(1/\delta)))$. A schematic of the asymptotic structure in this case is given in Figure 5.6, and the changes of variable in each region is summarised in Table 5.3.

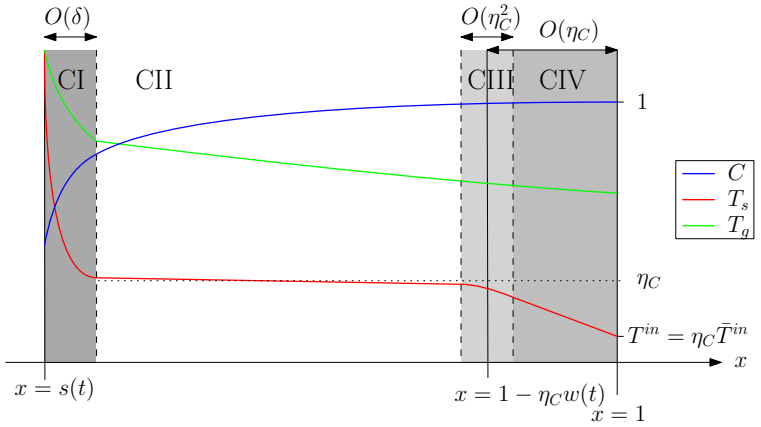

Figure 5.6: Schematic of the solution structure in case C: $\mu = O(1)$.

Region	Spatial Variable	Size of Q	Dominant terms in (5.3)	Dependent Variables
CI	$x = s(t) + \delta X$	$Q = O(1)$	1, 2, 5	C, f, T_s, T_g
CII	x	$Q = O(\delta)$	3, 5	$C = \hat{C}$, $f = \hat{F}$, $T_s = \eta(1 + \eta\hat{T}_s)$, $T_g = \hat{T}_g$
CIII	$x = 1 - \eta w(t) - \eta^2 y$	$Q = O(\delta)$	1, 3, 5	$C = \tilde{C}$, $f = \tilde{f}$, $T_s = \eta(1 + \eta\tilde{T}_s)$, $T_g = \tilde{T}_g$
CIV	$x = 1 - \eta Y$	$Q \ll \delta$	1, 3	$C = \bar{C}$, $f = \bar{f}$, $T_s = \eta\bar{T}_s$, $T_g = \bar{T}_g$

Table 5.3: Summary of the asymptotic regions of the domain, and the changes of variable in these regions, for case C: $\mu = O(1)$.

5.5.1 Region CI

As in the previous cases, there is an $O(\delta)$ conduction boundary layer (region CI) at $x = s(t)$. As before, we make the change of variables $x = s(t) + \delta X$, and expand the dependent variables in powers of η_C, by

$$\begin{aligned} T_s &= T_s^0(X,t) + \eta_C T_s^1(X,t) + O(\eta_C^2), \quad C = C^0(X,t) + \eta_C C^1(X,t) + O(\eta_C^2), \\ T_g &= T_g^0(X,t) + \eta_C T_g^1(X,t) + O(\eta_C^2), \quad f = f^0(X,t) + \eta_C f^1(X,t) + O(\eta_C^2), \\ s &= s_0(t) + \eta_C s_1(t) + O(\eta_C^2). \end{aligned} \tag{5.49}$$

We obtain the same leading-order system of equations (5.13a)–(5.13c) in region CI as in cases A and B. As $X \to \infty$, we still require $T_s^0 \to 0$ in order for the problem to be correctly specified. However, since the chemical reaction rate is $O(1)$ in the outer region, we will no longer have uniform concentration at leading order in the outer region. We must therefore impose the far-field conditions

$$T_s^0 \to 0, \qquad C^0 \to C^\infty(t) \qquad \text{as } X \to \infty, \tag{5.50}$$

where $C^\infty(t)$ is yet to be determined by matching with the outer region. Thus we can no longer solve the region CI problem independently of the rest of the domain: it is now intrinsically coupled with the outer problem, since C varies at leading order over the outer region. The leading-order gas variables within region CI are given by (5.14), but the far-field values as $X \to \infty$ are now

$$f^0 \to F_s(t) := f_* + (1 + \dot{s}_0)(C^\infty - C_*), \tag{5.51a}$$

$$T_g^0 \to G_s(t) := \frac{\frac{f_*\rho}{s_0} + K^{-1}\int_{\bar{X}=0}^{\infty} T_s^0 C^0 \exp\left(A\left(1 - \frac{1}{T_s^0}\right)\right) \mathrm{d}\bar{X}}{f_* + (1 + \dot{s}_0)(C^\infty - C_*)}. \tag{5.51b}$$

5.5.2 Region CII

Outside region CI, over an $O(1)$ lengthscale, we make the rescaling

$$T_s = \eta_C(1 + \eta_C \hat{T}_s). \tag{5.52}$$

In this region, denoted region CII, we also use the notation $C = \hat{C}$, $f = \hat{f}$, and $T_g = \hat{T}_g$ for clarity. The equations (5.1) become

$$\frac{\partial \hat{C}}{\partial t} - \frac{\partial \hat{C}}{\partial x} = -\hat{C}\exp\left(A\left(1 + \hat{T}_s\right)\right) + O(\eta_C), \tag{5.53a}$$

$$\frac{\partial \hat{f}}{\partial x} = \hat{C}\exp\left(A\left(1 + \hat{T}_s\right)\right) + O(\eta_C), \tag{5.53b}$$

$$\eta_C^2 \hat{C}\left(\frac{\partial \hat{T}_s}{\partial t} - \frac{\partial \hat{T}_s}{\partial x}\right) = \delta\eta_C^2 \frac{\partial^2 \hat{T}_s}{\partial x^2} + \mu(\hat{T}_g - \eta_C(1 + \eta_C\hat{T}_s)) - \gamma\hat{C}\exp\left(A\left(1 + \hat{T}_s\right)\right) + O(\eta_C), \tag{5.53c}$$

$$K\frac{\partial}{\partial x}(\hat{f}\hat{T}_g) = \eta_C(1 + \eta_C\hat{T}_s)\hat{C}\exp\left(A\left(1 + \hat{T}_s\right)\right) - \mu(\hat{T}_g - \eta_C(1 + \eta_C\hat{T}_s)) + O(\eta_C^2). \tag{5.53d}$$

We expand the dependent variables in powers of η_C, setting

$$\begin{aligned} \hat{T}_s &= \hat{T}_s^0(x,t) + O(\eta_C), \quad \hat{C} = \hat{C}^0(x,t) + O(\eta_C), \\ \hat{T}_g &= \hat{T}_g^0(x,t) + O(\eta_C), \quad \hat{f} = \hat{f}^0(x,t) + O(\eta_C). \end{aligned} \tag{5.54}$$

At leading order, (5.53) becomes

$$\frac{\partial \hat{C}^0}{\partial t} - \frac{\partial \hat{C}^0}{\partial x} = -\hat{C}^0\exp\left(A\left(1 + \hat{T}_s^0\right)\right), \tag{5.55a}$$

$$\frac{\partial \hat{f}^0}{\partial x} = \hat{C}^0\exp\left(A\left(1 + \hat{T}_s^0\right)\right), \tag{5.55b}$$

$$\mu\hat{T}_g^0 = \gamma\hat{C}^0\exp\left(A\left(1 + \hat{T}_s^0\right)\right), \tag{5.55c}$$

$$K\frac{\partial}{\partial x}\left(\hat{f}^0\hat{T}_g^0\right) = -\mu\hat{T}_g^0. \tag{5.55d}$$

Combining (5.55b)–(5.55d) we obtain the reduced system

$$\frac{\partial \hat{f}^0}{\partial x} = \frac{\mu}{\gamma}\hat{T}_g^0, \qquad\qquad K\frac{\partial}{\partial x}\left(\hat{f}^0\hat{T}_g^0\right) = -\mu\hat{T}_g^0, \tag{5.56a}$$

for $\hat{f}^0$ and $\hat{T}_g^0$. Physically, this system describes how the convective heat loss from the gas is all used in the endothermic chemical reaction to produce more of the gas. Matching with region CI at $x = s$, we must have

$$\hat{f}^0 = F_s(t), \qquad \hat{T}_g^0 = G_s(t), \qquad \text{at } x = s_0. \tag{5.56b}$$

Combining (5.56a), and using the boundary conditions (5.56b) we find the first integral

$$\hat{f}^0(\gamma + K\hat{T}_g^0) = F_s(\gamma + KG_s). \tag{5.57}$$

Using (5.57) to eliminate $\hat{f}^0$ from the first equation (5.56a), we obtain a separable equation for $\hat{T}_g^0$, namely

$$\frac{1}{\hat{T}_g^0(\gamma + K\hat{T}_g^0)^2}\frac{\partial \hat{T}_g^0}{\partial x} = -\frac{\mu}{\gamma K F_s(\gamma + KG_s)}. \tag{5.58}$$

Integrating, making use of (5.56b), and rearranging, we find the implicit expression

$$\log\left(\frac{K\hat{T}_g^0}{\gamma + K\hat{T}_g^0}\right) - \frac{K\hat{T}_g^0}{\gamma + K\hat{T}_g^0} = \log\left(\frac{KG_s}{\gamma + KG_s}\right) - \frac{1}{\gamma + KG_s}\left(KG_s + \frac{\mu\gamma(x - s_0)}{KF_s}\right), \tag{5.59}$$

for $\hat{T}_g^0$. We note that this equation (5.59) has the form $\omega + \log(-\omega) = c$, where

$$\omega = \frac{-K\hat{T}_g^0}{\gamma + K\hat{T}_g^0}, \tag{5.60}$$

and c, the right-hand side of (5.59), is independent of $\hat{T}_g^0$. Equivalently, ω satisfies $\omega e^{\omega} = -e^c$, which has solution $\omega = W(-e^c)$ where W is the principle branch of the Lambert W function. Thus we see that the solution $\hat{T}_g^0$ of (5.59) may be expressed as

$$\hat{T}_g^0(x,t) = -\frac{\gamma W(a_{\mathrm{C}})}{K(1 + W(a_{\mathrm{C}}))}, \tag{5.61a}$$

where $a_{\mathrm{C}} = a_{\mathrm{C}}(x,t)$ is given by

$$a_{\mathrm{C}}(x,t) = -\frac{KG_s}{\gamma + KG_s}\exp\left(-\frac{1}{\gamma + KG_s}\left(\frac{\gamma\mu}{KF_s}(x - s_0) + KG_s\right)\right), \tag{5.61b}$$

and from (5.57),

$$\hat{f}^0 = \frac{F_s(\gamma + KG_s)}{\gamma + K\hat{T}_g^0}. \tag{5.61c}$$

Given $\hat{T}_g^0$ from (5.61), the leading-order concentration $\hat{C}^0$ satisfies (5.55a), or

$$\frac{\partial \hat{C}^0}{\partial t} - \frac{\partial \hat{C}^0}{\partial x} = -\frac{\mu}{\gamma}\hat{T}_g^0. \tag{5.62a}$$

Matching with region CI at $x = s_0(t)$, we require

$$\hat{C}^0 = C^\infty(t) \qquad \text{at } x = s_0(t), \tag{5.62b}$$

and we will see below that the correct matching condition for $\hat{C}^0$ at the right side of region CII is

$$\hat{C}^0 = 1 \qquad \text{at } x = 1. \tag{5.62c}$$

By the method of characteristics, (5.62a) with (5.62c) has solution

$$\hat{C}^0(x,t) = 1 - \frac{\mu}{\gamma}\int_{\xi=0}^{1-x} \hat{T}_g^0(1-\xi, \xi + t + x - 1)\,\mathrm{d}\xi, \tag{5.63}$$

for $\hat{T}_g^0(x,t)$ given by (5.61a). Evaluating at $x = s_0(t)$, the matching condition (5.62b) becomes

$$C^\infty(t) = 1 - \frac{\mu}{\gamma}\int_{\xi=0}^{1-s_0(t)} \hat{T}_g^0(1-\xi, \xi + t + s_0(t) - 1)\,\mathrm{d}\xi. \tag{5.64}$$

Since $\hat{T}_g^0$ depends on s_0, F_s, and G_s, we see that C^∞ depends on these as well. Physically, the heat and flux of gas leaving region CI determine the rate of solid material consumption in region CII, which affects the position of the free boundary s_0 (found as part of the solution of the region CI problem), and therefore the gas temperature. The processes in regions CI and CII are thus fully coupled. However, since we have solved the region CII problem to find $C^\infty(t)$, at leading order we are left with the region CI problem (5.13a)–(5.13c) with far-field condition (5.50), with $C^\infty(t)$ given by (5.64).

Concluding the analysis in region CII, we find from (5.55c) that

$$\hat{T}_s^0 = \frac{1}{A}\log\left(\frac{\mu\hat{T}_g^0}{\gamma\hat{C}^0}\right) - 1. \tag{5.65}$$

given the forms (5.61a) of $\hat{T}_g^0$ and (5.63) of $\hat{C}^0$.

5.5.3 Region CIV

In region CII, we have $T_s = \eta_C + O(\eta_C^2)$, and so we cannot impose the boundary condition $T_s = T^{\text{in}}$ at $x = 1$ (as discussed for case B, the condition (5.2) ensures $T^{\text{in}} < \eta_C$). There must therefore be a second boundary layer at $x = 1$, within which the solid temperature adjusts from η_C to T^{in}. We denote this boundary layer region CIV. In region CIV we change variables, setting

$$T_s = \eta_C \bar{T}_s, \tag{5.66}$$

with $\bar{T}_s < 1$, so that

$$\bar{Q} := Q(C, \eta_C \bar{T}_s) = O\left(\delta^{1/\bar{T}_s}\right) \ll \delta, \tag{5.67}$$

and thus we cannot expect a dominant balance in the solid heat equation (5.1c) between the heating from the gas and heat lost to chemical reaction. Instead, we find a balance between the heating from the gas and the advection term, which fixes the lengthscale of region CIV to be $O(\eta_C)$. Within region CIV we therefore make the change of variables $x = 1 - \eta_C Y$, where $Y = O(1)$ is positive. Setting, for clarity of notation, $C = \bar{C}$, $f = \bar{f}$, and $T_g = \bar{T}_g$, we obtain the system

$$\eta_C \frac{\partial \bar{C}}{\partial t} + \frac{\partial \bar{C}}{\partial Y} = -\eta_C \delta^{-1} \bar{Q}, \tag{5.68a}$$

$$-\frac{\partial \bar{f}}{\partial Y} = \eta_C \delta^{-1} \bar{Q}, \tag{5.68b}$$

$$\eta_C \bar{C} \frac{\partial \bar{T}_s}{\partial t} + \bar{C} \frac{\partial \bar{T}_s}{\partial Y} = \delta \eta_C^{-1} \frac{\partial^2 \bar{T}_s}{\partial Y^2} + \mu(\bar{T}_g - \eta_C \bar{T}_s) - \gamma \delta^{-1} \bar{Q}, \tag{5.68c}$$

$$-K \frac{\partial}{\partial Y}(\bar{f} \bar{T}_g) = \eta_C \delta^{-1} \bar{T}_s \bar{Q} - \eta_C \mu(\bar{T}_g - \eta_C \bar{T}_s). \tag{5.68d}$$

We also rewrite the input temperature $T^{\text{in}} = \eta_C \bar{T}^{\text{in}}$, so that the boundary condition becomes

$$\bar{T}_s = \bar{T}^{\text{in}} \quad \text{at } Y = 0. \tag{5.69}$$

Again, we expand in powers of η_C, setting

$$\begin{aligned} \bar{T}_s &= \bar{T}_s^0(Y,t) + O(\eta_C), \quad \bar{C} = \bar{C}^0(Y,t) + O(\eta_C), \\ \bar{T}_g &= \bar{T}_g^0(Y,t) + O(\eta_C), \quad \bar{f} = \bar{f}^0(Y,t) + O(\eta_C). \end{aligned} \tag{5.70}$$

At leading order in (5.68a), (5.68b), and (5.68d), we see that all of $\bar{C}^0$, $\bar{f}^0$, and $\bar{T}_g^0$ are uniform across region CIV. The boundary condition at $Y = 0$ (or $x = 1$) fixes

$\bar{C}^0 = 1$, while $\bar{f}^0$ and $\bar{T}_g^0$ must be fixed by matching to the left. At leading order in (5.68c), the solid temperature $\bar{T}_s^0$ satisfies

$$\frac{\partial \bar{T}_s^0}{\partial Y} = \mu \bar{T}_g^0, \tag{5.71}$$

and thus, using the boundary condition (5.69), we find that $\bar{T}_s^0$ is linear in Y:

$$\bar{T}_s^0 = \bar{T}^{\text{in}} + \mu \bar{T}_g^0 Y. \tag{5.72}$$

5.5.4 Region CIII

The solution (5.72) in region CIV is valid only while $\bar{T}_s^0 < 1$, and we cannot directly match the linear profile (5.72) with the constant $T_s \sim \eta_C$ in region CII. Thus, as in case B, we introduce a transition layer, region CIII, between regions CII and CIV. In this transition layer, we must have $T_s \approx \eta_C$, and we expect a balance between all three of the heat advection (term 1), heat transfer from the gas (term 3), and heat loss to the chemical reaction (term 5) in (5.3). We accordingly make the change of variables $Y = w(t) + \eta_C y$, where $y = O(1)$ is the scaled space variable, and $w(t) = O(1)$, to be determined, is the position of the transition layer CIII within the boundary layer CIV. We also rescale the solid temperature, setting

$$T_s = \eta_C (1 + \eta_C \tilde{T}_s), \tag{5.73}$$

and write $C = \tilde{C}$, $f = \tilde{f}$, and $T_g = \tilde{T}_g$ for clarity. The equations (5.1) therefore become, in region CIII,

$$\eta_C^2 \frac{\partial \tilde{C}}{\partial t} + (1 - \eta_C \dot{w}) \frac{\partial \tilde{C}}{\partial y} = -\eta_C^2 \tilde{C} \exp\Big(A(1 + \tilde{T}_s)\Big) + O(\eta_C^3), \tag{5.74a}$$

$$-\frac{\partial \tilde{f}}{\partial y} = \eta_C^2 \tilde{C} \exp\Big(A(1 + \tilde{T}_s)\Big) + O(\eta_C^3), \tag{5.74b}$$

$$\eta_C^2 \tilde{C} \frac{\partial \tilde{T}_s}{\partial t} + \tilde{C}(1 - \eta_C \dot{w}) \frac{\partial \tilde{T}_s}{\partial y} = \delta \frac{\partial^2 \tilde{T}_s}{\partial y^2} + \mu(\tilde{T}_g - \eta_C(1 + \eta_C \tilde{T}_s) - \gamma \tilde{C} \exp\Big(A(1 + \tilde{T}_s)\Big) + O(\eta_C), \tag{5.74c}$$

$$-K \frac{\partial}{\partial y}(\tilde{f} \tilde{T}_g) = \eta_C^2 \tilde{C} \exp\Big(A(1 + \tilde{T}_s)\Big) - \eta_C^2 \mu(\tilde{T}_g - \eta_C(1 + \eta_C \tilde{T}_s)) + O(\eta_C^3). \tag{5.74d}$$

We expand all dependent variables in powers of η_C, setting

$$\begin{aligned} \tilde{T}_s &= \tilde{T}_s^0(y,t) + O(\eta_C), \quad \tilde{C} = \tilde{C}^0(y,t) + O(\eta_C), \\ \tilde{T}_g &= \tilde{T}_g^0(y,t) + O(\eta_C), \quad \tilde{f} = \tilde{f}^0(y,t) + O(\eta_C). \end{aligned} \tag{5.75}$$

We find from (5.74a), (5.74b), and (5.74d) that, as in region CIV, all of $\tilde{C}^0$, $\tilde{f}^0$, and $\tilde{T}_g^0$ are uniform over region CIII. Thus, matching across regions CII–CIV, we see that

$$\hat{C}^0|_{x=1} = \tilde{C}^0 = \bar{C}^0 = 1, \quad F_1(t) := \hat{f}^0|_{x=1} = \tilde{f}^0 = \bar{f}^0, \quad G_1(t) := \hat{T}_g^0|_{x=1} = \tilde{T}_g^0 = \bar{T}_g^0. \tag{5.76}$$

This fixes the boundary condition for $\hat{C}^0$, (5.62c) in region CII. From (5.74c), the solid temperature variation $\tilde{T}_s^0$ therefore satisfies

$$\frac{\partial \tilde{T}_s^0}{\partial y} = \mu G_1 - \gamma \exp\left(A(1+\tilde{T}_s^0)\right), \tag{5.77}$$

which has the general solution

$$\tilde{T}_s^0 = -\frac{1}{A}\log\left(\frac{\gamma}{\mu G_1}\left(1 + De^{-\mu G_1 A y}\right)\right) - 1, \tag{5.78}$$

for constant of integration $D(t)$. Similarly to case B in Section 5.4, the values of D and w must be fixed by matching with regions CII and CIV. As $y \to \infty$ we see from (5.65) that for any w and D,

$$\tilde{T}_s^0 \to \frac{1}{A}\log\left(\frac{\mu G_1}{\gamma}\right) - 1 = \hat{T}_s^0\big|_{x=1}, \tag{5.79}$$

and so the matching CII–CIII holds automatically. The position $w(t)$ of the transition layer is found by matching T_s across regions CIII–CIV, which, at leading order, requires

$$1 = \bar{T}^{\text{in}} + \mu G_1 w, \tag{5.80}$$

and so

$$w(t) = \frac{1}{\mu G_1(t)}(1 - \bar{T}^{\text{in}}). \tag{5.81}$$

The constant D in (5.78) is fixed by matching at $O(\eta_C)$ between regions CIII–CIV, which requires the $O(\eta_C)$ correction in all regions CI, CII, CIII and CIV, and is presented in Appendix B.

5.5.5 Composite solution

As in previous cases, we may construct a leading-order composite solution. Since C, f, and T_g are $O(1)$ in all regions, and uniform in regions CIII and CIV, the composite solutions are

$$C^{\text{C}} = C^0\left(\frac{x - s_0(t)}{\delta}\right) + \hat{C}^0(x,t) - C^\infty(t), \tag{5.82}$$

$$f^{\text{C}} = f^0\left(\frac{x - s_0(t)}{\delta}\right) + \hat{f}^0(x,t) - F_s(t), \tag{5.83}$$

$$T_g^{\mathrm{C}} = T_g^0\left(\frac{x - s_0(t)}{\delta}\right) + \hat{T}_g^0(x,t) - G_s(t). \tag{5.84}$$

The solid temperature is $O(1)$ in region CI but $O(\eta_C)$ elsewhere. We therefore construct a composite solution by setting the $O(\eta_C)$ correction in region CI to be simply η_C, so that the composite solution is accurate at leading order in all regions. As in case B, the composite solution for T_s is defined piecewise about the centre, $1-\eta_C w(t)$, of the transition layer CIII. Thus we use the composite solution

$$T_s^{\mathrm{C}} = \begin{cases} T_s^0\left(\frac{x-s_0(t)}{\delta}\right) + \eta_C, & \text{if } x < 1 - \eta_C w(t), \\ \eta_C \bar{T}_s^0\left(\frac{1-x}{\eta_C}\right), & \text{if } x \geq 1 - \eta_C w(t). \end{cases} \tag{5.85}$$

We have seen that case C is very similar to case B. In each, the solid is heated up from its input temperature T^{in} by heat transferred from the gas in region IV. Once it has reached the critical temperature η the chemical reaction then starts to take place, and the heat transferred from the gas to the solid in this region (II) is used primarily for the reaction, with no change in the solid temperature at leading order until it reaches the hot boundary layer (I) at $x = s$. The differences in case C are that, since the convective heat transfer from the gas is now greater, the solid material heats up much faster (over the $O(\eta_C)$ lengthscale of region CIV, rather than the $O(1)$ lengthscale of BIV), and that the reaction rate in region CII is now high enough to affect all of the solid concentration C, gas mass flux f, and gas temperature T_g at leading order. As we increase μ still further, the gas temperature must lose so much heat to the solid that it ceases to be $O(1)$. This is the situation considered in case D below.

5.6 Case D: $-\log(\eta) \ll \mu \ll \delta^{-1}e^{-A}$, large heat transfer

The analysis in case C above, with $\mu = O(1)$, holds so long as T_g remains $O(1)$ over the entirety of the domain. From the form (5.61) of $\hat{T}_g$ in region CII, we see that for large enough μ, $\hat{T}_g$ will decay quickly enough to become $O(\eta)$ within the domain, at which point the equations (5.55) of region II are no longer valid.

In this section we study the case $\mu \gg 1$ when this occurs. Since $\mu \gg 1$, the heat transfer between phases is fast enough that the two temperatures T_s and T_g become near equal over a short lengthscale. We find that the lengthscale over which the temperatures equilibrate in this way is $O(-\log(\eta)/\mu)$. In this section, we therefore restrict our attention to the case where μ is sufficiently large, $\mu \gg -\log(\eta) \gg$

Region	Spatial Variable	Size of Q	Dominant terms in (5.3)	Dependent Variables
DI	$x = s + \delta X$	$Q = O(1)$	1, 2, 5	C, f, T_s, T_g
DII & DII'	$x = s + y/\mu$	$Q = O(\delta\mu)$,	3, 5	$C = \hat{C}$, $f = \hat{f}$, $T_s = \eta_D(1 + \eta_D\hat{T}_s)$, $T_g = \hat{T}_g$
DIII & DIII'	$x = x_1 + z/\mu$	$Q = O(\delta\mu\eta_D)$	3, 4, 5	$C = \mathcal{C}$, $f = \mathcal{F}$, $T_g = \eta_D\mathcal{T}_g$ $T_s = \eta_D(1 + \eta_D \log(\eta_D)/A + \eta_D\mathcal{T}_s)$,
DaIV	$x = x_c + \eta_D Y/\mu$	$Q = O(\delta\mu\eta_D)$	1, 3, 4, 5	$C = \tilde{C}$, $f = \tilde{f}$, $T_g = \eta_D\tilde{T}_g$, $T_s = \eta_D(1 + \eta_D \log(\eta_D)/A + \eta_D\tilde{T}_s)$,
DaV	$x = x_c + Z/\mu$ $(Z > 0)$	$Q \ll \delta\mu\eta_D$	1, 3, 4	$C = \bar{C}$, $f = \bar{f}$, $T_s = \eta_D\bar{T}_s$, $T_g = \eta_D\bar{T}_g$
DaV'	x	$Q \ll \delta\mu\eta_D$	1	-
DbIV	$x = x_2 + Z/\mu$	$Q = O(\delta\mu\eta_D^2)$	1, 3, 4, 5	$C = \tilde{C}$, $f = \tilde{f}$, $T_g = \eta_D(1 + 2\eta_D \log(\eta_D)/A + \eta_D\tau_g)$, $T_s = \eta_D(1 + 2\eta_D \log(\eta_D)/A + \eta_D\tau_s)$,
DbV	x	$Q \ll \delta\mu\eta_D^2$	1	-
DbVI	$x = 1 + Z/\mu$	$Q \ll \delta\mu\eta_D^2$	1, 3, 4	$C = \bar{C}$, $f = \bar{f}$, $T_s = \eta_D\bar{T}_s$, $T_g = \eta_D\bar{T}_g$

Table 5.4: Summary of the asymptotic regions of the domain, and the changes of variable in these regions, for the steady-state cases D (a and b): $-\log(\eta_D) \ll \mu \ll \delta^{-1}$.

1, that the two temperatures equilibrate over a lengthscale smaller than $O(1)$, i.e. within the domain $x \in [s, 1]$. With $\mu \gg 1$, the solid temperature scaling (5.4), is denoted η_D, and we note $\eta_D > \eta_C > \eta_B$. We also require that $\mu \ll \delta^{-1}e^{-A}$, so that $\eta_D \ll 1$. This ensures that the asymptotic expansion in powers of η_D remains valid. Although not strictly a distinguished limit of the problem, it is interesting to study this regime $-\log(\eta_D) \ll \mu \ll \delta^{-1}e^{-A}$ — which we may equivalently express as $\log(\log(1/\delta)) \ll \mu \ll \delta^{-1}e^{-A}$ — in order to understand how the solution structure evolves as μ increases from $O(1)$ in case C to the distinguished limit $\mu = O(\delta^{-1})$, which we study in Case E below.

We note that we do not study the case $1 \ll \mu \ll -\log(\eta_D)$, since this limit has the same structure as case C, as we will show below. We also do not deal fully with the distinguished limit $\mu = O(-\log(\eta_D))$, since there are a plethora of subcases for the asymptotic structure in this case, depending on whether the two temperatures equilibrate over the domain or not, and how close the point at which they equilibrate is to the boundary $x = 1$ of the domain. We discuss some of these possible subcases in more detail in the discussion below.

For simplicity, we look for steady-state solutions only in this section. We find

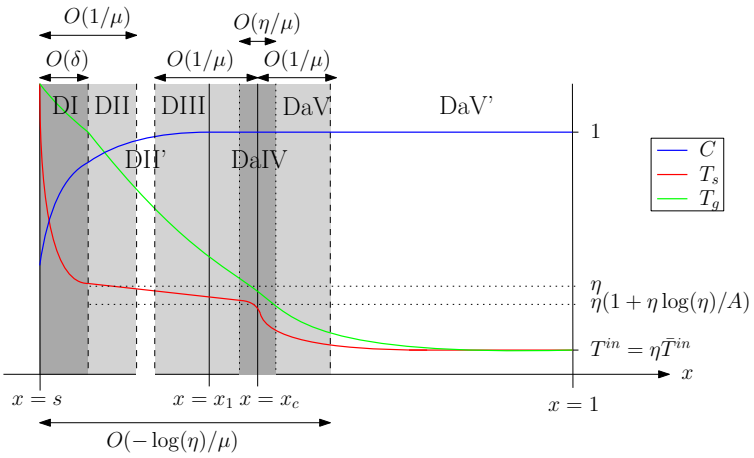

(a) Case Da, $KF_* < 1$

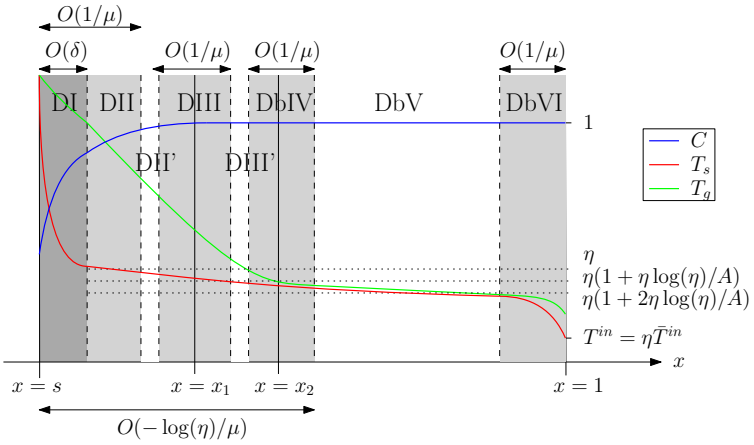

(b) Case Db, $KF_* > 1$

Figure 5.7: Schematics of the steady-state solution structures in case D: $\mu = O(1)$.

that there are two separate steady-state behaviours in the regime $-\log(\eta_D) \ll \mu \ll \delta^{-1}e^{-A}$, depending on the model parameters. Specifically, in case Da we suppose $Kf < 1$ near $x = 1$, so that the heat flux in the gas is smaller in magnitude than the heat flux in the solid in the opposite direction. In case Db we consider the opposite case, in which $Kf > 1$ near $x = 1$. The schematics illustrating the solution structure in these two steady-state cases Da and Db are shown in Figure 5.7, and the changes of variable for each region are summarised in Table 5.4.

5.6.1 Behaviour common to cases Da and Db

There are several regions of the domain near to the free boundary $x = s$ where the behaviour is the same for both cases Da and Db.

5.6.1.1 Region DI

As usual we find a boundary layer, region DI, of width $O(\delta)$ at $x = s$. Expanding the dependent variables in powers of η_D, by setting

$$\begin{aligned} T_s &= T_s^0(X) + \eta_D T_s^1(X) + O(\eta_D^2), \quad C = C^0(X) + \eta_D C^1(X) + O(\eta_D^2), \\ T_g &= T_g^0(X) + \eta_D T_g^1(X) + O(\eta_D^2), \quad f = f^0(X) + \eta_D f^1(X) + O(\eta_D^2), \\ s &= s_0 + \eta_D s_1 + O(\eta_D^2), \end{aligned} \tag{5.86}$$

we obtain the same equations (5.13a)–(5.13c) at leading order since $\mu \ll \delta^{-1}$ (although with $\dot{s}_0 = 0$, since we restrict to steady state). The far-field solid concentration must satisfy (5.50) as in case C, where C^∞ is yet to be determined by matching with the outer problem.

5.6.1.2 Region DII

Outside region DI, we require $T_s \sim \eta_D$, in order to balance the terms 3 and 5 in the solid heat equation (5.3). However, since then $Q = O(\mu) \gg 1$, this region, which we denote region DII, must have a shorter lengthscale than $O(1)$ in order to obtain a balance in the gas temperature equation. Region DII is therefore a second, wider boundary layer, width $O(\mu^{-1})$, about $x = s_0$, and so we make the change of variables $x = s_0 + y/\mu$. We look for a solution

$$T_s = \eta_D(1 + \eta_D \hat{T}_s), \tag{5.87}$$

and we also use the notation $C = \hat{C}$, $f = \hat{f}$, and $T_g = \hat{T}_g$ in region DII for clarity. The equations (5.1) in region DII then become

$$-\frac{\mathrm{d}\hat{C}}{\mathrm{d}y} = -\hat{C}\exp\left(A\left(1 + \hat{T}_s\right)\right) + O(\eta_D), \tag{5.88a}$$

$$\frac{\mathrm{d}\hat{f}}{\mathrm{d}y} = \hat{C}\exp\left(A\left(1 + \hat{T}_s\right)\right) + O(\eta_D), \tag{5.88b}$$

$$-\eta_D^2 \hat{C}\frac{\mathrm{d}\hat{T}_s}{\mathrm{d}y} = \delta\eta_D^2\mu\frac{\mathrm{d}^2\hat{T}_s}{\mathrm{d}y^2} + \hat{T}_g - \gamma\hat{C}\exp\left(A\left(1 + \hat{T}_s\right)\right) + O(\eta_D), \tag{5.88c}$$

$$K\frac{\mathrm{d}}{\mathrm{d}y}(\hat{f}\hat{T}_g) = \eta_D(1 + \eta_D\hat{T}_s)\hat{C}\exp\left(A\left(1 + \hat{T}_s\right)\right) - \hat{T}_g + O(\eta_D^2). \tag{5.88d}$$

We expand in powers of $\eta_D \ll 1$, setting

$$\begin{aligned} \hat{T}_s &= \hat{T}_s^0(y) + O(\eta_D), \quad \hat{C} = \hat{C}^0(y) + O(\eta_D), \\ \hat{T}_g &= \hat{T}_g^0(y) + O(\eta_D), \quad \hat{f} = \hat{f}^0(y) + O(\eta_D). \end{aligned} \tag{5.89}$$

Substituting into (5.88), we find that at leading order

$$-\frac{\mathrm{d}\hat{C}^0}{\mathrm{d}y} = -\hat{C}^0 \exp\left(A\left(1+\hat{T}_s^0\right)\right), \tag{5.90a}$$

$$\frac{\mathrm{d}\hat{f}^0}{\mathrm{d}y} = \hat{C}^0 \exp\left(A\left(1+\hat{T}_s^0\right)\right), \tag{5.90b}$$

$$\hat{T}_g^0 = \gamma\hat{C}^0 \exp\left(A\left(1+\hat{T}_s^0\right)\right), \tag{5.90c}$$

$$K\frac{\mathrm{d}}{\mathrm{d}y}(\hat{f}^0\hat{T}_g^0) = -\hat{T}_g^0. \tag{5.90d}$$

Precisely as in (5.61) for region CII of case C, we find the solutions

$$\hat{T}_g^0 = -\frac{\gamma W(a_\mathrm{D})}{K(1+W(a_\mathrm{D}))}, \qquad \hat{f}^0 = \frac{F_s(\gamma+KG_s)}{\gamma+K\hat{T}_g^0}, \tag{5.91}$$

of equations (5.90b) and (5.90d), where

$$a_\mathrm{D} = -\frac{KG_s}{\gamma+KG_s}\exp\left(-\frac{1}{\gamma+KG_s}\left(\frac{\gamma}{KF_s}y+KG_s\right)\right), \tag{5.92}$$

and the matching constants F_s and G_s are as defined in (5.51) (with $\dot{s}_0 = 0$, since we are in steady state). The leading-order solid concentration satisfies (5.90a), which therefore becomes

$$-\frac{\mathrm{d}\hat{C}^0}{\mathrm{d}y} = \frac{W(a_\mathrm{D})}{K(1+W(a_\mathrm{D}))}, \tag{5.93}$$

along with $\hat{C}^0 = C^\infty$ at $y = 0$, and a matching condition to the right, as y becomes large. We will find below that C is uniform to leading order in all regions to the right of region DII, in both cases Da and Db. Thus the matching condition is

$$\hat{C}^0 \to 1 \qquad \text{as } y \to \infty. \tag{5.94}$$

From (5.91) we see that $\hat{T}_g^0 \to 0$ as $y \to \infty$, and so the solution of (5.93) is

$$\hat{C}^0 = 1 - \frac{KF_s(\gamma+KG_s)\hat{T}_g^0}{\gamma(\gamma+K\hat{T}_g^0)}. \tag{5.95}$$

Applying the boundary conditions at $y = 0$, where $\hat{T}_g^0 = G_s$, we therefore fix the value of C^∞ to be

$$C^\infty = 1 - \frac{KF_sG_s}{\gamma}. \tag{5.96}$$

Having found $\hat{C}^0$, the solid temperature variation, given by (5.90c), is then

$$\begin{aligned}\hat{T}_s^0 &= \frac{1}{A}\log\left(\frac{\hat{T}_g^0}{\gamma\hat{C}^0}\right) - 1 \\ &= -1 - \frac{1}{A}\log\left(K\big(1+W(a_\mathrm{D})\big)\left(\frac{1}{-W(a_\mathrm{D})} - \frac{F_s(\gamma+KG_s)}{\gamma}\right)\right).\end{aligned} \tag{5.97}$$

We note that this region DII is exactly analogous to region CII in case C with $\mu = O(1)$, except that since μ is now larger, the decay length of $\hat{T}_g^0$ is shorter. We see that the equations (5.90) hold until $\hat{T}_g^0$ becomes order η_D, at which point term 4 must enter the dominant balance of equation (5.3). Since for small a_D, $W(a_\mathrm{D}) \sim a_\mathrm{D}$, we see that $\hat{T}_g^0 \sim \eta_D$ when $-\gamma a_\mathrm{D}/K = \eta_D$, which occurs at the point $y = y_*$, defined by $\gamma a_\mathrm{D}(y_*)/K = \eta_D$. Rearranging, this gives

$$y_* = \frac{1}{\gamma} K F_s(\gamma + K G_s) \left(-\log(\eta_D) + \log\left(\frac{\gamma G_s}{\gamma + K G_s}\right) - \frac{K G_s}{\gamma + K G_s} \right). \tag{5.98}$$

We see that the point $y_* = O(-\log(\eta_D))$ is large. As y becomes larger than $O(1)$, we strictly leave region DII, and enter region DII', an extension of DII, within which the lengthscale is $O(-\log(\eta_D)/\mu)$. The dominant physical processes in region DII' are the same as in region DII, except that f is uniform at leading order, and thus T_g is exponentially decaying.

In the original variables, the point y_* is at $x_1 := s_0 + y_*/\mu$. As mentioned at the start of this section, we notice that if $1 \ll \mu \ll -\log(\eta_D)$ then $x_1 - s_0 \gg 1$ and so we revert to a structure like case C, since $\hat{T}_g$ remains $O(1)$ throughout the domain. Conversely, in the regime $-\log(\eta_D) \ll \mu$ studied in this section, we have $x_1 - s_0 \ll 1$ and so $\hat{T}_g^0$ becomes small within the domain. In the distinguished limit $\mu = O(-\log(\eta_D))$, we see that $x_1 - s_0 = O(1)$, and we may be in either of these cases, or instead have x_1 close to 1, for which a number of additional subcases arise.

5.6.1.3 Region DIII

With $\mu \gg -\log(\eta_D)$, the point x_1 is an $O(-\log(\eta_D)/\mu) \ll 1$ distance from s_0 (and so is definitely contained within the domain). Around this point x_1, there must be an $O(\mu^{-1})$ transition layer, denoted region DIII, in which term 4 enters the dominant balance in (5.3). In this region we use the change of spatial variables $x = x_1 + z/\mu$. Since now $T_g = O(\eta_D)$, the balance of terms 3 and 5 requires that term 5, the chemical reaction rate, be $O(\delta\mu\eta_D)$. Thus, the solid temperature must be of the form

$$T_s = \eta_D \left(1 + \frac{\eta_D \log(\eta_D)}{A} + \eta_D \mathcal{T}_s \right). \tag{5.99}$$

We also use the change of variables $T_g = \eta_D \mathcal{T}_g$ in region DIII, and set $f = \mathcal{F}$, $C = \mathcal{C}$ for clarity of notation. Substituting into (5.1), the resulting steady-state equations in region DIII are

$$-\frac{\mathrm{d}\mathcal{C}}{\mathrm{d}z} = -\eta_D \mathcal{C} \exp\left(A\left(1 + \mathcal{T}_s\right)\right) + O(\eta_D^2), \tag{5.100a}$$

$$\frac{\mathrm{d}\mathcal{F}}{\mathrm{d}z} = \eta_D \mathcal{C} \exp\left(A\left(1 + \mathcal{T}_s\right)\right) + O(\eta_D^2), \tag{5.100b}$$

$$-\eta_D \mathcal{C}\frac{\mathrm{d}\mathcal{T}_s}{\mathrm{d}z} = \delta\eta_D\mu\frac{\mathrm{d}^2\mathcal{T}_s}{\mathrm{d}z^2} + \mathcal{T}_g - \left(1+\eta_D\left(\frac{\log(\eta_D)}{A}+\mathcal{T}_s\right)\right) - \gamma\mathcal{C}\exp\left(A\left(1+\mathcal{T}_s\right)\right) + O(\eta_D), \tag{5.100c}$$

$$K\frac{\mathrm{d}}{\mathrm{d}z}(\mathcal{F}\mathcal{T}_g) = \eta_D\left(1+\eta_D\left(\frac{\log(\eta_D)}{A}+\mathcal{T}_s\right)\right)\mathcal{C}\exp\left(A\left(1+\mathcal{T}_s\right)\right) - \mathcal{T}_g + \left(1+\eta_D\left(\frac{\log(\eta_D)}{A}+\mathcal{T}_s\right)\right) + O(\eta_D^2). \tag{5.100d}$$

We expand in powers of η_D, setting

$$\begin{aligned} \mathcal{T}_s &= \mathcal{T}_s^0(z) + O(\eta_D), \quad \mathcal{C} = \mathcal{C}^0(z) + O(\eta_D), \\ \mathcal{T}_g &= \mathcal{T}_g^0(z) + O(\eta_D), \quad \mathcal{F} = \mathcal{F}^0(z) + O(\eta_D). \end{aligned} \tag{5.101}$$

At leading order in (5.100a) and (5.100b), we find that both $\mathcal{C}^0$ and $\mathcal{F}^0$ are uniform in region DIII. This is because the chemical reaction rate is now $Q = O(\delta\eta_D\mu)$, and so there is only an $O(\eta_D)$ mass consumption over region DIII. Indeed, we will find that in all regions to the right of region DIII (in either case Da or Db), C and f are uniform up to $O(\eta_D)$. Thus by matching to the right we will find that $\mathcal{C}^0 = 1$, and matching at leading order with region DII, we have

$$\mathcal{F}^0 = F_* := \frac{F_s(\gamma + KG_s)}{\gamma} = \hat{f}^0|_{y=y_*} + O(\eta_D). \tag{5.102}$$

At leading order, the remaining equations (5.100c) and (5.100d) for $\mathcal{T}_s^0$ and $\mathcal{T}_g^0$ become

$$\mathcal{T}_g^0 - \left(1+\eta_D\frac{\log(\eta_D)}{A}\right) = \gamma\exp\left(A\left(1+\mathcal{T}_s^0\right)\right), \tag{5.103}$$

$$KF_*\frac{\mathrm{d}\mathcal{T}_g^0}{\mathrm{d}z} = -\mathcal{T}_g^0 + \left(1+\eta_D\frac{\log(\eta_D)}{A}\right). \tag{5.104}$$

Here we have included the $O(-\eta_D\log(\eta_D))$ terms, since these are larger than the next order η_D, and we can find an explicit solution taking both $O(1)$ and $O(-\eta_D\log(\eta_D))$ terms into account together. The ODE (5.104) for $\mathcal{T}_g^0$ has the general solution

$$\mathcal{T}_g^0 = 1 + \eta_D\frac{\log(\eta_D)}{A} + c\exp\left(-\frac{1}{KF_*}z\right). \tag{5.105}$$

The constant of integration, c, must be fixed by matching with region DII. To do this, we use the intermediate variable $\bar{y}$, with $y = y_* - (-\log(\eta_D))^\beta\bar{y}$ in region DII, and $z = -(-\log(\eta_D))^\beta\bar{y}$ in region DIII, with $\beta \in (0,1)$ and $\bar{y} > 0$. Near $y = y_*$, a_D

is small, and so in region DII we find that T_g is approximated by

$$\begin{aligned} T_g \sim \hat{T}_g^0 &\sim -\frac{\gamma}{K} a_{\mathrm{D}} \\ &= \frac{\gamma G_s}{\gamma + KG_s} \exp\left(-\frac{1}{\gamma + KG_s} \left(\frac{\gamma}{KF_s} y_* + KG_s \right) \right) \\ &\qquad \times \exp\left(\frac{\gamma}{KF_s(\gamma + KG_s)} (-\log(\eta_D))^\beta \bar{y} \right) \\ &= \eta_D \exp\left(\frac{\gamma}{KF_s(\gamma + KG_s)} (-\log(\eta_D))^\beta \bar{y} \right), \end{aligned} \tag{5.106}$$

by the definition of y_* in (5.98). Meanwhile, in region DIII we have

$$\begin{aligned} T_g \sim \eta_D \mathcal{T}_g^0 &= \eta_D c \exp\left(\frac{1}{KF_*} (-\log(\eta_D))^\beta \bar{y} \right) + \eta_D \left(1 + \eta_D \frac{\log(\eta_D)}{A} \right) \\ &= \eta_D c \exp\left(\frac{\gamma}{KF_s(\gamma + KG_s)} (-\log(\eta_D))^\beta \bar{y} \right) + \eta_D \left(1 + \eta_D \frac{\log(\eta_D)}{A} \right), \end{aligned} \tag{5.107}$$

by the definition of F_* in (5.102). Since $\beta > 0$, the constant $O(\eta_D)$ term is small relative to the exponential. Matching the leading-order terms in these expansions we see that $c = 1$.

Finally, from (5.103) we compute

$$\mathcal{T}_s^0 = -\frac{1}{A} \left(\log(\gamma) + \frac{1}{KF_*} z \right) - 1, \tag{5.108}$$

completing the analysis in region DIII.

5.6.1.4 Region DaV and DbVI

Regions DI–DIII as described above are common to both cases Da and Db. We now pause in our analysis moving left to right through the domain, and instead investigate the behaviour near the $x = 1$ boundary. We will find different behaviour for the cases Da and Db, depending on whether the overall heat flux $Kf - 1 = KF_* - 1 + O(\eta_D)$ is negative or positive, respectively.

On the right side of the domain, the solid temperature must decrease from close to η_D at the left of the domain to the input value $T^{\mathrm{in}} = \eta_D \bar{T}^{\mathrm{in}}$. We therefore rescale

$$T_s = \eta_D \bar{T}_s \qquad \text{and} \qquad T_g = \eta_D \bar{T}_g, \tag{5.109}$$

noting that T_g must be $O(\eta_D)$ in this region too because it is $O(\eta_D)$ in region DIII, and can only decrease through the rest of the domain. With $\bar{T}_s < 1 + \eta_D \log(\eta_D)/A$,

we notice that the chemical reaction rate $\bar{Q} \ll \delta\mu\eta_D$ is small. We set $f = \bar{f}$ and $C = \bar{C}$ in this region for clarity of notation. In order to balance the heat advection with heat transfer between phases in the gas heat equation, we must scale the space variable to an $O(1/\mu)$ domain. Thus the region over which T_s changes must be a boundary layer. We make the change of variables $x = x_c + Z/\mu$, where $Z = O(1)$, and x_c (the position of this boundary layer) is an order 1 point in the domain, to be determined. With these changes of variable, the equations (5.1) become

$$-\frac{\mathrm{d}\bar{C}}{\mathrm{d}Z} = -(\delta\mu)^{-1}\bar{Q}, \tag{5.110a}$$

$$\frac{\mathrm{d}\bar{f}}{\mathrm{d}Z} = (\delta\mu)^{-1}\bar{Q}, \tag{5.110b}$$

$$-\bar{C}\frac{\mathrm{d}\bar{T}_s}{\mathrm{d}Z} = \delta\mu\frac{\mathrm{d}^2\bar{T}_s}{\mathrm{d}Z^2} + \bar{T}_g - \bar{T}_s - \gamma(\delta\eta_D\mu)^{-1}\bar{Q}, \tag{5.110c}$$

$$K\frac{\mathrm{d}}{\mathrm{d}Z}(\bar{f}\bar{T}_g) = (\delta\mu)^{-1}\bar{T}_s\bar{Q} - (\bar{T}_g - \bar{T}_s). \tag{5.110d}$$

We expand in powers of η_D, by setting

$$\begin{aligned} \bar{T}_s &= \bar{T}_s^0(Z) + O(\eta_D), \quad \bar{C} = \bar{C}^0(Z) + O(\eta_D), \\ \bar{T}_g &= \bar{T}_g^0(Z) + O(\eta_D), \quad \bar{f} = \bar{f}^0(Z) + O(\eta_D). \end{aligned} \tag{5.111}$$

Since $\bar{Q} \ll \delta\mu\eta_D$, we see from (5.110a) and (5.110b) that $\bar{C}^0 = 1$ and $\bar{f}^0 = F_*$ are uniform over this region at leading order, fixed by matching with regions to the right and left, respectively. At leading order (5.110c) and (5.110d) therefore become

$$-\frac{\mathrm{d}\bar{T}_s^0}{\mathrm{d}Z} = \bar{T}_g^0 - \bar{T}_s^0, \qquad KF_*\frac{\mathrm{d}\bar{T}_g^0}{\mathrm{d}Z} = -\bar{T}_g^0 + \bar{T}_s^0, \tag{5.112}$$

and these admit a general solution

$$\bar{T}_s^0 = b_1 + KF_*b_2\exp\left(\frac{KF_* - 1}{KF_*}Z\right), \quad \bar{T}_g^0 = b_1 + b_2\exp\left(\frac{KF_* - 1}{KF_*}Z\right), \tag{5.113}$$

where b_1 and b_2 are constants to be determined. We notice that the position of the boundary layer, x_c, must depend on the sign of $KF_* - 1$, and we consider the cases Da ($KF_* < 1$) and Db ($KF_* > 1$) separately below. In case Da with $KF_* < 1$, we find that this boundary layer must be at the left side of the domain (region DaV), whereas in case Db with $KF_* > 1$, we must take $x_c = 1$ so that the boundary layer is region DbVI, on the right side of the domain. From the nondimensionalisation, we see that

$$KF_* < 1 \qquad \text{if} \qquad c_{p,g}f < c_{p,s}u_sC_s, \tag{5.114}$$

and vice versa. Thus we are comparing the heat flux in the gas (left-to-right) with that in the solid (right-to-left).

5.6.2 Case Da: $KF_* < 1$

If $KF_* < 1$, then the heat flux in the solid is greater than that in the gas, and so the overall heat transport is right-to-left.

5.6.2.1 Region DaV

From the form of the solution (5.113), we require that x_c is on the left side of the domain, so that the solution remains bounded as $Z \to \infty$ and we leave the boundary layer, which is denoted region DaV in Figure 5.7.

As $Z \to \infty$, we have $\bar{T}_s^0, \bar{T}_g^0 \to b_1$, so in this case we must take

$$b_1 = \bar{T}^{\text{in}}, \tag{5.115}$$

in order to satisfy the boundary condition at $x = 1$. The value of b_2 is fixed by matching at $Z = 0$, or $x = x_c$. We notice that the difference in solutions at $Z = 0$ is

$$(\bar{T}_g^0 - \bar{T}_s^0)\Big|_{Z=0} = (1 - KF_*)b_2 = O(1), \tag{5.116}$$

thus $T_g - T_s = O(\eta_D)$ at $Z = 0$. We must therefore have x_c within the $O(1/\mu)$ transition layer DIII about x_1, in which $T_g - T_s = O(\eta_D)$. Since $T_s = \eta_D(1 + \eta_D \log(\eta_D)/A) + O(\eta_D^2)$ (by (5.99)) throughout region DIII, we fix b_2 by

$$b_2 = \frac{1}{KF_*}\left(1 + \eta_D \frac{\log(\eta_D)}{A} - \bar{T}^{\text{in}}\right), \tag{5.117}$$

so that the solutions (5.113) in this boundary layer region DaV (to the right of $x = x_c$) are

$$\bar{T}_s^0 = \bar{T}^{\text{in}} + \left(1 + \eta_D \frac{\log(\eta_D)}{A} - \bar{T}^{\text{in}}\right) \exp\left(-\frac{1 - KF_*}{KF_*} Z\right), \tag{5.118a}$$

$$\bar{T}_g^0 = \bar{T}^{\text{in}} + \frac{1}{KF_*}\left(1 + \eta_D \frac{\log(\eta_D)}{A} - \bar{T}^{\text{in}}\right) \exp\left(-\frac{1 - KF_*}{KF_*} Z\right). \tag{5.118b}$$

At $x = x_c$, or $Z = 0$, we have $\bar{T}_g^0 = (1 + \eta_D \log(\eta_D)/A)/(KF_*)$. Imposing continuity of T_g at $x = x_c$ determines the position of x_c within region DIII, i.e., x_c is the point at which

$$\mathcal{T}_g^0 = \frac{1 + \eta_D \log(\eta_D)/A}{KF_*}. \tag{5.119}$$

Using the form of $\mathcal{T}_g^0$ given by (5.105), we find that

$$x_c = x_1 + \frac{1}{\mu} KF_* \log\left(\frac{1}{(1 - KF_*)(1 + \eta_D \log(\eta_D)/A)}\right). \tag{5.120}$$

5.6.2.2 Region DaIV

In order to match between the $O(1/\mu)$ regions DIII and DaV on either side of x_c, we must introduce a narrower transition layer of width $O(\eta_D/\mu)$ at $x = x_c$, which we refer to as region DaIV. In this region, we make the change of variables $x = x_c + \eta_D Y/\mu$, and set

$$T_s = \eta_D \left(1 + \frac{\eta_D \log(\eta_D)}{A} + \eta_D \tilde{T}_s\right). \tag{5.121}$$

We also write $f = \tilde{f}$, $C = \tilde{C}$, and $T_g = \eta_D \tilde{T}_g$ in region DaIV for clarity. The equations (5.1) in region DaIV therefore become

$$-\frac{\mathrm{d}\tilde{C}}{\mathrm{d}Y} = -\eta_D^2 \tilde{C} \exp\left(A\left(1 + \tilde{T}_s\right)\right) + O(\eta_D^3), \tag{5.122a}$$

$$\frac{\mathrm{d}\tilde{f}}{\mathrm{d}Y} = \eta_D^2 \tilde{C} \exp\left(A\left(1 + \tilde{T}_s\right)\right) + O(\eta_D^3), \tag{5.122b}$$

$$\begin{aligned} -\tilde{C}\frac{\mathrm{d}\tilde{T}_s}{\mathrm{d}Y} = \delta\mu\eta_D^{-1}\frac{\mathrm{d}^2\tilde{T}_s}{\mathrm{d}Y^2} + \tilde{T}_g - \left(1 + \eta_D\left(\frac{\log(\eta_D)}{A} + \tilde{T}_s\right)\right) \\ - \gamma\tilde{C}\exp\left(A\left(1 + \tilde{T}_s\right)\right) + O(\eta_D), \end{aligned} \tag{5.122c}$$

$$\begin{aligned} K\frac{\mathrm{d}}{\mathrm{d}Y}(\tilde{f}\tilde{T}_g) = \eta_D^2\left(1 + \eta_D\left(\frac{\log(\eta_D)}{A} + \tilde{T}_s\right)\right)\tilde{C}\exp\left(A\left(1 + \tilde{T}_s\right)\right) \\ - \eta_D\left(\tilde{T}_g - \left(1 + \eta_D\left(\frac{\log(\eta_D)}{A} + \tilde{T}_s\right)\right) + O(\eta_D^2)\right). \end{aligned} \tag{5.122d}$$

We expand in powers of η_D, setting

$$\begin{aligned} \tilde{T}_s &= \tilde{T}_s^0(Y) + O(\eta_D), \quad \tilde{C} = \tilde{C}^0(Y) + O(\eta_D), \\ \tilde{T}_g &= \tilde{T}_g^0(Y) + O(\eta_D), \quad \tilde{f} = \tilde{f}^0(Y) + O(\eta_D). \end{aligned} \tag{5.123}$$

From (5.122a), (5.122b), and (5.122d) at leading order, we then see that all of

$$\tilde{C}^0 = 1, \qquad \tilde{f}^0 = F_*, \qquad \tilde{T}_g^0 = \frac{1 + \eta_D \log(\eta_D)/A}{KF_*}, \tag{5.124}$$

are uniform over region DaIV, and we are left with a single ODE for $\tilde{T}_s^0$. So long as $\mu \ll \eta_D\delta^{-1}$, the solid temperature variation, $\tilde{T}_s^0$, therefore satisfies the ODE

$$-\frac{\mathrm{d}\tilde{T}_s^0}{\mathrm{d}Y} = \frac{1 - KF_*}{KF_*}\left(1 + \eta_D\frac{\log(\eta_D)}{A}\right) - \gamma\exp\left(A(1 + \tilde{T}_s^0)\right). \tag{5.125}$$

Equation (5.125) has a solution of the form

$$\begin{aligned} \tilde{T}_s^0 = -1 - \frac{1}{A}\log\Bigg(\frac{\gamma KF_*}{(1 - KF_*)(1 + \eta_D\log(\eta_D)/A)} \\ \times\left(1 + E\exp\left(\frac{(A + \eta_D\log(\eta_D))(1 - KF_*)}{KF^*}Y\right)\right)\Bigg), \end{aligned} \tag{5.126}$$

where E is an integration constant. As with cases B and C, this thin transition layer (analogous to regions BIII and CIII, respectively) simply acts to smooth the transition between the neighbouring regions DIII and DaV. As in those cases, (5.126) matches automatically to the left by construction, and the integration constant E is fixed by matching with the $O(\eta_D^2)$ correction to the right, although we do not perform this analysis, since, as in the previous cases, we must go to next order in all other regions of the domain. If instead $\mu = O(\delta^{-1}\eta_D)$, then this transition layer DaIV has width δ, and so the heat conduction term also enters the dominant balance in this layer (yet remains negligible in all other regions DII–DIII and DaV–DaV').

To the right of region DaV is region DaV', filling the remainder of the domain. This is essentially an extension of region DaV, in which all variables are uniform at leading order, with $C = 1 + O(\eta_D)$, $f = F_* + O(\eta_D)$, $T_s = \eta_D \bar{T}^{\text{in}} + O(\eta_D^2)$, and $T_g = T_s + O(\eta_D^2)$.

5.6.2.3 Composite solution

We can form a leading-order, composite, steady-state solution as follows. Since $C = 1$ at leading order in regions DIII-DaV', the leading-order composite solution is simply

$$C^{\text{Da}} = C^0\left(\frac{x - s_0}{\delta}\right) + \hat{C}^0(\mu(x - s_0)) - C^\infty. \tag{5.127}$$

The gas temperature is $O(1)$ in regions DI and DII, but $O(\eta_D)$ in regions DIII–DaV'. Since we have not computed the $O(\eta_D)$ correction in regions DI–DII, we assume that this correction is $\eta_D(1 + \eta_D \log(\eta_D)/A)$ so that the composite solution is correct to $O(\eta_D)$ in regions DIII–DaV'. The composite solution is defined piecewise on either side of the transition layer DaIV. The centre of this transition layer is x_c, given by (5.120), which is defined so that there is a continuous transition between $T_g = \eta_D \mathcal{T}_g^0$ in region DIII and $T_g = \eta_D \bar{T}_g$ in region DaV. For the composite solution, we choose to define a slightly different changeover point $x_c^* = x_c + O(\eta_D/\mu)$, so that the composite solution is continuous at this point. We therefore use

$$T_g^{\text{Da}} = \begin{cases} T_g^0\left(\frac{x-s_0}{\delta}\right) + \hat{T}_g^0(\mu(x - s_0)) - G_s \\ \qquad +\eta_D \mathcal{T}_g^0(\mu(x - x_1)) - \exp\left(-\frac{\mu}{KF_*}(x - x_1)\right), & \text{if } x < x_c^*, \\ \eta_D \bar{T}_g^0(\mu(x - x_c^*)), & \text{if } x > x_c^*, \end{cases} \tag{5.128}$$

which, from the form of $\mathcal{T}_g^0$ in (5.105), simplifies to

$$T_g^{\text{Da}} = \begin{cases} T_g^0\left(\frac{x-s_0}{\delta}\right) + \hat{T}_g^0(\mu(x - s_0)) - G_s + \eta_D\left(1 + \eta_D \frac{\log(\eta_D)}{A}\right), & \text{if } x < x_c^*, \\ \eta_D \bar{T}_g^0(\mu(x - x_c^*)), & \text{if } x > x_c^*. \end{cases} \tag{5.129}$$

The solid temperature is similarly $O(1)$ in region DI, but $O(\eta_D)$ everywhere else. As in previous cases, we set the $O(\eta_D)$ correction in region DI to be $\eta_D(1+\eta_D \log(\eta_D)/A)$ so that the composite solution is accurate to $O(\eta_D)$ in regions DII–DaV'. We neglect the $O(\eta_D^2)$ corrections in regions DII and DIII for this composite solution. We form the leading-order composite solution:

$$T_s^{\mathrm{Da}} = \begin{cases} T_s^0\left(\frac{x-s_0}{\delta}\right) + \eta_D\left(1+\eta_D\frac{\log(\eta_D)}{A}\right), & \text{if } x < x_c^*, \\ \eta_D \bar{T}_s^0(\mu(x-x_c^*)), & \text{if } x > x_c^*. \end{cases} \tag{5.130}$$

5.6.3 Case Db: $KF_* > 1$

In the case $KF_* > 1$, the heat flux in the gas is greater than in the solid. We therefore require the position of the boundary layer over which T_s decays to T_s^{in} to be at the far right of the domain, at $x_c = 1$. This is so that the variable $Z < 0$, and the solution (5.113) is bounded as we leave the boundary layer ($Z \to -\infty$). This boundary layer is therefore region DbVI in Figure 5.7.

In this case, we notice that as $Z \to -\infty$, both $\bar{T}_s^0, \bar{T}_g^0 \to b_1$, so that far from $x = 1$, we have $T_g - T_s = O(\eta_D^2)$. In region DIII, we have $T_g - T_s = O(\eta_D)$. We therefore cannot match directly with region DIII: there must be another region within which $T_s - T_g = O(\eta_D^2)$. We denote this region DbIV.

5.6.3.1 Region DbIV

We note that equations (5.100) of region DIII hold so long as $T_g - T_s \gg \eta_D^2$. As T_g is decaying through region DIII, $T_g - T_s$ is decreasing. At the point where $T_g - T_s = O(\eta_D^2)$, the advection (term 1 in (5.3)) must also be included in the dominant balance. From (5.105), we see that $T_g - T_s = \eta_D^2$ when

$$\exp\left(-\frac{1}{KF_*}z\right) = \eta_D, \tag{5.131}$$

i.e., at the point

$$z_* = -KF_* \log(\eta_D). \tag{5.132}$$

Like y_* given by (5.98), we note that $z_* = O(-\log(\eta_D))$ is large. Strictly speaking, there is therefore another region DbIII' with lengthscale $O(-\log(\eta_D)/\mu)$ to the right of region DIII, but since this is an extension of DIII (the same equations hold, simply over a longer lengthscale), we do not analyse this region separately. Although z_* is large, in the original variables, this is the point $x_2 := s_0 + (y_* + z_*)/\mu \ll 1$, since

$\mu \gg -\log(\eta_D)$. Thus x_2 remains within the $O(-\log(\eta_D)/\mu)$ boundary layer around $x = s_0$.

Region DbIV is the transition layer around the point x_2, in which all the terms 1, 3, 4, and 5 balance in the solid heat equation (5.3). Since $T_g - T_s = O(\eta_D^2)$ in region DbIV, we make the change of variables

$$T_s = \eta_D \left(1 + 2\eta_D \frac{\log(\eta_D)}{A} + \eta_D \frac{\tau_s}{A}\right), \qquad T_g = \eta_D \left(1 + 2\eta_D \frac{\log(\eta_D)}{A} + \eta_D \frac{\tau_g}{A}\right), \tag{5.133}$$

so that at leading order both T_s and T_g are uniform through region DbIV. The heat exchange terms (3 and 4) now combine to be $O(\mu\eta_D^2)$, and the heat lost to the chemical reaction, term 5, is likewise $O(\mu\eta_D^2)$, since

$$Q(C, T_s) = \delta\mu \left(\eta_D^2 C e^{A+\tau_s} + O(\eta_D^3)\right). \tag{5.134}$$

As in regions DII and DIII, we require an $O(1/\mu)$ lengthscale to balance advection and heat transfer terms in the gas heat equation. With the change of variables $x = x_2 + Z/\mu$, and writing $C = \bar{\mathcal{C}}$, $f = \bar{\mathcal{F}}$ for clarity of notation, equations (5.1) in region DbIV become

$$-\frac{\mathrm{d}\bar{\mathcal{C}}}{\mathrm{d}Z} = -\eta_D^2 \bar{\mathcal{C}} e^{A+\tau_s} + O(\eta_D^3), \tag{5.135a}$$

$$\frac{\mathrm{d}\bar{\mathcal{F}}}{\mathrm{d}Z} = \eta_D^2 \bar{\mathcal{C}} e^{A+\tau_s} + O(\eta_D^3), \tag{5.135b}$$

$$-\bar{\mathcal{C}}\frac{\mathrm{d}\tau_s}{\mathrm{d}Z} = \delta\mu \frac{\mathrm{d}^2\tau_s}{\mathrm{d}Z^2} + \tau_g - \tau_s - \gamma A \bar{\mathcal{C}} e^{A+\tau_s} + O(\eta_D), \tag{5.135c}$$

$$K\frac{\mathrm{d}}{\mathrm{d}Z}(\bar{\mathcal{F}}\tau_g) = \eta_D(A + 2\eta_D \log(\eta_D) + \eta_D\tau_s)\bar{\mathcal{C}} e^{A+\tau_s} - (\tau_g - \tau_s) + O(\eta_D^2). \tag{5.135d}$$

We expand in powers of η_D, taking

$$\begin{aligned} \tau_s &= \tau_s^0(Z) + O(\eta_D), \quad \bar{\mathcal{C}} = \bar{\mathcal{C}}^0(Z) + O(\eta_D), \\ \tau_g &= \tau_g^0(Z) + O(\eta_D), \quad \bar{\mathcal{F}} = \bar{\mathcal{F}}^0(Z) + O(\eta_D). \end{aligned} \tag{5.136}$$

At leading order in (5.135a) and (5.135b), respectively, we find that $\bar{\mathcal{C}}^0 = 1$ is constant, fixed by matching to the right, while $\bar{\mathcal{F}}^0 = F_*$ is uniform, fixed by matching with region DIII to the left. At leading order, equations (5.135c)–(5.135d) become

$$-\frac{\mathrm{d}\tau_s^0}{\mathrm{d}Z} = (\tau_g^0 - \tau_s^0) - \gamma A e^{A+\tau_s^0}, \qquad KF_*\frac{\mathrm{d}\tau_g^0}{\mathrm{d}Z} = -(\tau_g^0 - \tau_s^0). \tag{5.137}$$

This transition region DbIV plays the same role as regions BIII, CIII, and DaIV, in cases B, C, and Da, respectively. It is in this region that term 1 enters the dominant

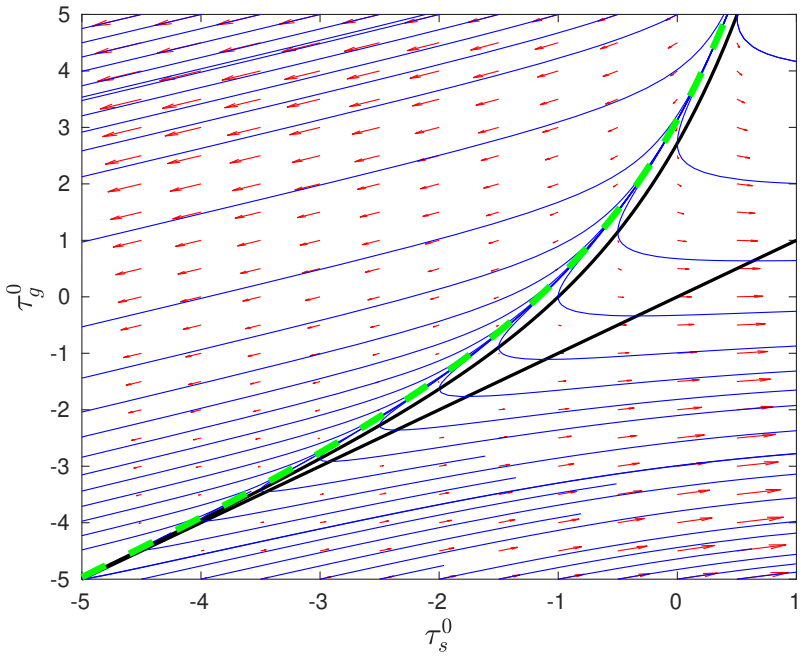

Figure 5.8: Phase plane for the steady-state system (5.138). Nullclines are in black and trajectories in blue. The green dashed curve is the line $\tau_g^0 = \tau_g^{\text{limit}}(\tau_s^0)$ given by (5.141). We take physically relevant values $\gamma = A = 1$ and $KF_* = 1$, so that $c_1 = 2$, and $c_2 = 5.44$.

balance of (5.3), while term 5 leaves the dominant balance. However, while T_g is uniform at leading order over the transition region DbIV, we must solve for the variation, τ_g^0, simultaneously with the solid temperature variation, τ_s^0, via the coupled system (5.137), rather than solving a single ODE for the solid temperature variation, as we did in regions BIII, CIII, and DaIV.

While we cannot solve the system (5.137) explicitly, we can study solutions using a phase-plane analysis. We first rescale $\bar{Z} = KF_*Z$ so that the system (5.137) becomes

$$\frac{\mathrm{d}\tau_s^0}{\mathrm{d}\bar{Z}} = -c_1(\tau_g^0 - \tau_s^0) + c_2 e^{\tau_s^0}, \qquad \frac{\mathrm{d}\tau_g^0}{\mathrm{d}\bar{Z}} = -(\tau_g^0 - \tau_s^0). \tag{5.138}$$

in terms of the two parameters $c_1 = KF_*$ and $c_2 = KF_*\gamma A e^A$. Solutions of this system (5.138) are shown as trajectories in the phase-plane diagram in Figure 5.8. The black lines shown in Figure 5.8 are the nullclines

$$\tau_g^0 = \tau_s^0 \quad \text{and} \quad \tau_g^0 = \tau_s^0 + \frac{c_2}{c_1} e^{\tau_s^0}, \tag{5.139}$$

on which $\mathrm{d}\tau_g/\mathrm{d}\bar{Z} = 0$ and $\mathrm{d}\tau_s/\mathrm{d}\bar{Z} = 0$, respectively. As $\bar{Z} \to -\infty$, both τ_s^0 and τ_g^0 must grow exponentially, in order to match with region DIII. From the phase-plane diagram in Figure 5.8, we see that all such trajectories follow just above the

$\mathrm{d}\tau_s^0/\mathrm{d}\bar{Z} = 0$ nullcline as $\bar{Z} \to -\infty$. This is to be expected, since the advection term 1 must become small as $\bar{Z} \to -\infty$ in order to obtain the dominant balance between terms 3 and 5 in DIII. We observe in Figure 5.8 that these trajectories stay just above the $\mathrm{d}\tau_s^0/\mathrm{d}\bar{Z} = 0$ nullcline, before either peeling away to the left, or turning the corner and crossing both nullcines, eventually approaching curves with τ_g^0 equal to a constant. In order to match to the right of region DbIV, the solution trajectory must not cross the nullclines, so that $\tau_g^0 > \tau_s^0$ everywhere, and both $\tau_g^0, \tau_s^0 \to -\infty$ as $\bar{Z} \to \infty$.

The trajectories do not cross the nullclines for any $\bar{Z}$, provided that the inequality

$$\frac{\mathrm{d}\tau_g^0}{\mathrm{d}\bar{Z}} \Bigg/ \frac{\mathrm{d}\tau_s^0}{\mathrm{d}\bar{Z}} = \frac{\mathrm{d}\tau_g^0}{\mathrm{d}\tau_s^0} < \frac{\mathrm{d}}{\mathrm{d}\tau_s^0}\left(\tau_s^0 + \frac{c_2}{c_1}e^{\tau_s^0}\right) \tag{5.140}$$

holds at all points on the solution trajectory. Substituting in the derivatives from (5.138), we see that (5.140) reduces to the inequality

$$\tau_g^0 > \frac{(c_1\tau_s^0 + c_2 e^{\tau_s^0})\left(1 + \frac{c_2}{c_1}e^{\tau_s^0}\right) - \tau_s^0}{c_1 + c_2 e^{\tau_s^0} - 1} =: \tau_g^{\mathrm{limit}}. \tag{5.141}$$

The trajectory $\tau_g^0 = \tau_g^{\mathrm{limit}}(\tau_s^0)$ is plotted as the dashed green curve in Figure 5.8, and is seen to divide the trajectories crossing the nullclines from those remaining above them. As $\tau_s^0 \to \infty$, we have

$$\tau_g^{\mathrm{limit}} \sim \tau_s^0 + \frac{c_2}{c_1}e^{\tau_s^0} + \frac{1}{c_1} + \cdots. \tag{5.142}$$

Therefore, as long as $\tau_g^0 > \tau_s^0 + \gamma \exp\left(A(1+\tau_s^0)\right) + 1/c_1$ in the limit as $\bar{Z} \to -\infty$ (which must be true from the matching with region DIII), the trajectories never cross the nullclines.

We notice that, on these trajectories, τ_s^0 becomes negative as $\bar{Z} \to \infty$, and so the exponential term in (5.138), representing the heat consumed by the chemical reaction, becomes exponentially small in this limit. As $\bar{Z} \to \infty$, we therefore see by combining (5.138) that $\tau_s^0 - c_1\tau_g^0$ approaches a constant, so that the trajectories approach straight lines, as can be seen in Figure 5.8. We also notice that some such trajectories follow the curve $\tau_g^{\mathrm{limit}}(\tau_s^0)$ for a long time before peeling off to the $\tau_s^0 - c_1\tau_g^0$ behaviour. The curve $\tau_g^{\mathrm{limit}}(\tau_s^0)$ approaches the nullclines as both τ_s^0 and τ_g^0 decrease below zero, and the nullclines become closer together. Thus on these trajectories remaining close to $\tau_g^{\mathrm{limit}}(\tau_s^0)$, both the exponential chemical reaction term in (5.138) and the heat transfer terms $\tau_g^0 - \tau_s^0$ are very small, so that both $\mathrm{d}\tau_g^0/\mathrm{d}\bar{Z}$ and $\mathrm{d}\tau_s^0/\mathrm{d}\bar{Z}$ are small. The solution we are concerned with must lie on one of these very slowly

moving trajectories, since $\tau_g^0 - \tau_s^0$ cannot grow until we reach the boundary layer region DbVI. Thus the transition layer region DbIV must actually extend fully into region DbV, which may equally be considered a subregion of either DbIV or DbVI.

5.6.3.2 Regions DbV and DbVI

To the right of region DbIV, the heat lost to the chemical reaction, term 5 in (5.3), is not included in the dominant balance, so the system is purely advective, until the heat transfer between phases becomes important again in region DbVI. Thus in region DbV all dependent variables are constant at leading order, namely

$$T_s = T_g = \eta_D \left(1 + 2\eta_D \frac{\log(\eta_D)}{A}\right), \qquad f = F_*, \qquad C = 1, \tag{5.143}$$

where we have fixed the constants $f = F_*$ by matching with region DbIV, and $C = 1$ by matching with region DbVI.

Using this behaviour in region DbV, we may complete our solution in region DbVI. By matching between regions DbV and DbVI, we find

$$b_1 = 1 + 2\eta_D \frac{\log(\eta_D)}{A}, \tag{5.144}$$

and applying the boundary condition $\bar{T}_s = \bar{T}^{\text{in}}$ at $Z = 0$, we find

$$b_2 = \frac{1}{KF_*}(\bar{T}^{\text{in}} - a_1) = \frac{1}{KF_*}\left(\bar{T}^{\text{in}} - 1 - 2\eta_D \frac{\log(\eta_D)}{A}\right). \tag{5.145}$$

Thus, in region DbVI,

$$\bar{T}_s = 1 + 2\eta_D \frac{\log(\eta_D)}{A} + \left(\bar{T}^{\text{in}} - 1 - 2\eta_D \frac{\log(\eta_D)}{A}\right) \exp\left(\frac{KF_* - 1}{KF_*} Z\right), \tag{5.146}$$

$$\bar{T}_s = 1 + 2\eta_D \frac{\log(\eta_D)}{A} + \frac{1}{KF_*}\left(\bar{T}^{\text{in}} - 1 - 2\eta_D \frac{\log(\eta_D)}{A}\right) \exp\left(\frac{KF_* - 1}{KF_*} Z\right), \tag{5.147}$$

completing the analysis of case Db.

5.6.3.3 Composite solution

We can therefore construct a leading-order, steady-state composite solution for case Db. Since C and f are everywhere $O(1)$, and are constant to leading order in regions DIII–DbVI, the composite expansions are simply

$$C^{\text{Db}} = C^0\left(\frac{x - s_0}{\delta}\right) + \hat{C}^0\left(\mu(x - s_0)\right) - C^\infty, \tag{5.148}$$

$$f^{\text{Db}} = f^0\left(\frac{x - s_0}{\delta}\right) + \hat{f}^0\left(\mu(x - s_0)\right) - F_s. \tag{5.149}$$

Both T_s and T_g are $O(1)$ at $x = s$, but become $O(\eta_D)$ as we move further into the domain. As in the previous cases there is freedom to choose a composite solution. Since $T_s \sim \eta_D$ is uniform through regions DII–DbV, we use the composite solid temperature

$$T_s^{\mathrm{Db}} = T_s^0\left(\frac{x - s_0}{\delta}\right) + \eta_D \bar{T}_s^0\left(\mu(x-1)\right), \tag{5.150}$$

so that T_s is accurate with error $O(\eta_D)$ in region DI, with error $O(\eta_D^2)$ in regions DbIV–DbVI, but with $O(\eta_D \log(\eta_D))$ error in regions DII–DbIII. Similarly, we choose the composite gas temperature

$$T_g^{\mathrm{Db}} = T_g^0\left(\frac{x - s_0}{\delta}\right) + \hat{T}_g^0\left(\mu(x-s_0)\right) - G_s + \eta_D \bar{T}_g^0\left(\mu(x-1)\right), \tag{5.151}$$

accurate to $O(\eta_D)$ in regions DI–DII, to $O(\eta_D \log(\eta_D))$ in region DIII, and to $O(\eta_D^2)$ in regions DbIV–DbVI.

5.7 Case E: $\mu = O(\delta^{-1})$, large heat transfer

In this section we study the behaviour of solutions of (5.1) for large $\mu = O(\delta^{-1})$. As for case D above, the heat transfer between the phases is large enough that over the majority of the domain the solid and gas temperatures are the same. Now, however, the two temperatures may only differ at leading order in regions of width $O(\delta)$. In particular, heat is transferred between phases in the conduction boundary layer, region EI, at $x = s$. Therefore, unlike in all previous cases A–D, we can no longer decouple the gas and solid equations in region EI. In the previous cases, we used the notation F_s and G_s given by (5.51) for the leading-order flux and temperature of gas leaving region I, respectively. We use the different notation f^∞ and T_g^∞ for case E to highlight that the far-field forms (5.51) no longer hold for case E.

As in case D, we find that the structure of the solution outside of region EI depends on the direction of the characteristic curves for the temperature problem, in relation to the speed of the free boundary $\dot{s}$. In particular, we find two distinct steady-state regimes for the cases where $Kf^\infty - 1$ either is negative (which we call case Ea) or positive (case Eb). The case Da with $KF_* < 1$ is related to the case Ea with $Kf^\infty < 1$, as μ increases, and we can similarly relate cases Db and Eb. The structures of the two types of steady-state solution in case E are illustrated in Figure 5.9, and the changes of variable are summarised in Table 5.5. For non-steady solutions there are a number of additional possible solution structures, which we will discuss

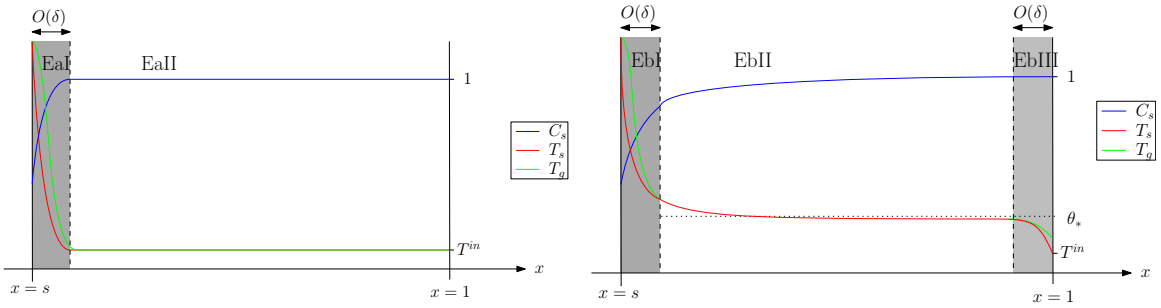

(a) Case Ea, with $Kf^\infty < 1$.

(b) Case Eb, with $Kf^\infty > 1$.

Figure 5.9: Schematic diagrams illustrating the asymptotic solution structures, in steady state, for case E, where $\mu = O(\delta^{-1})$. Time dependent solutions may have these, or other structures.

Region	Spatial Variable	Size of Q	Dominant terms in (5.3)	Dependent Variables
EI	$x = s + \delta X$	$Q = O(1)$	1, 2, 3, 4, 5	C, f, T_s, T_g
EaII	x	$Q \ll \delta T^{\text{in}}$	1	$C = 1$, $f = f^\infty$, $T_s = T_g = T^{\text{in}}$
EbII	x	$Q = O(\delta\theta_*^2)$	1, 5	$C = 1 + \theta_*^2\hat{C}$, $T_s = T_g = \theta_*(1 + \theta_*\hat{T})$
EbIII	$x = 1 - \delta Y$	$Q \ll \delta\theta_*^2$	1, 2	$C = 1$, $f = f^\infty$, $T_s = \theta_*\bar{T}_s$, $T_g = \theta_*\bar{T}_g$

Table 5.5: Summary of the notation in each asymptotic region in the cases Ea ($\mu = O(\delta^{-1})$, $Kf^\infty < 1$) and Eb ($\mu = O(\delta^{-1})$, $Kf^\infty > 1$), corresponding to the diagrams in Figure 5.9.

in Section 5.7.2, but for simplicity we will focus on the steady-state structures. Since in this section we assume $\mu = O(\delta^{-1})$, we change notation and write $\mu = M\delta^{-1}$, for $M = O(1)$.

5.7.1 Region EI

As usual we look for a boundary layer, region EI, of width $O(\delta)$ at $x = s$, setting $x = s + \delta X$. Unlike the previous cases, we now have heat transfer between the solid and gas phases on the $O(\delta)$ lengthscale, and so the solid and gas equations in region EI do not decouple. At leading order in δ, the equations in region EI are quasi-steady, so that we have $f = f_* + (1 + \dot{s})(C - C_*) + O(\delta)$ in region EI. To leading order in δ, the equations for C, T_s, and T_g are

$$-(1 + \dot{s})\frac{\partial C}{\partial X} = -C \exp\left(A\left(1 - \frac{1}{T_s}\right)\right), \tag{5.152a}$$

$$-(1+\dot{s})C\frac{\partial T_s}{\partial X} = \frac{\partial^2 T_s}{\partial X^2} + M(T_g - T_s) - \gamma C \exp\left(A\left(1 - \frac{1}{T_s}\right)\right), \tag{5.152b}$$

$$K\frac{\partial}{\partial X}(fT_g) = T_s C \exp\left(A\left(1 - \frac{1}{T_s}\right)\right) - M(T_g - T_s), \tag{5.152c}$$

with boundary conditions

$$C = C_*, \quad T_s = T_g = \frac{\rho}{s} \quad \text{at } X = 0. \tag{5.152d}$$

We have neglected the $O(\delta)$ terms in (5.152), but the error may be greater than $O(\delta)$, depending on the far-field behaviour/matching of this system, as we will discuss in Section 5.7.2. We note that all the physical processes come into the dominant balance in this boundary layer EI, except for the time derivatives.

The system (5.152) is closed by applying appropriate matching conditions as $X \to \infty$, but it is not immediately clear what the correct conditions are. In the far field, as $X \to \infty$, we require that the chemical reaction rate becomes small in order that the rate of change of C becomes small. This means we expect T_s to be small as we leave the boundary layer. Using the far-field conditions

$$T_s \to 0, \quad C \to C^\infty(t) \qquad \text{as } X \to \infty, \tag{5.153}$$

as in cases C and D, where $C^\infty(t)$ is to be determined, the system (5.152) may be shown to be correctly specified by a similar argument to that in Appendix A, so long as

$$K\left(f_* + (1+\dot{s})(C^\infty - C_*)\right) < (1+\dot{s})C^\infty, \tag{5.154}$$

where, as always, s is found as part of the solution of the region-I problem. Since $\dot{s}$ and C^∞ are functions of time, we note that (5.154) may hold for certain times, and not others. This condition (5.154) is precisely the requirement that, in the far-field of the moving boundary layer EI, the heat flux left-to-right in the gas is less than the heat flux right-to-left in the solid. Thus the far-field conditions (5.153) can only be imposed if the overall direction of heat flow is right-to-left within the moving boundary layer, i.e., *into* the boundary layer. In this case, we note that the conditions (5.153) ensure that $T_g \to 0$ as $X \to 0$ also, and so $T_s - T_g \to 0$ in the far-field limit.

We restrict to the case $K < 1$ which is relevant for the silicon furnace (in Chapter 3 we found $K = 0.66$), noting that in this case

$$C^\infty - K(C^\infty - C_*) = C^\infty(1-K) + C_* > 0 \tag{5.155}$$

is positive. In this case, the inequality (5.154) may therefore be rearranged to

$$\dot{s} > -1 + \frac{Kf_*}{C^\infty - K(C^\infty - C_*)} =: U(C^\infty), \tag{5.156}$$

i.e., the matching conditions (5.153) are appropriate if the position of the free boundary does not decrease too rapidly.

We note that (regardless of the size of μ) for physically relevant solutions we require $\dot{s} > -1$, since the fastest the free boundary can move inwards is the speed of the solid material. Since $K > 1$, we see from (5.156) that $U > -1$. Thus we expect both the situations when (5.156) does and does not hold to be possible, and physically relevant. If (5.156) does not hold, so that $\dot{s} < U$, the far-field conditions (5.153) cannot be imposed. The overall direction of heat transfer in the far field of the boundary layer is now left-to-right, and so we must understand the decay behaviour of the region EI problem, in order to choose the correct far-field conditions. Since all physical effects are included in the region EI equations (5.152), in the far field we will simply have some of these effects dropping out of the dominant balance as the lengthscale becomes large. We will find the appropriate far-field behaviour of the region EI model by examining the system on greater lengthscales.

5.7.2 The O(1) domain

We now investigate the behaviour in the majority of the domain for either of the cases $\dot{s} > U$ or $\dot{s} < U$. On an $O(1)$ lengthscale, we note from the mass equations (5.1a)–(5.1b) that the chemical reaction rate must be small, at most $O(\delta)$. Since the chemical reaction rate is small, T_s must be small. We suppose that $T_s = O(\theta)$ for some small $\theta \ll 1$ to be determined. From the (dominant) $M(T_g - T_s)$ term in either energy equation (5.1c) or (5.1d), we must therefore have $T_g = O(\theta)$, as well. By balancing the advection or chemical reaction terms in the solid heat equation, we see that the difference $T_g - T_s$ must be at most order

$$\epsilon := \max\left(\delta\theta, \exp\left(-\frac{A}{\theta}\right)\right) \ll \theta, \tag{5.157}$$

so that the two temperatures are equal at leading order in θ. Thus the model (5.1) reduces to a single-temperature system over $O(1)$ lengthscales.

Specifically, we write $T_s = \theta T + \epsilon T_s^1$ and $T_g = \theta T + \epsilon T_g^1$. Adding the two heat equations (5.1c) and (5.1d) together, the convective heat transfer between the phases cancel, and we obtain a single equation for the leading-order temperature T, namely

$$\delta\theta\left(\frac{\partial}{\partial t}(CT) + \frac{\partial}{\partial x}\big((Kf - C)T\big)\right) = -\gamma C \exp\left(A\left(1 - \frac{1}{\theta T}\right)\right). \tag{5.158}$$

Here we have absorbed the term for the heat transfer between phases due to the mass transfer into the advection term, by using the solid mass equation (5.1a). We

have neglected the heat diffusion term, which is always smaller than the advection term on lengthscales greater than $O(\delta)$. Only the two remaining terms in (5.158) — heat advection, and heat consumed by chemical reaction — can possibly enter the dominant balance, and we must choose the appropriate θ to ensure the correct balance. We will see that the $O(\epsilon)$ correction is smaller than the corrections due to other effects, and so the single-temperature model (5.158) is indeed valid. We note that equation (5.158) is a first-order, hyperbolic equation for T, and so our entire system is hyperbolic on the $O(1)$ lengthscale: the C characteristic curves travel right-to-left, the f characteristic curves travel left-to-right, and the T characteristic curves from (5.158) travel in direction $Kf - C$. The correct choice of scaling θ, and so the balance in (5.158), depends on the direction of the T characteristics, and hence on the sign of $Kf - C$.

We notice that the chemical reaction rate must be at most order $\delta\theta$ over this $O(1)$ lengthscale in order to be balanced by the advection term in (5.158). From the equations of conservation of mass (5.1a)–(5.1b), this means that both C and f are uniform at leading order in θ over $O(1)$ domains. We will later see that there are no regions of $O(1)$ variation in C or f outside of region EI, and thus both

$$C = 1 + \epsilon_C \hat{C} \qquad \text{and} \qquad f = f^\infty(t) + \epsilon_C \hat{f} \tag{5.159}$$

are uniform at leading order over the entire $O(1)$ domain $x > s(t)$. Here the scaling $\epsilon_C \ll 1$ of the correction terms is yet to be determined. This depends on which boundary the T characteristic curves originate: we will find $\epsilon_C \sim \delta^{-1} Q(T^{\text{in}}) = o(T^{\text{in}})$ for when these originate at the $x = 1$ boundary, and ϵ_C is given by (5.170) when these originate at $x = s$ (in either case $\epsilon_C \gg \epsilon$, the error in the single-temperature approximation, defined by (5.157)). In (5.159) we have fixed $C^\infty = 1$ at leading order using the boundary condition at $x = 1$, and the uniform (but not constant in time)

$$f^\infty(t) = f_* + (1 + \dot{s}(t))(1 - C_*), \tag{5.160}$$

by matching with the boundary layer EI as $X \to \infty$. Thus the direction of the characteristic curves for T are uniform over the entire $O(1)$ domain, and are given by

$$Kf - C = Kf^\infty(t) - 1 + O(\epsilon_C). \tag{5.161}$$

Since the characteristic curve slopes depend only on time and do not vary spatially, we do not expect characteristic curves to cross anywhere in the domain.

We will have different behaviour (and different θ scalings) in regions where the characteristics of (5.158) originate at different boundaries of the (x, t) domain. We

note that these T-characteristic curves, with gradient $Kf^\infty - 1$, can originate at $x = 1$ only if $Kf^\infty < 1$, or equivalently only if

$$\dot{s} < V := \frac{1 - K(f_* + (1 - C_*))}{K(1 - C_*)}. \tag{5.162}$$

Also, characteristic curves can originate at $x = s(t)$ only if $Kf^\infty - 1 > \dot{s}$, or equivalently (since we are assuming throughout that $K < 1$) only if

$$\dot{s} < U, \tag{5.163}$$

where (in a slight abuse of notation) we write $U := U|_{C^\infty=1}$ for the function $U(C^\infty)$ defined as in (5.156), evaluated at $C^\infty = 1$. Thus characteristic curves in the outer domain originate at $x = s$ if and only if the heat transfer is left-to-right in the far-field of the (moving) boundary layer EI. We note that U and V have opposite signs: if (as in case Ea) $K(f_* + 1 - C_*) < 1$ then $V > 0$, and by rearranging U given by (5.156) (with $K > 1$) we have $U < 0$. Conversely if (as in case Eb) $K(f_* + 1 - C_*) > 1$ then $U > 0 > V$. For either sign of $K(f_* + 1 - C_*) - 1$, there are a variety of solution structures depending on which, if any, of (5.162) and (5.163) hold, since (5.162) and (5.163) are neither mutually exclusive nor mutually inclusive. In particular, the steady-state solutions in the cases Ea and Eb, are illustrated in Figures 5.9a and 5.9b. The characteristic diagrams for the T problem (5.158), showing the different structures possible (in the general, non-steady case), are presented in Figure 5.10. As $\dot{s}$ changes continuously in time, there are other structures possible than those shown here.

We consider regions with characteristic curves originating at $x = 1$ and $x = s$ separately, as the temperature scaling θ, and so too the solution behaviour, is different in these two cases. To fully determine the non-steady solutions, we should also investigate the case when characteristic curves originate at the $t = 0$ axis in the diagrams of Figure 5.10. The solution in this case is determined by the initial conditions, in particular on the magnitude of the temperature, but for simplicity we do not discuss this here.

5.7.2.1 T characteristics originate at $x = 1$

In a region with the characteristics originating from $x = 1$, since $T = T^{\text{in}}$ at $x = 1$, we take $\theta = T^{\text{in}} \ll 1$. Since $Q(T^{\text{in}}) \ll \delta T^{\text{in}}$, the chemical reaction terms in both the heat and mass equations are negligible, and so at leading order (expanding in powers of T^{in}) we find $T_s = T_g = T^{\text{in}}$, and of course as above we have $C = 1$ and $f = f^\infty$

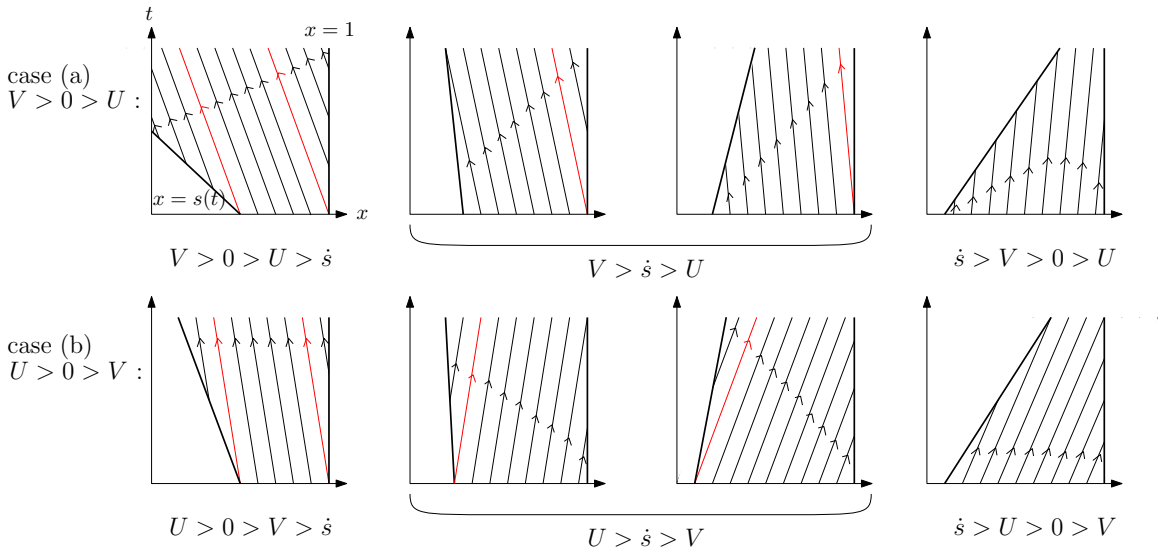

Figure 5.10: Characteristic diagrams in the cases $V > 0 > U$ and $V < 0 < U$, for different sizes of $\dot{s}$. The red characteristics mark the boundaries between regions with the characteristics originating at different boundaries of the domain, or at the initial data. In general, we expect to have different dominant behaviour on either side of these bounding characteristics.

throughout this region. This is true for the steady-state case Ea, with $Kf^{\infty} < 1$. The leading-order, steady-state, composite solution in this case is given in (5.185) below.

5.7.2.2 T characteristics originate at $x = s(t)$

In a region where the characteristics originate at $x = s$, then the temperature scaling θ must be determined by the temperature leaving the boundary layer EI. We suppose that the temperature is approximately constant, and make the changes of variables $T = \theta(1 + \epsilon_T \hat{T})$ for some small $\theta, \epsilon_T \ll 1$, and $C = 1 + \epsilon_C \hat{C}$ and $f = f^{\infty} + \epsilon_C \hat{f}$, for $\epsilon_C \ll 1$. We look for values of θ, ϵ_T, and ϵ_C in terms of δ that give a valid dominant balance in (5.158) with the mass equations on the $O(1)$ lengthscale. Retaining only the leading-order part of the each term (and neglecting the negligibly small diffusion term), the equations of mass conservation (5.1a)–(5.1b) and equation (5.158) become

$$\delta\epsilon_C \left(\frac{\partial \hat{C}}{\partial t} - \frac{\partial \hat{C}}{\partial x} \right) = -\exp\left(-\frac{A}{\theta}\right) \exp\left(A\left(1 + \frac{\epsilon_T}{\theta}\hat{T}\right)\right), \tag{5.164}$$

$$\delta\epsilon_C \frac{\partial \hat{f}}{\partial x} = \exp\left(-\frac{A}{\theta}\right) \exp\left(A\left(1 + \frac{\epsilon_T}{\theta}\hat{T}\right)\right), \tag{5.165}$$

$$\delta\theta\left(\epsilon_C\left(\frac{\partial\hat{C}}{\partial t}+\frac{\partial}{\partial x}(K\hat{f}-\hat{C})\right)+\epsilon_T\left(\frac{\partial\hat{T}}{\partial t}+(Kf^\infty-1)\frac{\partial\hat{T}}{\partial x}\right)\right)$$
$$=-\gamma\exp\left(-\frac{A}{\theta}\right)\exp\left(A\left(1+\frac{\epsilon_T}{\theta}\hat{T}\right)\right). \tag{5.166}$$

Since $\hat{T}$ may be positive or negative, we need $\epsilon_T \leq \theta$ for a valid balance. We take $\epsilon_T = \theta$ for the distinguished limit. Our scalings are only sensible in (5.164)–(5.165) if $\delta\epsilon_C \geq \exp(-A/\theta)$. For an overall dominant balance, the chemical reaction term must balance the $\hat{T}$ advection term in (5.166). We therefore require that $\theta = \theta_*$ is the solution of

$$\delta\theta_*^2 e^{A/\theta_*} = 1. \tag{5.167}$$

There are two positive solutions of (5.167), similarly to the two solutions for η_B given by (5.20) in case B. As in case B, we require the smaller root, given in terms of the Lambert W branch W_{-1}. Expanding this root of (5.167) in $\delta \ll 1$, we find

$$\theta_* = \frac{-A}{2W_{-1}\left(-\frac{A}{2}\sqrt{\delta}\right)} = \frac{A}{\log(\frac{1}{\delta})}\left(1+\frac{\log(\log(\delta)^2)}{\log(\delta)}+\cdots\right), \tag{5.168}$$

so that $\theta_* \to 0$ as $\delta \to 0$. As an aside, we also note that the temperature through the majority of the domain in case Db is

$$\eta_D\left(1+2\eta_D\frac{\log(\eta_D)}{A}\right) = \frac{A}{\log\left(\frac{1}{\delta\mu}\right)}\left(1+\frac{\log\left(\log(\delta\mu)^2\right)}{\log(\delta\mu)}+\cdots\right), \tag{5.169}$$

which is the same as θ_* to leading order, since we had $\mu \ll \delta^{-1}$ in case Db. Indeed all of $\eta_B, \eta_C, \eta_D \sim A/(-\log(\delta))$ at leading order, although the correction terms differ, and, being logarithmic, are not particularly small.

Given this balance in (5.166), we may choose ϵ_C to balance (5.164), and thus we find that

$$\epsilon_C = \theta_*^2. \tag{5.170}$$

We note that the correction terms in case Eb are therefore $\epsilon_C = \theta_*\epsilon_T = \theta_*^2 \gg \epsilon$, for the error ϵ defined in (5.157), in assuming that $T_s = T_g = T$, validating our single-temperature model. At leading order in θ_*, the equations (5.164)–(5.166) then become

$$\frac{\partial\hat{C}}{\partial t}-\frac{\partial\hat{C}}{\partial x} = -\exp\left(A\left(1+\hat{T}\right)\right), \qquad \frac{\partial\hat{f}}{\partial x} = \exp\left(A\left(1+\hat{T}\right)\right), \tag{5.171}$$

$$\frac{\partial\hat{T}}{\partial t}+(Kf^\infty-1)\frac{\partial\hat{T}}{\partial x} = -\gamma\exp\left(A\left(1+\hat{T}\right)\right). \tag{5.172}$$

Solving (5.172) by the method of characteristics, we find the characteristic curves, parameterised by ξ and the time t_0 at which $x = s_0$,

$$t(\xi, t_0) = \xi + t_0, \tag{5.173}$$

$$x(\xi, t_0) = s(t_0) + \int_{\hat{\xi}=0}^{\xi} \left[K\left(f_* + (1 + \dot{s}(\hat{\xi} + t_0))(1 - C_*) \right) - 1 \right] \mathrm{d}\hat{\xi}. \tag{5.174}$$

Along these characteristic curves,

$$\hat{T}(\xi) = -\frac{1}{A} \log\left(Ae^A \gamma \xi \right). \tag{5.175}$$

Here we have fixed the constant of integration so that $\hat{T}$ blows up as $\xi \to 0$, i.e., as the characteristic curve approaches $x = s_0$. We may then find $\hat{C}$ and $\hat{f}$ from (5.171), with the requirements that $\hat{C} = 0$ at $x = 1$ and $\hat{f} = 0$ at $x = s(t)$.

In particular, in steady state, the full solution is

$$T = \theta_* - \frac{\theta_*^2}{A} \log\left(\frac{A\gamma e^A}{KF^\infty - 1}(x - s) \right), \quad C = 1 + \theta_*^2 \frac{Kf^\infty - 1}{A\gamma} \log\left(\frac{x - s}{1 - s} \right), \tag{5.176}$$

(and, as always in steady state, $f = f_* + C - C_*$). Specifically, this is the region EbII solution in the steady-state case Eb, illustrated in Figure 5.9b, since in case Eb, characteristic curves originate at $x = s$ and end at $x = 1$. Given this steady-state solution, we may impose this as the far-field behaviour for region EbI. Since equation (5.152a) is first order in C, we prescribe the leading-order far-field behaviour

$$C \to 1 \quad \text{as } X \to \infty, \tag{5.177}$$

while for the T_s boundary condition, we can impose the correct far-field balance

$$(Kf^\infty - 1)\frac{\mathrm{d}T_s}{\mathrm{d}X} + \gamma \exp\left(A\left(1 - \frac{1}{T_s} \right) \right) \to 0 \qquad \text{as } X \to \infty. \tag{5.178}$$

We note that when characteristics of the outer problem move *into* region I, the leading-order problem (5.152) is accurate to order $\theta \ll 1$, because the temperature (which is order θ) outside the boundary layer induces a switchback correction within the boundary layer. In particular, in the steady-state case Ea, we found $\theta = T^{\mathrm{in}}$, and thus the switchback error in case Ea is $O(T^{\mathrm{in}})$. Conversely, when $\dot{s} < U$ and so the characteristics of the outer problem originate at $x = s$, the boundary conditions are given by (5.177)–(5.178), and we do not have a switchback correction due to the outer region. Instead the main source of error is the $O(\theta_*^2)$ error in the far-field boundary condition (5.177) for C.

5.7.3 Region EbIII

In situations where characteristics start at $x = s$ and end at $x = 1$ (such as in the steady-state case Eb in Figure 5.9b), we must introduce a boundary layer at $x = 1$ of width $O(\delta)$, in order to impose the boundary condition $T = T^{\text{in}}$ at $x = 1$. (In steady state, we denote this boundary layer region EbIII.) We make the change of variables $x = 1 - \delta Y$, and set

$$T_s = \theta_* \bar{T}_s, \qquad T_g = \theta_* \bar{T}_g, \tag{5.179}$$

for $\bar{T}_s < 1$. The chemical reaction rate is then

$$\bar{Q} \sim \exp\left(-\frac{A}{\theta_* \bar{T}_s}\right) \ll e^{-A/\theta_*} = \delta\theta_*^2, \tag{5.180}$$

by definition of θ_*. Thus the chemical reaction rate is small, so that $C = 1 + O(\theta_*^2)$ and $f = f^\infty + O(\theta_*^2)$ are uniform to leading order in the boundary layer. We expand

$$\bar{T}_s = \bar{T}_s^0(Y,t) + O(\theta_*), \qquad \bar{T}_g = \bar{T}_g^0(Y,t) + O(\theta_*). \tag{5.181}$$

At leading order in the heat equations (5.1c) and (5.1d), we find the quasi-steady equations

$$\frac{\partial \bar{T}_s^0}{\partial Y} = \frac{\partial^2 \bar{T}_s^0}{\partial Y^2} + M(\bar{T}_g^0 - \bar{T}_s^0), \qquad Kf^\infty \frac{\partial \bar{T}_g^0}{\partial Y} = M(\bar{T}_g^0 - \bar{T}_s^0), \tag{5.182a}$$

(the time-dependence is through $f^\infty(t)$), with boundary conditions

$$\bar{T}_s^0 = \frac{T^{\text{in}}}{\theta_*} \quad \text{at } Y = 0, \qquad \bar{T}_s^0, \bar{T}_g^0 \to 1 \quad \text{as } Y \to \infty. \tag{5.182b}$$

The solution of (5.182) is

$$\bar{T}_s^0 = 1 - \left(1 - \frac{T^{\text{in}}}{\theta_*}\right)\exp(\chi Y), \quad \bar{T}_g^0 = 1 + \frac{\chi - 1}{Kf^\infty}\left(1 - \frac{T^{\text{in}}}{\theta_*}\right)\exp(\chi Y), \tag{5.183}$$

where the function of time $\chi(t)$ is given by

$$\chi = \frac{1}{2}\left(\frac{M}{Kf^\infty} + 1\right) - \frac{1}{2}\sqrt{\left(\frac{M}{Kf^\infty} - 1\right)^2 + 4M}. \tag{5.184}$$

5.7.4 Composite solutions for cases Ea and Eb

In case Ea, the characteristic curves originate at $x = 1$, and so all dependent variables are uniform to leading order outside region EI. In this case the steady-state composite solution is

$$C^{\text{Ea}} = C^0\left(\frac{x - s_0}{\delta}\right), \quad T_s^{\text{Ea}} = T_s^0\left(\frac{x - s_0}{\delta}\right) + T^{\text{in}}, \quad T_g^{\text{Ea}} = T_g^0\left(\frac{x - s_0}{\delta}\right) + T^{\text{in}}. \tag{5.185}$$

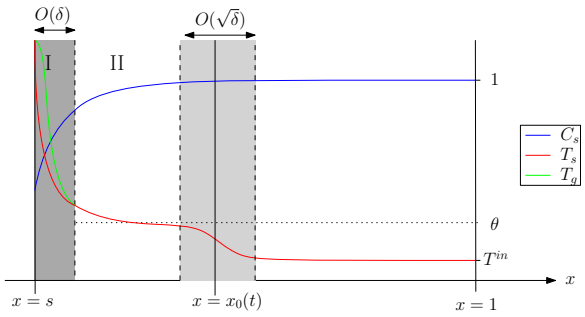

Figure 5.11: Schematic in a case where characteristics originate at both $x = 1$ and $x = s(t)$ (with initial condition $T = T^{\text{in}}$ for $x > s$).

The steady-state composite solution in case Eb, when characteristics originate at $x = s$, is

$$C^{\text{Eb}} = C^0\left(\frac{x - s_0}{\delta}\right), \tag{5.186a}$$

$$T_s^{\text{Eb}} = T_s^0\left(\frac{x - s_0}{\delta}\right) + \theta_* \bar{T}_s^0\left(\frac{1 - x}{\delta}\right) - \theta_*, \tag{5.186b}$$

$$T_g^{\text{Eb}} = T_g^0\left(\frac{x - s_0}{\delta}\right) + \theta_* \bar{T}_g^0\left(\frac{1 - x}{\delta}\right) - \theta_*. \tag{5.186c}$$

5.7.5 Additional structures in some time-dependent cases

Some time-dependent solutions will have the same structure as the steady-state cases Ea and Eb. Additional structures are also possible in situations where characteristic curves originate at both $x = 1$ and $x = s$. The boundary between these regions is the characteristic curve (5.174) which comes from $x = s$ at the point where $\dot{s} = \min(U, V)$ and subsequently $\dot{s} < \min(U, V)$ (shown in red in Figure 5.10). We denote this dividing characteristic curve by $x_0(t)$. Around this characteristic curve, there must be a thin layer in which diffusion comes back into the dominant balance, in order to smooth out the discontinuity between the two regions. Changing variables to move with the dividing characteristic curve, we set $x = x_0(t) + \xi y$ for some lengthscale ξ to be determined, and $T = \theta_* \tilde{T}$. The advection term is lost in this change of variables, and thus we require a balance between diffusion and the time-derivative of $\hat{T}$ at leading order. The lengthscale of such a transition layer must therefore be $\xi = \sqrt{\delta}$, and in this transition layer we obtain the leading-order problem

$$\frac{\partial \tilde{T}}{\partial t} = \frac{\partial^2 \tilde{T}}{\partial y^2}, \qquad \tilde{T} \to 1 \text{ as } y \to -\infty, \qquad \tilde{T} \to \frac{T^{\text{in}}}{\theta_*} \text{ as } y \to \infty, \tag{5.187}$$

along with an initial condition at the point where $x_0 = s$. A similarity solution of the form

$$\tilde{T} = 1 - \left(1 - \frac{T^{\text{in}}}{\theta_*}\right) \operatorname{erf}\left(\frac{y}{2\sqrt{t}}\right) \tag{5.188}$$

may be appropriate at late times. A schematic of the solution structure in this case is shown in Figure 5.11.

Combining the analyses above we can understand the time-dependent solutions from a number of initial states and values of $\dot{s}$. Of course, $\dot{s}$ is found as part of the solution of the boundary layer problem (5.152), so that the solution structure may change at different times, and not all ranges of $\dot{s}$ considered in this chapter may be obtainable from physically relevant initial conditions.

5.8 Case F: $\mu \gg \delta^{-1}$, very large heat transfer

In this section we consider $\mu \gg \delta^{-1}$, so that the heat transfer between phases is the dominant term in each of the heat equations, unbalanced by any other term on lengthscales greater than $O(\mu^{-1})$. Thus, on lengthscales greater than $O(\mu^{-1})$, we must have a single temperature $T_s = T_g =: T$ with $O(\mu^{-1})$ corrections. Writing $T_s = T + \mu^{-1}T_s^1$ and $T_g = T + \mu^{-1}T_g^1$, and adding the two heat equations at leading order in μ^{-1}, as in case E, we are left with a single equation for T,

$$\delta\left(\frac{\partial}{\partial t}(CT) + \frac{\partial}{\partial x}\left((Kf - C)T\right)\right) = \delta^2\frac{\partial^2 T}{\partial x^2} - \gamma C \exp\left(A\left(1 - \frac{1}{T}\right)\right). \tag{5.189a}$$

As in case E, we have absorbed the term for the heat transfer between phases due to the mass transfer into the advection term, by using the solid mass equation (5.1a). Since $T_s = T + O(\mu^{-1})$, the equations of conservation of mass, (5.1a) and (5.1b), may be written, to leading order in μ^{-1}, as

$$\delta\left(\frac{\partial C}{\partial t} - \frac{\partial C}{\partial x}\right) = -C\exp\left(A\left(1 - \frac{1}{T}\right)\right), \tag{5.189b}$$

$$\delta\frac{\partial f}{\partial x} = C\exp\left(A\left(1 - \frac{1}{T}\right)\right). \tag{5.189c}$$

The equations (5.189) are valid — at leading order in μ^{-1} — in the entirety of the domain except in boundary layers of width $O(\mu^{-1})$, in which T_s and T_g may differ at leading order. Since at $x = s$ we have imposed $T_s = T_g = \rho/s$ are equal, we do not encounter any such regions, and the system (5.189) holds at leading order throughout the domain. We would, however, need to include the $O(\mu^{-1})$ terms in order to look for corrections to the leading-order solutions.

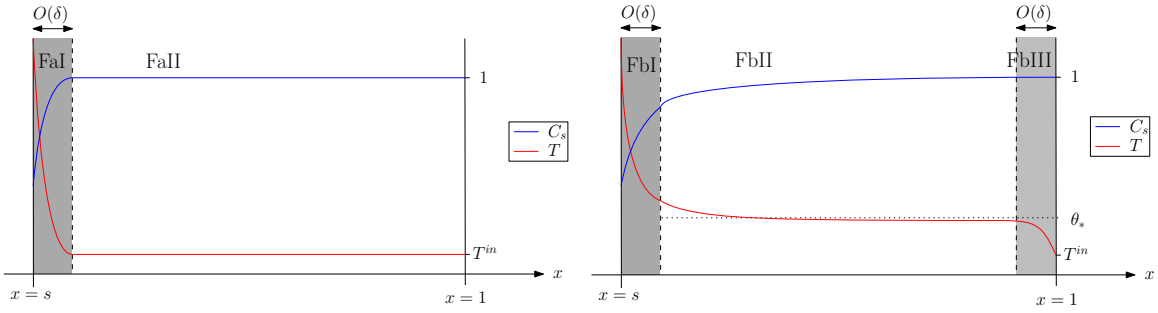

(a) Case Fa: $\mu \gg \delta^{-1}$, with $K(f_* + 1 - C_*) < 1$.

(b) Case Fb: $\mu \gg \delta^{-1}$, with $K(f_* + 1 - C_*) > 1$.

Figure 5.12: Schematic diagrams illustrating the asymptotic solution structures, in steady state, for case F $\mu \gg \delta^{-1}$.

As in Section 5.7, we find different behaviour depending on the relative sizes of $\dot{s}$, U, and V. The structure of solutions for large μ are very similar to those obtained in the case $\mu = O(\delta^{-1})$ as described in Section 5.7. We find identical behaviour to case E in the $O(1)$ region of the domain, but in the boundary layer(s) of width $O(\delta)$, the gas and solid temperatures remain equal at leading order in μ^{-1}.

Specifically, in the boundary layer of width δ located at $x = s$, denoted region FI, we make the usual change of variables $x = s + \delta X$. We find that $f = f_* + (1 + \dot{s})(C - C_*) + O(\delta)$. We expand the remaining dependent variables as

$$C = C^0(X,t) + O(\zeta), \qquad T = T^0(X,t) + O(\zeta), \qquad s = s_0(t) + O(\zeta), \tag{5.190}$$

where the switchback error $\zeta \ll 1$ is determined — as in case E — by the size of the temperature in the outer problem in case Fa, so that $\zeta = T^{\text{in}}$, and by the error in C in the outer region in case Fb, so that $\zeta = \theta_*^2$. At leading order, the equations (5.189b) and (5.189a) then become

$$(1 + \dot{s}_0)\frac{\partial C^0}{\partial X} = C^0 \exp\left(A\left(1 - \frac{1}{T^0}\right)\right), \tag{5.191a}$$

$$\frac{\partial}{\partial X}\left(\Big(K\big(f_* + (1 + \dot{s}_0)(C^0 - C_*)\big) - (1 + \dot{s}_0)C^0\Big)T^0\right) = \frac{\partial^2 T^0}{\partial X^2} - \gamma C^0 \exp\left(A\left(1 - \frac{1}{T^0}\right)\right). \tag{5.191b}$$

The leading-order boundary conditions are

$$C^0 = C_* \quad \text{and} \quad T^0 = \frac{\rho}{s_0} \qquad \text{at } X = 0, \tag{5.191c}$$

along with appropriate matching conditions as $X \to \infty$, which take the same forms as in case E, depending on whether the T characteristic curves move into or out of region FI.

Region	Spatial Variable	Size of Q	Dominant terms in (5.3)	Dependent Variables
FI	$x = s + \delta X$	$Q = O(1)$	1, 2, 3, 4, 5	C, f, $T_s = T_g = T$
FaII	x	$Q \ll \delta T^{\rm in}$	1	$C = 1$, $f = f^\infty$, $T_s = T_g = T^{\rm in}$
FbII	x	$Q = O(\delta\theta_*^2)$	1, 5	$C = 1 + \theta_*^2\hat{C}$, $T_s = T_g = \theta_*(1 + \theta_*\hat{T})$
FbIII	$x = 1 - \delta Y$	$Q \ll \delta\theta_*^2$	1, 2	$C = \bar{C}$, $f = f^\infty$, $T_s = T_g = \theta_*\bar{T}$

Table 5.6: Summary of the notation in each asymptotic region in the cases Fa ($\mu \gg \delta^{-1}$, $K(f_* + 1 - C_*) < 1$) and Fb ($\mu \gg \delta^{-1}$, $K(f_* + 1 - C_*) > 1$), corresponding to the diagrams in Figure 5.12.

The only other region which differs from case E is the boundary layer of width δ located at $x = 1$, in situations for which this boundary layer is needed. In this region, denoted region FbIII in the steady-state case Fb, we set $x = 1 - \delta Y$, and rescale $T = \theta_*\bar{T}$. As in case Eb, we see that for $\bar{T} < 1$, the chemical reaction rate is small, $O(\delta\theta_*^2)$, and drops out of the dominant balance. Thus we find from (5.189b)–(5.189c) that both $C = 1+O(\theta_*^2)$ and $f = f^\infty+O(\theta_*^2)$ are uniform at leading order. Expanding $\bar{T} = \bar{T}^0+O(\theta_*)$, at leading order the temperature equation (5.189a) therefore becomes

$$(1 - Kf^\infty)\frac{\partial\bar{T}^0}{\partial Y} = \frac{\partial^2\bar{T}^0}{\partial Y^2}, \tag{5.192}$$

which admits the solution

$$\bar{T}^0 = 1 - \left(1 - \frac{T^{\rm in}}{\theta_*}\right)\exp\left((1 - Kf^\infty)Y\right). \tag{5.193}$$

Here we have used the boundary conditions at $Y = 0$ and matching as $Y \to \infty$, as in region EbIII. The rest of the analysis for case F follows precisely as for case E, with $T_s = T_g$ in the majority of the domain. Steady-state solutions for each case Fa and Fb are illustrated in Figures 5.12a–5.12b, and the changes of variable are summarised in Table 5.6. The respective leading-order, steady-state composite solutions take the form

$$C^{\rm Fa} = C^0\left(\frac{x - s_0}{\delta}\right), \qquad T^{\rm Fa} = T^0\left(\frac{x - s_0}{\delta}\right) + T^{\rm in}, \tag{5.194}$$

and

$$C^{\rm Fb} = C^0\left(\frac{x - s_0}{\delta}\right), \qquad T^{\rm Fb} = T^0\left(\frac{x - s_0}{\delta}\right) + \theta_*\bar{T}^0\left(\frac{1 - x}{\delta}\right) - \theta_*. \tag{5.195}$$

5.9 Numerical solution of the leading-order problems in region I

In all cases A to F, we have found leading-order solutions analytically in all regions of the domain except for in region I. In this section, for all cases A to F we solve the relevant region-I model numerically. In particular, in all cases A to F, we solve for the leading-order position, $x = s_0$, of the free boundary as part of the solution of the region-I problem. The region-I problems are all quasi-steady in that the only time derivatives in the leading-order models are the $\dot{s}$ terms due to the moving interface. However, in cases C to F, the values or the form of the boundary conditions for region I depend on the genuinely time-varying behaviour in other regions of the domain. To examine the region-I problem in isolation, we therefore restrict to the steady-state region-I equations in all cases C to F. However, we will examine the quasi-steady behaviour for cases A and B, by viewing $\dot{s}_0$ as another parameter to solve for in the system. We therefore still treat the quasi-steady region-I problem for cases A and B as a boundary value problem.

The numerical solutions of the region-I boundary value problems studied in this section are computed in MATLAB using the inbuilt solver bvp4c. This uses a Runge-Kutta finite-difference formula and collocation method to choose and refine the mesh [53]. The algorithm is fourth-order accurate as the mesh is refined, uniformly over the domain [53].

5.9.1 Cases A–D

In cases A–D, we saw that the gas variables decoupled from the leading-order problem in region I, and we obtained the system (5.13), although with different matching conditions for cases C and D. The leading-order region-I problem in all cases A–D may be summarised as

$$-(\dot{s}_0 + 1)\frac{\partial C^0}{\partial X} = -C^0 \exp\left(A\left(1 - \frac{1}{T_s^0}\right)\right), \tag{5.196a}$$

$$-(\dot{s}_0 + 1)\, C^0 \frac{\partial T_s^0}{\partial X} = \frac{\partial^2 T_s^0}{\partial X^2} - \gamma C^0 \exp\left(A\left(1 - \frac{1}{T_s^0}\right)\right), \tag{5.196b}$$

with the boundary conditions

$$C^0 = C_*, \quad T^0 = \frac{\rho}{s_0}, \quad \text{at } X = 0, \tag{5.196c}$$

and

$$T_s^0 \to 0, \qquad C^0 \to \begin{cases} 1, & \text{in cases A and B,} \\ C^\infty, & \text{in cases C and D,} \end{cases} \qquad \text{as } X \to \infty. \tag{5.196d}$$

In Cases C and D, we found that the value of C^∞ was given in terms of s_0, F_s, and G_s. In steady state, we have (from (5.64) and (5.96))

$$C^\infty = \begin{cases} 1 - F_s K \frac{G_s - \hat{T}_g^0|_{x=1}}{\gamma + K\hat{T}_g^0|_{x=1}} & \text{in case C,} \\ 1 - \frac{KF_sG_s}{\gamma} & \text{in case D.} \end{cases} \tag{5.197}$$

The steady-state values F_s and G_s are

$$F_s = f_* + C^\infty - C_*, \tag{5.198}$$

$$G_s = \frac{\frac{f_*\rho}{s_0} + K^{-1}\int_{\bar{X}=0}^{\infty} T_s^0 C^0 \exp\left(A\left(1 - \frac{1}{T_s^0}\right)\right) \mathrm{d}\bar{X}}{f_* + C^\infty - C_*}, \tag{5.199}$$

and in case C, $\hat{T}_g^0|_{x=1}$ is given by

$$\hat{T}_g^0\Big|_{x=1} = -\frac{\gamma W(a_{\mathrm{C}}(1))}{K(1 + W(a_{\mathrm{C}}(1)))}, \tag{5.200}$$

where

$$a_{\mathrm{C}}(1) = -\frac{KG_s}{\gamma + KG_s} \exp\left(-\frac{1}{\gamma + KG_s}\left(\frac{\gamma\mu}{KF_s}(1 - s_0) + KG_s\right)\right). \tag{5.201}$$

To reduce the required domain size for numerical solutions, we replace the far-field condition $T_s^0 \to 0$ with the mixed condition

$$\frac{\partial T_s^0}{\partial X} + C^0 T_s^0 \to 0, \tag{5.202}$$

derived by considering the limit $X \to \infty$ in (5.196b). In Figure 5.13 we show the numerical error in the solution parameter $\dot{s}_0$ as the domain size is increased using the far-field condition (5.202).

In steady state (setting $\dot{s}_0 = 0$), the system (5.196) is a third-order system, with four boundary conditions, allowing us to also solve for s_0 as part of the solution. In cases A and B we find quasi-steady solutions by prescribing the value of s_0 in (5.196), and solving for $\dot{s}_0$ as part of the solution. We could equivalently prescribe $\dot{s}_0$ (as we do for the steady-state case) and solve for s_0.

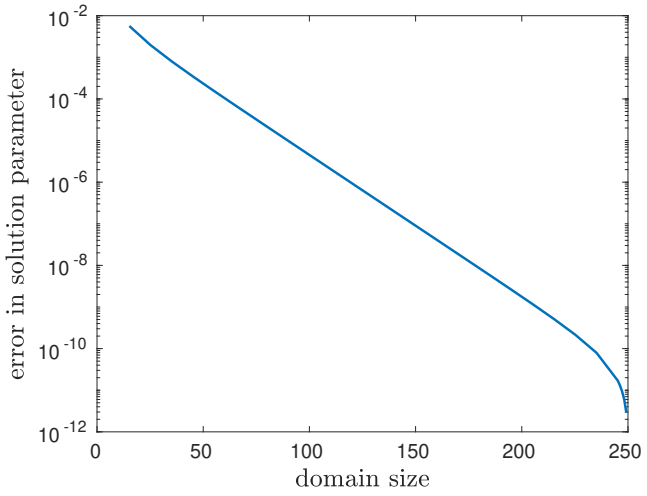

Figure 5.13: The error in the solution parameter $\dot{s}_0$ (relative to the solution s_0 at the largest domain size computed) as the domain size is increased, for the case A or B region-I problem (5.196), with matching condition (5.202).

5.9.1.1 Numerical solutions in case A or B

Numerical solutions of (5.196) are shown in Figure 5.14 in case A or B. We sweep through a range of values of s_0, and so can understand the time-evolution of the entire system by plotting the solution $\dot{s}_0$ as a function of s_0, as shown in Figure 5.14a. We see that $\dot{s}_0$ becomes large and positive as $s_0 \to 0$, and that as s_0 becomes large, $\dot{s}_0 \to -1$, which is the dimensionless speed of the solid material. We observe that there is a single steady-state solution (where $\dot{s}_0 = 0$) at $s_0 \approx 0.106$. Since $\dot{s}_0 > 0$ for s_0 below the steady state, and $\dot{s}_0 < 0$ for s_0 above the steady state, this unique steady-state solution of (5.196) is stable. In Figure 5.14b, we show the quasi-steady solution profiles T_s^0 and C^0 for three different values of s_0, marked with circles in Figure 5.14a, including the steady-state solution (dashed lines). For smaller s_0, the surface temperature at $X = 0$ is greater, as required by the boundary condition (5.196c). We also see that T_s^0 decays more slowly to zero for larger s_0. The C^0 profile does not vary significantly with s_0, although we see variation in C^0 for a slightly larger region of X for larger s_0, since the temperature T_s^0 decays more slowly.

In Figure 5.15 we investigate how the solution of (5.196) in case A or B depends on the model parameters A and γ. In Figures 5.15a and b, we plot $\dot{s}_0$ against s_0, and the steady-state solutions C^0 and T_s^0, respectively, for three values of A, the dimensionless activation energy of the chemical reaction. The temperature profile $T_s^0(X)$ at the steady state varies only slightly with A, but we see that for larger A the rate of reaction is faster, so that the steady-state C^0 varies from C_* to 1 over a shorter

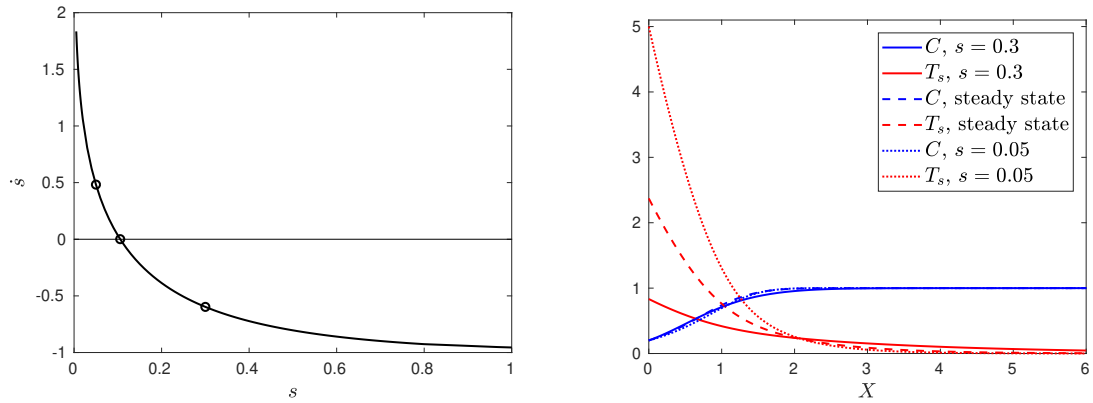

(a) $\dot{s}_0$ as a function of s_0.

(b) Quasi-steady solutions

Figure 5.14: Numerical solutions of the region-I problem (5.196) for case A or B, taking parameter values $\gamma = 1$, $A = 1$, $C_* = 0.2$, and $\rho = 0.25$.

region of X. We also observe from Figure 5.15a that for larger A the time-evolution curve is steeper, so that the system evolves more quickly towards its steady state.

Increasing the dimensionless energy consumed in the reaction, γ, has the effect of decreasing s_0, as seen in Figure 5.15c. In particular, the steady-state position s_0 decreases as γ increases, so that the surface temperature $T_s^0(0)$ increases with increasing γ, as seen in Figure 5.15d. The temperatures must be higher at the steady state in order for there to be enough energy in the system for the chemical reactions to consume all of the incoming solid material.

We do not show the variation of solutions with the parameter ρ, as this simply introduces a scaling of s_0, as may be seen from the form (5.196) of the model, or indeed of the full model (5.1).

5.9.1.2 Numerical solutions in case C

We show steady-state numerical solutions of (5.196) for case C in Figure 5.16. The profiles of C^0 and T_s^0 are similar in shape to those plotted for case A or B in Figure 5.15, but now the far-field value $C^\infty < 1$ is determined as part of the solution. Compared with solutions for case A or B, the steady-state solutions have a larger s_0, and correspondingly cooler temperatures T_s^0. This is because some material consumption occurs in the outer region CII, so C^∞ is smaller and we do not require such high temperatures in order for the chemical reaction to balance the influx of material. There are additional parameters in the region CI model compared to case A and B, namely μ, K, and f_*, which come into the problem through the value of C^∞. In Figure 5.16 we investigate varying f_* and μ (while keeping $\mu = O(1)$). We do not

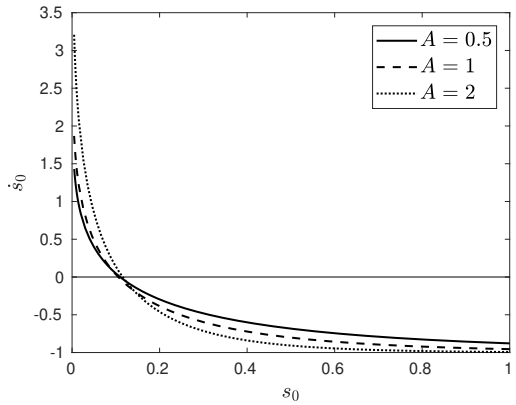

(a) $\dot{s}_0$ as a function of s_0, varying A.

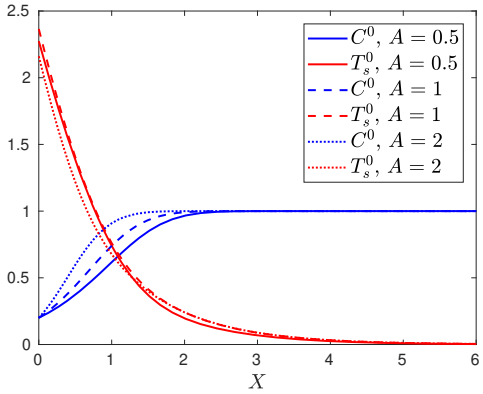

(b) Steady-state solutions, varying A.

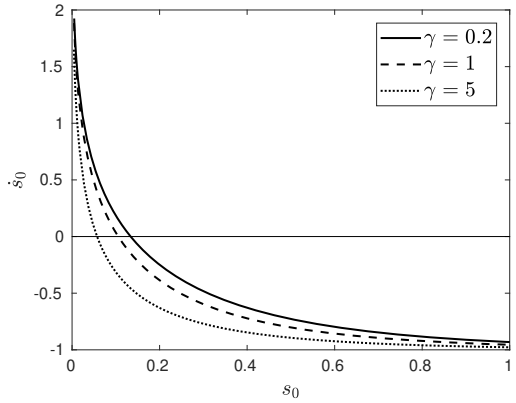

(c) $\dot{s}_0$ as a function of s_0, varying γ.

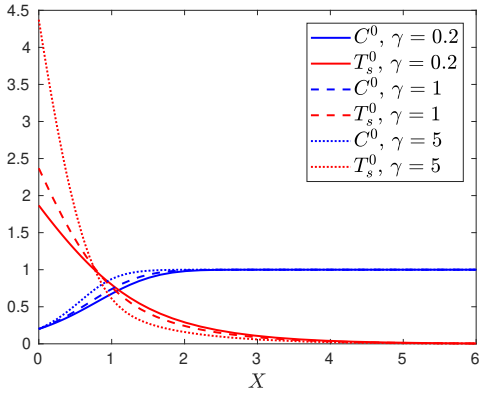

(d) Steady-state solutions, varying γ.

Figure 5.15: Numerical solutions of (5.196) for case A or B, varying the parameter values A (top) and γ (bottom). Unless otherwise stated, we take parameter values $\gamma = 1$, $A = 1$, $C_* = 0.2$, and $\rho = 0.25$.

show the variation with K as this cannot easily be controlled in practice, and does not affect the solution much so long as K is not too small.

As well as showing the solution profiles C^0 and T_s^0 for various f_* and μ, in Figures 5.16a and c, respectively, we also show the variation of the solution parameters s_0, C^∞, F_s, and G_s, sweeping through f_* and μ, in Figures 5.16b and d, respectively. For larger f_*, there is a greater flux of gas, and so more heat may be transferred from the gas to the solid in the outer region of the domain. We see that C^∞ decreases as f_* increases, since more material is consumed in the outer region. Less heat is therefore needed in region I, and so s_0 increases. Similarly, we see that as μ increases, more material consumption can occur outside of region CI, and so C^∞ decreases, while s_0 increases. The gas flux F_s leaving region CI is a linear shift of C^∞ in this steady-state case, so decreases similarly. As s_0 increases with μ or f_*, the temperature T_s^0 becomes

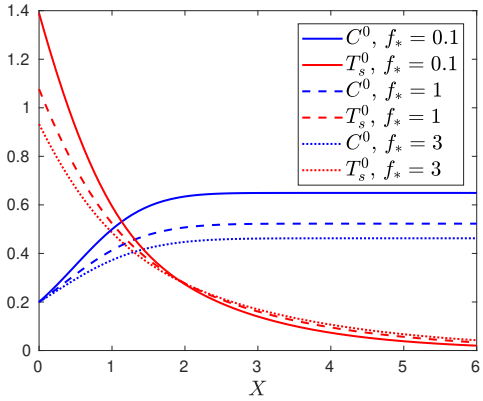

(a) Steady-state solutions, varying f_*.

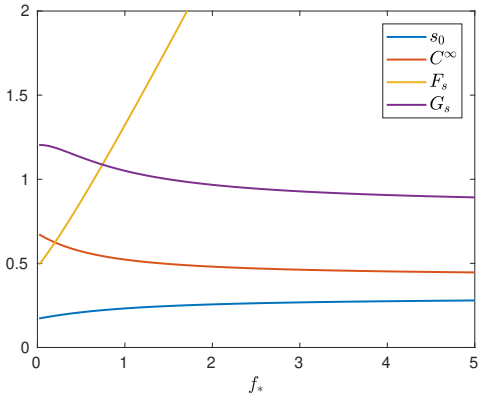

(b) Steady-state solution parameters, varying f_*.

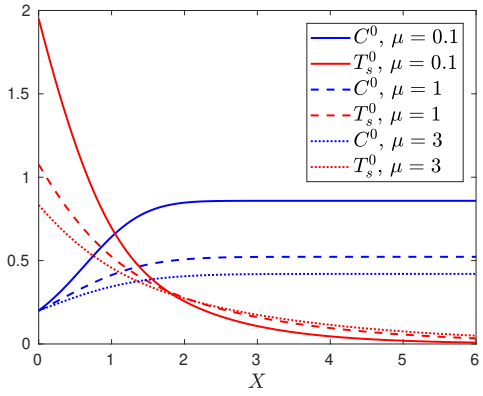

(c) Steady-state solutions, varying μ.

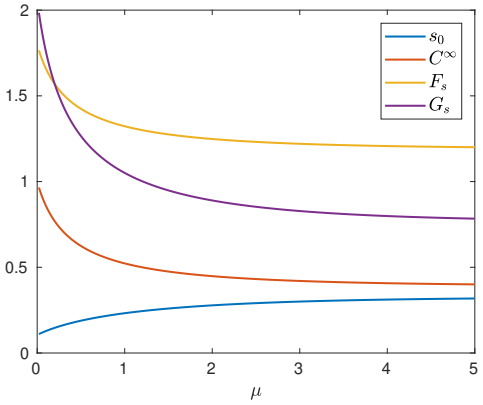

(d) Steady-state solution parameters, varying μ.

Figure 5.16: Numerical solutions of (5.196) for case C, varying the parameter values f_* (top) and μ (bottom). Unless otherwise stated, we take parameter values $\gamma = 1$, $A = 1$, $C_* = 0.2$, $\rho = 0.25$, $K = 0.66$, $f_* = 1$, and $\mu = 1$.

cooler, and this is also reflected in the decreasing temperature G_s of the gas leaving region CI.

5.9.1.3 Numerical solutions in case D

Solutions of the region-I problem (5.196) in case D depend on f_* and K as in case C, but do not explicitly depend on the size of μ, since the far-field concentration is $C^\infty = 1 - KF_sG_s/\gamma$. This is because the gas loses all its heat to the chemical reactions (to leading order) in the outer region, and for the region-DI analysis it does not matter exactly where in the outer region this happens.

The flux of gas through the $x = s$ boundary, f_*, is a crucial parameter for de-

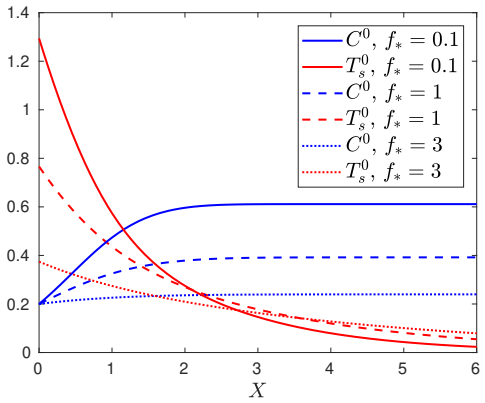

(a) Steady-state solutions, varying f_*.

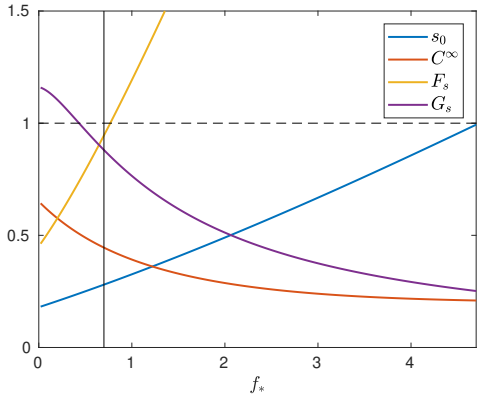

(b) Steady-state solution parameters, varying f_*.

Figure 5.17: Steady-state numerical solutions of (5.196) for case D, varying f_*. The vertical black line in (b) at $f_* = C_* - 1 + 1/K$ separates case Da (to the left) and case Db (to the right). We take the other parameter values $\gamma = 1$, $A = 1$, $C_* = 0.2$, $\rho = 0.25$, and $K = 0.66$.

termining the gas flux F_* at the right of the domain, and thus in separating the cases Da and Db. We show the dependence of solutions to the leading-order region-I model (5.196) on f_* in Figures 5.17a and b. Since $f = C - C_* + f_*$ everywhere in steady state, we must have $F_* = 1 - C_* + f_* + O(\eta)$. Thus, to leading order, $KF_* < 1$ if $f_* < C_* - 1 + 1/K$. The vertical black line in Figure 5.17b shows this value $C_* - 1 + 1/K$, so that case Da is to the left of this line, while case Db is to the right. As was true in case C, we see that C^∞ decreases with f_*, although much more quickly in case D, rapidly approaching $C_* = 0.2$ for these solutions. Thus for large f_*, the majority of the solid material is consumed outside of region I. Meanwhile, we see that s_0 increases with f_*, again much more quickly than in case C. By the relatively small value of $f_* \approx 4.6$, s_0 reaches the edge of the domain at $x = 1$.

5.9.2 Case E

In case E the leading-order region-I problem includes all the physics of the original system. The form of the matching condition as $X \to \infty$ depends on the direction of characteristic curves in the outer problem. In steady state, the form of the matching condition is determined by the model parameters, with the steady-state case Ea when $K(f_* + 1 - C_*) < 1$, and Eb when $K(f_* + 1 - C_*) > 1$. The steady-state region-EI

model is given by $f = f_* + C - C_*$, with

$$-\frac{\mathrm{d}C^0}{\mathrm{d}X} = -C^0 \exp\left(A\left(1 - \frac{1}{T_s^0}\right)\right), \tag{5.203a}$$

$$-C^0\frac{\mathrm{d}T_s^0}{\mathrm{d}X} = \frac{\mathrm{d}^2T_s^0}{\mathrm{d}X^2} + M(T_g^0 - T_s^0) - \gamma C^0 \exp\left(A\left(1 - \frac{1}{T_s^0}\right)\right), \tag{5.203b}$$

$$K\frac{\mathrm{d}}{\mathrm{d}X}\big((f_*+C^0 - C_*)T_g^0\big) = T_s^0 C^0 \exp\left(A\left(1 - \frac{1}{T_s^0}\right)\right) - M(T_g^0 - T_s^0), \tag{5.203c}$$

with boundary conditions

$$C^0 = C_*, \quad T_s^0 = T_g^0 = \frac{\rho}{s^0} \quad \text{at } X = 0, \tag{5.203d}$$

and in case Ea

$$C^0 \to 1, \quad T_s^0 \to 0 \quad \text{as } X \to \infty, \tag{5.203e}$$

while in case Eb

$$C^0 \to 1, \quad (K(f_* + 1 - C_*) - 1)\frac{\mathrm{d}T_s^0}{\mathrm{d}X} + \gamma \exp\left(A\left(1 - \frac{1}{T_s^0}\right)\right) \to 0 \quad \text{as } X \to \infty. \tag{5.203f}$$

To reduce the required domain size for the numerical solutions, in case Ea we analyse the system as $X \to \infty$ and hence replace the far-field condition (5.203e) for T_s^0 with

$$\frac{\mathrm{d}T_s^0}{\mathrm{d}X} + (K(f_* + 1 - C_*) - 1)T_s^0 \to 0. \tag{5.204}$$

Numerical solutions for both cases Ea and Eb are shown in Figure 5.18, varying the parameters f_* and M, on the left and right of the plot, respectively. For our choice of parameters K and C_*, we are in case Ea when $f_* < 0.7$, and in case Eb when $f_* > 0.7$. We see that s_0 increases with f_* in both cases Ea and Eb, so that temperatures are lower at $X = 0$. We also see that as f_* increases, the decay rate of the temperatures becomes much slower. The solutions appear to vary continuously as we pass from case Ea to Eb, at the critical value 0.7. On the right of Figure 5.18, we see that the solution s_0 decreases slightly with M, and the temperatures at $X = 0$ correspondingly increase slightly. The rate of heat transfer between the two phases increases with M, and the rate at which these temperatures decay to zero also increases. We observe similar dependence on M for both cases Ea and Eb.

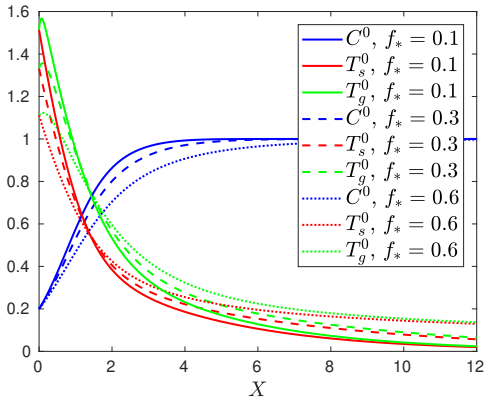

(a) Steady-states in case Ea, varying f_*.

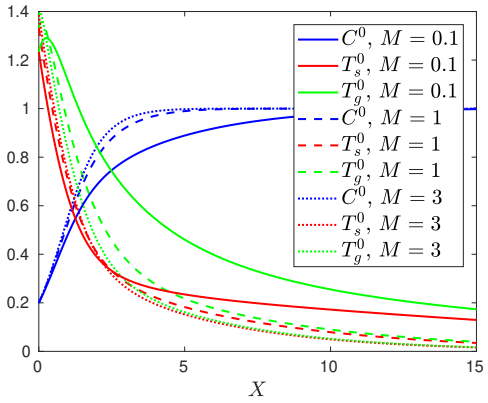

(b) Steady-states in case Ea, varying M.

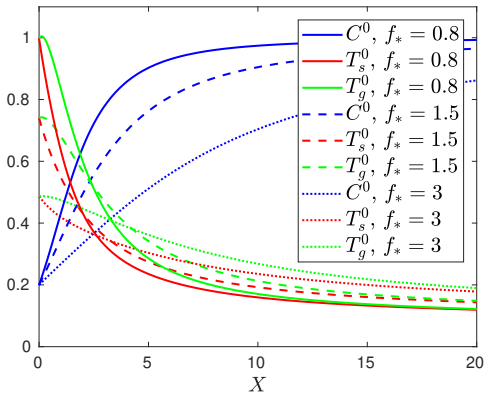

(c) Steady-states in case Eb, varying f_*.

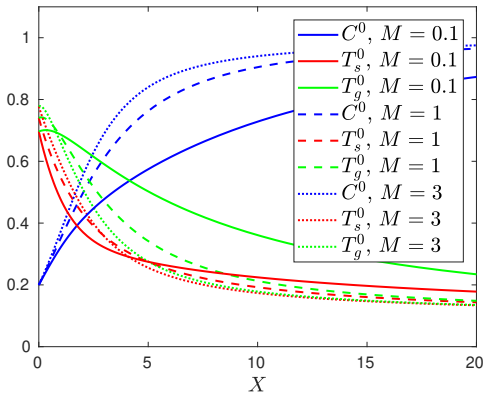

(d) Steady-states in case Eb, varying M.

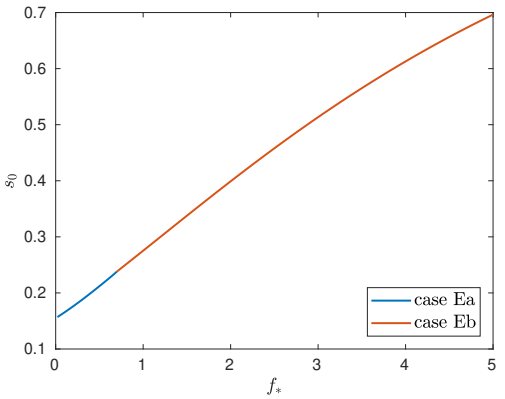

(e) Steady-state s_0, varying f_*.

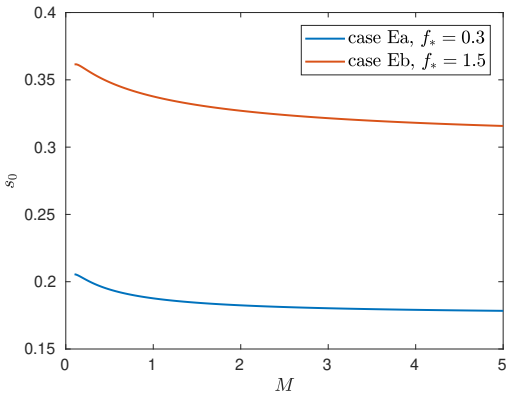

(f) Steady-state s_0, varying M.

Figure 5.18: Steady-state numerical solutions of (5.203) for cases Ea and Eb, varying the parameter values f_* (left) and M (right). Unless otherwise stated, we take parameter values $\gamma = 1$, $A = 1$, $C_* = 0.2$, $\rho = 0.25$, $K = 0.66$, $M = 1$, and $f_* = 0.3$ in case Ea, but $f_* = 1.5$ in case Eb.

5.9.3 Case F

In case F, both temperatures are equal throughout the domain. The leading-order steady-state region FI problem is

$$\frac{\mathrm{d}^0 C}{\mathrm{d}X} = C^0 \exp\left(A\left(1 - \frac{1}{T^0}\right)\right), \tag{5.205a}$$

$$\frac{\mathrm{d}}{\mathrm{d}X}\left(\Big(K\big(f_* + 1)(C^0 - C_*)\big) - C^0\Big)T^0\right) = \frac{\mathrm{d}^2 T^0}{\mathrm{d}X^2} - \gamma C^0 \exp\left(A\left(1 - \frac{1}{T^0}\right)\right), \tag{5.205b}$$

with

$$C^0 = C_*, \quad T^0 = \frac{\rho}{s^0} \quad \text{at } X = 0, \tag{5.205c}$$

and in case Fa (when $K(f_* + 1 - C_*) < 1$)

$$C^0 \to 1, \quad T^0 \to 0 \quad \text{as } X \to \infty, \tag{5.205d}$$

while in case Fb (when $K(f_* + 1 - C_*) > 1$)

$$C^0 \to 1, \quad (K(f_* + 1 - C_*) - 1)\frac{\mathrm{d}T^0}{\mathrm{d}X} + \gamma \exp\left(A\left(1 - \frac{1}{T^0}\right)\right) \to 0 \quad \text{as } X \to \infty. \tag{5.205e}$$

To reduce the required numerical domain, in case Fa, we use the far-field condition

$$\frac{\mathrm{d}T^0}{\mathrm{d}X} + (K(f_* + 1 - C_*) - 1)T^0 \to 0. \tag{5.206}$$

Numerical solutions of (5.205) in both cases Fa and Fb are shown in Figure 5.19 where we vary the parameter f_*, with similar qualitative results to case E.

5.10 Comparison of composite and numerical steady-state solutions

Having computed the solution of the region-I problem, we can then construct the composite solution for each case A to F from the analytical forms found in Sections 5.3–5.8. We also compute numerical solutions of the full model (5.1) in steady state, using the same MATLAB solver bvp4c, having rescaled the spatial variable x in order to solve the system on a fixed domain. In this section, we compare the numerical solutions of (5.1) with the steady-state composite asymptotic solutions. Since we have restricted to steady-state solutions of the region-I model (except for the quasi-steady solutions for cases A and B), we only consider steady-state solutions in this section.

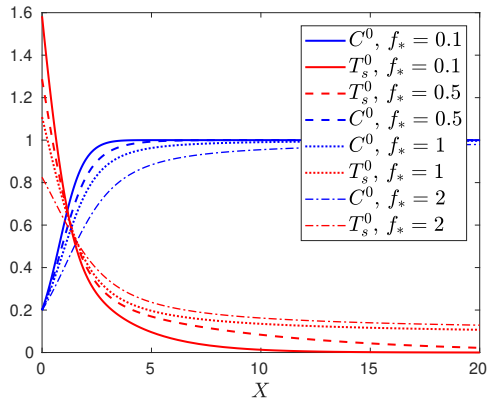

(a) Steady-states in cases Fa and Fb, varying f_*.

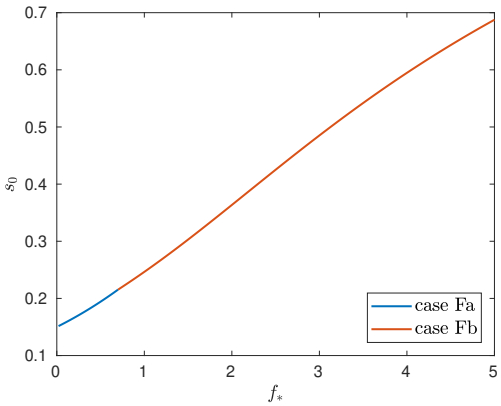

(b) Steady-state s_0, varying f_*.

Figure 5.19: Steady-state numerical solutions of (5.205) for cases Fa and Fb, varying the parameter f_*. We take the other parameter values $\gamma = 1$, $A = 1$, $C_* = 0.2$, $\rho = 0.25$, $K = 0.66$.

In Figures 5.20 and 5.21 we compare the steady-state composite solution to the steady-state numerical solutions of the full model (5.1). For the numerical solutions of both the full model (5.1), and of the region-I problem as discussed in Section 5.9, we ensure the numerical error is two orders of magnitude smaller than δ, and so well below the expected error in the composite solutions. In the insets for each figure we show the same solutions but looking more closely at region I, which is too narrow to see clearly otherwise.

In all cases, we observe that the error in s_0 is larger than the width of the $O(\delta)$ region I, as expected. In particular, the error is $O(T^{\text{in}})$ in case A, $O(\eta)$ in cases B, C, and D, $O(T^{\text{in}})$ again in cases Ea and Fa, and $O(\theta_*^2)$ in cases Eb and Fb. In all cases, the maximal error is due to the switchback correction; in cases A–D, Ea and Fa this is the size of the small but non-zero temperature in region II, while in cases Eb and Fb this is the size of the error in C. Although the position of s_0 has error greater than $O(\delta)$, the function profiles in region I appear in all cases to have the correct shape.

We note that the leading-order problem (5.13) in regions AI and BI are identical, and that region I contains the majority of the variation in the solutions in these cases. In Figure 5.20a with $\mu = 0$ we see very good agreement between the numerical and composite solutions, since the error is $O(T^{\text{in}})$ in this case. For case B, shown in Figure 5.20b, there is a small $O(\mu) = O(\eta_B)$ amount of material consumption outside of region I, but this is not taken into account in our leading-order asymptotic structure. Thus in this case the leading-order solution s_0 is below the true value,

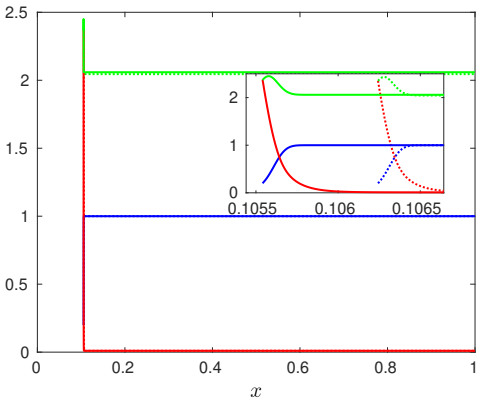

(a) Case A, $\mu = 0$.

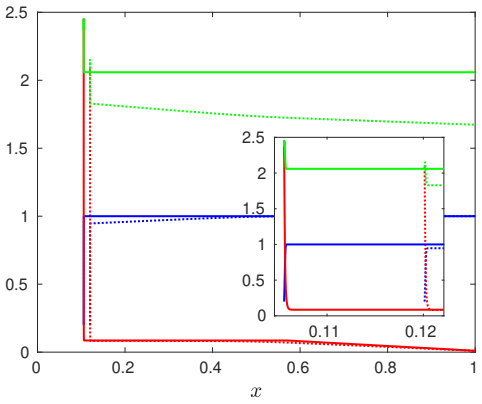

(b) Case B, $\mu = \eta_B = 0.09$.

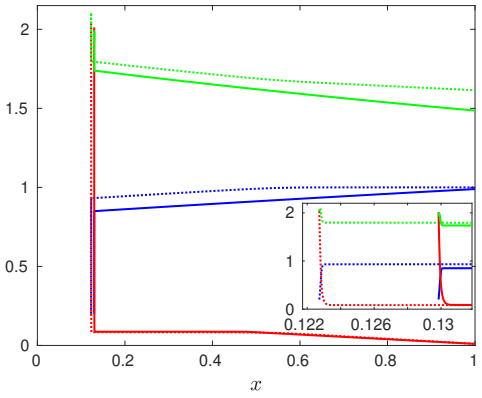

(c) Case C, $\mu = 0.1$.

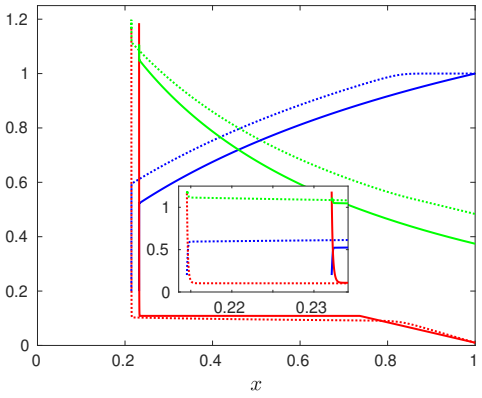

(d) Case C, $\mu = 1$.

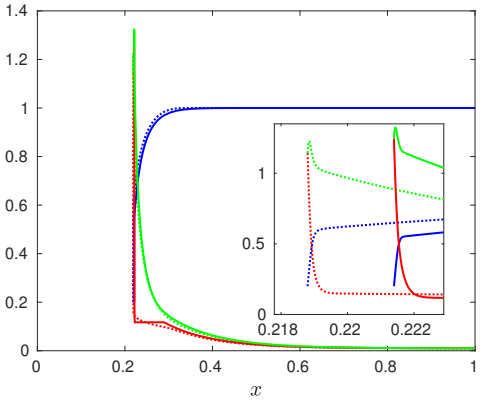

(e) Case Da, $\mu = 25$, $f_* = 0.3$.

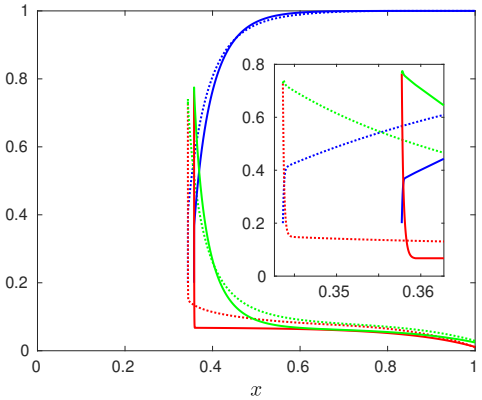

(f) Case Db, $\mu = 25$, $f_* = 1.2$.

Figure 5.20: Numerical steady-state solutions of (5.1) (dotted lines) and composite solutions as derived in Sections 5.3–5.6 (solid lines), with T_s red, T_g green, and C blue. The insets show the same solutions, near the free boundary $x = s$. In all cases we take $\delta = 10^{-4}$, $A = \gamma = 1$, $\rho = 0.25$, $K = 0.66$, $C_* = 0.2$, $T^{\text{in}} = 0.01$, and unless otherwise stated $f_* = 1$.

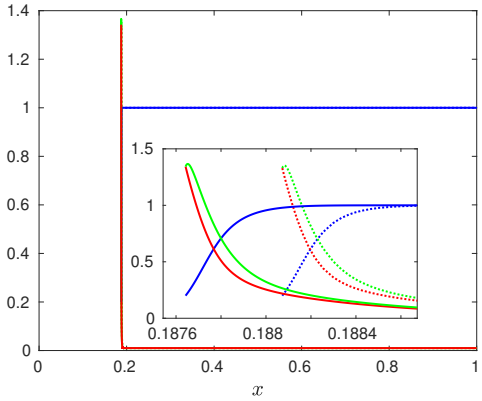

(a) Case Ea, $\mu = \delta^{-1}$, $f_* = 0.3$.

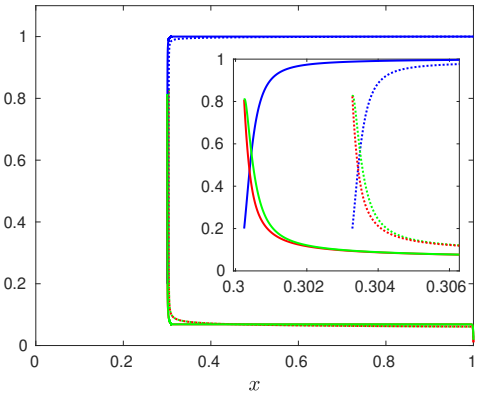

(b) Case Eb, $\mu = \delta^{-1}$, $f_* = 1.2$.

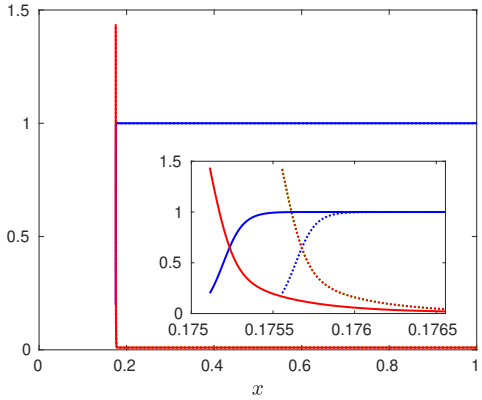

(c) Case Fa, $\mu = 10^3\delta^{-1}$, $f_* = 0.3$.

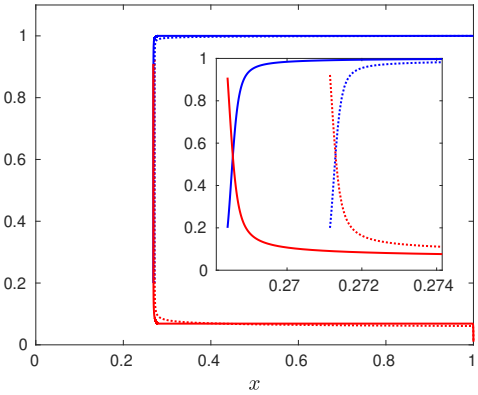

(d) Case Fb, $\mu = 10^3\delta^{-1}$, $f_* = 1.2$.

Figure 5.21: Numerical steady-state solutions of (5.1) (dotted lines) and composite solutions as derived in Sections 5.7–5.8 (solid lines), with T_s red, T_g green, and C blue. The insets show the same solutions, near the free boundary $x = s$. In all cases we take $\delta = 10^{-4}$, $A = \gamma = 1$, $\rho = 0.25$, $K = 0.66$, $C_* = 0.2$, and $T^{\text{in}} = 0.01$.

since the material needs to be hotter in order for all the material consumption to take place in region BI.

For cases C and D, an $O(1)$ amount of material consumption occurs outside of region I. The steady-state position of the free boundary s therefore increases, since the temperatures in region I do not need to be so high, as less material consumption needs to happen in region I. This can also be understood in terms of an energy balance: since less heat is lost to the system through hot gas flowing out through $x = 1$, the system needs less heating overall to stay in steady state. Unlike in case B, the asymptotic composite solutions now account for the material consumption outside of region I, and so the leading-order value s_0 is seen to be within $O(\eta)$ of the true value in all cases. However, this value of s_0 is now an overestimate for the true value of s

(unlike in case B, where s_0 is below the true value of s). In case C this is because there is material consumption occurring throughout region CII, which is the entire domain up to $O(\eta)$. Since in reality no material consumption occurs within the $O(\eta)$ boundary layer CIV, the leading-order solution overestimates the amount of material consumption occurring in region CII, and thus overestimates s_0. In addition, as μ becomes large, the leading-order gas temperature $\hat{T}_g^0$ in region CII is assumed to stay $O(1)$ throughout the domain. However, even for the relatively small $\mu = 1$, shown in Figure 5.20d, by $x = 1$ we see T_g getting fairly small. As T_g gets close to T_s, the leading-order asymptotic solution overestimates the heat transferred from the gas to the solid, and thus overestimates the chemical reaction rate. In Figure 5.20c, we take $\mu = 0.1 \approx \eta_B$, so that the numerical solution of the full model (5.1) is almost identical to that shown in Figure 5.20b. The asymptotic composite solution using the structure of case C does a reasonable job of capturing the T_s profile as well as the T_g and C curves, despite the fact that the "boundary layer" CIV now fills the majority of the domain.

For Case D, all the thermal energy leaving region DI in the hot gas is used for chemical reactions in the outer domain (with a small error less than $O(\eta_D)$). Thus we see better agreement between the asymptotic composite solutions and numerical solutions of the full model than in case C, despite the error $O(\eta_D)$ being larger for case D than for case C. For cases E and F, the two temperatures are equal, or differ only in the $O(\delta)$ regions. We see good agreement between the solution of the full problem (5.1) and our composite solutions in all cases shown in Figure 5.21.

5.10.1 Solution dependence on the model parameters

Finally, we investigate how our composite solutions depend on some of the model parameters. We have already explored some of the model parameters in Section 5.9 when solving the region-I problems. In this section we focus on two parameters which are easiest to alter in a physical system, namely the input temperature of the solid material, T^{in}, and the gas flux through the free boundary, f_* (although the flux of gas out of the crater cannot be easily controlled for the silicon furnace, in other possible applications such as rotary kilns, f_* is an readily-varied parameter). The velocity of the solid material — another variable that might be relatively easily altered in practice — has been scaled out in the nondimensionalisation through the parameter δ, which we have assumed is always small.

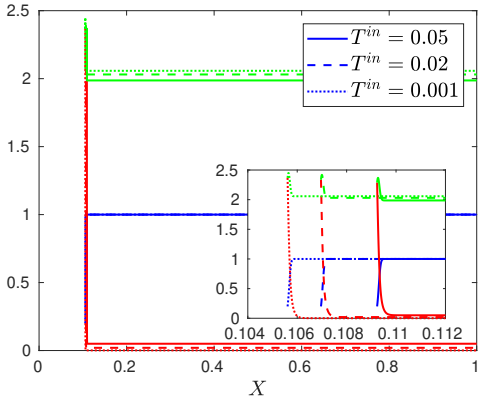

(a) Steady-state solutions in case A

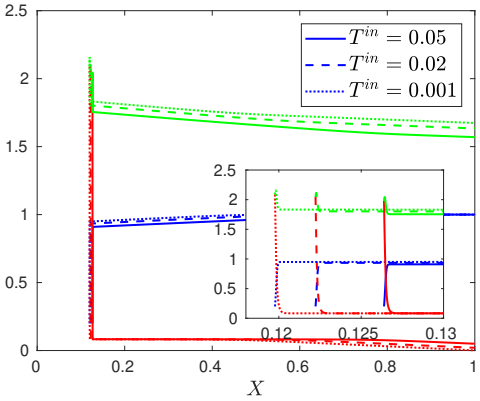

(b) Steady-state solutions in case B

Figure 5.22: Numerical steady-state solutions of the full problem (5.1) for cases A ($\mu = 0$) and B ($\mu = \eta_B = 0.09$), varying T^{in}. As usual T_s is shown in red, C in blue, and T_g in green. We take parameter values $\delta = 10^{-4}$, $f_* = 1$, $\gamma = 1$, $A = 1$, $C_* = 0.2$, and $\rho = 0.25$.

5.10.1.1 Input solid temperature T^{in}

The input temperature, T^{in}, of the solid material might vary in practice, for instance, with the season or weather, or by deliberately pre-heating the raw materials. So long as T^{in} is sufficiently small that (5.2) still holds, our asymptotic analysis suggests that this will have little effect on the system: in cases C, Db, Eb, and Fb, the size of T^{in} only affects the solution in a boundary layer at $x = 1$. In cases Da, Ea, and Fa, the material has temperature T^{in} through the majority of the domain, but this does not have a significant effect on the solution in region I, as the error here is $O(\theta_*^2)$, which is expected to be larger than T^{in}.

The value of T^{in} has the most significant effect on cases A and B. In case A, the error in the leading-order asymptotic expansion is $O(T^{\text{in}})$. From the numerical solutions of the full model (5.1) in Figure 5.22a, we see that s increases slightly with T^{in}, since there is more heat entering the system in the warmer solid material, and the temperatures at $x = s$ decrease accordingly. In case B, the position v of the transition layer BIII, given by (5.44), is

$$v = 1 - \frac{1 - \bar{T}^{\text{in}}}{MG_s^0}. \tag{5.207}$$

in steady state, which increases linearly with $\bar{T}^{\text{in}} = T^{\text{in}}/\eta_B$. Thus, the warmer the incoming material, the more quickly it is heated up to the reacting temperature $O(\eta_B)$. This can be seen in the solutions of the full model (5.1) shown in Figure 5.22b.

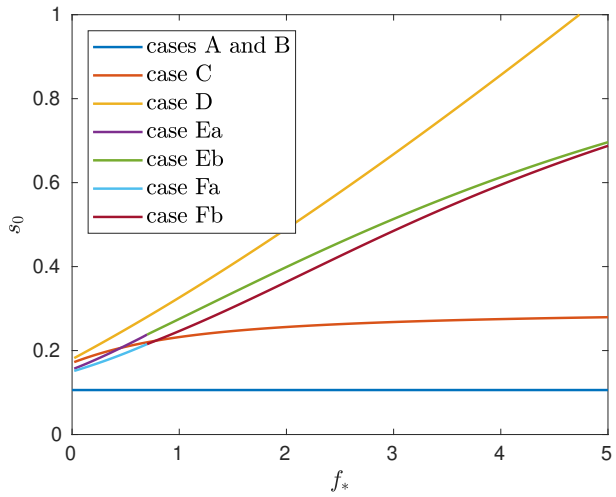

Figure 5.23: The leading-order steady-state position of the free boundary, s_0, as a function of the gas flux, f_*, for all cases A–F. We take parameter values $\gamma = 1$, $A = 1$, $C_* = 0.2$, $K = 0.66$, and $\rho = 0.25$ throughout, with $\mu = 1$ in case C, and $M = 1$ in case E.

5.10.1.2 Gas flux f_* through the free boundary

In Section 5.9 we explored the effect of varying f_* on the solution of the region-I problems for cases C to F. We summarise these findings by showing the leading-order position s_0 of the free boundary as a function of f_* for all cases A–F in Figure 5.23. We note that s_0 increases with f_* for all values of $\mu > 0$, since there is a greater flux of hot gas through the material, so that more energy is supplied to the system, and hence there can be greater heat transfer from the gas to the solid.

We understand this behaviour by thinking about the heat balance in the model. In all cases A to F, there are two sources of heat to the system: the heating of the solid material at $x = s$, and also the flux of hot gas through $x = s$. In cases A to C, energy is lost due to the hot gas escaping through the $x = 1$ boundary. This occurs since μ is relatively small, so while more energy is supplied to the system at $x = s$ for greater f_*, more is also lost through $x = 1$. However, in cases D–F, all of the energy entering the system at $x = s$ is used for the chemical reaction to leading order, so that s_0 increases more dramatically with f_* than for case C. The material consumption occurs in region I for cases E and F, but in both regions DI and DII for case D.

5.11 Discussion

In this chapter we have used the method of matched asymptotic expansions to investigate the solution structures of (5.1) characterised by an interacting counter-current flow and an endothermic chemical reaction, with the reaction rate taken to be an Arrhenius function of the solid temperature. We have considered $\delta > 0$ small, and found a range of distinguished limits corresponding to different sizes of μ.

For small $\mu \leq O(\eta_B)$ and for large $\mu \geq O(\delta^{-1})$, we found that all chemical reaction and material consumption at leading order occur in a boundary layer (region I) of width $O(\delta)$ at the free boundary $x = s$, which is heated by the s-dependent solid surface temperature. For $O(1) \leq \mu \ll \delta^{-1}$, however, we found $O(1)$ material consumption in both region I and in (part of) the outer region of the domain. For $\mu \leq O(\eta_B)$, the leading-order model is quasi-steady, and so the dynamics of the full system may be easily understood. We found time-dependent solutions for cases A to C, but restricted to steady state in case D for simplicity. For large μ in cases E and F we saw that we may obtain very different structures of solutions depending on the direction of flow of information, and discussed how the solution structure can vary in time. We would expect similar time-varying structures in case D to those observed in cases E and F.

For the numerical solutions in this chapter, we have almost always restricted to the steady-state case. The leading-order steady-state solution in cases A and B was shown to be stable to perturbations within the quasi-steady limit, but we should verify that this is indeed stable under perturbations on the faster timescale. For cases C to F, we have not investigated the stability of the steady-state solutions, but since they reduce to the case A or B solutions in the limit as $\mu \to 0$, we expect that these are also stable. For cases C to F, the structure of the region-I problem becomes much more complicated in the time-dependent case, as the form of the boundary conditions varies in time, and we can no longer compute numerical solutions of the region-I problem independently from the outer problem. Stability analyses, or numerical simulations of the full time-dependent problem (5.1), could be undertaken in order to determine the stability of the steady states we have found, and the more general time-dependent behaviour of the system. The asymptotic structures that we have found in this chapter give insight into how one might solve the model (5.1) numerically in the general time-dependent case. Specifically, for large μ, a numerical solver must be able to take into account the different directions of information transfer, which is different for the solid, and gas dependent variables, and may also change both in time and in different

regions of the domain. Stability analysis is also not expected to be particularly simple due to the nonlinearity of the system.

We have assumed throughout that the chemical reaction rate has Arrhenius dependence on the solid temperature T_s. This led to the logarithmic dependence of the critical solid temperature η on $\delta\mu$, in cases B to D, and the form of θ_* in cases Eb and Fb. Indeed, the slow logarithmic decay of the temperature in cases Eb and Fb is due to the exponentially small behaviour of the Arrhenius form of Q at small temperatures. Regardless of the form of the chemical reaction rate Q, we would still, in cases B to D, expect a dominant balance in the solid heat equation between the heat consumed in the chemical reaction, and the heat transferred from the gas to the solid, in regions of the domain where T_s is small. Thus, while the form of the critical temperature η would depend on the functional form of Q, we might still expect similar solution structures, with regions of small, near-constant T_s, and the heat transferred from gas to solid used for the chemical reaction. Similarly in cases E and F we would still expect the vast majority of chemical reaction to occur in region I. However, the balance of advection and heat consumed by chemical reaction in cases Eb and Fb relied on the fact that the chemical reaction was exponentially small here. If the chemical reaction rate took a different form, we might observe different behaviour, such as the simple advection-dominated behaviour of cases Ea and Fa.

Many of the structures that we have found in this Cartesian geometry carry through to the cylindrical radial case of our furnace model from Chapter 3: the boundary layer structures remain the same, but the functional forms of the solutions are different in the regions of $O(1)$ lengthscale, although we may still solve for these explicitly. From measurements of industrial furnace temperatures [1, 46] it seems that the gas leaving the top of the furnace is likely to be significantly hotter than the solid material at the surface, but much cooler than the crater gases. From the solution structures we have found, the relevant regimes to the silicon furnace are therefore $\mu = O(\eta_B)$ and $\mu = O(1)$. In Chapter 6, we return to our homogenised cylindrical furnace model (3.84) derived in Chapter 3, and study the two distinguished limits, $\mu = O(\eta_B)$ and $\mu = O(1)$, which are likely to be the most industrially relevant, as well as the case $1 \ll \mu \ll \delta^{-1}$ for the sake of comparison. The model (3.84) includes Ohmic heating, coupling with the electrical problem, and more detailed boundary conditions at the free boundary $r = s(t)$, which we dropped from the simplified model (5.1) in this chapter.

Chapter 6

Solutions of the homogenised submerged arc furnace model

In this chapter we study the idealised, homogenised furnace model developed in Chapter 3, namely (3.83)–(3.84). Making use of the asymptotic reductions derived in Chapter 5, we simplify the model (3.84) in the charge material, finding reduced leading-order models for the ranges of μ that we expect to be most industrially relevant, namely $\mu \ll \delta^{-1}$. We find steady-state solutions of each of these reduced models numerically, and compare the different models. In particular, we investigate how the distribution of electric current between the arc and charge pathways depends on the parameters μ and $\hat{I}$. We also investigate the quasi-steady dynamics in the case of small μ, interpreting the dynamics in terms of an overall energy balance argument, and investigating how the efficiency of the system may be improved by stoking.

6.1 Statement of reduced models

In the radial geometry of the idealised model derived in Chapter 3, we may perform the same asymptotic analyses as for the simplified model (5.1) in Chapter 5, which was on a Cartesian domain. Assuming throughout that the electrical conductivity of the charge material only becomes non-zero for temperatures T_s well above η, we see that there can be no electrical current conduction in the charge material except in the $O(\delta)$ boundary layer at the free boundary $r = s(t)$. Thus the asymptotic solution structures of the charge model (3.84) are very similar to those of (5.1) derived in Chapter 5, with the main differences being due to the radially varying solid velocity $-1/r$, and the radial derivatives. As in Chapter 5, we find that the leading-order behaviour is contained in the reduced model for the conduction boundary layer (region I) at the

interface $r = s$, which may be coupled to the region II behaviour, depending on the size of μ.

In the subsections below, we state the resulting leading-order models, for the small-μ case (corresponding to cases A and B in Chapter 5), and for intermediate $\mu = O(1)$, and $\log(\eta) \ll \mu \ll \delta^{-1}$ (cases C, and D in Chapter 5). We retain time-dependence in the small-μ case as the system is quasi-steady, but reduce to steady state for intermediate μ. We will only consider the leading-order behaviour in this chapter, and so we drop the superscript 0 used in Chapter 5 to denote leading-order variables.

6.1.1 Small $\mu \leq O(\eta_B)$

As in cases A and B of Chapter 5, when $\mu = O(\eta_B)$ or smaller, to leading order the model (3.84) reduces to simply the region-I problem for the solid variables. With the change of variables $r = s(t) + \delta X$, where $\delta \ll 1$, the radial derivatives in (3.84) become

$$\frac{1}{r}\frac{\partial}{\partial r}(\cdot) = \frac{1}{s}\frac{\partial}{\partial X}(\cdot) + O(\delta) \quad \text{and} \quad \frac{1}{r}\frac{\partial}{\partial r}(r\,\cdot) = \frac{\partial}{\partial X}(\cdot) + O(\delta). \tag{6.1}$$

Thus at leading order in region I, $X \in (0, \infty)$, we obtain

$$-\left(\dot{s} + \frac{1}{s}\right)\frac{\partial C}{\partial X} = -Q, \tag{6.2a}$$

$$-\left(\dot{s} + \frac{1}{s}\right)C\frac{\partial T_s}{\partial X} = \frac{\partial^2 T_s}{\partial X^2} + \alpha\sigma_c\langle E^2\rangle - \gamma Q, \tag{6.2b}$$

with boundary conditions at $X = 0$,

$$C_s = C_*, \qquad s^2 H(T_s - T^\infty) + s^2 R_p(T_s + \gamma) = (1 + s\dot{s})\,CT_s + s\frac{\partial T_s}{\partial X} + \langle T_a^4\rangle, \tag{6.2c}$$

and as $X \to \infty$,

$$C_s \to 1, \qquad T_s \to 0. \tag{6.2d}$$

As in Chapter 5, the leading-order solution in the remainder of the charge domain, and for both the gas variables in region I, may be computed from the solution of (6.2). In particular, the boundary-layer gas variables are given by

$$f(X,t) = R_p s + \left(\frac{1}{s} + \dot{s}\right)(C - C_*), \tag{6.3}$$

$$T_g(X,t) = \frac{R_p s T_s\big|_{X=0} + \int_{\bar{X}=0}^{X} T_s Q\,\mathrm{d}\bar{X}}{K\left(R_p s + \left(\frac{1}{s} + \dot{s}\right)(C - C_*)\right)}. \tag{6.4}$$

6.1.2 Intermediate $O(1) \leq \mu \ll \delta^{-1}$

For intermediate values of μ, as in cases C and D in Chapter 5 we find that there is $O(1)$ solid material consumption in both regions I and II of the domain. At leading order in region I the same equations (6.2a–c) hold as for the small-μ case, but with boundary conditions as $X \to \infty$ given by

$$C_s \to C^\infty(t), \qquad T_s \to 0, \tag{6.5}$$

for $C_s^\infty(t) < 1$ determined by matching with region II.

In region II we find that at leading order

$$\hat{T}_g = \frac{-\gamma W(a)}{K(1+W(a))}, \qquad \hat{f} = \frac{sF_s}{r}\frac{\gamma + KG_s}{\gamma + K\hat{T}_g}, \tag{6.6}$$

with W the principal branch of the Lambert-W function, and where, in radial coordinates,

$$a = -\frac{KG_s}{\gamma + KG_s}\exp\left(-\frac{1}{\gamma + KG_s}\left(KG_s + \frac{\mu\gamma}{2sKF_s}(r^2 - s^2)\right)\right). \tag{6.7}$$

As in Chapter 5, we have used the notation

$$F_s := R_p s + \left(\frac{1}{s} + \dot{s}\right)(C^\infty - C_*), \quad G_s := \frac{R_p s T_s\big|_{X=0} + \int_{\bar{X}=0}^\infty T_s Q \,\mathrm{d}\bar{X}}{K\left(R_p s + \left(\frac{1}{s} + \dot{s}\right)(C^\infty - C_*)\right)}, \tag{6.8}$$

for the gas variable matching constants at $r = s$. The problem for the leading-order solid concentration in region II, which retains the radial derivatives of (3.84), is then

$$\frac{\partial \hat{C}}{\partial t} - \frac{1}{r}\frac{\partial \hat{C}}{\partial r} = \frac{\mu W(a)}{K(1+W(a))}, \tag{6.9a}$$

with boundary conditions

$$\hat{C} = C^\infty \text{ at } r = s, \qquad \hat{C} = 1 \text{ at } r = r_f, \tag{6.9b}$$

and an appropriate initial condition.

In steady state, we solve (6.9), and applying both the boundary conditions obtain

$$C_{\mathrm{C}}^\infty = 1 - \frac{sF_s}{\gamma}\Big(KG_s + W(a|_{r=r_f})\big(\gamma + KG_s\big)\Big), \tag{6.10}$$

which closes the steady-state system (6.2a-c), with (6.5) (taking $\dot{s} = 0$).

As in Chapter 5, the value (6.10) for C^∞ is valid so long as T_g remains $O(1)$ at $r = r_f$. For larger values of μ (as in case D of Chapter 5) region II becomes a

boundary layer of width μ^{-1} at $r = s$. In radial coordinates we may solve for the region II behaviour as in Section 5.6, and obtain the steady-state value

$$C_{\mathrm{D}}^{\infty} = 1 - \frac{sF_sG_sK}{\gamma}, \tag{6.11}$$

to close the steady-state system (6.2a-c) and (6.5) (with $\dot{s} = 0$).

To summarise, in steady state the leading-order problem for $O(1) \leq \mu \ll \delta^{-1}$ is

$$\frac{1}{s}\frac{\mathrm{d}C}{\mathrm{d}X} = Q, \tag{6.12a}$$

$$-\frac{1}{s}C\frac{\mathrm{d}T_s}{\mathrm{d}X} = \frac{\mathrm{d}^2T_s}{\mathrm{d}X^2} + \alpha\sigma_c\langle E^2\rangle - \gamma Q, \tag{6.12b}$$

with boundary conditions at $X = 0$,

$$C = C_*, \qquad s^2H(T_s - T^{\infty}) + s^2R_p(T_s + \gamma) = CT_s + s\frac{\mathrm{d}T_s}{\mathrm{d}X} + \langle T_a^4\rangle, \tag{6.12c}$$

and as $X \to \infty$,

$$T_s \to 0, \qquad C \to \begin{cases} 1 - \frac{sF_s}{\gamma}\Big(KG_s + W(a|_{r=r_f})\big(\gamma + KG_s\big)\Big), & \text{for } \mu = O(1), \\ 1 - \frac{sF_sG_sK}{\gamma}, & \text{for } 1 \ll \mu \ll \delta^{-1}. \end{cases} \tag{6.12d}$$

We note that as μ becomes large, $W(a|_{r=r_f})$ decays exponentially to zero, and so the $\mu = O(1)$ far-field condition approaches the condition for $1 \ll \mu \ll \delta^{-1}$.

6.2 Numerical method

We now solve numerically the quasi-steady small-μ problem (6.2), and the steady-state system for intermediate μ (6.12).

In each case, the reduced model in the charge material is coupled to the fast-timescale arc model (3.83), which we rewrite here for convenience:

$$\chi\frac{\partial T_a}{\partial \tau} = \sigma_a(T_a)E^2 - T_a^4, \tag{6.13a}$$

$$\hat{I}I_{AC}(\tau) = E\left(\sigma_a(T_a) + \sigma_{\mathrm{ch}}\right). \tag{6.13b}$$

Since there is no electrical current conduction outside of region I, the charge conductivity σ_{ch} is now given by

$$\sigma_{\mathrm{ch}}(t) = \alpha s\int_{X=0}^{\infty}\sigma_c\,\mathrm{d}X. \tag{6.14}$$

Solutions of (6.13) for prescribed σ_{ch} were found and discussed in Chapter 4. For all the solutions in this chapter, we assume a sinusoidal, alternating applied current, as

in Section 4.1.2. As described in Section 4.1.2, we solve (6.13) for prescribed values of the current amplitude $\hat{I}$ and charge conductivity σ_{ch}, tabulating the resulting averaged quantities $\langle E^2 \rangle$ and $\langle T_a^4 \rangle$. We then solve the boundary value problem ((6.2) or (6.12)) in the charge material for the concentrations and temperatures, as well as for $\langle E^2 \rangle$, and $\langle T_a^4 \rangle$, and σ_{ch} using our previously-computed look-up table.

In steady state, we also solve for the position, s, of the free boundary of charge material. For small μ, when we solve for the quasi-steady dynamics, as in Chapter 5 we must prescribe one of s or $\dot{s}$ and solve for the other. We choose to prescribe s and solve for $\dot{s}$ as this allows us to find unstable steady-state solutions. As in Sections 5.9 and 5.10, the numerical solutions in this chapter are computed using the MATLAB in-built solver bvp4c. This solver enables us to solve for the parameters $\langle E^2 \rangle$, $\langle T_a^4 \rangle$, σ_{ch}, s (or $\dot{s}$ in the small-μ case), and C^∞ in the intermediate-μ cases, as part of the numerical scheme.

We impose the integral constraint in (6.13) by introducing the additional variable

$$Z(X) = \alpha s \int_0^X \sigma_c(\hat{X}) \, \mathrm{d}\hat{X}, \tag{6.15}$$

and converting the integral constraint to an additional differential equation, which gives the boundary value problem

$$Z'(X) = \alpha s \sigma_c(X), \qquad Z(0) = 0, \qquad Z(\infty) = \sigma_{\text{ch}}. \tag{6.16}$$

We use a similar method to compute the far-field gas temperature G_s in the intermediate-μ case, which is required to solve for the value of C^∞ via (6.12d).

For cases when the far-field behaviour requires that we impose $T_s \to 0$, we replace this with the mixed condition

$$\frac{\partial T_s}{\partial X} + \left(\frac{1}{s} + \dot{s} \right) C^\infty T_s \to 0 \quad \text{as} \quad X \to \infty, \tag{6.17}$$

(with $C^\infty = 1$ in the small-μ case, and $\dot{s} = 0$ in the intermediate-μ case), which reduces the required domain size.

To initialise the numerical solutions we take a much narrower domain for X, over which heat conduction dominates, and so we can compute the (linear) analytic solution, which we use as an initial guess for the numerical solver. We then increase the domain size until the solution converges. From this initialised solution we may continue to different parameter values.

Throughout this chapter, unless otherwise stated, we use the values of α, χ, γ, K, H, and R_p given in Table 3.6, which are expected to be reasonable for industrial

operating regimes. Since the model (3.84) in the charge material reduces to the region-I problems, we do not need to specify the value of δ, although of course this must be small for our asymptotic reductions to be valid. We set $T^\infty = 0$ (in the heat flux boundary condition at $X = 0$, parameterising the heat flux to the electrode and crater base). We also take the critical solid concentration to be $C_* = 0.2$, the size of the furnace to be $r_f = 3$, and, following the nondimensionalisation in Chapter 3, we use the dimensionless reaction rate and conductivities

$$Q = C_s \exp\left(A\left(1 - \frac{1}{T_s}\right)\right), \quad \sigma_a = \exp\left(-\frac{\alpha_3}{T_a}\right), \quad \sigma_c = \exp\left(-\frac{s_c}{T_s - T_c}\right), \quad (6.18)$$

with dimensionless coefficients

$$A = 3, \qquad \alpha_3 = 1.4, \qquad s_c = 0.1, \qquad T_c = 0.7. \quad (6.19)$$

6.3 Steady-state solutions

We now present numerical, steady-state solutions of both of the small- and intermediate-μ models (6.2) and (6.12), respectively, with (6.13). The temperature and concentration profiles in the boundary layer at $r = s$ are shown in Figure 6.1 for both of these models, for a prescribed $\hat{I} = 3$ and the corresponding solution s is given in the figure captions. In contrast to the Cartesian domain of Chapter 5, we find two distinct steady-state solutions of the small-μ model (6.2), which we refer to as the s_1 and $s_2 > s_1$ steady states, respectively. (We will discuss the (quasi-)stabilities of these steady states in Section 6.4 below.) However, for the intermediate-μ model (6.12), we have only been able to find one steady-state solution numerically.

The temperatures and concentrations in region I of the charge material are very similar to those observed in Chapter 5, with T_s decreasing monotonically as X increases, and C increasing from C_* to C^∞ or 1. For our chosen parameter values, the gas temperature T_g decreases monotonically to G_s. Since our solutions are steady states, the gas flux is $f(X) = \frac{1}{s}(C(X) - C_*) + R_p s$, and so is determined by the solid concentration and position of s.

For the small-μ case, we see that the s_1 solution is characterised by much larger temperatures at $X = 0$ than for the s_2 solution. This is because s_1 is much smaller than s_2 and so the surface area over which the heat radiation from the arc is distributed is smaller for the s_1 steady state. We also observe a larger maximum of f for the s_1 steady state, again because of the much smaller value of s. For the intermediate-μ case, we see that the value of s increases with increasing μ, and that

the temperatures and concentrations reduce accordingly. The value of C^∞ also decreases as μ increases, as in Chapter 5.

In Figure 6.2 we show the position, s, of the steady-state free boundary as μ is varied, for both of the steady-state models. For small μ, the leading-order problem (6.2) is independent of μ (we show here only the larger steady state $s = s_2$). The intermediate-μ problem (6.12) with $C_{\rm D}^\infty$ also has no dependence on μ, but we find a larger steady-state value s. In the intermediate-μ case with $C_{\rm C}^\infty$ we see that the steady-state s increases smoothly with μ, approaching the small μ solution as $\mu \to 0$, and the intermediate-μ solution with $C^\infty = C_{\rm D}^\infty$ as μ becomes large. We see that this

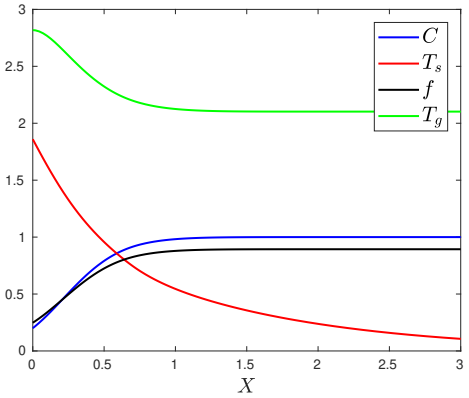

(a) Small μ model, $s_2 \approx 1.24$.

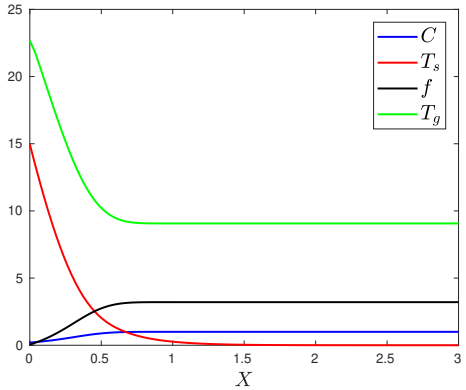

(b) Small μ model, solution $s_1 \approx 0.25$.

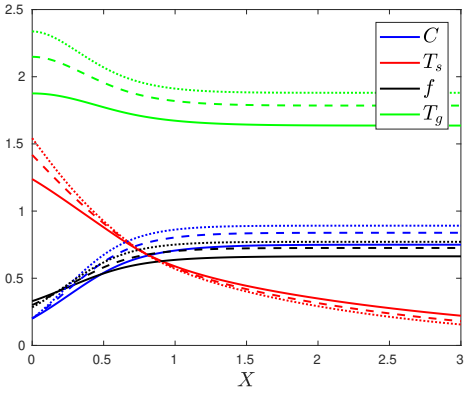

(c) Intermediate μ, taking $\mu = 0.1$ (dotted, solution $s \approx 1.41$), $\mu = 0.2$ (dashed, solution $s \approx 1.50$), and $\mu = 1$ (solid, solution $s \approx 1.65$).

Figure 6.1: Steady-state solutions of the small-μ (6.2), and intermediate-μ (6.12) models, showing the profiles of the temperatures and concentrations in the boundary layer (region I). The solution s is stated in the captions for each case. Throughout we take $\hat{I} = 3$, $r_f = 3$, and all other parameters as in Table 3.6.

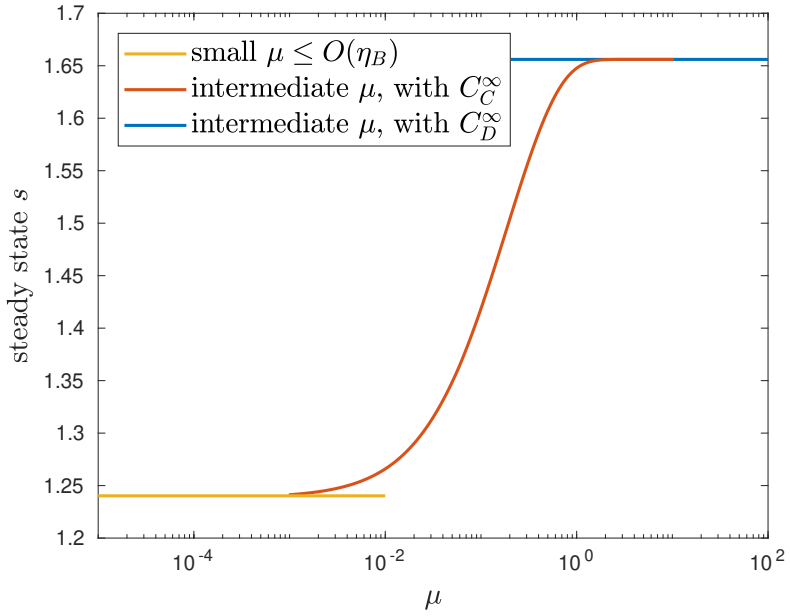

Figure 6.2: The steady-state solution s as μ is varied, for each of the reduced models (only the larger s_2 steady state is shown for the small-μ case). Throughout we use $\hat{I} = 3$, and the standard parameter values in Table 3.6.

variation occurs for μ below around 1. This is because the domain extends to $r_f = 3$ (rather than to $x = 1$ in Chapter 5, as we have a different nondimensionalisation), and so the rate of heat transfer over the entire domain is better captured by the value of μr_f than by μ.

Above, we have discussed the steady-state solutions for a fixed value of $\hat{I}$. In Figure 6.3 we instead vary $\hat{I}$, the applied current magnitude, and show the values of the steady-state solution s, for both of our reduced models. In fact, to compute this figure we have interchanged the roles of s and $\hat{I}$ in our numerics, and now prescribe s and solve for $\hat{I}$. This allows us to find steady-state solutions for smaller values of s than is otherwise feasible numerically, and in particular, this allows us to find both branches of steady-state solutions for the small-μ case.

Firstly we note that for both of our reduced models, we are unable to find steady-state solutions if $\hat{I}$ is too small. Since the electric current is the source of energy to the system, if $\hat{I}$ is too small then there is insufficient energy to react away all the incoming solid material, and thus there is no steady-state solution. We also notice that the minimum value of $\hat{I}$ for which steady states exist depends on the size of μ, both in terms of which reduced model we use, and also the value of μ used within the intermediate-μ model.

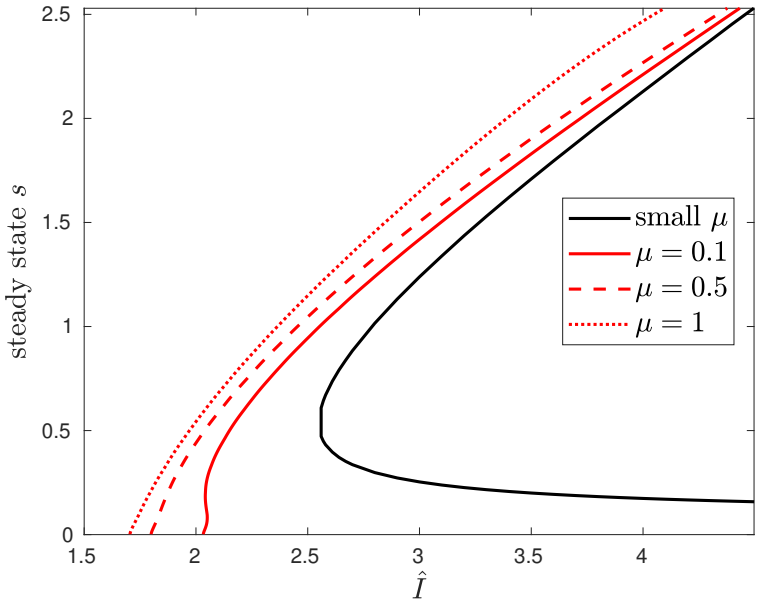

Figure 6.3: Comparison of bifurcation diagrams for the two reduced models (6.2) and (6.12), showing steady-state solution(s) s as the applied current magnitude $\hat{I}$ is varied. Throughout we take $r_f = 3$, and all other parameters as in Table 3.6.

For the small-μ model we require a larger $\hat{I}$ to obtain steady states. This is because a large amount of the energy in the system is lost through the hot gases escaping the furnace. Above the critical $\hat{I}$, we find the two steady states, $s_1 < s_2$, for each value of $\hat{I}$. The stability of these steady states is discussed below in Section 6.4, but we note here that the s_1 steady state is unstable while the s_2 steady state is stable.

For the intermediate-μ model (6.12) we have computed the bifurcation diagram for various $\mu = O(1)$, and we generally only find one steady-state solution, corresponding to the upper, s_2 branch of the small-μ model. As we expect from Figure 6.2, for smaller μ the intermediate-μ solution approaches the upper branch of the small-μ solution. This occurs more quickly for larger values of $\hat{I}$, since the value of s is larger, approaching the edge of the domain $r_f = 3$, and so the outer region is becoming too small for significant material consumption to occur. As μ increases in the intermediate-μ model, the critical $\hat{I}$ below which there is no steady-state solution decreases, to a minimum around 1.7. There is only one steady-state solution for cases with $\mu = 0.5$ and greater. However we notice that for $\mu = 0.1$ we have found a very small range of $\hat{I}$ for which there are two solutions, close to the critical value. It almost appears that the bifurcation digram will turn back on itself, as it does in the small-μ case, but on further decreasing s towards zero, we instead find solutions with

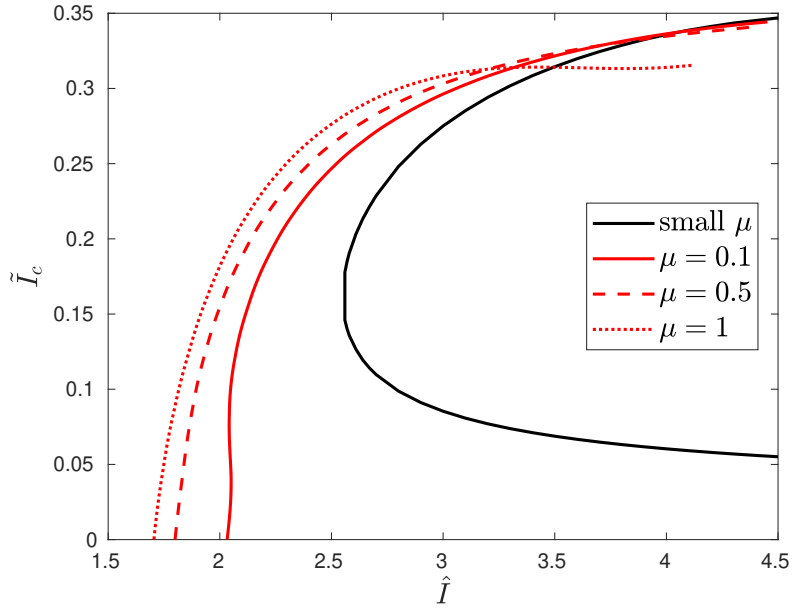

Figure 6.4: Bifurcation diagrams corresponding to Figure 6.3 showing the fraction of current passing through the charge $\tilde{I}_c$ at the steady-state solution, as $\hat{I}$ is varied.

$\hat{I}$ decreasing again. We should note that our model is not expected to give valid or physical results at such small values of s as this; at such small s the temperatures are far higher than physically possible, and indeed for $s < 0.1$ the arc and charge domains overlap.

One aim of our modelling approach has been to better understand how the two electric current paths interact, both with each other and with the chemical and material flow system. We have taken into account both the radiative heating from the electric arc and the Ohmic heating within the charge material in determining the material flow and chemical properties, and we also solve for the distribution of current. The fraction $\tilde{I}_c \in [0, 1]$, of the total current passing through the charge material, as defined in (4.10) is shown in Figure 6.4 at the steady-state solution for varying $\hat{I}$, with the solutions corresponding directly to those shown in Figure 6.3. In particular, the lower branch of the small-μ solution in Figure 6.4 corresponds to the lower (s_1) branch in Figure 6.3. In this small-μ case we see that a smaller fraction of the total current passes through the charge at the s_1 steady state than at the s_2 steady state. We also see that $\tilde{I}_c$ decreases with $\hat{I}$ at the s_1 steady state. However, at $s = s_2$ we observe that $\tilde{I}_c$ increases with $\hat{I}$. For the intermediate-μ case we see $\tilde{I}_c$ approaches zero as $\hat{I}$ decreases to its minimum, since s is also small here, and purely geometrically we have $\sigma_{\text{ch}} \propto s$ from (6.14). As $\hat{I}$ (and s) increases we see $\tilde{I}_c$ increases to a

maximum, but thereafter decreases slightly. This is because for large $\hat{I}$ we have large s, and so the solid temperature T_s in the charge decreases, and so the charge becomes less electrically conductive.

6.4 Quasi-steady dynamics for small μ

In the previous section we found steady-state solutions numerically for both of our reduced models. Like in Chapter 5, of our reduced models, only the small-μ case is quasi-steady, with the factors of $\dot{s}$ in region I the only time-derivatives to appear in the leading-order model throughout all the regions of the charge domain. This quasi-steady property of the small-μ reduced model makes it much easier to study the dynamics of the overall system in this case than in the intermediate-μ case. In this section we analyse the quasi-steady model (6.2), finding numerical solutions in Section 6.4.1, and interpreting these in terms of the overall energy balance of the system in Section 6.4.2. In Section 6.4.3 we apply our understanding of the system dynamics to investigate how the industrial procedure of stoking the furnace affects the overall rate of material consumption. In Section 6.4.4 we discuss possible inferences we can make for the intermediate-μ case.

6.4.1 Numerical quasi-steady solutions

As described in Section 6.2, we may solve the small-μ problem (6.2) numerically either by imposing $\dot{s}$ and solving for s, or by imposing s and solving for $\dot{s}$. In this section we do the latter, with solutions presented in Figure 6.5 for various values of the imposed current amplitude $\hat{I}$.

In Figure 6.5a we show the variation of $\dot{s}$ with s for various values of $\hat{I}$. For small $\hat{I}$, below the critical value $\hat{I}_{\text{crit}} \approx 2.55$ observed in Figure 6.3, we see that $\dot{s} < 0$ for all s, so that there is no steady state: the crater collapses inwards since there is insufficient energy for the chemical reactions to consume the incoming material. For $\hat{I} > \hat{I}_{\text{crit}}$, we see that

$$\dot{s} < 0 \quad \text{if } s < s_1 \text{ or } s > s_2, \qquad \text{and} \qquad \dot{s} > 0 \quad \text{if } s \in (s_1, s_2), \tag{6.20}$$

so that all solutions evolve towards s_2 unless initially $s < s_1$. For $s > s_2$, the solutions all initiate near the curve $\dot{s} = -1/s$, which corresponds to the crater wall $r = s$ moving inward at the same speed, $-1/s$, as the inflowing solid material: at this value of s, the solid material is too cold for the chemical reactions to take place. As we increase $\hat{I}$, the stable steady state $s = s_2$ increases, so that we expect larger craters in furnaces

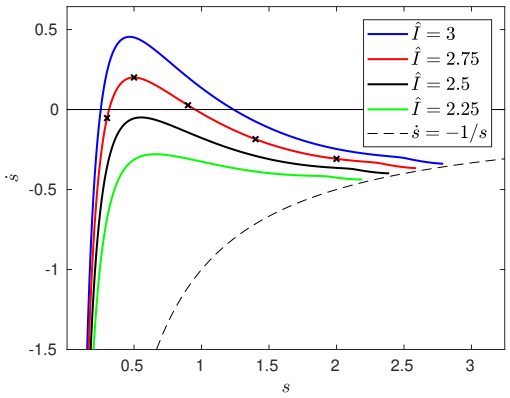

(a) Solution curves $\dot{s}$ against s for various $\hat{I}$, for $\dot{s} > -1/s$.

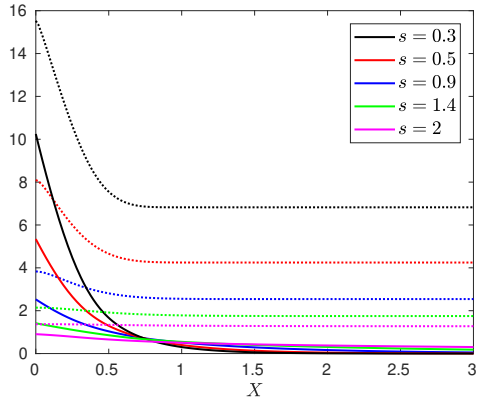

(b) Profiles of T_s (solid line) and T_g (dotted line) at various points along the solution curve with $\hat{I} = 2.75$, marked in (a).

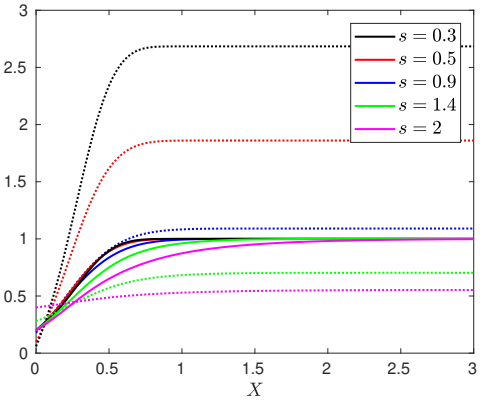

(c) Profiles of C (solid line) and f (dotted line) at various points along the solution curve with $\hat{I} = 2.75$, marked in (a).

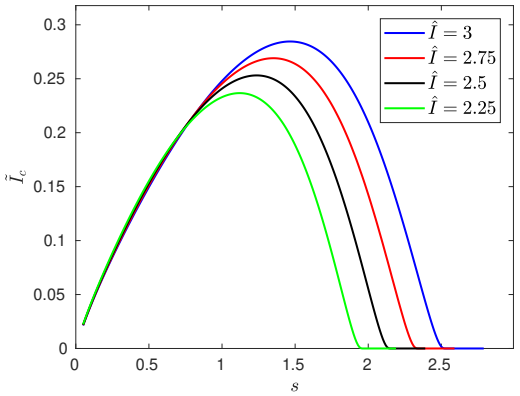

(d) Average charge current fraction $\tilde{I}_c$ along the solution curves in (a).

Figure 6.5: Numerical solutions of the quasi-steady small-μ model (6.2) using parameter values in Table 3.6.

with higher currents. We discuss the structure and evolution of these solutions further in Section 6.4.2, in terms of the overall balance of energy in the system.

The temperature profiles T_s and T_g are shown in Figure 6.5b, and the concentration profiles C and f are shown in Figure 6.5c, in both cases at various points along the $\hat{I} = 2.75$ solution, marked with crosses in Figure 6.5a. As for the steady-state solutions found in Section 6.3, the magnitude of the temperatures is largely determined by the size of s, with rapidly growing temperatures as s becomes small. The rate of decay of T_s with X is also faster for smaller s, so that the region of X for which Q is non-negligible and C, f, and T_g vary, becomes narrower. The gas concentration flux $f = \left(\frac{1}{s} + \dot{s}\right)(C - C_*) + R_p s$ is now given in terms of both $\dot{s}$ and s (related by the

solution curve in Figure 6.5a), as well as the solid concentration profile C.

In Figure 6.5d, we plot the fraction of the average of the current magnitude passing through the charge material, $\tilde{I}_c$, as s varies. For large s, the charge material is cold, and all the current flows through the arc. As s decreases and T_s increases above T_c, the charge becomes electrically conductive and a significant fraction of the current passes through the charge. However, as s decreases further, the local conductivity $\sigma_c(T_s)$ is bounded, while the volume of conductive charge material, which scales with s, decreases. The overall fraction of current through the charge material therefore decreases again, until all the current passes through the arc. For larger $\hat{I}$, the maximum of $\tilde{I}_c$ is greater, and occurs at a larger value of s.

6.4.2 Overall energy balance

We can understand the structure of the quasi-steady solutions of the small-μ model found in the previous section by considering the overall balance of power in the system.

Adding the equations for conservation of energy in the gas and in the solid, the terms modelling the heat transfer between the solid and gas cancel, and we obtain

$$\frac{\partial}{\partial X}\left[K\left(\left(\frac{1}{s}+\dot{s}\right)(C-C_*)+R_p s\right)T_g-\left(\frac{1}{s}+\dot{s}\right)C(T_s-\gamma)-\frac{\partial T_s}{\partial X}\right]=\alpha\sigma_c\langle E^2\rangle, \tag{6.21}$$

where we have also used the conservation of mass in the solid to write the heat lost to the chemical reaction as a derivative of C. Integrating over the entire charge domain $X\in[0,\infty)$, applying the boundary conditions at $X=0$ and as $X\to\infty$, and multiplying through by s we obtain a total energy balance of the system, namely

$$\langle EI\rangle=\gamma\left((1+s\dot{s})(1-C_*)+R_p s^2\right)+KG_s\left((1+s\dot{s})(1-C_*)+R_p s^2\right)+s^2HT_s(0), \tag{6.22}$$

where G_s is the gas temperature leaving region I, given by (6.8). On the left of (6.22) we have the total electrical energy dissipated in the system per unit time over both the arc and the charge which, by averaging the fast-timescale equations (6.13b), is given by

$$\langle EI\rangle=\langle T_a^4\rangle+\alpha s\langle E^2\rangle\int_0^\infty\sigma_c\,\mathrm{d}X. \tag{6.23}$$

The terms on the right of (6.22) are the power consumed by chemical reactions, $\gamma((1+s\dot{s})(1-C_*)+R_ps^2)$, both in region I of the charge and in the melt-pool, the power lost in the flow of hot gases out of region I, $KG_s\left((1+s\dot{s})(1-C_*)+R_ps^2\right)$, and the power lost by heat flux through the top and base of the crater, $s^2HT_s(0)$. The unknowns in (6.22) are therefore $E, s, \dot{s}, T_s(0)$, and G_s. We may consider these

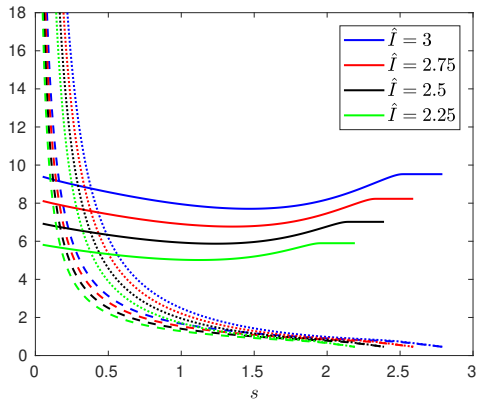

(a) Variation of $\langle EI \rangle$ (solid line), $T_s(0)$ (dotted line), and G_s (dashed line) with s.

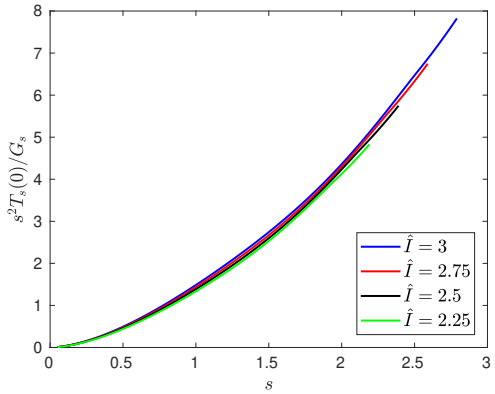

(b) Variation of $s^2 T_s(0)/G_s$ with s.

Figure 6.6: Behaviour of $\langle EI \rangle$, $T_s(0)$, G_s, and $s^2 T_s(0)/G_s$ with s, corresponding to the numerical solutions presented in Figure 6.5.

to be functions of the position of the free boundary s rather than of time t, since (numerically) we have found a single solution, and so a single value of $\langle EI \rangle$, $\dot{s}$, $T_s(0)$, and G_s, for each value s.

Rearranging (6.22), we find

$$s\dot{s} = \frac{\langle EI \rangle - H_R}{H_R} - \frac{H_V}{H_R} s^2, \tag{6.24}$$

where

$$H_R = (\gamma + KG_s)(1 - C_*), \qquad H_V = HT_s(0) + R_p(\gamma + KG_s), \tag{6.25}$$

are, respectively, the heat losses in the radial direction (the heat lost to the chemical reaction in the charge material, and the heat lost in the hot gas that escapes region I) and the heat losses per unit area in the vertical direction (chemical and conductive heat losses in the melt pool at the base of the cylindrical crater, and through the electrode at the top). We note that both H_R and H_V are positive.

In order for a steady-state solution, with $\dot{s} = 0$, to exist, we see from (6.24) that we require $\langle EI \rangle - H_R > 0$, and hence we need a sufficiently high electrical power $\langle EI \rangle$. If the electrical power is too low, then the first term of (6.24) is negative, or small and positive, and so $\dot{s} < 0$ for all s. In this case, the crater will collapse inward, as the electrical power dissipated will be insufficient to react away the incoming flux of solid material. This is the behaviour observed for the numerical solutions in Section 6.4.1, when the applied current had too small an amplitude $\hat{I} < \hat{I}_{\text{crit}}$.

If the applied current is sufficiently large that solutions $\langle EI \rangle - H_R > 0$ exist, then we expect there to be steady-state solutions. In Figure 6.6a we show the variation of $T_s(0), G_s$, and $\langle EI \rangle$ with s, from the numerical solutions computed in Section 6.4.1. For large enough s, all three of $T_s(0), G_s$, and $\langle EI \rangle$ vary slowly with s, so that $\langle EI \rangle, H_R$, and H_V are approximately constants. Therefore, if there is a steady-state solution s^* in this range of sufficiently large s, then from (6.24), we see that for $s > s^*$, we have $\dot{s} < 0$, while for $s < s^*$, we have $\dot{s} > 0$. Thus such a steady state is stable. This describes the behaviour of the larger steady state $s = s_2$ seen numerically in Section 6.4.1. We note that it is the changing geometry of the system that determines the stability of this steady state: since H_R, H_V, and $\langle EI \rangle$ are all approximately constant, the increasing surface area of the crater top and base, which behaves like s^2, means that as s increases from s_2 the heat loss in the vertical direction increases while the total energy produced does not vary much, and hence $\dot{s}$ decreases through the steady state, making it stable.

From Figure 6.6a we see that as s becomes small, while $\langle EI \rangle$ remains roughly constant, $T_s(0)$ and G_s increase dramatically. This is because the energy radiated from the arc remains roughly constant, but is distributed over an increasing small surface area, causing $T_s(0)$ to blow up, which causes a similar, but lesser, increase in G_s. Since both H_V and H_R are linear in G_s or $T_s(0)$, these blow up as s becomes small, causing $\dot{s}$ to become negative for small s. This is the cause of the second steady state, s_1, observed numerically. Specifically, from the numerical solutions in Figure 6.6b we see that, even though $T_s(0)$ increases faster than G_s as s becomes small, $(T_s(0)/G_s)s^2$ is bounded, and approaches zero as $s \to 0$. Thus the quadratic-type term, $(H_V/H_R)s^2$, in (6.24) remains bounded. The change in the sign of $\dot{s}$ as s becomes small is therefore due to the change in sign of the first term, or of $\langle EI \rangle - H_R$. Thus it is the blow-up in the heat, $KG_s(1 - C_*)$, lost in the gas escaping region I as $X \to \infty$, that creates the small steady state s_1.

The above energy balance argument holds only for the small-μ model. However, this interpretation of the s_1 steady state as only existing because of the heat lost in the gas escaping the boundary layer provides intuition for why a similar steady state s_1 does not appear to exist for the intermediate-μ cases: for $\mu = O(1)$ or larger, the energy in the gas leaving the boundary layer is used for chemical reactions in the outer regions of the charge domain, and so is not lost from the system.

6.4.3 The effect of stoking

We have seen that when $\hat{I}$ is large enough for steady states s_1 and s_2 to exist, the small-μ system evolves from any initial state with $s > s_1$ to the larger steady state s_2 over the timescale $[t_s] \approx 4$ hours (as in Section 3.2). However, the steady state s_2 is unlikely to be attained in reality, due to the practice of stoking.

In realistic industrial configurations, the furnace is stoked at regular intervals (on the order of 45 minutes to an hour). The stoking process involves manually breaking up and mixing the top layer of charge material in the furnace, using a large pole (in the same way as one might stoke a fire with a poker). The stoking machine is illustrated on the left of the furnace diagram Figure 1.1 in Chapter 1. This practice ensures the gases can flow out through the charge, preventing gas blows, and ensuring efficient silicon production. Stoking is also seen to increase the flow of solid material down towards the crater, and it is understood that during stoking the crater quickly shrinks, before slowly growing back outwards until the next stoking.

While our model is not designed to capture rapid changes in the flux of solid material to the crater, we can understand the stoking cycle in terms of an instantaneous re-setting of the crater radius s during the stoking. Since in the small-μ case the temperature and concentration fields are all quasi-steady on the $[t_s]$ timescale, we expect to rapidly revert to the quasi-steady $\dot{s}(s)$ solution curve of Figure 6.5a. Stoking can therefore be thought of as rapidly reducing the crater radius to a smaller value of s, and the system instantaneously reverting to the $\dot{s}(s)$ solution curve for the new value of s. The system then evolves slowly along the $\dot{s}(s)$ curve, with s increasing towards s_2 until the next stoking period. The current distribution through the furnace varies as we pass along the curve. Immediately after stoking, we would expect the fraction of the current passing through the charge to be greater, and then to decrease steadily again as s increases.

Within this framework, we can also understand the effect of stoking on the overall reaction rate. We consider the total chemical reaction in the charge bed, defined by

$$Q_T = s \int_{X=0}^{\infty} Q \, \mathrm{d}X, \tag{6.26}$$

which, if redimensionalised, would have dimensions $[\mathrm{mol\,s^{-1}}]$. Since this is the rate at which charge material is consumed, we may consider it a proxy for the silicon production rate. By integrating the equation of conservation of mass in the solid, we find

$$Q_T = s \int_{X=0}^{\infty} \left(\dot{s} + \frac{1}{s} \right) \frac{\partial C}{\partial X} \, \mathrm{d}X = (1 + s\dot{s})(1 - C_*). \tag{6.27}$$

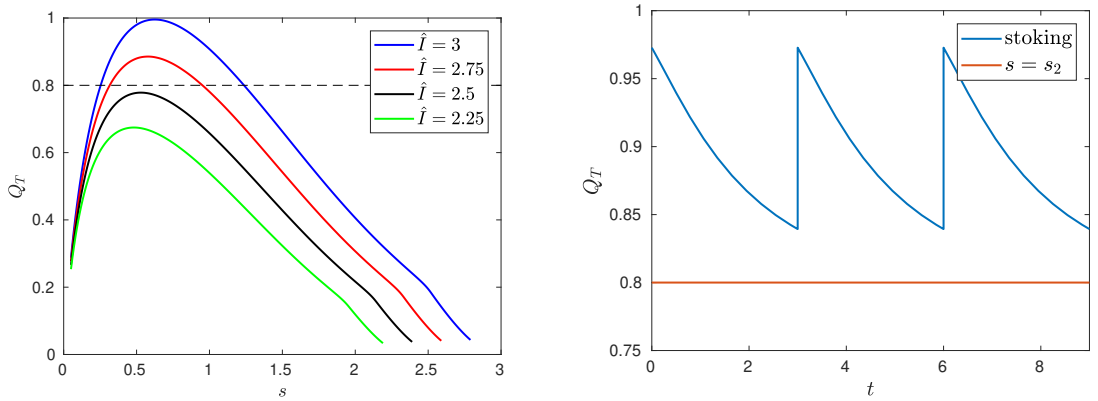

(a) Q_T as a function of s, for various $\hat{I}$. (b) Q_T as a function of time t, for $\hat{I} = 3$.

Figure 6.7: Total reaction rate and stoking. In (a) we show the variation of the total reaction rate Q_T with s for various $\hat{I}$, corresponding to the quasi-steady, small-μ numerical solutions presented in Figure 6.5. The dotted line shows the value of $Q_T = 1 - C_*$ at the steady states $s = s_1$ and s_2. In (b) we fix $\hat{I} = 3$ and show Q_T as a function of time for an example stoking pattern, compared with the steady-state solution.

While this expression has no explicit dependence on the functional form of Q, we note that the dependence is through the values of s and $\dot{s}$ in the solution.

Taking partial derivatives of (6.27) with respect to s we see that

$$\frac{\partial Q_T}{\partial s} = (1 - C_*)\left(\dot{s} + s\frac{\partial \dot{s}}{\partial s}\right). \tag{6.28}$$

We suppose that the furnace is running at sufficiently high current that steady states of our model exist: $s = s_1$ and $s = s_2 > s_1$. At each of these steady states, $Q_T = 1 - C_*$, and further, since

$$\frac{\partial \dot{s}}{\partial s} > 0 \text{ at } s = s_1 \quad \text{and} \quad \frac{\partial \dot{s}}{\partial s} < 0 \text{ at } s = s_2, \tag{6.29}$$

we see that

$$\frac{\partial Q_T}{\partial s} > 0 \text{ at } s = s_1 \quad \text{and} \quad \frac{\partial Q_T}{\partial s} < 0 \text{ at } s = s_2. \tag{6.30}$$

Hence the maximum value of Q_T must always be between s_1 and s_2. This is illustrated in Figure 6.7a, in which we show the variation of Q_T with s.

By stoking the furnace, and so repeatedly pushing s below s_2, we must increase Q_T. Thus, by integrating Q_T over the time of many stoking cycles, we see that the overall rate of consumption of solid material will be increased by the stoking, compared with the crater remaining at the $s = s_2$ steady state. An example is shown in Figure 6.7b.

Here we periodically stoke the system by resetting s to the value $1 < s_2$ at times $t = 0$, 3, and 6. We see that as s evolves toward s_2 we have Q_T decreasing towards the steady state value 0.8, until the furnace is again stoked. The overall reaction rate of the stoked system is greater than if $s = s_2$ for all time. However, if the stoking decreases s such that $s < s_1$, the charge material will move inwards, extinguishing the arc. Thus there is a limit to the improvement that can be made to the furnace efficiency by stoking. In Figure 6.7a we see that the maximum of Q_T increases with $\hat{I}$. Thus, while $Q_T = 1 - C_*$ at $s = s_2$ does not vary with $\hat{I}$, for larger values of $\hat{I}$ we would expect stoking to have a greater effect on the overall rate of chemical reaction, since the maximum of Q_T is greater.

For the small-μ model, there is no dependence of the model on the size r_f of the furnace. In certain parameter regimes, such as a sufficiently large $\hat{I}$, we may actually find that $s_2 > r_f$, and so the stable steady-state solution of the model is outside of the furnace. In this case, our model predicts growth of the crater between stoking events, with the stoking necessary to push material in towards the crater. Depending on where the maximum of Q_T is relative to the size of the furnace, stoking in this case may either increase or decrease the rate of material consumption.

6.4.4 Dynamics with non-zero μ

For the intermediate-μ case it is more difficult to understand the dynamics of the system than in the quasi-steady small-μ case. However, due both to the ease with which the numerical steady-state solution is found (it is much more difficult to find the unstable branch s_1 of the small-μ model), and also the fact that (as seen in Figure 6.2) the intermediate-μ steady-state solution approaches the s_2 solution of the small-μ model as $\mu \to 0$, it seems likely that the intermediate-μ steady state is also stable.

Furthermore, the overall energy balance argument from Section 6.4.2 is almost identical in the intermediate-μ case, except that C^∞ is no longer 1 in general. Thus the radial heat loss term in (6.25) becomes instead

$$H_R = (\gamma + KG_s)(C^\infty - C_*), \tag{6.31}$$

while H_V takes the same form as (6.25). If C^∞ varies sufficiently slowly with s and t about the steady-state solution, then we might still expect H_R, H_V, and $\langle E^2 \rangle$ to be approximately constant around this steady state. If so, we may draw the same conclusion as in Section 6.4.2: that such a steady state is indeed stable.

We could also investigate time-dependent behaviour of the intermediate-μ model directly. For $\mu = O(1)$ this would require solving the quasi-steady region-I problem

(6.2a–c) and (6.5), coupled with the fully time-dependent region-II problem (6.9). A proper investigation of the dynamics of the intermediate-μ system is needed to confirm these inferences, and to explore dynamics further from the steady state.

Chapter 7

Discussion and conclusions

To conclude, we provide a summary and discussion of the research undertaken in this thesis. We summarise our findings, highlighting key results in Section 7.1. In Section 7.2, we then discuss some possible areas for future work. Finally, in Section 7.3, we discuss how our results apply to the production of silicon, both by contributing to better models, and also directly, for furnace operators.

7.1 Summary of modelling and results

We have taken a high-level view of the interacting electrical, thermal, and chemical processes in silicon furnaces. The detailed model presented in Chapter 2 is complicated, with many different timescales, and it would be difficult and computationally expensive to solve the full form of this model directly. We therefore looked for simplifications of this model, which still included the crucial dominant physical processes relevant to industry, in Chapter 3. Based on dimensional analysis of the MHD arc model, we posed a simplified model for the electric arc as a cylinder of uniform temperature, heated by Ohmic heating and with heat lost only to radiation. Another key aspect of the reduced furnace model of Chapter 3 was the simplification of the heat flux boundary condition at the edge of the crater. This simplification is based on the observation that the surface radiation is likely to dominate over the volumetric radiation from the electric arc. Taking advantage of the many disparate timescales in the model, we performed a multiple-timescales homogenisation analysis to average out the fast AC effects. The fast-timescale variation of the electrical system was then incorporated into the slow-timescale system in a computationally efficient way.

In Chapter 4 we studied the fast-timescale model which forms the cell problem used in our homogenisation analysis. This cell problem describes the variation of the electrical system over the AC timescale, providing a bridge between the fast-timescale

modelling of the electrical system and the slow-timescale analysis of the heat and mass transfer in the furnace. Analysis of the simpler DC and prescribed-current AC versions of the cell problem informed analysis of the more detailed equivalent-circuit problem, and helped us to interpret the solutions. We then compared our simple radiation arc model with commonly-used empirical arc models. At high currents the arc models behave quasi-steadily, following their steady-state current-voltage relationship; of the arc models considered, only our radiation arc model has a rising current-voltage relationship, which is expected from simulations of more complicated arc models in the literature. This highlights the benefit of our "first-principles" derivation for the arc model.

In Chapter 5 we studied a simplified version of our homogenised furnace model derived in Chapter 3: an idealised system of counter-current flow and endothermic reactions, without including the electrical effects or the heat transfer boundary condition at the edge of the crater. We also simplified the geometry to a Cartesian domain. The goal of analysing this sub-problem was to understand how the counter-current flow and endothermic chemical reactions interact, without unnecessary additional complications. Using the method of matched asymptotic expansions, we studied the limit of large Péclet number (small δ) in the solid material, and found a variety of different structures across the full range of values of the heat transfer coefficient, μ. Our asymptotic analyses reduce the computational complexity of the model, and give insight into the dominant physical mechanisms at play in different regions of the domain, for each range of μ. Some features of our analysis were common for all sizes of μ, such as a natural temperature scaling (depending on both μ and δ), as well as a boundary layer at the free boundary of the domain. Our choice of an Arrhenius chemical reaction rate resulted in logarithmic functional forms for the natural temperature scalings. For small μ, the flow of gas played a limited role, with the dominant heating mechanism for the solid material due to the radiation incident on the free surface. At large μ, we found more typical counter-current behaviour, with the solution structures dependent on the direction of net heat flux through the domain.

Our solutions for endothermic chemical reactions provide an interesting contrast to asymptotic analyses of combustion, or other multiphase flow systems with exothermic chemical reactions, present in the literature [13, 21, 75]. The asymptotic structures identified in Chapter 5 also provide justification for the simplistic geometry of the model assumed in Chapter 3. In particular, for parameter regimes where the majority of the chemical reaction occurs in a boundary layer at the edge of the charge material,

the wider geometry of the furnace will have relatively little effect, and we are justified in our choice of a simple geometry.

In Chapter 6, we made use of the asymptotic reductions of Chapter 5 to simplify the homogenised model of Chapter 3 for appropriate ranges of μ. The resulting reduced models include all of the AC electrical effects, thermal and material flow processes, and the dominant chemical reaction near to the crater, but are simple and computationally efficient to solve compared with the general model of Chapter 2. In Chapter 6, we found steady-state solutions of these reduced problems numerically, and also analysed the dynamical system in the small-μ case, which is quasi-steady. Analysis of the simplified furnace models in Chapter 6 allows us to better understand the steady-state furnace operation, and, in certain parameter regimes, the dynamics of a realistic SAF. Our findings are directly applicable to furnace operation, as discussed in Section 7.3 below.

7.2 Future work

There are a number of areas of potential future work that we consider to be of interest, both mathematically and to Elkem ASA. We discuss these below.

Reductions of the magnetohydrodynamic arc model Interactions between the coupled electromagnetism, heat transfer, and fluid flow in the electric arcs might be understood by asymptotic analysis of the MHD model presented in Chapter 2. The dimensional analysis of the MHD model in Section 3.1.1 shows that both the arc current and fluid flow are predominantly axial in the case that the arc is longer than it is wide, and that the dominant heat loss mechanism from the arc is by radiation. In the case that the heat conduction in the arc dominates over heat convection, the steady-state MHD model reduces to the cylindrical model analysed in the study group report [19], and illustrated on the left of Figure 7.1. For SAF arcs, we instead expect that heat convection is at least as important as heat conduction, and we might therefore look for arc structures more like that on the right of Figure 7.1, with the arc temperature piecewise constant in r but varying in z, and with a transition layer in which both heat conduction and convection play a role in determining the radial extent of the arc $a(z)$. From such an analysis of the arc structure, we could gain an improved understanding of what determines the size and shape of the arc, and the interactions between the heat loss mechanisms, as well as how these are influenced by the amount of current through the arc.

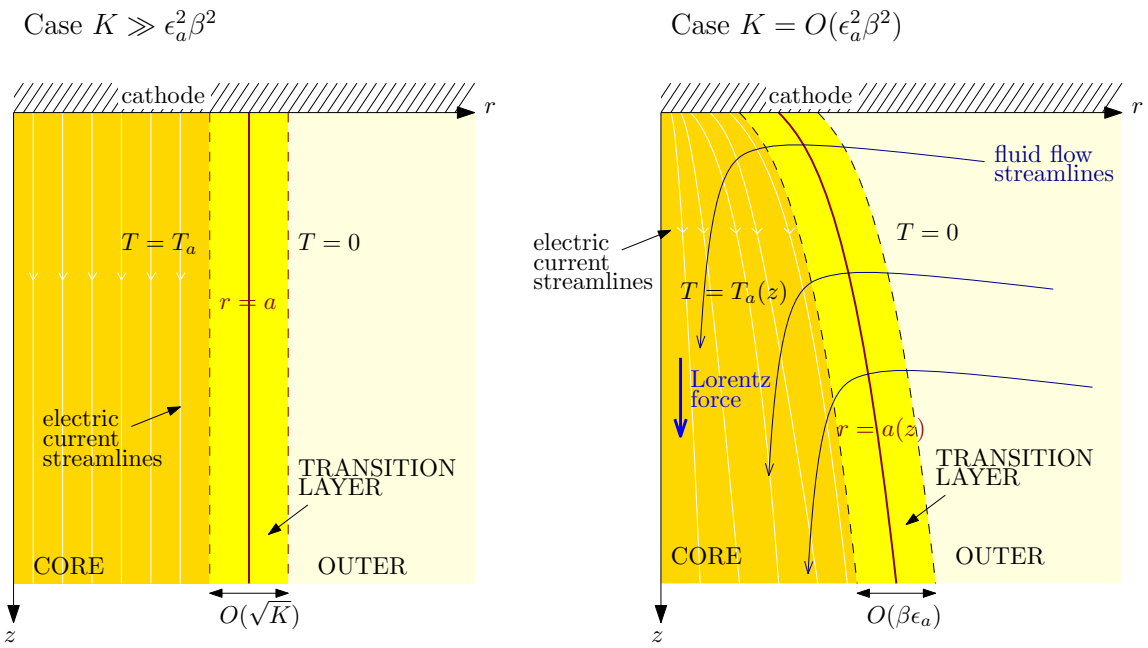

Figure 7.1: Possible asymptotic structures of an electric arc. Left: the cylindrical arc structure found by [19]; right: the possible structure if heat convection is as important as heat conduction.

Electrical circuits and AC effects The AC effects described by the equivalent-circuit model in Chapter 4 merit further investigation. Electrical measurements are usually asymmetric between the three phases, while for simplicity we only considered the symmetric system: the asymmetric model is more complicated, with many more parameters. Varying the model parameters and comparing solutions with industrial measurements is the forward problem; ideally, we would like to understand the inverse problem, and infer model parameters given the electrical measurements. One difficulty with such an optimisation problem is the number of parameters in the model, compared with the limited electrical measurements that can be obtained from an operational furnace. Especially in the asymmetric case, it might be easy to over-fit the data. Care should be taken to restrict to physical parameter ranges, and so physically derived models like our radiation arc model may be better than empirical arc models.

Counter-current flows with multiple chemical reactions In Chapter 5 we considered only a single, endothermic chemical reaction, converting solid material to gas. In the silicon furnace there are multiple chemical reactions occurring, with different temperature-dependent reaction rates. Depending on the relative rates of the different endothermic reactions, we might expect to find multiple critical solid temperatures, and nested boundary layer structures. Furthermore, in cooler regions of

the furnace away from the crater, the SiO gas condenses onto the solid material, which is an exothermic reaction. It would be interesting to investigate the interaction of multiple chemical reactions, both endothermic and exothermic, within the framework of the two-phase model explored in Chapter 5.

Further exploration of the homogenised models There are many ways we could extend the analysis of Chapter 6 to investigate the workings of a silicon furnace in more detail. Firstly, as discussed in Section 3.1.4, we have not been careful to relate the mass lost through the crater wall $r = s$ to the reaction rate in the melt pool. Ensuring global conservation of mass in this way will introduce additional coupling into the model which would be interesting to investigate. We should explore the time-evolution of our solutions found in Chapter 6, as discussed in that chapter. In the simulations of Chapter 6 we used solutions of the simplified cell problem in which the electrode current was prescribed. It would be interesting to investigate the effect of using the full equivalent circuit as the cell problem instead. Furthermore, we could extend our model to investigate the asymmetric system, using the three-phase EC electrical system, but also three versions of the homogenised model for the charge material surrounding each of the three electrodes. In this case we might need to investigate how the temperature and chemical reactions in the charge around one crater might affect those around another, although in the small-μ case it might be appropriate to assume that the three charge regions are independent of each other, and coupled only by the electrical system.

Solutions with the majority of the current passing through the charge The steady-state and quasi-steady solutions of our furnace model found in Chapter 6 seem to agree well with the standard observed furnace behaviour, with the majority of the current passing through the arc. However, a different type of furnace behaviour is occasionally observed, in which there is a sudden and significant increase in the amount of current passing through the charge. This results in poor silicon production: too much quartz is melted at a slower rate and higher in the furnace, but without sufficient energy for the reduction reactions near the crater. This spurious mode occurs rarely, but is difficult to recover from, suggesting that it is a stable furnace behaviour. We have not been able to find solutions of our model with these characteristics.

However, if the critical temperature T_c at which the charge becomes electrically conductive (which is not well-known) is smaller, then we find solutions of the small-μ model with non-monotone temperature profiles for $\dot{s} \neq 0$, as shown in Figure 7.2a.

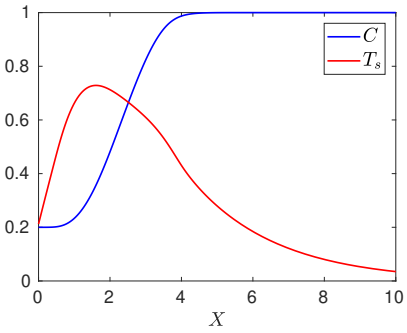

(a) Non-steady solution of the small-μ model for a smaller value of T_c.

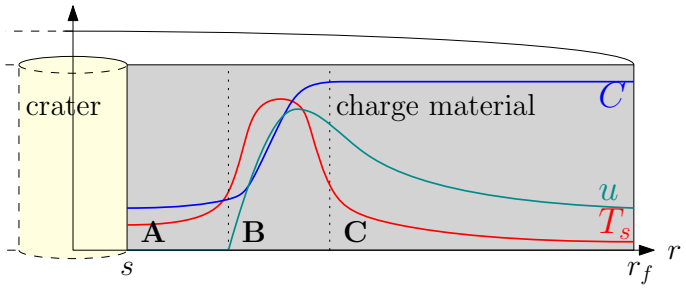

(b) Solution schematic with most of the current passing through the charge. This type of solution could only occur in steady state if the solid velocity $u = 0$ in region A.

Figure 7.2: Illustration of a possible mechanism for a solution with the majority of the current passing through the charge material.

Here, the Ohmic heating causes the T_s maximum to be in the interior of the charge domain, and the heat generated here is used for the chemical reaction. Furthermore, we notice that the current fraction, $\tilde{I}_c$, increases as T_c is decreased.

Our model cannot support a non-monotone solution such as that in Figure 7.2a in steady state because we have prescribed the velocity of the solid material, which is constant through the boundary layer. If we solved for the solid velocity in some way rather than prescribing it, we might obtain solutions such as that sketched in Figure 7.2b. A large proportion of the current passes through the charge material, within the hot region labelled B. The Ohmic heating generated by the current here provides all the heat needed to consume the material moving in toward it. At smaller r, in region A, the temperature is cooler, so very little material is consumed, but because there is no material pushing it inwards, it sits there, stationary and not reacting. To investigate if such solutions exist, a more detailed understanding of the flow of charge material is needed, and we suggest this as an important area for future work.

What can we infer about the general furnace model? For the majority of this thesis we have dealt with simplifications of the general model presented in Chapter 2. Our multiple-timescales analysis of the simplified problem might be extended to more complicated geometries, chemical systems, and fluid flows, and we might anticipate similar structures with the charge material independent of the AC timescale, but depending on averaged radiative and Ohmic heating terms. Complications could arise in the gas flow, which might in fact vary on the AC timescale if coupled more accurately to the changing fluid flow in the crater, driven by the Lorentz forces in the electric arc. We might also expect to see boundary layer structures similar to those

found in Chapter 5, with high temperatures and the majority of the consumption of the solid material occurring near to the craters. However, a more detailed chemical system including exothermic chemical reactions could give rise to additional structures higher up in the charge material.

7.3 Industrial applications

The processes inside of a silicon furnace are both complicated and difficult to observe, so that techniques such as mathematical modelling are important for understanding the many interacting processes at play. Our modelling approach, which involves deriving simpler sub-problems and asymptotic solutions, is quite different to the large-scale simulations or empirical models more commonly found in the furnace-modelling literature, and therefore provides a different type of insight into the operation of SAFs, and the silicon production process. The applications of our work to silicon furnaces may be grouped into fast-timescale dynamics, occurring over the timescale of the alternating current, and the longer-timescale dynamics of the heating, flow and chemical consumption of the charge material.

7.3.1 Fast-timescale (AC) effects

The electrical current and voltage across the furnace is one of the few things that can be measured directly during furnace operation. Improved understanding of the electric arc and the electrical system will enable silicon producers to better understand the fluctuations in these electrical signals, and to interpret them in terms of the conditions within the furnace. The simplified arc model with heat loss by radiation, presented in Chapter 3 and based on a dimensional analysis of the MHD model, is a new addition to the many arc models in the SAF literature. As we explored in Chapter 4, it may be viewed as an alternative to the commonly-used empirical Cassie and Mayr models for studying the fast-timescale electrical system, and interpreting the electrical measurements of operational furnaces.

We showed that our radiation arc model has several advantages over the Cassie and Mayr models. Firstly, it is derived from first principles rather than empirically-derived, hence the model parameters all have a physical meaning and may be estimated from properties of the arc gases. Secondly, the radiation model is designed for SAF arcs (rather than for circuit-breaker arcs), taking into account the heat radiation which is known to be important for such high-current arcs. Finally, the radiation arc

model captures important features of furnace electric arcs, including a rising steady-state current-voltage characteristic (unlike both the Cassie and Mayr models), while being almost as simple, with only one additional parameter.

The homogenisation analysis of Chapter 3 incorporated the fast-timescale effects into a model for the slower heat and mass transfer within the charge material. The homogenisation analysis is valuable to users in industry for two reasons. Firstly, it provides a rational justification for the assumption, often made in slower-timescale models, that the temperatures and chemical concentrations in the charge material do not vary on the timescale of the alternating current. While many studies assume that there is no variation in the charge over the AC timescale, to the best of our knowledge this has never been formally justified. This also justifies the assumption made in fast-timescale EC models that the conductivity or resistance of the charge material is constant over the timescale of interest. Secondly, the homogenisation analysis links two separate bodies of furnace-modelling literature, by demonstrating how the fast AC processes may be accurately and efficiently incorporated into a model of the slower thermal and chemical processes in the charge material, through the values of the averaged heat radiation, $\langle T_a^4 \rangle$, and averaged square of the electric field across the crater, $\langle E^2 \rangle$. Our radiation arc model provides the link between these fast and slow timescales: the heat radiated from the arc is incident onto the surrounding material, providing a heat source for the slower-timescale processes in the charge.

7.3.2 Longer-timescale effects

Our homogenised model is unusual in the furnace literature in that it includes electrical, thermal, and chemical processes: the majority of furnace models studying the heat transfer and chemical processes neglect electrical effects. However, we have seen that all three of these are closely linked processes, each affecting the other.

The observation that the Péclet number in the solid charge material is large indicates that heating from the electric arc due to radiation cannot penetrate very far into the charge material, since the conduction lengthscale is too small. This means that the heating higher up in the furnace can only be due to the hot gases flowing through the porous charge material (or due to exothermic chemical reactions, which we have neglected from our simplified chemical system, although these would still need to be initiated, as they have temperature-dependent reaction rate). The asymptotic analysis of Chapter 5 provides an understanding of the structure of the charge material, in this large Péclet number limit. A range for the heat transfer coefficient may be estimated by measuring both the gas and solid temperatures at the surface of the

furnace charge: if these are quite different, then μ is $O(1)$ or less, but if they are very similar, then $\mu \gg 1$. Our asymptotic analysis confirms the industrial expectation that material consumption occurs fastest within a thin layer at the edge of the crater. However, if $\mu = O(1)$, then a comparable amount of material consumption also occurs within the entirety of the domain, with the heat from the gas providing the energy for the endothermic reaction. While the model used in Chapter 5 is based on silicon-producing SAFs, other applications may also be modelled through this framework. For instance, the rotary kiln simulated in [2] has regions of constant solid temperature, while the energy for the chemical reactions — in this case the evaporation of moisture — is provided by the counter-current flow of gas, reminiscent of our cases B and C. Similar structure is seen in [98] for the reactions in a cement kiln. These studies [2, 98] are numerical; further investigation is needed to understand how our asymptotic results may provide insight into these different chemical systems.

The analysis of steady-state solutions of the reduced homogenised furnace models we provide in Chapter 6 gives insight into the interaction of the coupled electrical, thermal, and dominant chemical processes, and the position of the free boundary of the crater wall. Firstly, we note that from an industrial perspective, the existence of steady-state solutions of the models is an interesting concept in itself: it is difficult to observe the crater structure during operation, but it is generally understood that the crater grows between stoking events. Furthermore, we found that steady-state solutions of the system only exist for sufficiently large applied currents. This is physically intuitive, since if insufficient electrical power is supplied to the system, then the reaction rate cannot balance the flow of material, and the crater falls inward. For sufficiently large currents, we observed exactly one stable steady-state solution for all relevant sizes of μ. At this steady state, there is a balance between the heat energy provided to the system by the electric current and that consumed in the chemical reactions, as well as a balance of mass provided by the steady in-flow of charge material and the material consumed in the reaction. In the small-μ case, we also found an unstable steady state at a smaller radius, characterised by much hotter temperatures in the charge material. A steady state at such a small crater radius cannot be supported by the moderate $\mu = O(1)$ model, since the heat in the gas is not lost from the chemical system, but provides energy for material consumption in the outer domain.

Knowledge of the dynamics of the quasi-steady (small-μ) model allows us to understand the natural evolution of the furnace, but also suggests how furnace operators

might change this behaviour by stoking. We observed that the maximum rate of material consumption is attained at a crater radius smaller than its stable steady-state position, since there the material is hotter and so reacts more quickly. By stoking the furnace and pushing more material in towards the crater, the system is kept closer to this optimal radius, and so material is consumed at a higher rate overall. This also explains the industrial observation that the crater grows between stoking cycles, as our models predicts the crater evolves back towards its natural, stable, steady state. However, we found that for very small crater radii the crater collapses, and so there is a limit to the improvement to efficiency by stoking. In practice, stoking should be carefully controlled to avoid pushing too much material into the crater, which will stifle the arc. Indeed, this finding coincides with common industrial practice: furnace operators are instructed not to stoke "too deeply", as this is found to result in poor silicon production [1].

Appendix A

Degree of freedom count for the region-I problems derived in Chapter 5

In this appendix we show that both the $O(1)$ problem (5.13) and the next-order problem (5.16) (which is $O(T^{\text{in}})$ in case A, and $O(\eta)$ in cases B–D) are correctly specified. Rather than the far-field boundary conditions $C^0 \to 1$ and $C^1 \to 0$ as $X \to \infty$, we use the general boundary conditions $C^0 \to C_0^\infty(t)$, and $C^1 \to C_1^\infty(t)$ to cover all the cases A–D. Although we do not prove it here, the leading-order region-I problems for cases E and F may be shown by a similar argument to have the correct number of boundary conditions, and so are correctly specified, in the case that the characteristics of the $O(1)$ problem travel *into* the boundary layer (region I).

We examine the behaviour of (5.13) and (5.16) near the $X = 0$ boundary by expanding

$$C^0 = c_0^0 + c_0^1 X + O\left(X^2\right), \qquad T_s^0 = \tau_0^0 + \tau_0^1 X + \tau_0^2 X^2 + O\left(X^3\right), \tag{A.1}$$

$$C^1 = c_1^0 + c_1^1 X + O\left(X^2\right), \qquad T_s^1 = \tau_1^0 + \tau_1^1 X + \tau_1^2 X^2 + O\left(X^3\right), \tag{A.2}$$

with all coefficients $\tau, c = O(1)$, and independent of X. Using the boundary conditions at $X = 0$, we fix

$$c_0^0 = C_*, \qquad c_1^0 = 0, \qquad \tau_0^0 = \frac{\rho}{s_0}, \qquad \tau_1^0 = -\frac{\rho s_1}{s_0^2}, \tag{A.3}$$

in terms of the unknown s_0 at leading order, and both s_0 and s_1 at next order. Substituting (A.1) into (5.13a)–(5.13b), and linearising, we find that

$$-(\dot{s}_0 + 1)c_0^1 = -C_* \exp\left(A\left(1 - \frac{s_0}{\rho}\right)\right), \tag{A.4}$$

$$-(\dot{s}_0 + 1)C_*\tau_0^1 = \tau_0^2 - \gamma C_* \exp\left(A\left(1 - \frac{s_0}{\rho}\right)\right), \tag{A.5}$$

so that, upon rearranging, we may express c_0^1 and τ_0^2 in terms of $\dot{s}_0, s_0$, and τ_0^1,

$$c_0^1 = \frac{C_*}{\dot{s}_0 + 1} \exp\left(A\left(1 - \frac{s_0}{\rho}\right)\right), \qquad \tau_0^2 = \gamma C_* \exp\left(A\left(1 - \frac{s_0}{\rho}\right)\right) - (\dot{s}_0 + 1) C_* \tau_0^1. \tag{A.6}$$

By going to higher order in these equations, we can compute all higher-order coefficients, c_0^n and τ_0^n, in terms of $\dot{s}_0$, s_0, and τ_0^1. We note that, given an initial condition for s_0, we can compute s_0 at all subsequent times from $\dot{s}_0$. Thus, we actually have just two degrees of freedom in the leading-order problem near $X = 0$, $\dot{s}_0$ and τ_0^1.

At next order, substituting (A.2) into (5.16a–b) and using the forms of solutions found at leading order (A.6), we find precisely the same structure as at leading order, and may express c_1^1 and τ_1^2 as

$$c_1^1 = -\frac{1}{\dot{s}_0 + 1}\left(\frac{\dot{s}_1 C_*}{\dot{s}_0 + 1} + \frac{A C_* s_1}{\rho}\right) \exp\left(A\left(1 - \frac{s_0}{\rho}\right)\right), \tag{A.7}$$

$$\tau_1^2 = -C_*\left((\dot{s}_0 + 1)\tau_1^1 + \dot{s}_1 \tau_0^1\right) - \frac{\gamma A C_* s_1}{\rho} \exp\left(A\left(1 - \frac{s_0}{\rho}\right)\right), \tag{A.8}$$

which are in terms of $\dot{s}_1, s_1$, and τ_1^1, in addition to the degrees of freedom of the leading-order problem. As at leading order, this is really just two degrees of freedom for the BVP, since s_1 may be expressed in terms of $\dot{s}_1$ for a given initial condition.

Thus we have found that both (5.13) and (5.16) have two degrees of freedom near $X = 0$.

In the far field, we make the expansions

$$C^0 = \bar{c}_0^0 + \bar{c}_0^1(X), \quad T_s^0 = \bar{\tau}_0^0 + \bar{\tau}_0^1(X), \quad C^1 = \bar{c}_1^0 + \bar{c}_1^1(X), \quad T_s^1 = \bar{\tau}_1^0 + \bar{\tau}_1^1(X), \tag{A.9}$$

with all $\bar{c}_i^0, \bar{\tau}_i^0 = O(1)$ and independent of X, and the correction terms small as $X \to \infty$.

The boundary conditions as $X \to \infty$ (in both the leading-order, and next-order problems) result in

$$\bar{c}_0^0 = C_0^\infty(t), \qquad \bar{c}_1^0 = C_1^\infty(t), \qquad \bar{\tau}_0^0 = 0, \qquad \bar{\tau}_1^0 = 1, \tag{A.10}$$

as well as

$$\bar{c}_0^1, \bar{c}_1^1, \bar{\tau}_0^1, \bar{\tau}_1^1 \to 0 \qquad \text{as } X \to \infty. \tag{A.11}$$

Since $\bar{\tau}_0^1$ becomes small in the far field, the chemical reaction rate is exponentially small in this limit. Thus by substituting the leading-order variables in (A.9) into the equations (5.13a)–(5.13b), and linearising, we find that $\bar{c}_0^1$ and $\bar{\tau}_0^1$ satisfy

$$-(\dot{s}_0 + 1)\frac{\partial \bar{c}_0^1}{\partial X} = 0, \qquad -(\dot{s}_0 + 1)\bar{c}_0^0 \frac{\partial \bar{\tau}_0^1}{\partial X} = \frac{\partial^2 \bar{\tau}_0^1}{\partial X^2}. \tag{A.12}$$

Using the boundary conditions (A.11) (and since we have, as always, that $\dot{s}_0 > -1$) we find that

$$\bar{c}_0^1 = 0, \qquad \bar{\tau}_0^1 = b_0 \exp\left(-(\dot{s}_0 + 1) C_0^\infty X\right), \tag{A.13}$$

where b_0 is a constant of integration. This b_0 is the only additional degree of freedom in the far field. Together with the two degrees of freedom we found at $X = 0$, there are three degrees of freedom in total. Since (5.13) is a third order system, we have shown that the BVP (5.13) is correctly specified.

Similarly, substituting (A.9) into the equations (5.16a–b) and neglecting exponentially small terms, we find

$$-(\dot{s}_0 + 1)\frac{\partial \bar{c}_1^1}{\partial X} - \dot{s}_1 \frac{\partial \bar{c}_0^1}{\partial X} = 0, \tag{A.14}$$

$$-(\dot{s}_0 + 1)\left(C_1^\infty \frac{\partial \bar{\tau}_0^1}{\partial X} + C_0^\infty \frac{\partial \bar{\tau}_1^1}{\partial X}\right) - \dot{s}_1 C_0^\infty \frac{\partial \bar{\tau}_1^1}{\partial X} = \frac{\partial^2 \bar{\tau}_1^1}{\partial X^2}. \tag{A.15}$$

Using the forms of the leading-order solutions $\bar{c}_0^1$ and $\bar{\tau}_0^1$, we find solutions

$$\bar{c}_1^1 = 0, \qquad \bar{\tau}_1^1 = \left(b_1 - b_0 X \left(C_1^\infty(\dot{s}_0 + 1) + C_0^\infty \dot{s}_1\right)\right) \exp(-C^\infty(\dot{s}_0 + 1)X). \tag{A.16}$$

Here, b_0 is the degree of freedom in the leading-order problem, so there is only one additional degree of freedom, b_1, in this next-order problem in the far field. Thus, as for the leading-order problem, there are a total of three degrees of freedom for the next-order problem (5.16), which is third order, and therefore (5.16) is correctly specified.

Appendix B

Matching at next order between regions in Section 5.5

In this appendix we analyse the $O(\eta)$ correction in case C, in order to fix the constant of integration D in the region CIII solid temperature $\tilde{T}_s^0$ (5.78). To do this, we must consider the $O(\eta)$ corrections in all regions CI–CIV of the domain.

In region CI we find the $O(\eta)$ problem is given by (5.16) with the far-field solid concentration C_1^∞ that must be fixed by matching with the outer region.

The $O(\eta)$ terms in the region CII equations (5.53) are

$$\frac{\partial \hat{C}^1}{\partial t} - \frac{\partial \hat{C}^1}{\partial x} = -Q^1, \qquad \frac{\partial \hat{f}^1}{\partial x} = Q^1, \qquad \mu(\hat{T}_g^1 - 1) = \gamma Q^1, \tag{B.1a}$$

$$K\frac{\partial}{\partial x}\left(\hat{f}^0\hat{T}_g^1 + \hat{f}^1\hat{T}_g^0\right) = \hat{C}^0 \exp\left(A(1+\hat{T}_s^0)\right) - \mu(\hat{T}_g^1 - 1), \tag{B.1b}$$

where

$$Q^1 = \exp\left(A(1+\hat{T}_s^0)\right)\left(\hat{C}^1 + A\hat{C}^0(\hat{T}_s^1 - (\hat{T}_s^0)^2)\right) \tag{B.2}$$

is the correction to the chemical reaction rate.

Matching with region CI, we require

$$\hat{f}^1\big|_{x=s_0} = F_s^1 - s_1\frac{\partial \hat{f}^0}{\partial x}\Big|_{x=s_0}, \qquad \hat{T}_g^1\big|_{x=s_0} = G_s^1 - s_1\frac{\partial \hat{T}_g^0}{\partial x}\Big|_{x=s_0}, \tag{B.3}$$

where

$$F_s^1 := \lim_{X\to\infty} f^1(X,t), \qquad G_s^1 := \lim_{X\to\infty} T_g^1(X,t). \tag{B.4}$$

We note that, while region CI is $O(\delta)$, our asymptotic expansion is in powers of $\eta \gg \delta$, and therefore all terms in the region-CII expansion must equal those in the CI expansion. However, since the boundary layer is positioned at $x = s = s_0 + \eta s_1$,

we obtain correction terms when evaluating the outer solutions at $x = s_0$, which give rise to the $s_1(\partial \hat{T}_g^0/\partial x)|_{x=s_0}$ terms in these expansions.

The equations (B.1) reduce to the system

$$\frac{\partial \hat{f}^1}{\partial x} = \frac{\mu}{\gamma}(\hat{T}_g^1 - 1), \tag{B.5}$$

$$K\frac{\partial}{\partial x}\left(\hat{f}^0\hat{T}_g^1 + \hat{f}^1\hat{T}_g^0\right) = \hat{C}^0 \exp\left(A(1+\hat{T}_s^0)\right) - \mu(\hat{T}_g^1 - 1), \tag{B.6}$$

for $\hat{f}^1$ and $\hat{T}_g^1$, in terms of the leading-order solution. Combining these equations, and using the leading-order equation for $\hat{f}^0$, we may take a first integral, and find that

$$K(\hat{f}^0\hat{T}_g^1 + \hat{f}^1\hat{T}_g^0) + \gamma\hat{f}^1 - \hat{f}^0 = H^1 \tag{B.7}$$

is constant. Using the matching conditions (B.3) we fix

$$H^1 = KF_s\left(G_s^1 - s_1\frac{\partial \hat{T}_g^0}{\partial x}\Big|_{x=s_0}\right) + \frac{H^0}{F_s}\left(F_s^1 - s_1\frac{\partial \hat{f}^0}{\partial x}\Big|_{x=s_0}\right) - F_s. \tag{B.8}$$

We similarly define the constant

$$H^0 := F_s(KG_s + \gamma) = \hat{f}^0(K\hat{T}_g^0 + \gamma) \tag{B.9}$$

by combining the leading-order equations. Rearranging (B.7) we see that

$$\hat{f}^1 = \frac{1}{H^0}\hat{f}^0\left(\hat{f}^0 - K\hat{f}^0\hat{T}_g^1 + H^1\right), \tag{B.10}$$

and so the equation of gas conservation of energy becomes an equation for $\hat{T}_g^1$:

$$\frac{\partial \hat{T}_g^1}{\partial x} + (\hat{T}_g^1 - 1)\left(\frac{\hat{f}_x^0}{\hat{f}^0} + \frac{\mu H^0}{\gamma K(\hat{f}^0)^2}\right) = \left(\frac{2}{K} - 1 + \frac{H^0}{K\hat{f}^0}\right)\frac{\hat{f}_x^0}{\hat{f}^0}, \tag{B.11}$$

using the shorthand $\hat{f}_x^0 = \partial \hat{f}^0/\partial x$. Equation (B.11) has the solution

$$\begin{aligned}\hat{T}_g^1 = 1 + \exp&\left(-\int_{x'=s_0}^{x}\frac{\hat{f}_x^0}{\hat{f}^0} + \frac{\mu H^0}{\gamma(\hat{f}^0)^2}\,\mathrm{d}x'\right)\\ &\times\left[G_s^1 - s_1\frac{\partial \hat{T}_g^0}{\partial x}\Big|_{x=s_0}\right.\\ &\left.+\int_{x'=s_0}^{x}\left(\frac{2}{K} - 1 + \frac{H^0}{K\hat{f}^0}\right)\frac{\hat{f}_x^0}{\hat{f}^0}\exp\left(-\int_{x''=s_0}^{x'}\frac{\hat{f}_x^0}{\hat{f}^0} + \frac{\mu H^0}{\gamma(\hat{f}^0)^2}\,\mathrm{d}x''\right)\,\mathrm{d}x'\right],\end{aligned} \tag{B.12}$$

where we have fixed the integration constant using (B.3).

The gas flux correction $\hat{f}^1$ is then given by (B.10). The solid concentration correction, $\hat{C}^1$ then satisfies the problem

$$\frac{\partial \hat{C}^1}{\partial t} - \frac{\partial \hat{C}^1}{\partial x} = -\frac{\mu}{\gamma}\left(\hat{T}_g^1 - 1\right) \qquad \text{for } x \in [s_0, 1], \tag{B.13a}$$

$$\hat{C}^1 = w\frac{\partial \hat{C}^0}{\partial x}\Big|_{x=1} + \lim_{y\to\infty} \tilde{C}_s^1 \qquad \text{at } x = 1, \tag{B.13b}$$

$$\hat{C}^1 = 0 \qquad \text{at } t = 0, \tag{B.13c}$$

$$\hat{C}^1 = C_1^\infty - s_1\frac{\partial \hat{C}^0}{\partial x}\Big|_{x=s_0} \qquad \text{at } x = s_0, \tag{B.13d}$$

where the correction term $w(\partial C^0/\partial x)|_{x=1}$ is required for the matching with region CIII, since here we have evaluated the region CII problem at $x = 1$. We will see below that in region CIII we have $\tilde{C}^1 = 0$, and so, just as at $O(1)$, the region CI problem (3.81) must be solved simultaneously with (B.13) (coupled via C_1^∞, and the values F_s^1 and G_s^1).

We may also find the $O(\eta)$ correction to $\hat{T}$ in the outer region,

$$\hat{T}_s^1 = \frac{\mu}{\hat{C}_s^0\gamma}(K\hat{T}_g^1 - A)e^{-\hat{T}^0} - \left(\frac{\hat{C}_s^1}{\hat{C}_s^0} + (\hat{T}_s^0)^2\right) \tag{B.14}$$

(although we do not need this to fix D).

In region CIV the $O(\eta)$ terms in (5.68) are

$$\frac{\partial \bar{C}^1}{\partial Y} = 0, \qquad \bar{C}^0\frac{\partial \bar{T}_s^0}{\partial t} + \bar{C}^0\frac{\partial \bar{T}_s^1}{\partial Y} + \bar{C}^1\frac{\partial \bar{T}_s^0}{\partial Y} = \mu(\bar{T}_g^1 - \bar{T}_s^0), \tag{B.15a}$$

$$\frac{\partial \bar{f}^1}{\partial Y} = 0, \qquad -K\frac{\partial}{\partial Y}(\bar{f}^0\bar{T}_g^1 + \bar{f}^1\bar{T}_g^0) = \mu\bar{T}_g^0. \tag{B.15b}$$

Using the leading-order solutions, and the boundary conditions $\bar{C}_s^1 = 0 = \bar{T}_s^1$ at $Y = 0$ ($x = 1$), we can solve (B.15) to find $\bar{C}^1 = 0$, and $\bar{f}^1 = c_1(t)$ is uniform, (the value of c_1 is fixed by matching to the left, as below). Using the leading-order solutions, and the fact that $\bar{T}_s^1 = 0$ at $Y = 0$, the temperature corrections are then given by

$$\bar{T}_g^1 = -\frac{\mu G_1}{KF_1}Y + c_2, \quad \bar{T}_s^1 = \mu(c_2 - \bar{T}^{\text{in}})Y - \frac{\mu}{2}\left(\frac{\mathrm{d}G_1}{\mathrm{d}t} + \frac{\mu G_1(1 + KF_1)}{KF_1}\right)Y^2, \tag{B.16}$$

for constant $c_2(t)$ of integration, again to be fixed by matching to the left.

In the transition layer region CIII, the $O(\eta)$ problem requires that all of $\tilde{C}^1, \tilde{f}^1$, and $\tilde{T}_g^1$ are uniform over the transition layer. (We do not need to find the correction $\tilde{T}_s^1$ in the transition layer, as this is $O(\eta^3)$.) Matching regions CII and CIII as $y \to \infty$,

$$\tilde{f}^1 = \hat{f}^1\Big|_{x=1} - w\frac{\partial \hat{f}^0}{\partial x}\Big|_{x=1}, \qquad \tilde{T}_g^1 = \hat{T}_g^1\Big|_{x=1} - w\frac{\partial \hat{T}_g^0}{\partial x}\Big|_{x=1}, \tag{B.17}$$

and (B.13b). Now matching the transition layer to the boundary layer as $y \to -\infty$, since $\bar{C}_s^0 = 1$, $\bar{f}_g^0 = F_1$, and $\bar{T}_g^0 = G_1$ are all uniform, we have

$$c_1 = \bar{f}_g^1\Big|_{Y=w} = \lim_{y\to-\infty}\left(\tilde{f}_g^1 - y\frac{\partial \bar{f}_g^0}{\partial Y}\Big|_{Y=w}\right) = \tilde{f}_g^1, \tag{B.18}$$

$$c_2 - \frac{\mu G_1}{KF_1}w = \bar{T}_g^1\Big|_{Y=w} = \lim_{y\to-\infty}\left(\tilde{T}_g^1 - y\frac{\partial \bar{T}_g^0}{\partial Y}\Big|_{Y=w}\right) = \tilde{T}_g^1, \tag{B.19}$$

$$0 = \bar{C}^1\Big|_{Y=w} = \lim_{y\to-\infty}\left(\tilde{C}_s^1 - y\frac{\partial \bar{C}^0}{\partial Y}\Big|_{Y=w}\right) = \tilde{C}_s^1. \tag{B.20}$$

Thus using (B.17), we obtain

$$c_1 = \hat{f}^1\Big|_{x=1} - w\frac{\partial \hat{f}^0}{\partial x}\Big|_{x=1}, \qquad c_2 = \frac{\mu G_1}{KF_1}w + \hat{T}_g^1\Big|_{r=r_f} - w\frac{\partial \hat{T}_g^0}{\partial x}\Big|_{x=1}. \tag{B.21}$$

Except for D in (5.78), this fixes all the constants of integration to $O(\eta)$ in regions CII–CIV, in terms of the $O(\eta)$ corrections in region CI. The value of D is fixed by matching the solid temperature at $O(\eta)$ between regions CIII–CIV, according to

$$\bar{T}^1\Big|_{Y=w} = \lim_{y\to-\infty}\left(\tilde{T}^0 - y\frac{\partial \bar{T}^0}{\partial Y}\Big|_{Y=w}\right). \tag{B.22}$$

The left-hand side of (B.22) is (B.16), evaluated at $Y = w$, with c_2 as in (B.21) and w as in (5.81). The right-hand side of (B.22) is

$$\begin{aligned}
\lim_{y\to-\infty}\left(\tilde{T}^0 - y\frac{\partial \bar{T}^0}{\partial Y}\Big|_{Y=w}\right) &= \lim_{y\to-\infty}\left(-\frac{1}{A}\log\left(\frac{\gamma}{\mu G_1}(1 + De^{-\mu G_1 A y})\right) - 1 - \mu G_1 y\right) \\
&= \lim_{y\to-\infty}\left(-\frac{1}{A}\log\left(\frac{\gamma}{\mu G_1}De^{-\mu G_1 A y}\right) - 1 - \mu G_1 y\right) \\
&= \lim_{y\to-\infty}\left(-\frac{1}{A}\log\left(\frac{\gamma D}{\mu G_1}\right) + \mu G_1 y - 1 - \mu G_1 y\right) \\
&= -\frac{1}{A}\log\left(\frac{\gamma D}{\mu G_1}\right) - 1.
\end{aligned} \tag{B.23}$$

Therefore, D is given by rearranging (B.22), so that

$$\begin{aligned}
D = \frac{\mu G_1 e^{-A}}{\gamma}\exp\Bigg(-\frac{A(1-\bar{T}^{\mathrm{in}})}{G_1}\Bigg[\hat{T}_g^1\Big|_{x=1} - \bar{T}^{\mathrm{in}} \\
+ (1-\bar{T}^{\mathrm{in}})\left(\frac{1-KF_1}{2KF_1} - \frac{1}{\mu G_1}\left(\frac{\partial \hat{T}_g^0}{\partial x}\Big|_{x=1} - \frac{1}{2}\frac{\mathrm{d}G_1}{\mathrm{d}t}\right)\right)\Bigg]\Bigg).
\end{aligned} \tag{B.24}$$

Bibliography

[1] Internal Elkem ASA data, personal communication.

[2] A. Agrawal and P.S. Ghoshdastidar. Numerical simulation of heat transfer during production of rutile titanium dioxide in a rotary kiln. *International Journal of Heat and Mass Transfer*, 106:263–279, 2017.

[3] T. Ahnert, A. Münch, and B. Wagner. Models for the two-phase flow of concentrated suspensions. *European Journal of Applied Mathematics*, 30(3):585–617, 2019.

[4] J. Alexis, M. Ramirez, G. Trapaga, and P. Jönsson. Modeling of a DC electric arc furnace – heat transfer from the arc. *ISIJ International*, 40(11):1089–1097, 2000.

[5] B. Andresen. *Process model for carbothermic production of silicon metal.* PhD thesis, NTNU, Norway, 1995.

[6] G.R. Awagan and A.G. Thosar. Mathematical modeling of electric arc furnace to study the flicker. *International Journal of Scientific & Engineering Research*, 7(5):684–695, 2016.

[7] M.R. Baer and J.W. Nunziato. A two-phase mixture theory for the deflagration-to-detonation transition (DDT) in reactive granular materials. *International Journal of Multiphase Flow*, 12(6):861–889, 1986.

[8] J.A. Bakken, L. Gu, H.L. Larsen, and V.G. Sevastyanenko. Numerical modeling of electric arcs. *Journal of Engineering Physics and Thermophysics*, 70(4):530–543, 1997.

[9] I.J. Barker, M.S. Rennie, C.J. Hockaday, and P.J. Brereton-Stiles. Measurement and control of arcing in a submerged-arc furnace. In *The 11th International Ferroalloys Congress*, 2007.

[10] D. Bercovici, Y. Ricard, and G. Schubert. A two-phase model for compaction and damage: 1. General theory. *Journal of Geophysical Research: Solid Earth*, 106(B5):8887–8906, 2001.

[11] A. Bermúdez, M.C. Muñiz, F. Pena, and J. Bullón. Numerical computation of the electromagnetic field in the electrodes of a three-phase arc furnace. *International Journal for Numerical Methods in Engineering*, 46(5):649–658, 1999.

[12] D.C. Bhonsle and R.B. Kelkar. New time domain electric arc furnace model for power quality study. In *The 6th India International Conference on Power Electronics (IICPE)*, pages 1–6. IEEE, 2014.

[13] M.R. Booty and B.J. Matkowsky. Modes of burning in filtration combustion. *European Journal of Applied Mathematics*, 2(1):17–41, 1991.

[14] B. Bowman and K. Krüger. *Arc Furnace Physics*. Verlag Stahleisen Düsseldorf, 2009.

[15] F. Boyer, É. Guazzelli, and O. Pouliquen. Unifying suspension and granular rheology. *Physical Review Letters*, 107(18):188301, 2011.

[16] C.E. Brennen. *Fundamentals of multiphase flow*. Cambridge University Press, 2005.

[17] C. Budd, S.J. Chapman, J. King, A.A. Lacey, D. Larson, M. Peletier, C.P. Please, D. Riley, A. Wheeler, and G. Wood. Temperature variations and control of a calciner. Study group report, ESGI28, http://www.maths-in-industry.org/miis/359/1/Temprature-variations-and-control-of-calciner.pdf, 1995.

[18] C. Budd, S.J. Chapman, A.A. Lacey, and J.R. Ockendon. Electric arc problem. Study group report. http://www.maths-in-industry.org/miis/651/1/p2.pdf, 1990.

[19] C. Budd, A. Jones, H. Biesenbach, and S. Halvorsen. Elkem arc problem. Study group report, personal communication from Elkem ASA, c1990.

[20] H. Byrne and J. Norbury. Stable solutions for a catalytic converter. *SIAM Journal on Applied Mathematics*, 54(3):789–813, 1994.

[21] H. Byrne and J. Norbury. The effect of solid conversion on travelling combustion waves in porous media. *Journal of Engineering Mathematics*, 32(4):321–342, 1997.

[22] A.M. Cassie. Arc rupture and circuit severity: A new theory. In *Conférence Internationale des Grands Réseaux Électriques à Haute Tension (CIGRE)*, volume 102, pages 588–608, 1939.

[23] I. Cohen and A. Whitman. On the Steenbeck minimum principle for arc discharges and its comparison with the constant property arc. *Journal of Applied Physics*, 44(4):1557–1561, 1973.

[24] R.M. Corless, G.H. Gonnet, D.E.G. Hare, D.J. Jeffrey, and D.E. Knuth. On the LambertW function. *Advances in Computational Mathematics*, 5(1):329–359, 1996.

[25] R. Courant and D. Hilbert. *Methods of Mathematical Physics: Partial Differential Equations, Volume 2*. John Wiley & Sons, 1961.

[26] M.D. Cowley. Integral methods of analysing electric arcs: I. Formulation. *Journal of Physics D: Applied Physics*, 7(16):2218, 1974.

[27] P.A. Davidson. *Introduction to Magnetohydrodynamics*. Cambridge University Press, 2001.

[28] M. Dhainaut. Simulation of the electric field in a submerged arc furnace. In *Proceedings of the Tenth International Ferroalloy Congress*, pages 605–613, 2004.

[29] A. Egerton, K. Gugan, and F.J. Weinberg. The mechanism of smouldering in cigarettes. *Combustion and Flame*, 7:63–78, 1963.

[30] P.A. Eidem. *Electrical resistivity of coke beds*. PhD thesis, NTNU, Norway, 2008.

[31] Y. Forterre and O. Pouliquen. Flows of dense granular media. *Annual Review of Fluid Mechanics*, 40:1–24, 2008.

[32] A.C. Fowler, I. Frigaard, and S.D. Howison. Temperature surges in current-limiting circuit devices. *SIAM Journal on Applied Mathematics*, 52(4):998–1011, 1992.

[33] M. Fromreide, D. Gómez, S.A. Halvorsen, E.V. Herland, and P. Salgado. Reduced 2D/1D mathematical models for analyzing inductive effects in submerged arc furnaces. *Applied Mathematical Modelling*, 98:59–70, 2021.

[34] D. Gaskell. *Introduction to metallurgical thermodynamics*. Hemisphere Publishing Corporation New York, 1981.

[35] S. Golestani and H. Samet. Generalised Cassie–Mayr electric arc furnace models. *IET Generation, Transmission & Distribution*, 10(13):3364–3373, 2016.

[36] R. González-Fariña, A. Münch, J.M. Oliver, and R.A. Van Gorder. Modeling microsilica particle formation and growth due to the combustion reaction of silicon monoxide with oxygen. *SIAM Journal on Applied Mathematics*, 80(2):1003–1033, 2020.

[37] N. Gustavsson. Evaluation and simulation of black-box arc models for high-voltage circuit-breakers. Master's thesis, Institutionen för systemteknik, Norway, 2004.

[38] S.A. Halvorsen, H.A.H. Olsen, and M. Fromreide. An efficient simulation method for current and power distribution in 3-phase electrical smelting furnaces. *IFAC-PapersOnLine*, 49(20):167–172, 2016.

[39] S.A. Halvorsen, A. Schei, and J.H. Downing. A unidimensional dynamic model for the (ferro-) silicon process. In *Electrical Furnace Conference Proceedings*, volume 50, pages 45–59, 1992.

[40] T.H. Hannesson. The Si process drawings. Elkem Iceland, 2016.

[41] E.V. Herland, M. Sparta, and S.A. Halvorsen. Skin and proximity effects in electrodes and furnace shells. *Metallurgical and Materials Transactions B*, 50(6):2884–2897, 2019.

[42] I.J. Hewitt. *Mathematical modelling of geophysical melt drainage*. DPhil thesis, Universtiy of Oxford, 2009.

[43] E.J. Hinch. *Perturbation Methods*. Cambridge University Press, 1991.

[44] J.R. Howell and R. Siegel. *Thermal Radiation Heat Transfer, 4th edition*. Taylor and Francis, 2002.

[45] M.F. Hoyaux. *Arc Physics*. Springer, 1968.

[46] S.T. Johansen, H. Tveit, S. Grådahl, A.M. Valderhaug, and J. Byberg. Environmental aspects of ferro-silicon furnace operations - an investigation of waste gas dynamics. In *The 8th International Ferroalloys Congress, Pekin*, 1998.

[47] G.R. Jones and M.T.C. Fang. The physics of high-power arcs. *Reports on Progress in Physics*, 43(12):1415–1465, 1980.

[48] M. Kadkhodabeigi. *Modeling of Tapping Processes in Submerged Arc Furnaces*. PhD thesis, NTNU, Norway, 2011.

[49] M. Kadkhodabeigi, H. Tveit, and K.H. Berget. Silicon process — new hood design for tapping gas collection. In *Twelfth International Ferroalloys Congress*, pages 109–119, 2010.

[50] M. Karasik. Driven motion and instability of an atmospheric pressure arc. Technical report, Princeton Plasma Physics Lab., NJ (US), 1999.

[51] M. Kaviany. *Principles of heat transfer in porous media*. Springer Science & Business Media, 2012.

[52] E.H. Kerner. The electrical conductivity of composite media. *Proceedings of the Physical Society. Section B*, 69(8):802, 1956.

[53] J. Kierzenka and L.F. Shampine. A BVP solver based on residual control and the MATLAB PSE. *ACM Transactions on Mathematical Software*, 27(3):299–316, 2001.

[54] K.B. Kiradjiev, S.A. Halvorsen, R.A. Van Gorder, and S.D. Howison. Maxwell-type models for the effective thermal conductivity of a porous material with radiative transfer in the voids. *International Journal of Thermal Sciences*, 145:106009, 2019.

[55] R-J. Koopmans, J.S. Shrimpton, G.T. Roberts, and A.J. Musker. A one-dimensional multicomponent two-fluid model of a reacting packed bed including mass, momentum and energy interphase transfer. *International Journal of Multiphase Flow*, 57:10–28, 2013.

[56] W.B. Kunkel. Generalized Ohms law for plasma including neutral particles. *The Physics of Fluids*, 27(9):2369–2371, 1984.

[57] J. Kunze and R. Degel. New trends in submerged arc furnace technology. *Proceedings: Tenth International Ferroalloys Congress*, 1:444–454, 2004.

[58] A.A. Lacey. Thermal runaway in a non-local problem modelling Ohmic heating. Part I: Model derivation and some special cases. *European Journal of Applied Mathematics*, 6(2):127–144, 1995.

[59] A.A. Lacey. Thermal runaway in a non-local problem modelling Ohmic heating. Part II: General proof of blow-up and asymptotics of runaway. *European Journal of Applied Mathematics*, 6(3):201–224, 1995.

[60] F. Lago, J.J. Gonzalez, P. Freton, and A. Gleizes. A numerical modelling of an electric arc and its interaction with the anode: Part I. The two-dimensional model. *Journal of Physics D: Applied Physics*, 37(6):883–897, 2004.

[61] L.D. Landau, L.P. Pitaevskii, and E.M. Lifshitz. *Electrodynamics of continuous media, 2nd edition*. Pergamon Press, 1984.

[62] R. Landauer. Electrical conductivity in inhomogeneous media. In *AIP conference proceedings*, volume 40, pages 2–45. AIP, 1978.

[63] V. Logar, D. Dovžan, and I. Škrjanc. Mathematical modeling and experimental validation of an electric arc furnace. *ISIJ International*, 51(3):382–391, 2011.

[64] J.J. Lowke. Simple theory of free-burning arcs. *Journal of Physics D: Applied Physics*, 12(11):1873–1886, 1979.

[65] E.K. Luckins, J.M. Oliver, C.P. Please, B.M. Sloman, and R.A. Van Gorder. Homogenised model for the electrical current distribution within a submerged arc furnace for silicon production. *European Journal of Applied Mathematics*, pages 1–36, 2021.

[66] F. Marias, H. Roustan, and A. Pichat. Modelling of a rotary kiln for the pyrolysis of aluminium waste. *Chemical Engineering Science*, 60(16):4609–4622, 2005.

[67] O. Mayr. Beiträge zur Theorie des statischen und des dynamischen Lichtbogens. *Archiv für Elektrotechnik*, 37(12):588–608, 1943.

[68] O. Mayr. Über die Theorie des Lichtbogens und seiner Löschung. *Elektrotechnische Zeitschrift*, 64(49/50):645–652, 1943.

[69] I. McDougall. Finite element modelling of electric currents in AC submerged arc furnaces. In *The 11th International Ferroalloys Congress*, pages 630–637, 2007.

[70] D. McKenzie. The generation and compaction of partially molten rock. *Journal of Petrology*, 25(3):713–765, 1984.

[71] C.R. Meyer and I.J. Hewitt. A continuum model for meltwater flow through compacting snow. *The Cryosphere*, 11(6):2799–2813, 2017.

[72] M.F. Modest. *Radiative Heat Transfer*. Academic Press, 2013.

[73] S. Mrozowski. Semiconductivity and diamagnetism of polycrystalline graphite and condensed ring systems. *Physical Review*, 85(4):609, 1952.

[74] J. Ni and C. Beckermann. A volume-averaged two-phase model for transport phenomena during solidification. *Metallurgical Transactions B*, 22(3):349–361, 1991.

[75] J. Norbury and A.M. Stuart. Travelling combustion waves in a porous medium. Part I – existence. *SIAM Journal on Applied Mathematics*, 48(1):155–169, 1988.

[76] A. Parizad, H.R. Baghaee, A. Tavakoli, and S. Jamali. Optimization of arc models parameter using genetic algorithm. In *2009 International Conference on Electric Power and Energy Conversion Systems,(EPECS)*, pages 1–7. IEEE, 2009.

[77] E. Pfender. Electric arcs and arc gas heaters. *Gaseous Electronics*, 1(5):291–298, 1978.

[78] C.P. Please, F. Liu, and D.L.S. McElwain. Condensed phase combustion travelling waves with sequential exothermic or endothermic reactions. *Combustion Theory and Modelling*, 7:129–143, 2003.

[79] Y. Raizer. *Gas Discharge Physics*. Springer-Verlag, 1991.

[80] S. Ramakrishnan, A.D. Stokes, and J.J. Lowke. An approximate model for high-current free-burning arcs. *Journal of Physics D: Applied Physics*, 11(16):2267–2280, 1978.

[81] M.A. Ramírez-Argáez, C. González-Rivera, and G. Trápaga. Mathematical modeling of high intensity electric arcs burning in different atmospheres. *ISIJ International*, 49(6):796–803, 2009.

[82] P. Rivière and A. Soufiani. Updated band model parameters for H_2O, CO_2, CH_4 and CO radiation at high temperature. *International Journal of Heat and Mass Transfer*, 55(13-14):3349–3358, 2012.

[83] C.M. Rooney. *Homogenisation of the electrothermal behaviour of granular material*. DPhil thesis, University of Oxford, 2019.

[84] C.M. Rooney, C.P. Please, and S.D. Howison. Homogenisation applied to thermal radiation in porous media. *European Journal of Applied Mathematics*, pages 1–22, 2020.

[85] G. Sævarsdóttir. *High current AC arcs in silicon and ferrosilicon furnaces*. PhD thesis, NTNU, Norway, 2002.

[86] G.A. Sævarsdóttir and J.A. Bakken. Current distribution in submerged arc furnaces for silicon metal/ferrosilicon production. In *The 12th International Ferroalloys Congress*, pages 717–728, 2010.

[87] E. Scheepers, A. Adema, Y. Yang, and M. Reuter. The development of a CFD model of a submerged arc furnace for phosphorus production. *Minerals Engineering*, 19(10): 1115–1125, 2006.

[88] A. Schei, J.K. Tuset, H. Tveit, et al. *Production of high silicon alloys*. Tapir Trondheim, Norway, 1998.

[89] L.Z. Schlitz, S.V. Garimella, and S.H. Chan. Gas dynamics and electromagnetic processes in high-current arc plasmas. Part I. Model formulation and steady-state solutions. *Journal of Applied Physics*, 85(5):2540–2546, 1999.

[90] D.D. Schnack. *Lectures in magnetohydrodynamics: with an appendix on extended MHD*, volume 780. Springer, 2009.

[91] L.F. Shampine and M.W. Reichelt. The MATLAB ODE suite. *SIAM Journal on Scientific Computing*, 18(1):1–22, 1997.

[92] B.M. Sloman. *Mathematical modelling of silicon furnaces*. DPhil thesis, University of Oxford, UK, 2018.

[93] B.M. Sloman, C.P. Please, and R.A. Van Gorder. Asymptotic analysis of a silicon furnace model. *SIAM Journal on Applied Mathematics*, 78(2):1174–1205, 2018.

[94] B.M. Sloman, C.P. Please, and R.A. Van Gorder. Homogenization of a shrinking core model for gas–solid reactions in granular particles. *SIAM Journal on Applied Mathematics*, 79(1):177–206, 2019.

[95] B.M. Sloman, C.P. Please, and R.A. Van Gorder. Melting and dripping of a heated material with temperature-dependent viscosity in a thin vertical tube. *Journal of Fluid Mechanics*, 905:A16, 2020.

[96] B.M. Sloman, C.P. Please, R.A. Van Gorder, A.M. Valderhaug, R.G. Birkeland, and H. Wegge. A heat and mass transfer model of a silicon pilot furnace. *Metallurgical and Materials Transactions B*, 48(5):2664–2676, 2017.

[97] B.V. Somov. *Plasma Astrophysics, Part I: Fundamentals and Practice*, volume 391. Springer Science & Business Media, 2012.

[98] H.A. Spang III. A dynamic model of a cement kiln. *Automatica*, 8(3):309–323, 1972.

[99] L. Spitzer. *Physics of fully ionized gases*. Courier Corporation, 2006.

[100] Y.A. Tesfahunegn, T. Magnusson, M. Tangstad, and G. Sævarsdóttir. Dynamic current distribution in the electrodes of submerged arc furnace using scalar and vector potentials. In *International Conference on Computational Science*, pages 518–527. Springer, 2018.

[101] Y.A. Tesfahunegn, T. Magnusson, M. Tangstad, and G. Sævarsdóttir. Comparative study of AC and DC solvers based on current and power distributions in a submerged arc furnace. *Metallurgical and Materials Transactions B*, 51(2):510–518, 2020.

[102] Y.A. Tesfahunegn, T. Magnusson, M. Tangstad, and G.A. Sævarsdóttir. Effect of electrode shape on the current distribution in submerged arc furnaces for silicon production - a modelling approach. *Journal of the Southern African Institute of Mining and Metallurgy*, 118(6):595–600, 2018.

[103] A.B. Thompson, G. Richardson, P. Dellar, M. McGuinness, and C. Budd. Arc phenomena in low-voltage current limiting circuit breakers. Study group report. https://www.researchgate.net/publication/265402542_Arc_Phenomena_in_low-voltage_current_limiting_circuit_breakers, 2010.

[104] A.M. Valderhaug. *Modelling and control of submerged-arc ferrosilicon furnaces*. PhD thesis, NTNU, Norway, 1992.

[105] X. Wang, J. Liu, Y. Gong, G. Li, and T. Ma. An electrostatic magnetohydrodynamics theory for resistive-viscous helical instabilities of arc discharges. *Physics of Plasmas*, 4(8):2791–2797, 1997.

[106] Z. Wang, N.H. Wang, and T. Li. Computational analysis of a twin-electrode DC submerged arc furnace for MgO crystal production. *Journal of Materials Processing Technology*, 211(3):388–395, 2011.

[107] A. Westermoen. *Modelling of dynamic arc behaviour in a plasma reactor*. PhD thesis, NTNU, Norway, 2007.

[108] J. Westly. Resistance and heat distribution in a submerged-arc furnace. In *The International Ferroalloys Congress*, volume 1, page 121, 1974.

[109] L. Woods. *Principles of magnetoplasma dynamics*. Clarendon Press, 1987.

[110] L. Yuan, L. Sun, and H. Wu. Simulation of fault arc using conventional arc models. *Energy and Power Engineering*, 5(04):83, 2013.